Viscous Fingering and Liquid Crystals in Confinement

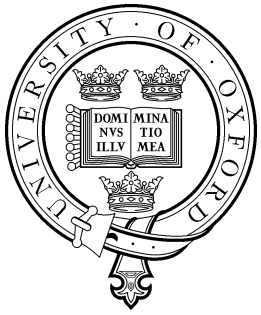

Ioannis Zacharoudiou
Wolfson College
University of Oxford

Thesis submitted in partial fulfilment of the requirements for the degree of Doctor of Philosophy in the University of Oxford

· Trinity Term, 2012 ·

Viscous Fingering and Liquid Crystals in Confinement

Ioannis Zacharoudiou
Wolfson College
University of Oxford

Thesis submitted in partial fulfilment of the requirements for the degree of Doctor of Philosophy in the University of Oxford
· Trinity Term, 2012 ·

Abstract

This thesis focuses on two problems lying within the field of soft condensed matter: the viscous fingering or Saffman-Taylor instability and nematic liquid crystals in confinement.

Whenever a low viscosity fluid displaces a high viscosity fluid in a porous medium, for example water pushing oil out of oil reservoirs, the interface between the two fluids is rendered unstable. Viscous fingers develop, grow and compete until a single finger spans all the way from inlet to outlet. Here, using a free energy lattice Boltzmann algorithm, we examine the Saffman-Taylor instability for two different wetting situations: (a) when neither of the two fluids wet the walls of the channel and (b) when the displacing fluids completely wets the walls. We demonstrate that curvature effects in the third dimension, which arise because of the wetting boundary conditions, can lead to a novel suppression of the instability. Recent experiments in microchannels using colloid-polymer mixtures support our findings.

In the second part of the thesis we examine nematic liquid crystals confined in wedge-structured geometries. In these systems the final stable configuration of the liquid crystal system is controlled by the complex interplay between confinement, elasticity and surface anchoring. Varying the wedge opening angle this competition leads to a splay to bend transition mediated by a defect in the bulk of the wedge. Using a hybrid lattice Boltzmann algorithm we study the splay-bend transition and compare to recent experiments on *fd* virus particles in microchannels. Our numerical results, in quantitative agreement with the experiments, enable us to predict the position of the defect as a function of opening angle, and elucidate its role in the change of director structure. This has relevance to novel energy saving, liquid crystal devices which rely on defect motion and pinning to create bistable director configurations.

To my family

Acknowledgements

First and foremost, I would like to thank my supervisors, Prof. Julia Yeomans, Dr. Dirk Aarts and Dr. Ard Louis for all their guidance, support and patience throughout my PhD studies at Oxford University. I will always be grateful for your commitment. This thesis would not have been what it is without your constructive comments and feedback.

The Rudolf Peierls Centre for Theoretical Physics at Oxford University has been a wonderful academic environment. I was fortunate to meet an excellent group of people, whose help has been invaluable in finishing this thesis, as I benefited greatly from discussions and exchange of ideas with them. Special thanks to Halim Kusumaatmaja, Matthew Blow, Rodrigo Ledesma Aguilar and Miha Ravnik, whose help is greatly appreciated. Furthermore, I would also like to express my gratitude to colleagues from the Physical and Theoretical Chemistry Laboratory, Siti Aminah Setu and Oliver J. Damonne for their experimental contribution to this work.

To all my friends and colleagues who I encountered at Oxford University and the University of Cyprus, especially Andreas Athenodorou, Spyros Sotiriadis, Irwin Zaid, Vic Putz, Nicolas Kanaris, Antonis Antoniou and Giannis Koutsou, I thank you very much for your support and for the invaluable advice you have offered me.

I could never have done this without the love and support of my wonderful wife, Avgousta Kyriakidou Zacharoudiou, my parents Michalis and Maria, my brothers, Spyros and Panagiotis, and my sister Dimitra. A special mention to my in-laws, George and Rena, and sisters in law, Evi and Maria, for embracing me in their family.

I would also like to thank Prof. Andreas Othonos at the University of Cyprus for his support and for establishing a collaboration network with the University of Oxford. Finally, I am grateful to the Cyprus Research Promotion Foundation (Republic of Cyprus) for supporting me financially under project PENEK/SUPPORT/0308/17 (Co-financed by the European Regional Development Fund) and the Leventis Foundation.

Contents

Chapter 1

Introduction

Interfaces are ubiquitous in nature. Understanding their behavior is not only of theoretical interest, but is also crucial for many technological and industrial applications. In this thesis we first study the forced displacement of a fluid-fluid interface that leads to the formation of viscous fingers. This interfacial instability is known as the Saffman-Taylor instability [1]. Although known from the beginning of last century, especially to engineers in the oil industry, the Saffman-Taylor instability is still not fully understood. In particular, the instability has usually been considered as a two dimensional problem and the role of the third dimension in its formation had been overlooked. Here we unravel the importance of the third dimension and describe, for the first time, a mechanism of controlling the onset of the instability. The development of viscous fingering is desired in some contexts and undesirable in others. For example the instability can be exploited to mix fluids or increase the interfacial area between fluids, especially in microfluidic devices, where inertial effects are no longer important. On the contrary the development of viscous fingering in the process of oil extraction from an oil field is, of course, economically unfavorable.

The second part of the thesis is devoted to the study of nematic liquid crystals in confinement. Labeled as *"mesomorphic phases"*, since they can be considered as an intermediate form of matter, they possess properties between those of solids and liquids. Beside the theoretical interest in liquid crystals, study of these systems is highly motivated by their many technological applications. For example liquid crystals are widely used in display technology. Confinement adds to the complexity of liquid crystal systems, since the confining boundaries may impose different ordering of the liquid crystal molecules to that in the bulk. Therefore, the equilibrium

configuration is determined by a complex interplay of confinement, elasticity and surface anchoring. Here we will examine numerically nematic liquid crystals confined in wedge-structured channels, and comparison will be made to experiments in structured microchannels.

This thesis is organised as folllows: Chapter 2 introduces the Saffman-Taylor instability and gives an outline of previous theoretical, experimental and numerical work on the viscous fingering problem. Then in Chapter 3, we present the basic concepts of the numerical algorithm that we shall use in the subsequent chapters to study the viscous fingering problem. This is the free energy lattice Boltzmann approach to solving the hydrodynamic equations of motion. Chapter 4 examines the Saffman-Taylor instability in the neutral wetting regime, when neither of the two fluids wets the walls, and gives a comparison of lattice Boltzmann simulations to previous work on the subject. The complete wetting regime, when the displacing fluid completely wets the walls, is then considered in Chapter 5. Lattice Boltzmann simulations are compared to recent experiments in microchannels using colloid-polymer mixtures showing a very good agreement. We argue that the shape of the interface in the third dimension is key to controlling the onset of viscous fingering.

An introduction to liquid crystals is given in Chapter 6. We review the physics of these systems and, in particular, the phenomenological Landau - de Gennes theory [2]. The modeling technique we use to study nematic liquid crystals in confinement, a hybrid lattice Boltzmann algorithm, is also discussed. Chapter 7 examines nematic liquid crystals confined in wedge-structured geometries. The primary motivation for the work presented in this chapter is recent experiments in structured microchannels using *fd* virus particles as a colloidal nematic liquid crystal. The equilibrium configuration in the wedge geometry is determined by the delicate coupling of confinement, surface anchoring and elasticity. A splay to bend transition is observed, which is mediated by a defect in the bulk of the wedge. We demonstrate that the position of the defect within the wedge depends on the splay and bend elastic constants, and can be controlled by varying the wedge opening angle.

Finally, in Chapter 8 we summarise the main conclusions of the thesis and suggest possible future research.

Chapter 2

Saffman-Taylor Instability

In this thesis we turn our attention first to the study of the viscous fingering problem or the so-called Saffman-Taylor instability, named after Philip Saffman and Sir Geoffrey Ingram Taylor [1]. This instability has received much attention in the previous half century due to its relative simplicity and its importance in a wide variety of practical/industrial applications, arguably the most important of which are in the oil industry. It is probably one of the classical fluid mechanics problems that is most easily accessible to theory and experiments [3]. However, despite its apparent simplicity as a problem of almost two-dimensional potential flow, it has not been fully understood so far. Discrepancies still remain between the experimental results and theoretical/numerical work.

We shall start in section 2.1 with introducing the Saffman-Taylor instability. Then in section 2.2 we shall present manifestations of the instability, which involve, among other things, the initial motivation that led Saffman and Taylor to the first account of the viscous fingering problem [1]. Section 2.3 will deal with an overview of previous work on Saffman-Taylor instability, both experimentally and theoretically. We will start with the pioneering work of Saffman and Taylor, followed by extensions to their original two-dimensional theory by other researchers. Finally, we shall present the derivation of the Saffman-Taylor instability in section 2.4, by performing a linear stability analysis of a flat interface that is subjected to a small perturbation.

2.1 The Saffman-Taylor instability

The Saffman-Taylor instability is an interfacial instability that refers to the formation of patterns on the unstable interface between two fluids. It occurs when a low viscosity fluid displaces a fluid with higher viscosity. In the reversed situation, with the more viscous fluid displacing the less viscous one, the interface between the two fluids remains stable.

In order to study the instability, experimental research was carried out in an almost two dimensional geometry – a channel formed of two long flat parallel plates separated by a narrow gap called a Hele-Shaw cell. Fig. 2.1 shows images, taken at different times, from experiments on the instability performed by Saffman and Taylor [1]. In these images, air, which is the upper fluid, is used to displace glycerine in a Hele-Shaw cell. The interface becomes unstable while it moves downwards, as depicted in Fig. 2.1(a), and leads to the formation of finger-like structures on the fluid-fluid interface. Fig. 2.1(c) shows that, gradually, one finger gets ahead of the neighboring fingers. Eventually, as can be seen from Fig. 2.2, a single finger spans the whole channel, moving with velocity U and occupying a fraction $\lambda_f = w_f/w$ of the channel width, where w_f and w are the finger and channel widths respectively.

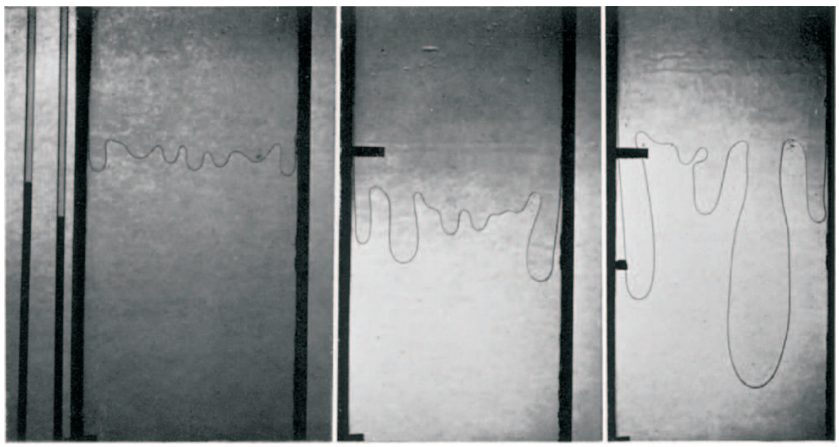

Figure 2.1: Images from the experiments of Saffman and Taylor showing air (upper fluid) displacing glycerine (lower fluid) in a Hele-Shaw cell [1]: (a) An early stage of the instability. (b) Development of Saffman-Taylor instability. (c) Inhibiting effect of a finger which gets ahead of its neighbours.

The convention that we shall use throughout this thesis is that the plane of the instability is the x-y plane as depicted in Fig. 2.2, while the channel thickness direction will be along the

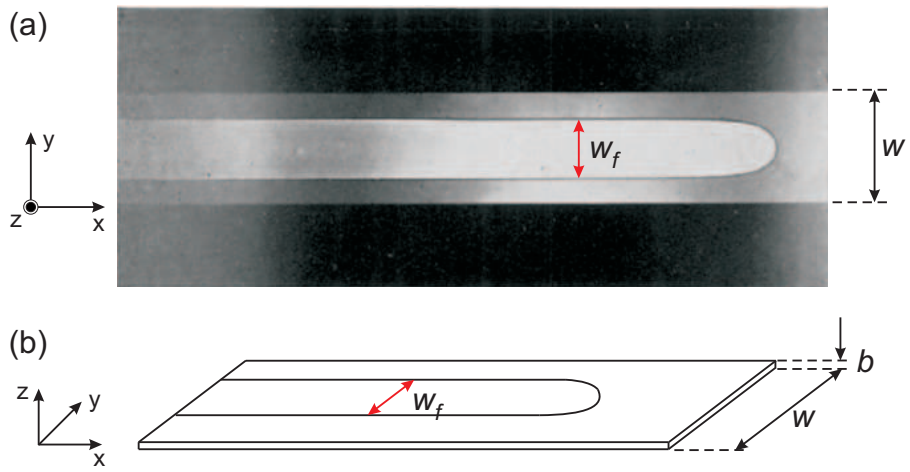

Figure 2.2: (a) A single finger of width $w_f = \lambda_f w$ advances in a Hele-Shaw cell. Image from the experiments of Saffman and Taylor [1]. (b) Schematic diagram of a Hele-Shaw cell with two long flat parallel plates in the x-y plane separated by a narrow gap of length b.

z-axis.

2.2 Physical examples

Arguably the most important manifestation of the Saffman-Taylor instability is in enhanced oil recovery. This becomes even more crucial as sources of energy run out. Oil is generally found in porous rock. Initially, due to high pressure in the reservoir the crude oil can easily be extracted. However, the pressure decreases rapidly and several techniques have been developed in order to increase the amount of crude oil that can be extracted from an oil field, for example gas (CO_2, natural gas or nitrogen) or water injection. These techniques are known as enhanced oil recovery or for more advanced, speculative, techniques as quaternary recovery.

Fingering phenomena can, however, be a serious problem, since the less viscous fluid – gas or water – used to push the oil penetrates into the porous rock without completely displacing the oil. As a result a significant amount of oil is left unexploited; sometimes up to 50% of the total reservoir.

The Saffman-Taylor instability is crucial in a wide variety of other engineering contexts as well. These include groundwater transport, packed bed separations and chemical process applications such as chromatography [4–8]. In these situations, as in secondary oil recovery, the appearance of viscous fingers by virtue of the Saffman-Taylor instability reduces the desired

efficiency. However, the instability in other contexts can be useful. For example it can be exploited in microfluidic devices to mix fluids and enhance their chemical reaction by increasing their interfacial area. Even research on the structure generation in flow below volcanic systems [9] involved the study of Saffman-Taylor instability.

2.3 Previous work – Overview

In the following subsections we present an overview of the theoretical and experimental research, which has been applied to study the viscous fingering problem.

2.3.1 Saffman and Taylor's original study of the instability

We have seen in section 2.2 that viscous fingering was well known to mining engineers from a very early stage. However, it was not until 1958 that the first detailed account of the instability was given by Saffman and Taylor [1] following a visit by Sir Geoffrey Taylor to the "Humble Oil Company" in about 1956.

Saffman and Taylor performed experiments in a Hele-Shaw cell to study the viscous fingering problem. The choice for this experimental geometry/apparatus was because flow in porous media and in a Hele-Shaw cell are both governed by Darcy's law. This describes the relation between the average velocity U parallel to the plates and the applied force $-\nabla P(x,y)+\rho_i g$ as

$$U(x,y) = -\frac{K}{\eta_i}\Big(\nabla P(x,y) - \rho_i g\Big), \tag{2.1}$$

where $i = 1, 2$ labels the two fluids and η_i, ρ_i denote the fluid viscosity and fluid density respectively. The coefficient K is the permeability of the porous medium, which for the Hele-Shaw apparatus is $K = -b^2/12$, with b the channel thickness.

As we have already described in section 2.1, experimentally, when a viscous fluid is driven steadily by a less viscous one through a Hele-Shaw cell, fingerlike structures emerge and compete. Eventually this leads to the formation of a single, dominant finger, which occupies a characteristic fraction of the channel width. Saffman and Taylor's aim was to:
a) measure the relative width of the finger $\lambda_f = w_f/w$, where w_f and w are the finger and channel widths respectively and
b) determine the dependence of the finger width on the finger's velocity.

Saffman and Taylor's experiments revealed that the finger width λ_f is a function of the velocity at which the finger moves, or more generally of the capillary number, defined as $Ca = \eta U/\sigma$ [1], which describes the relative effect of viscous forces to surface tension σ. Fig. 2.3 shows results for the finger width λ_f plotted versus Ca from Saffman and Taylor's experiments. At low Ca the less viscous fluid displaces almost all of the resident fluid, i.e. $\lambda_f \to 1$. As the Ca increases, λ_f decreases to an asymptotic limit of 1/2, so the advancing finger occupies half of the channel width.

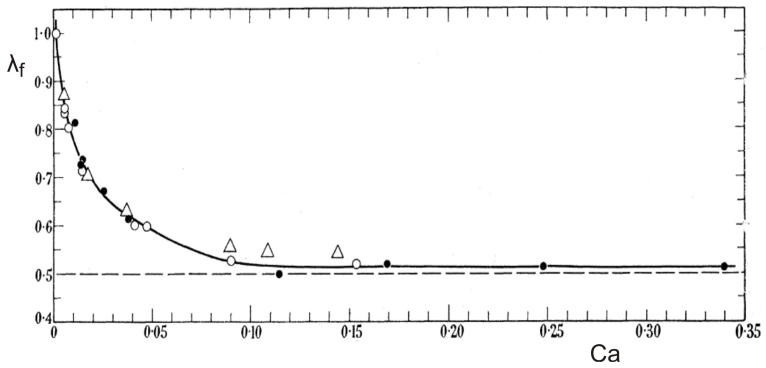

Figure 2.3: Finger width λ_f versus Ca for systems of water penetrating into different oils (different symbols) from Saffman and Taylor's experiments. Figure from [1].

Besides performing experiments, Saffman and Taylor also solved the problem analytically in two dimensions for the case of zero surface tension, which corresponds to neglecting the pressure drop at the interface due to surface tension. Their solutions predicted a whole family of finger widths λ_f at each velocity. This non-uniqueness of the solution for λ_f was not in agreement with their experimental results and meant that they were unable to predict the dependence of λ_f on the finger's velocity.

Saffman and Taylor did, however, obtain the finger shape as a function of the finger width λ_f. They predicted that the interface profile is described by

$$x' = \left(\frac{1-\lambda_f}{\pi}\right) \ln\left[\frac{1}{2}\left(1+\cos\frac{\pi y'}{\lambda_f}\right)\right], \tag{2.2}$$

where x', y' measure the distance from the finger tip in units of half the channel width w, i.e. $y' \in [-1, 1]$. They pointed out, though, that their prediction deviates from the actual

[1] Here, only the viscosity of the more viscous fluid appears in the Ca, since the less viscous fluid is considered inviscid.

interface profile; good agreement was obtained only as $\lambda_f \to 1/2$. Finger profiles evaluated using Eq. (2.2) are shown in Fig. 2.4.

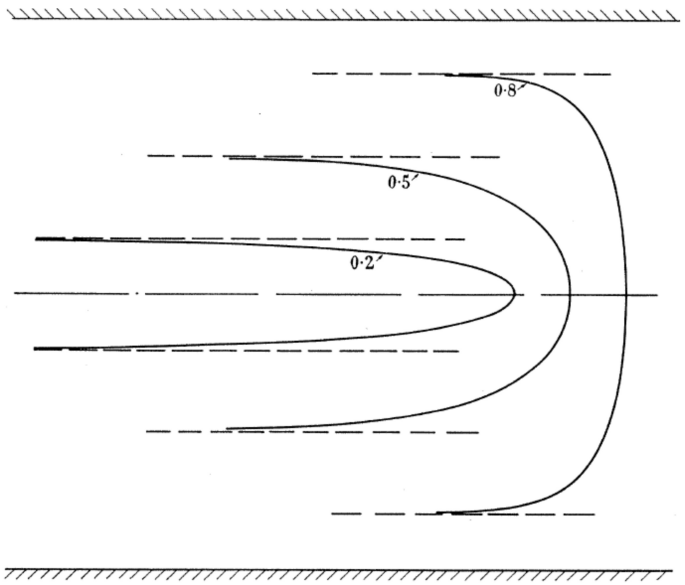

Figure 2.4: Finger profiles for $\lambda_f = 0.2, 0.5$ and 0.8 evaluated using Eq. (2.2). Image from [1].

Extending to the case where surface tension σ is included, and by performing a linear stability analysis of an initially flat interface that is being perturbed, Saffman and Taylor showed that the amplification factor $\omega(k)$ for a given perturbation of wavevector k is given by

$$\omega(k) = \frac{1}{(\eta_1 + \eta_2)} \Big\{ (\eta_1 - \eta_2) U k - \frac{\sigma k^3 b^2}{12} \Big\}, \tag{2.3}$$

where η_1, η_2, U are the viscosities of the two fluids ($\eta_1 > \eta_2$) and the finger velocity respectively. The linear stability analysis provides information about the growth rate of perturbations on the fluid-fluid interface.

The details and proof of Eq. (2.3) are postponed to section 2.4 to allow us to follow the historical development of the Saffman-Taylor instability without interruption. Eq. (2.3) is valid for the case of a horizontal Hele-Shaw cell, so that gravity is perpendicular to the plane of the instability and, hence, does not play any role.

If the amplification factor $\omega(k)$ is positive, then the initial perturbation will grow exponentially leading to the formation of a finger. It is clear from Eq. (2.3) that viscous fingers are the result of a competition between surface tension and viscous forces. Surface tension tends

to maximise the radius of curvature at the tip of the finger and, therefore, tends to widen the finger and restore the interface to its equilibrium shape, while viscous stresses tend to narrow the finger as they seek to decrease the resistance for the penetrating fluid.

2.3.2 Pitts account of the Saffman-Taylor instability

Pitts [10] achieved an improved phenomenological description of the interface profile by making the observation that the finger shape satisfies the relation $R\sin(\theta) = const$, with R the local radius of curvature and θ the angle between the tangent to the interface and the direction of motion of the finger. Using this condition Pitts described the shape of the fingers as

$$\cos\left(\pi y'/2\lambda_f\right) = \exp\left(\pi x'/2\lambda_f\right), \tag{2.4}$$

which proved to be in very good agreement with the experimental profiles. As Pitts himself stated, however, a satisfactory justification of this relation has not been found.

Furthermore, Pitts included the effect of surface tension on the pressure drop at the finger's interface and solved the problem analytically using conformal mapping techniques. His account of the Saffman-Taylor instability was based on two arguments: a) that the condition for the interface shape described in Eq. (2.4) is valid and b) the radius of curvature at the tip of the finger in the plane perpendicular to the plates, $R_\perp$, decreases from the static value of $b/2$ by a constant factor m, due to the motion of the finger; so $R_\perp = b/2m$. Pitts' solution suggested that the relative finger size λ_f should be a function of Ca/ϵ, where $\epsilon = b/w$ is the aspect ratio of the cell. However, we have to note here that the assumptions are not self-evident as pointed out by Pitts himself. In particular the second assumption, which implies that the radius of curvature in the gap of the cell remains constant and is insensitive to the Ca, is difficult to justify.

2.3.3 McLean & Saffman extensions to the theory

In 1981 McLean and Saffman [11] took into account the effect of surface tension and, with no assumptions on the finger shape, solved the viscous fingering problem numerically. Using free streamline techniques they reduced the equations for the movement of the interface to a pair of nonlinear integro-differential equations, which they solved numerically. They pointed out

that the width of the stationary finger is determined by a single control parameter, a modified capillary number defined as

$$\kappa^{-1} = Ca \frac{12(w/2)^2(1-\lambda_f)^2}{b^2\pi^2} \ . \tag{2.5}$$

So, contrary to Pitts, McLean and Saffman suggested that λ_f is a function of Ca/ϵ^2 and not Ca/ϵ. The qualitative behavior, though, remained the same, with λ_f being a monotonically decreasing function of Ca, with a limiting value of $\lambda_f = 1/2$ for large Ca. It is worth noting here that, for the case of small surface tension, which they examined by conventional singular perturbation methods, they found that the equations of motion do not have a unique solution, something that was in conflict with their numerical results.

From this time on, the control parameter found in the literature to describe the instability is a modified capillary number [4]

$$\frac{1}{B} = \frac{12}{\epsilon^2} \frac{\Delta\eta \, U}{\sigma} \ , \tag{2.6}$$

in which $\Delta\eta = \eta_1 - \eta_2$ is the viscosity difference of the two fluids. This control parameter should be attributed to McLean and Saffman, since they were the first to show that λ_f should be a function of Ca/ϵ^2.

2.3.4 Tabeling & Libchaber corrections to the two-dimensional theory

Despite the theoretical efforts to reproduce the experimental results for the finger width λ_f, the numerical study of McLean and Saffman [11] predicted finger sizes significantly below those found experimentally, in a wide range of the fingers' velocities. This is evident from Fig. 2.5, where the experimental results are compared to the theory. Tabeling and Libchaber showed that introducing the control parameter proposed by McLean and Saffman [11] alone is not enough to fully describe the instability [12]. They argued that this is partly due to a thin layer of the more viscous fluid next to the walls which is left behind the advancing finger. This changes the curvature of the advancing interface in the z direction, $R_\perp$, and renders the problem three dimensional. Theorists, including McLean and Saffman, neglected these variations in $R_\perp$ and assumed that $R_\perp$ is constant and equal to half of the channel thickness

($R_\perp = b/2$). Furthermore, they used the boundary condition

$$\Delta P = \sigma \frac{1}{R_\parallel} \tag{2.7}$$

for the pressure drop across the interface, with $R_\parallel$ the interface radius of curvature in the plane parallel to the plates. However, this only holds if the problem is really two-dimensional. Since the interface is actually three-dimensional with two radii of curvature, one in the plane of the instability $R_\parallel$ and one in the perpendicular direction $R_\perp$, it would also be applicable if $1/R_\parallel \gg 1/R_\perp$, i.e. for a weakly curved interface in the channel thickness direction. However, given the fact that experimentally, in most cases, the more viscous fluid is the wetting fluid, then the dominant term is actually the second one since $R_\perp \ll R_\parallel$.

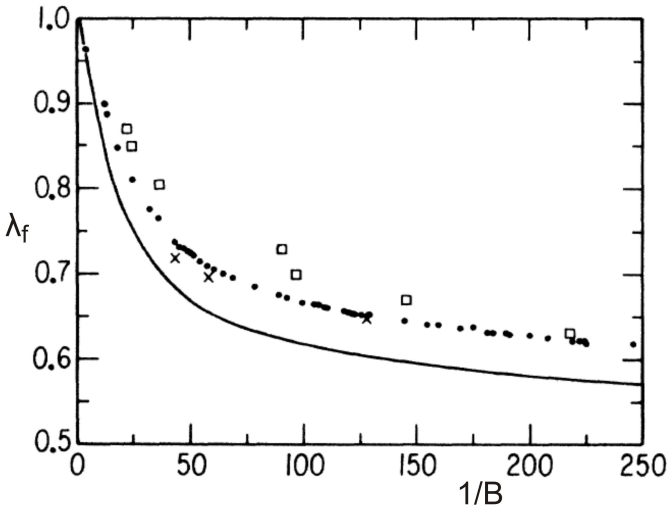

Figure 2.5: Finger width λ_f as a function of $1/B$. Experimental results of: a) Saffman and Taylor (□) and b) Tabeling and Libchaber (•,×). The solid line describes the theoretical results of McLean and Saffman [11]. Figure from [12].

Tabeling and Libchaber [12] proposed that the approximation Eq. (2.7) for the pressure drop can be valid if an appropriate rescaled surface tension is used. From the Young-Laplace condition

$$\Delta P = \sigma\Big(\frac{1}{R_\parallel} + \frac{1}{R_\perp}\Big) = \frac{\sigma}{R_\parallel}\Big(1 + \frac{R_\parallel}{R_\perp}\Big) = \frac{\sigma^*}{R_\parallel} \,. \tag{2.8}$$

Therefore, the rescaled surface tension should be

$$\sigma^* = \sigma\Big(1 + \frac{R_\parallel}{R_\perp}\Big) \,. \tag{2.9}$$

Experimentally, it was not easy to measure $R_\perp$ accurately, so Tabeling and Libchaber used the theoretical prediction of Park and Homsy [13] for the pressure drop across the interface at the limit of small Ca and weakly curved interface

$$\Delta P = \frac{\sigma}{b/2}\Big(1 + 3.80Ca^{2/3}\Big) + \frac{\pi}{4}\frac{\sigma}{R_\parallel}\,. \tag{2.10}$$

By applying this to their experiments they found that the pressure drop should be given by

$$\Delta P = \frac{\sigma}{R_\parallel}\left(\frac{\pi}{4} + 7.4Ca^{2/3}\cos^{2/3}(\theta)\frac{R_\parallel}{b}\right), \tag{2.11}$$

where θ is the angle of the normal of the interface and the direction of finger motion. Using this expression they introduced a rescaled surface tension

$$\sigma^* = \sigma\Big(\frac{\pi}{4} + 1.7\lambda_f(w/b)Ca^{2/3}\Big) \tag{2.12}$$

in the definition of the control parameter

$$1/B^* = (12/\epsilon^2)(\Delta\eta U/\sigma^*) = (1/B)\,(\sigma/\sigma^*)\,. \tag{2.13}$$

The experimental results obtained by Tabeling and Libchaber for the finger width collapsed on the two-dimensional prediction of McLean and Saffman, when plotted versus this rescaled modified capillary number $1/B^*$, for intermediate values of $1/B^*$. However, for large values of $1/B^*$, and sufficiently large aspect ratios ϵ, they showed that the finger width λ_f can go below the $1/2$ limit predicted by McLean and Saffman. They argued that this should be attributed to the effect of the thin film of the displaced fluid remaining on the surface of the cell as the finger advances.

Recently, Ledesma *et al.* [14, 15] used lattice Boltzmann simulations to study the Saffman-Taylor instability numerically. They considered neutral wetting, that is the two fluids wet the walls equally and, therefore, the equilibrium contact angle $\theta_{eq} = 90°$. They first examined the forced displacement of the fluid-fluid interface in the x-z plane to determine when the interface is advancing as a meniscus and when a thin film develops in the gap of the cell. They refer to the former as the Meniscus regime and the latter as the Thin Film regime. In this thesis we

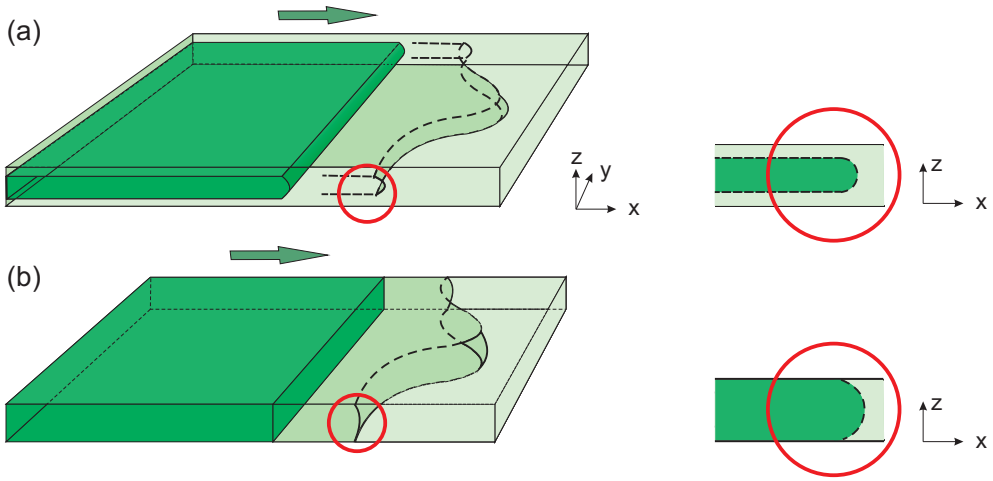

Figure 2.6: (a) A thin film of the displaced fluid wets the walls. This contributes to the capillary pressure at the tip of the finger and needs to be taken into account. We will refer to this configuration as the "Thin Film regime". (b) The less viscous fluid advances as a meniscus and completely displaces the resident fluid in the x-z plane, while the Saffman-Taylor instability develops in the x-y plane. We will refer to this configuration as the "Meniscus regime".

shall use the same nomenclature for the two regimes. These two possible configurations are shown in Fig. 2.6. The reasoning behind this investigation is that throughout the literature the resident fluid in the Hele-Shaw cell was wetting the walls. Therefore, experimentally, researchers were encountering a situation where a thin layer of the displaced fluid was on the walls as in Fig. 2.6(a).

Ledesma *et al.* showed that the interface profile in the x-z plane is governed by the interplay of capillary and Péclet numbers. The Péclet number $Pe = Ub/D$, where D is the diffusion coefficient, is a measure of the relative importance of advection to diffusion. For low values of $CaPe$ the interface is advancing as a meniscus, as in Fig. 2.6(b), while for large values of $CaPe$ a thin film develops in the channel thickness direction (see Fig. 2.6(a)). For the neutral wetting case they had examined, an upper bound for the Meniscus regime was found to be

$$CaPe \approx 0.5 \,, \tag{2.14}$$

while for larger values of $CaPe$ the less viscous fluid penetrates in the x-z plane.

Ledesma *et al.* then turned their attention to the plane of the Saffman-Taylor instability, the x-y plane, and examined the finger width λ_f for the Meniscus and the Thin Film regimes.

By measuring the interfacial curvature, at the tip of the finger, in the x-y and x-z planes they rescaled surface tension as in Eq. (2.9). Their results of λ_f versus $1/B^*$ collapsed on the two-dimensional prediction of McLean and Saffman for total displacement of the more viscous fluid in the x-z plane. Therefore, in the Meniscus regime the problem can be rendered two-dimensional, when curvature corrections are used as contributions to surface stresses. When a thin film develops in the x-z plane, however, they showed that the finger width λ_f decreases with increasing aspect ratio and that results deviate from the two-dimensional prediction, especially for high values of $1/B^*$.

2.4 Derivation of the Saffman-Taylor instability - Linear stability analysis in the two-dimensional limit

Here we present the linear stability analysis of an almost flat interface in a Hele-Shaw cell that is subjected to a small perturbation. This analysis assumes a two-dimensional interface, by averaging the equations of motion across the channel thickness direction.

From Darcy's law, the gap averaged velocity in a horizontal Hele-Shaw cell is

$$U = -\frac{b^2}{12\eta}\nabla P \ .$$

Therefore, the pressure gradients needed to maintain the motion of a flat interface such as the

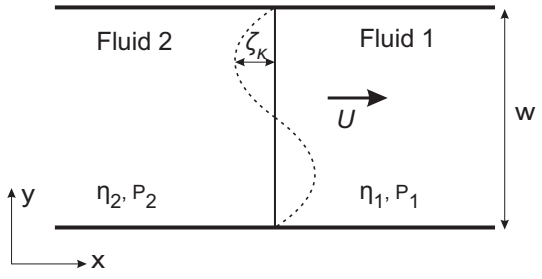

Figure 2.7: Schematic diagram of the fluid-fluid interface moving with velocity U.

one shown in Fig. 2.7 are

$$\frac{dP_1}{dx} = -\frac{12\eta_1 U}{b^2} \ , \tag{2.15a}$$

$$\frac{dP_2}{dx} = -\frac{12\eta_2 U}{b^2} \ . \tag{2.15b}$$

For a flat interface

$$P_1 = -\frac{12\eta_1 U}{b^2}(x - Ut) + P_0 \ , \tag{2.16a}$$

$$P_2 = -\frac{12\eta_2 U}{b^2}(x - Ut) + P_0 \ . \tag{2.16b}$$

Now, if we suppose that the interface is perturbed in such a way that at time t it lies at

$$x = X = Ut + \zeta_k \exp\{iky\} \tag{2.17}$$

there must be some corresponding perturbation in P_1 and P_2, which must have the same periodicity in the y direction. Assuming that the fluids are incompressible, the velocity field obeys the continuity equation $\nabla \cdot U = 0$. Hence, P_1 and P_2 obey Laplace's equation $\nabla^2 P = 0$ and they must vary like $\exp\{\pm kx\}$. For P_1, P_2 to remain finite as $x \to -\infty$ and $x \to \infty$ respectively

$$P_1 = -\frac{12\eta_1 U}{b^2}(x - Ut) + A_1 \exp\{k(x - Ut)\} \exp\{iky\} + P_0 \ , \tag{2.18a}$$

$$P_2 = -\frac{12\eta_2 U}{b^2}(x - Ut) + A_2 \exp\{-k(x - Ut)\} \exp\{iky\} + P_0 \ . \tag{2.18b}$$

The boundary conditions at the interface are: a) the velocity across the interface is continuous and b) the pressure drop across the interface is given by the Young-Laplace condition, that is the pressure drop equals the surface tension times the curvature κ.
Then the continuity of the velocity across the interface reads

$$U_{1x} = U_{2x} = \frac{\partial X}{\partial t} \ . \tag{2.19}$$

From Eq. (2.15) and Eq. (2.17), Eq. (2.19)

$$-\frac{b^2}{12\eta_1}\frac{\partial P_1}{\partial x} = -\frac{b^2}{12\eta_2}\frac{\partial P_2}{\partial x} = U + \frac{\partial \zeta_k}{\partial t}\exp\{iky\} \tag{2.20}$$

and using Eq. (2.18) leads to

$$-\frac{b^2}{12\eta_1} k A_1 = \frac{b^2}{12\eta_2} k A_2 = \frac{\partial \zeta_k}{\partial t} \ . \tag{2.21}$$

The second boundary condition at the interface that refers to the pressure drop across the interface

$$\Delta P = P_2 - P_1 = -\sigma\kappa \approx -\sigma\frac{\partial^2 X}{\partial y^2} \ . \tag{2.22}$$

Using Eq. (2.18) and Eq. (2.17) this yields

$$A_1 - A_2 = \left\{\sigma k^2 - (\eta_2 - \eta_1)\frac{12U}{b^2}\right\}\zeta_k \ . \tag{2.23}$$

Eliminating A_1 and A_2 using Eq. (2.21) leads to

$$\omega(k) = \frac{1}{\zeta_k}\frac{\partial \zeta_k}{\partial t} = \frac{1}{\eta_1 + \eta_2}\left\{(\eta_1 - \eta_2)Uk - \frac{\sigma b^2 k^3}{12}\right\} \ . \tag{2.24}$$

Eq. (2.24) gives the amplification factor or growth rate for a perturbation of wavevector k. If this is positive, then the interface is unstable and the amplitude of any perturbation of wavevector k increases at an exponential rate. If, however, the growth rate is negative then the interface remains stable since any deviation from a flat interface will die out.

If we define the dimensionless wavenumber $\tilde{k} = wB^{1/2}k$, Eq. (2.24) becomes

$$\omega(\tilde{k}) = \frac{\Delta\eta U}{(\eta_1 + \eta_2)}\frac{\tilde{k}}{wB^{1/2}}(1 - \tilde{k}^2) \ , \tag{2.25}$$

which leads to the universal dispersion relation

$$\tilde{\omega}(\tilde{k}) = \tilde{k}(1 - \tilde{k}^2) \ , \tag{2.26}$$

where $\tilde{\omega}(\tilde{k}) = \omega(k)wB^{1/2}/rU$ is the dimensionless frequency, and $r = \Delta\eta/(\eta_1 + \eta_2)$ the viscosity contrast ratio. From this, it is easily seen that there is a wavenumber cutoff

$$\tilde{k}_{cr} = 1 \Rightarrow k_{cr} = \frac{1}{wB^{1/2}} \tag{2.27}$$

and that maximum growth rate occurs for

$$\tilde{k}_{max} = \sqrt{1/3}\tilde{k}_{cr} \ . \tag{2.28}$$

Eq. (2.27) defines the region of unstable modes, $0 \leq k \leq k_{cr}$, and it is clear that it depends on the geometry of the cell, through the width w, and the control parameter $1/B$. The region of stable modes is characterised by $k > k_{cr}$.

2.5 Summary

In this chapter, we introduced the Saffman-Taylor instability in section 2.1, and presented several examples of viscous fingering in section 2.2. The most important of these is arguably in the oil industry and it was this that triggered the initial interest in the viscous fingering problem and led to the first detailed experimental and theoretical account of the instability by Saffman and Taylor in 1958 [1]. In section 2.3 an overview of previous work on Saffman-Taylor instability was presented, starting from the pioneering work of Saffman and Taylor. This initial attempt was incomplete and in subsequent subsections we discussed extensions to their original two-dimensional theory by other researchers [10–12, 14, 15].

Finally, in section 2.4 we derived the dispersion relation for the Saffman-Taylor instability, by performing a linear stability analysis of a flat interface that is subjected to a small perturbation. This defines the regions of stable and unstable modes and determines when viscous fingering occurs.

Chapter 3

Lattice Boltzmann Method

In this chapter we shall present the numerical algorithm we use to study the viscous fingering problem in subsequent chapters. This is based on the lattice Boltzmann method [16, 17], which is a computational algorithm for simulating a wide variety of complex fluid flow problems including single and multiphase flow in complex geometries. It constitutes a mesoscale approach [16], because it numerically solves the hydrodynamic equations of motion "by exploiting the underlying microscopic structure of these equations, without resorting to a description of the fluid in terms of molecular dynamics" [18].

We use an extension of the method, a numerical approach often called the free energy lattice Boltzmann method, first introduced by Swift *et al.* [19, 20]. This algorithm belongs to a class of hydrodynamic models, called diffuse interface models [21–24], where the fluid-fluid interface has a finite size. Far away from a contact line, the method solves the hydrodynamic equations of motion of the fluid, i.e. the Navier-Stokes equations and the continuity equation. In the vicinity of the contact line, however, due to the finite size of the interface, the method introduces a diffusive mechanism, which regularizes the viscous dissipation singularity [25] and allows the contact line to slip on a solid substrate.

One of the most important advantages of the method is that, when simulating a binary fluid, this approach avoids the need to track the time evolution of the interface between two different phases [26]. This makes it ideal to study problems involving the time evolution of driven fluid-fluid interfaces, like the Saffman-Taylor instability.

We shall describe in section 3.1 the thermodynamics for a binary fluid, where the two phases contain particles of two different types. In the standard binary model that we use, the

two phases have the same density. Then in section 3.2 we shall present the hydrodynamic equations of motion for a binary fluid, which are the continuity and Navier-Stokes equations coupled to a convection-diffusion equation that describes the dynamics of the order parameter. These equations are solved using a lattice Boltzmann algorithm, the implementation of which is presented in section 3.3 in a single relaxation time approximation. In section 3.4 we shall explain how solid boundaries are implemented in the algorithm.

Using a single relaxation time lattice Boltzmann algorithm, however, does not avoid unphysical currents at the three-phase contact point, when the two components of the binary fluid have different viscosities, and leads to incorrect equilibrium contact angles [27]. Since our study of the Saffman-Taylor instability will inevitably involve the study of moving contact lines and fluid-fluid interfaces, care needs to be taken in treating these boundaries. The use of a multiple relaxation time lattice Boltzmann algorithm [28, 29], that we shall describe in section 3.5, suppresses the spurious currents and proves to be extremely useful for the study of viscous fingering.

3.1 Thermodynamics of the fluid

The equilibrium properties of a two component, two phase fluid (binary fluid), can be described by a Landau free energy functional [24]

$$\mathcal{F} = \int_V \left(f_b + \frac{\kappa_\phi}{2} (\partial_\alpha \phi)^2 \right) dV + \int_S f_s \, dS \, . \tag{3.1}$$

The first term in the integrand is the bulk free energy density given by

$$f_b = \frac{c^2}{3} \rho \ln \rho + \frac{A}{2} \phi^2 + \frac{B}{2} \phi^4 \, , \tag{3.2}$$

where ϕ is the concentration or order parameter, ρ is the fluid mass density and c is a lattice velocity parameter. This choice of f_b allows binary phase separation into two phases if $A < 0$ and $B > 0$ with bulk equilibrium solutions $\phi_{eq} = \pm(-A/B)^{1/2}$. Throughout the thesis we make the choice $A = -B$, which leads to $\phi_{eq} = \pm 1$. The term $\frac{c^2}{3} \rho \ln \rho$ will give a familiar expression for the pressure.

The gradient term $\frac{\kappa_\phi}{2} (\partial_\alpha \phi)^2$ in Eq. (3.1) penalizes spatial variations of the order parameter

ϕ, for example across an interface, and is related to the interface tension by $\sigma = \sqrt{-8\kappa_\phi A^3/9B^2}$ and to the interface width through $\xi = \sqrt{-\kappa_\phi/A}$ [24].

The final term in the free energy functional (3.1) describes the interactions between the fluid and the solid surface and gives the surface free energy. Following Cahn [30], the surface energy density is taken to be of the form $f_s = -h\phi_s$, where ϕ_s is the value of the order parameter at the surface. Minimisation of the free energy gives an equilibrium wetting boundary condition [24]

$$\kappa_\phi \, \partial_\perp \phi = -\frac{df_s}{d\phi_s} = -h \; . \tag{3.3}$$

The value of the parameter h is related to the equilibrium contact angle θ_{eq}[1] via [24]

$$h = \sqrt{2\kappa_\phi A}\, \mathrm{sign}\left(\frac{\pi}{2} - \theta_{\mathrm{eq}}\right) \sqrt{\cos\left(\frac{\alpha}{3}\right)\left\{1 - \cos\left(\frac{\alpha}{3}\right)\right\}} \; , \tag{3.4}$$

where $\alpha = \arccos\left(\sin^2\theta_{eq}\right)$ and the function sign returns the sign of its argument.

From the free energy functional Eq. (3.1) we obtain the chemical potential

$$\mu = \frac{\delta \mathcal{F}}{\delta \phi} = A\phi + B\phi^3 - \kappa_\phi \partial_{\gamma\gamma}\phi \; , \tag{3.5}$$

and the pressure tensor [31]

$$P_{\alpha\beta} = \left[p_b - \kappa_\phi \phi \partial_{\gamma\gamma}\phi - \frac{\kappa_\phi}{2}(\partial_\gamma \phi)^2\right]\delta_{\alpha\beta} + \kappa_\phi (\partial_\alpha \phi)(\partial_\beta \phi) \; , \tag{3.6}$$

where $p_b = \frac{c^2}{3}\rho + \frac{1}{2}A\phi^2 + \frac{3}{4}B\phi^4$ is the bulk pressure. Eq. (3.6) determines the dynamics describing how the system approaches equilibrium.

3.2 Hydrodynamics of the fluid

The hydrodynamic equations of motion are the continuity (3.7) and the Navier-Stokes (3.8) equations for a nonideal fluid

$$\partial_t \rho + \partial_\alpha(\rho u_\alpha) = 0 \; , \tag{3.7}$$

$$\partial_t(\rho u_\alpha) + \partial_\beta(\rho u_\alpha u_\beta) = -\partial_\beta P_{\alpha\beta} + \partial_\beta\left[\eta\left(\partial_\beta u_\alpha + \partial_\alpha u_\beta\right)\right] + F_\alpha \; , \tag{3.8}$$

[1] with respect to the component with $\phi_{eq} = 1$.

where ρ, $\mathbf{u}$, $\mathbf{P}$, η, $\mathbf{F} = \rho\mathbf{g}$ are the local fluid mass density, velocity, pressure tensor, dynamic viscosity and body force respectively.

For a binary fluid the equations of motion are coupled with a convection-diffusion equation,

$$\partial_t \phi + \partial_\alpha(\phi u_\alpha) = M\nabla^2\mu \,, \tag{3.9}$$

that describes the dynamics of the order parameter ϕ. M is a mobility coefficient. The equilibrium thermodynamic properties of the fluid enter the equations of motion through the pressure tensor, Eq. (3.6), and the chemical potential, Eq. (3.5).

By expanding the chemical potential μ in powers of $\phi - \phi_{eq}$, for small deviations from equilibrium,

$$\mu = (A + 3B\phi_{eq}^2)(\phi - \phi_{eq}) + O((\phi - \phi_{eq})^2) \,, \tag{3.10}$$

the diffusive term $M\nabla^2\mu$ can be written as $D\nabla^2\phi$ with $D = M(A + 3B\phi_{eq}^2)$ the diffusion coefficient and Eq. (3.9) becomes

$$\partial_t \phi + \partial_\alpha(\phi u_\alpha) = D\nabla^2\phi \,. \tag{3.11}$$

3.3 Lattice Boltzmann implementation - Single relaxation time approximation

Conventional methods directly solve the Navier-Stokes equations in terms of the density ρ and velocity $\mathbf{u}$ and approximate the differential equations by finite differences. On the contrary, the lattice Boltzmann method introduces a number Q of particle distribution functions $f_i(\mathbf{r}, t)$ $(i = 0, ..., Q-1)$, discrete in time and space, which are associated to a set of velocity directions e_i. These distribution functions can be interpreted as the density of fluid, at position $\mathbf{r}$ and time t, which is moving in direction i. Fig. 3.1 shows the directions of the velocities in a three-dimensional model with 19 velocity vectors (D3Q19),

$$\begin{pmatrix} e_{x,0-6} \\ e_{y,0-6} \\ e_{z,0-6} \end{pmatrix} = \begin{bmatrix} 0 & c & -c & 0 & 0 & 0 & 0 \\ 0 & 0 & 0 & c & -c & 0 & 0 \\ 0 & 0 & 0 & 0 & 0 & c & -c \end{bmatrix} \,, \tag{3.12a}$$

$$\begin{pmatrix} e_{x,7-18} \\ e_{y,7-18} \\ e_{z,7-18} \end{pmatrix} = \begin{bmatrix} c & -c & c & -c & 0 & 0 & 0 & 0 & c & -c & c & -c \\ c & c & -c & -c & c & -c & c & -c & 0 & 0 & 0 & 0 \\ 0 & 0 & 0 & 0 & c & c & -c & -c & c & c & -c & -c \end{bmatrix} , \tag{3.12b}$$

where $c = \Delta x/\Delta t$ is the lattice velocity parameter, and Δx, Δt are the discretisation in space and time respectively.

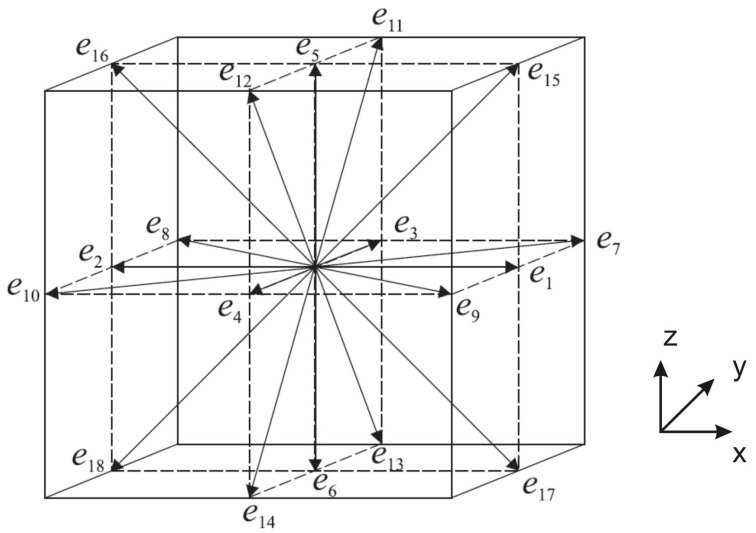

Figure 3.1: The velocity vectors e_i in the 19-velocity, three-dimensional lattice Boltzmann model (D3Q19).

The moments of the velocity distribution functions f_i are related to the physical quantities, mass density ρ and momentum density $\rho\mathbf{u}$

$$\sum_{i=0}^{18} f_i = \rho, \qquad \sum_{i=0}^{18} f_i e_{i\alpha} = \rho v_\alpha, \tag{3.13}$$

where $\mathbf{v}$ is related to the fluid velocity $\mathbf{u}$ through

$$\rho u_\alpha = \rho v_\alpha + \tfrac{1}{2} F_\alpha \Delta t. \tag{3.14}$$

The time evolution of the distribution functions f_i follows two steps

$$\text{Collision step:} \qquad f_i'(\mathbf{r},t) = f_i(\mathbf{r},t) - \frac{1}{\tau_f}[f_i(\mathbf{r},t) - f_i^{eq}(\mathbf{r},t)] + \Delta t F_i \ , \tag{3.15a}$$

$$\text{Propagation step:} \qquad f_i(\mathbf{r} + \mathbf{e_i}\Delta t, t + \Delta t) = f_i'(\mathbf{r},t) \ , \tag{3.15b}$$

where f_i^{eq}, τ_f and F_i are the local equilibrium distribution functions, the relaxation time and the external body force acting on the fluid respectively. Eq. (3.15a) represents one of the simplest collision models, proposed by Bhatnager, Gross and Krook [32], where a single relaxation time approximation is made. The distribution functions f_i relax towards their equilibrium values f_i^{eq} with a relaxation time τ_f, which is related to the dynamic viscosity of the fluid by

$$\eta = \rho c^2 \Delta t(\tau_f - 1/2)/3 \,. \tag{3.16}$$

The relaxation time τ_f has therefore to be greater than 1/2. The collision step is followed by a propagation step Eq. (3.15b), where the populations f_i stream to the next lattice site along e_i.

In order to recover the continuity (3.7) and the Navier-Stokes (3.8) equations in the continuum limit, the following restrictions have to be imposed on the distribution functions and on the forcing term:

$$\sum_{i=0}^{18} f_i^{eq} = \rho, \qquad \sum_{i=0}^{18} f_i^{eq} e_{i\alpha} = \rho u_\alpha, \qquad \sum_{i=0}^{18} f_i^{eq} e_{i\alpha} e_{i\beta} = P_{\alpha\beta} + \rho u_\alpha u_\beta, \tag{3.17a}$$

$$\sum_{i=0}^{18} f_i^{eq} e_{i\alpha} e_{i\beta} e_{i\gamma} = \frac{\rho c^2}{3} \left(u_\alpha \delta_{\beta\gamma} + u_\beta \delta_{\alpha\gamma} + u_\gamma \delta_{\alpha\beta}\right),$$

$$\sum_{i=0}^{18} F_i = 0, \qquad \sum_{i=0}^{18} F_i e_{i\alpha} = F_\alpha, \qquad \sum_{i=0}^{18} F_i e_{i\alpha} e_{i\beta} = u_\alpha F_\beta + u_\beta F_\alpha. \tag{3.17b}$$

3.3.1 Binary fluid

For a binary fluid two sets of particle distribution functions are needed, since there are two molecular species; one (f_i) that is related to the density and momentum by Eqs. (3.13) and (3.14) and a second (g_i) that is related to the concentration

$$\sum_{i=0} g_i = \phi. \tag{3.18}$$

Again, the evolution of the additional distribution functions follows

$$\text{Collision step:} \qquad g_i'(\mathbf{r},t) = g_i(\mathbf{r},t) - \frac{1}{\tau_g}[g_i(\mathbf{r},t) - g_i^{eq}(\mathbf{r},t)] \;, \tag{3.19a}$$

$$\text{Propagation step:} \qquad g_i(\mathbf{r} + \mathbf{e_i}\Delta t, t + \Delta t) = g_i'(\mathbf{r},t) \;, \tag{3.19b}$$

where g_i^{eq} are the equilibrium distribution functions. The relaxation time τ_g is related to the mobility coefficient in the advection-diffusion equation (3.9) by

$$M = \Delta t\, \Gamma(\tau_g - 1/2) \;, \tag{3.20}$$

where Γ is a tunable parameter. As we shall see in the subsequent chapters Γ can be used to tune the slip velocity of the contact line, as the contact line moves via diffusion. The distribution functions g_i^{eq} must obey the following constraints:

$$\sum_{i=0}^{18} g_i^{eq} = \phi, \qquad \sum_{i=0}^{18} g_i^{eq} e_{i\alpha} = \phi u_\alpha, \qquad \sum_{i=0}^{18} g_i^{eq} e_{i\alpha} = \Gamma\mu\delta_{\alpha\beta} + \phi u_\alpha u_\beta \tag{3.21}$$

to correctly reproduce the convection-diffusion equation (3.9).

Taking into account the constraints Eq. (3.17) and Eq. (3.21) for f_i^{eq}, g_i^{eq} and F_i the equilibrium distributions functions and the forcing terms, can be defined as a power series in the velocity [18]

$$\begin{aligned} f_i^{eq} =& \tfrac{w_i}{c^2}\left(p_b - \kappa_\phi \nabla^2\phi + e_{i\alpha}\rho u_\alpha + \tfrac{3}{2c^2}\left[e_{i\alpha}e_{i\beta} - \tfrac{c^2}{3}\delta_{\alpha\beta}\right]\rho u_\alpha u_\beta\right) \\ &+ \tfrac{\kappa_\phi}{c^2}\Big(w_i^{xx}\partial_x\phi\partial_x\phi + w_i^{yy}\partial_y\phi\partial_y\phi + w_i^{zz}\partial_z\phi\partial_z\phi \\ &\quad + w_i^{xy}\partial_x\phi\partial_y\phi + w_i^{xz}\partial_x\phi\partial_z\phi + w_i^{yz}\partial_y\phi\partial_z\phi\Big), \end{aligned} \tag{3.22}$$

$$g_i^{eq} = \tfrac{w_i}{c^2}\left(\Gamma\mu + e_{i\alpha}\phi u_\alpha + \tfrac{3}{2c^2}\left[e_{i\alpha}e_{i\beta} - \tfrac{c^2}{3}\delta_{\alpha\beta}\right]\phi u_\alpha u_\beta\right), \tag{3.23}$$

$$F_i = \tfrac{w_i}{c^2}\left(e_{i\alpha}F_\alpha + \tfrac{3}{2c^2}\left[e_{i\alpha}e_{i\beta} - \tfrac{c^2}{3}\delta_{\alpha\beta}\right](u_\alpha F_\beta + u_\beta F_\alpha)\right), \tag{3.24}$$

with the coefficients [18]

$$
\begin{gathered}
w_{1-6} = \tfrac{1}{6},\ w_{7-18} = \tfrac{1}{12}, \\
w^{xx}_{1,2} = w^{yy}_{3,4} = w^{zz}_{5,6} = \tfrac{5}{12}, \\
w^{xx}_{3-6} = w^{yy}_{1,2,5,6} = w^{zz}_{1-4} = -\tfrac{1}{3}, \\
w^{xx}_{7-10} = w^{xx}_{15-18} = w^{yy}_{7-14} = w^{zz}_{11-18} = -\tfrac{1}{24}, \\
w^{xx}_{11-14} = w^{yy}_{15-18} = w^{zz}_{7-10} = \tfrac{1}{12}, \\
w^{xy}_{1-6} = w^{yz}_{1-6} = w^{xz}_{1-6} = 0, \\
w^{xy}_{7,10} = w^{yz}_{11,14} = w^{xz}_{15,18} = \tfrac{1}{4}, \\
w^{xy}_{8,9} = w^{yz}_{12,13} = w^{xz}_{16,17} = -\tfrac{1}{4}, \\
w^{xy}_{11-18} = w^{yz}_{7-10} = w^{yz}_{15-18} = w^{xz}_{7-14} = 0.
\end{gathered}
$$

Although the choice for the coefficients in Eqs. (3.22)-(3.24) is not unique, it was shown that this choice reduces the unphysical currents, called spurious velocities, that appear close to curved interfaces in lattice Boltzmann simulations [18]. Note also the inter-coupling of the distribution functions f_i^{eg} and g_i^{eg} through the terms $\partial_\alpha \phi$ and $\nabla^2 \phi$ in f_i^{eq}.

The hydrodynamic equations of motion, continuity (3.7), Navier-Stokes (3.8) and convection diffusion equation (3.9), can be obtained by performing a Chapman-Enskog expansion [33] on Eq. (3.15) and Eq. (3.19).

3.4 Boundary conditions

In the lattice Boltzmann simulations we encounter two boundary conditions: the no-slip boundary condition on the velocity field and the wetting boundary condition, Eq. (3.3), on the concentration.

A no-slip boundary refers to the condition at a solid boundary, where the fluid has zero velocity relative to the boundary. The solid walls are introduced into the lattice Boltzmann model, by implementing a midlink bounce-back method proposed by Ladd and Verberg [34], in which incoming populations f_i' are reflected back towards the lattice nodes they came from. This is illustrated in Fig. 3.2 for the one dimensional case. In one dimension there are two distribution functions, $f_1(k,t)$ and $f_2(k,t)$, at x=k, where the subscripts 1, 2 denote the x and

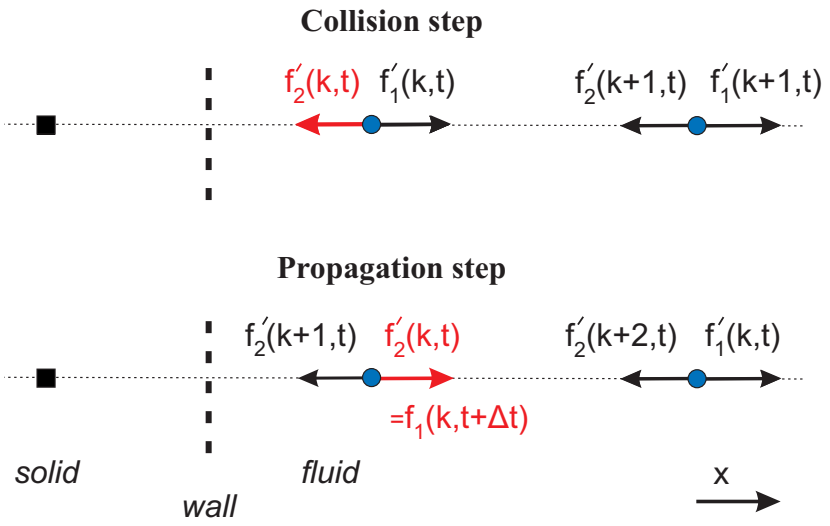

Figure 3.2: The midlink bounce-back method: distribution functions before and after the propagation step, in one dimension. The effective boundary, i.e. the wall, lies halfway between the solid and fluid node.

-x directions respectively. After the collision step, the populations $f_1'(k,t)$ and $f_2'(k,t)$ will propagate along the corresponding directions to the next fluid node. However, when the fluid node is located next to a solid wall, as in Fig. 3.2, the updated distribution function, after the propagation step, $f_1(k, t + \Delta t)$ is undetermined. In the midlink bounce-back method, $f_2'(k,t)$ is reflected and travels back to the node it came from so that $f_1(k, t + \Delta t) = f_2'(k,t)$. The bounce-back step is repeated at the end of each cycle of collision-propagation, and ensures that the no-slip boundary condition is recovered at the solid boundaries. More precisely, the effective boundary, defined as the position of the zero-velocity plane, is located halfway between the fluid and solid nodes.

For the three-dimensional case we follow the same procedure, with advected populations f_i' traveling along links connecting fluid and solid nodes being reflected back towards the fluid node they came from. So $f_{-i}(\mathbf{r}, t+\Delta t) = f_i'(\mathbf{r}, t)$, where the direction $-i$ denotes the direction opposite to i (see Fig. 3.1).

We next consider the implementation of the wetting boundary condition. Eq. (3.3) defines the value of the normal derivative of the concentration $\partial_\perp \phi$ at the substrate in equilibrium. Using this condition and the values for ϕ at the fluid nodes neighbouring the boundary we assign the appropriate values for ϕ at the neighbouring solid nodes. In the schematic diagram shown in Fig. 3.3, this corresponds to assigning a value for ϕ_6 using the value of ϕ_0 and

$d\phi/dz = -h/\kappa_\phi$ from Eq. (3.3)

$$\phi_6 = \phi_0 - d\phi/dz \ . \tag{3.25}$$

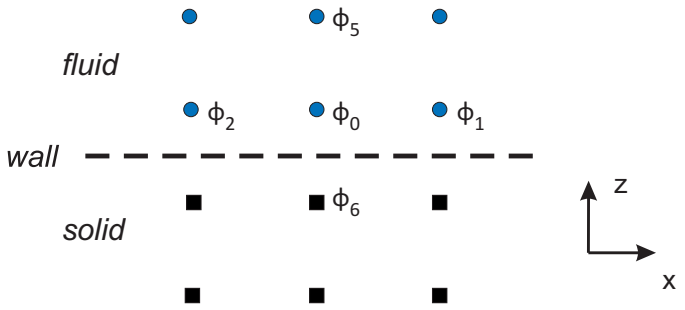

Figure 3.3: Implementation of the wetting boundary condition. Using Eq. (3.3) we assign an appropriate value for the concentration field at the solid nodes neighbouring the boundary.

The main advantage of this method is that the terms $\partial_\alpha\phi$ and $\nabla^2\phi$, needed for the evaluation of f_i^{eq} in Eq. (3.22), can be calculated in exactly the same way as for the fluid nodes in the bulk. Throughout this thesis we use the stencils for $\partial_\alpha\phi$ and $\nabla^2\phi$ reported in [18] that was shown to reduce spurious velocities.

3.5 Multiple relaxation time approximation

3.5.1 The need for multiple relaxation time lattice Boltzmann algorithm

When a single relaxation time approximation is used to study a binary fluid consisting of phases with different viscosities, strong spurious velocities appear at the fluid-fluid interface near the contact point [27]. This results in an incorrect equilibrium contact angle θ_{eq}, since the system is continuously pushed out of equilibrium. Spurious currents originate from long range contributions to the equilibrium distribution functions near the contact line and from the bounce-back boundary conditions. Making the choice $\tau_f = 1$ overcomes the problem. However, τ_f controls the fluid viscosity through Eq. (3.16) and, hence, it is not possible to keep it to unity for both phases of a binary fluid, if the two components have different viscosities.

Pooley *et al.* [27] showed that introducing a multiple-relaxation time approximation [28,29] significantly suppresses the spurious currents. This is achieved by eliminating the effect of the non-hydrodynamic modes by setting the relaxation time for these modes to $\tau_f = 1$, which results in automatically setting the distribution functions to their equilibrium values f_i^{eq} at

each time step. A different relaxation time τ_f is used for the hydrodynamic modes, which accounts for the different viscosities of the two fluid phases. Moreover, an important remark is that the introduction of a multiple relaxation time approach improves the numerical stability of the algorithm [35].

Finally, we note that a multiple relaxation time approximation is not required for g_i, as the mobility coefficient M in Eq. (3.9) can be tuned by the independent parameter Γ through Eq. (3.20). This allows us to fix the relaxation time $\tau_g = 1$ for g_i.

3.5.2 Multiple relaxation time methodology

Here we shall briefly present the basic methodology behind a multiple relaxation time lattice Boltzmann algorithm. The main idea is that different relaxation times are used for different linear independent combinations of the distribution functions f_i. In particular, the relaxation parameters responsible for generating the viscous terms in the Navier-Stokes equation (3.8) are set to τ_f, those related to conserved quantities to infinity and all the others, which correspond to non-hydrodynamic modes, to unity.

In the evolution equation of the distribution functions f_i, Eq. (3.15), the collision term $\frac{1}{\tau_f}(f_i - f_i^{eq})$ is replaced by

$$\mathbf{M}^{-1} \cdot \mathbf{S} \cdot \mathbf{M}[\mathbf{f} - \mathbf{f^{eq}}] \tag{3.26}$$

where f_i and f_i^{eq} are now written as column vectors. The matrix $\mathbf{M}$ performs a change of basis, such that the new basis contains more physically relevant variables. A possible choice

for $\mathbf{M}$ is [36]

$$\mathbf{M} = \begin{pmatrix}
1 & 1 & 1 & 1 & 1 & 1 & 1 & 1 & 1 & 1 & 1 & 1 & 1 & 1 & 1 & 1 & 1 & 1 & 1 \\
-30 & -11 & -11 & -11 & -11 & -11 & -11 & 8 & 8 & 8 & 8 & 8 & 8 & 8 & 8 & 8 & 8 & 8 & 8 \\
12 & -4 & -4 & -4 & -4 & -4 & -4 & 1 & 1 & 1 & 1 & 1 & 1 & 1 & 1 & 1 & 1 & 1 & 1 \\
0 & 1 & -1 & 0 & 0 & 0 & 0 & 1 & -1 & 1 & -1 & 0 & 0 & 0 & 0 & 1 & -1 & 1 & -1 \\
0 & -4 & 4 & 0 & 0 & 0 & 0 & 1 & -1 & 1 & -1 & 0 & 0 & 0 & 0 & 1 & -1 & 1 & -1 \\
0 & 0 & 0 & 1 & -1 & 0 & 0 & 1 & 1 & -1 & -1 & 1 & -1 & 1 & -1 & 0 & 0 & 0 & 0 \\
0 & 0 & 0 & -4 & 4 & 0 & 0 & 1 & 1 & -1 & -1 & 1 & -1 & 1 & -1 & 1 & 1 & 1 & 1 \\
0 & 0 & 0 & 0 & 0 & 1 & -1 & 0 & 0 & 0 & 0 & 1 & 1 & -1 & -1 & 1 & 1 & -1 & -1 \\
0 & 0 & 0 & 0 & 0 & -4 & 4 & 0 & 0 & 0 & 0 & 1 & 1 & -1 & -1 & 1 & 1 & -1 & -1 \\
0 & 2 & 2 & -1 & -1 & -1 & -1 & 1 & 1 & 1 & 1 & -2 & -2 & -2 & -2 & 1 & 1 & 1 & 1 \\
0 & -4 & -4 & 2 & 2 & 2 & 2 & 1 & 1 & 1 & 1 & -2 & -2 & -2 & -2 & 1 & 1 & 1 & 1 \\
0 & 0 & 0 & 1 & 1 & -1 & -1 & 1 & 1 & 1 & 1 & 0 & 0 & 0 & 0 & -1 & -1 & -1 & -1 \\
0 & 0 & 0 & -2 & -2 & 2 & 2 & 1 & 1 & 1 & 1 & 0 & 0 & 0 & 0 & -1 & -1 & -1 & -1 \\
0 & 0 & 0 & 0 & 0 & 0 & 0 & 1 & -1 & -1 & 1 & 0 & 0 & 0 & 0 & 0 & 0 & 0 & 0 \\
0 & 0 & 0 & 0 & 0 & 0 & 0 & 0 & 0 & 0 & 0 & 1 & -1 & -1 & 1 & 0 & 0 & 0 & 0 \\
0 & 0 & 0 & 0 & 0 & 0 & 0 & 0 & 0 & 0 & 0 & 0 & 0 & 0 & 0 & 1 & -1 & -1 & 1 \\
0 & 0 & 0 & 0 & 0 & 0 & 0 & 1 & -1 & 1 & -1 & 0 & 0 & 0 & 0 & -1 & 1 & -1 & 1 \\
0 & 0 & 0 & 0 & 0 & 0 & 0 & -1 & -1 & 1 & 1 & 1 & -1 & 1 & -1 & 0 & 0 & 0 & 0 \\
0 & 0 & 0 & 0 & 0 & 0 & 0 & 0 & 0 & 0 & 0 & -1 & -1 & 1 & 1 & 1 & 1 & -1 & -1
\end{pmatrix}. \tag{3.27}$$

For this choice, the first row will give the fluid density ρ when dotted with $\mathbf{f}$, while the fourth, sixth and eighth rows will give the components of the momentum density ρu_x, ρu_y and ρu_z respectively. The tenth, twelfth, fourteenth, fifteenth and sixteenth lines correspond to the components of the symmetric traceless viscous stress tensor $3p_{xx}$, $p_{yy} - p_{zz}$, p_{xy}, p_{yz} and p_{xz} respectively. The remaining rows are related to other 'kinetic' (non-hydrodynamic) moments [28, 29].

Each of the row vectors in $\mathbf{M}$ are mutually orthogonal, and therefore its inverse is given by

$$\mathbf{M}^{-1}_{ij} = \frac{1}{\Sigma_k \mathbf{M}^2_{jk}} \mathbf{M}_{ji}. \tag{3.28}$$

The matrix $\mathbf{S}$ in Eq. (3.26) is diagonal:

$$\mathbf{S} = \mathrm{diag}(0, 1, 1, 0, 1, 0, 1, 0, 1, \omega_f, 1, \omega_f, \omega_f, 1, \omega_f, \omega_f, \omega_f, 1, 1, 1), \tag{3.29}$$

where $\omega_f = 1/\tau_f$ is related to the fluid viscosity by Eq. (3.16). The zero values correspond to conserved quantities for which the relaxation time was set to infinity. This is an arbitrary choice because, whatever the relaxation parameters for these quantities, they are collision invariants since by definition $\mathbf{M}_{ji}[f_i - f_i^{eq}] = 0$ for $j = 0, 3, 5, 7$. Finally, the choice of unity for

the non-hydrodynamic modes minimises spurious velocities [27], as explained in section 3.5.1.

3.6 Summary

In this chapter we presented the numerical method that we shall use in our study of the viscous fingering problem in subsequent chapters. This will involve solving the hydrodynamic equations of motion for a binary fluid. These equations, which are the continuity and Navier-Stokes equations coupled to a convection-diffusion equation, are solved using a free energy lattice Boltzmann algorithm.

A key element in the method is a free energy functional that describes the equilibrium properties of the binary fluid. The thermodynamic properties of the binary fluid enter the hydrodynamic equations through the pressure tensor and the chemical potential that are derived from the free energy functional.

Finally we summarised the main features of a multiple relaxation time lattice Boltzmann algorithm. Our study of the viscous fingering problem can benefit from the use of this approach [28, 29], as it has been shown to reduce spurious velocities at the fluid-fluid interface near the contact line [27], and also to lead to an improvement in numerical stability.

Chapter 4

Saffman-Taylor Instability - Neutral Wetting Regime

In this chapter we shall examine the viscous fingering problem in the neutral wetting regime; under these wetting boundary conditions neither of the two fluids wets the walls. Therefore, the equilibrium contact angle is fixed to $\theta_{eq} = 90^{\circ}$ and there is no spontaneous flow in the channel in the absence of any external forcing. Lattice Boltzmann simulations enable us to explore numerically the instability in a wide range of parameters relevant to the problem and monitor the movement of the three-dimensional free boundary separating the two fluids, not only in the plane of the instability, but also in the perpendicular plane across the channel thickness direction.

If we consider the forced displacement of a viscous fluid by another one in a confined geometry like the one depicted in Fig. 4.1, we can divide the problem into two sub-problems: a) the first one deals with the movement of the fluid-fluid interface across the channel thickness direction, the x-z plane (see Fig. 4.1(a)), while b) the second one examines the evolution of the interface in the plane parallel to the walls, the x-y plane, as shown in Fig. 4.1(b).

In case (a), the x-z plane, we summarised in section 2.3.4 work by Ledesma *et al.* [14] who showed that, irrespective of the x-y plane and the presence of Saffman-Taylor fingers, the x-z interface profile can develop into two possible configurations, coined the Meniscus and Thin Film regimes. The former refers to the situation when the penetrating fluid completely displaces the resident fluid in the channel thickness direction, while the latter refers to the

situation where the penetrating fluid forms a finger in the x-z plane and a thin film of the displaced fluid is left behind on the walls. This should not be attributed to an instability and it is independent of the fluids' viscosities. These two possible interface configurations are shown in Fig. 4.1(a).

Regarding the second sub-problem and the evolution of the interface in the x-y plane, one encounters two possible situations. If the displacing liquid has higher viscosity, the result is a stable flat interface at z = $b/2$; if the driving liquid has lower viscosity, however, then the flat initial interface is rendered unstable and develops finger-like structures of the less viscous fluid penetrating the more viscous fluid (see Fig. 4.1(b)). This is the Saffman-Taylor instability or viscous fingering problem.

In this chapter we shall examine the two sub-problems in turn. We shall start in section 4.1 by presenting the channel implementation and then, in section 4.2, study the forced displacement of the fluid-fluid interface in the x-z plane. Our aim is to verify the Meniscus and Thin Film regimes identified in [14] and to show that the lattice Boltzmann method can capture the dynamics of the three-dimensional viscous fingering problem. Specifically, for the case of the Thin Film regime, we shall examine the thickness of the thin film and compare with previous experimental and numerical work.

Finally, in section 4.3 we shall turn our attention in the x-y plane. We will examine the Saffman-Taylor instability in the Meniscus and Thin Film regimes and establish the control parameter that describes the relative finger width λ_f.

4.1 Channel geometry - Simulation setup

Fig. 4.1 shows the geometry of the channel that we will consider for the study of the viscous fingering problem. This is formed by two parallel plates with length L and width w, separated at a distance b. The channel is implemented as follows. We set a cubic simulation box of dimensions $LX \times LY \times LZ$ with $LX = L$, $LY = w$, $LZ = b + 2$ and the walls located[1] at $z = 0$ and $z = b$. Periodic boundary conditions are implemented along the y-direction, while in the inlet and outlet of the channel we produce homogeneous flow by imposing the boundary conditions $\partial_x \rho \vec{U}(x = 0, y, z) = 0 = \partial_x \rho \vec{U}(x = L, y, z)$, $\partial_x \phi \vec{U}(x = 0, y, z) = 0 =$

[1] Using the midlink bounce-back method [34] the walls are located halfway between the solid and the fluid node.

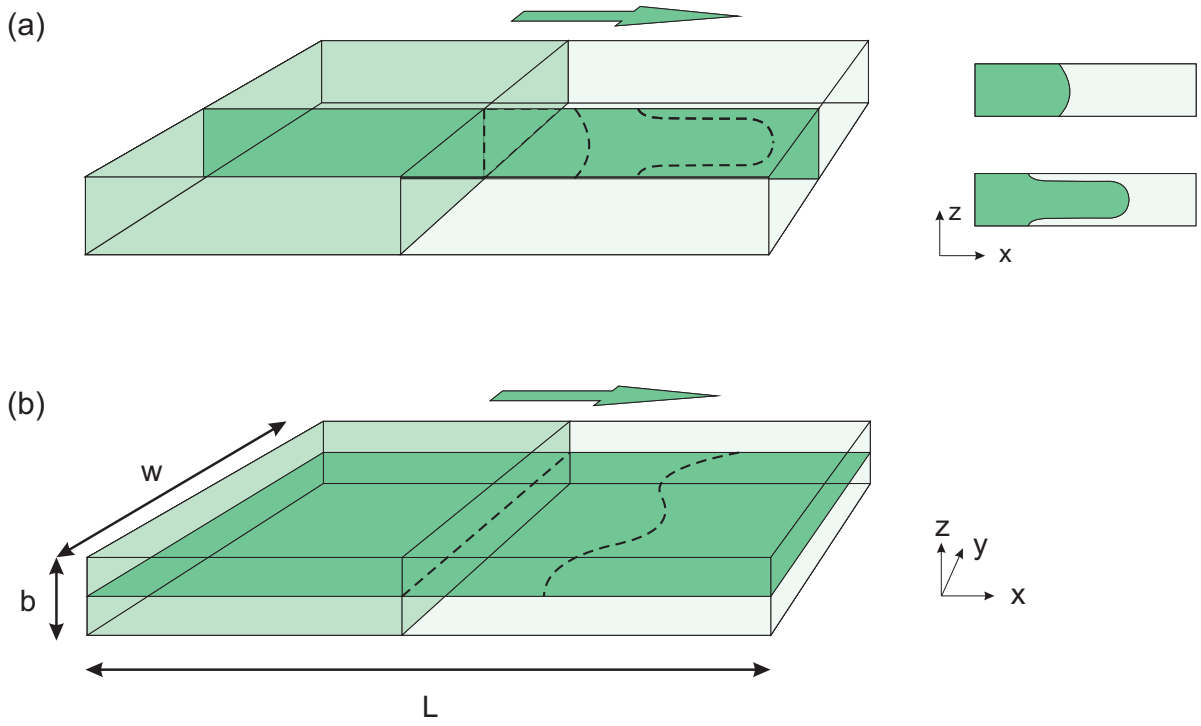

Figure 4.1: Channel geometry formed of two parallel plates with dimensions $w \times L$, located at z = 0 and z = b. The arrows indicate the direction of the flow. Examining the forced displacement of a fluid-fluid interface in a Hele-Shaw cell we divide the problem into two subproblems. (a) The movement of the fluid-fluid interface in the x-z plane. The two possible interface configurations are shown. (b) The evolution of the interface in the plane parallel to the walls, the x-y plane. The interface becomes unstable by virtue of the Saffman-Taylor instability when a less viscous fluid displaces a more viscous one.

$\partial_x \phi \vec{U}(x = L, y, z)$. The choice of periodic boundary conditions along y was made because we would like to study the instability in the absence of any effects due to the side walls. This does, however, pose a restriction in the maximum possible wavelength of a perturbation on the interface. Simulations reported at the end of this chapter that require larger computational domains were implemented on just one fourth of the real channel, ($x \in [0, LX]$, $y \in [0, LY/2]$, $z \in [0, LZ/2]$), by taking advantage of the flow symmetry. This was achieved by distinguishing the neighboring sites at the boundaries, so that during the propagation step, of the lattice Boltzmann method, the correct populations were being exchanged.

Next, we briefly explain the parameter selection process. Table 4.1 summarises all the parameters relevant to the simulations, as well as any quantities derived from these that will be regularly used throughout the following sections. First of all, the simulation lattice spacing Δx and timestep Δt are set to unity, leading to a lattice velocity parameter $c = \Delta x/\Delta t = 1$.

Table 4.1: List of the parameters relevant to the simulations on the Saffman-Taylor instability.

Description	Symbol	Dimension	Typical Value
Simulation lattice spacing	Δx	Length	1.0
Simulation timestep	Δt	Time	1.0
Density of fluid	ρ	Mass/Volume	1.0
Relaxation time	$\tau_{f,i}$ $(i = 1, 2)$	–	$0.52 - 2.5$
Relaxation time	τ_g	–	1
Dynamic viscosities of fluids	$\eta_i (i = 1, 2)$	Mass/(Length$\times$ Time)	$10^{-3} - 10^{-1}$
Viscosity contrast ratio	r	–	$0 - 0.97$
Mobility coefficient	M	Length$^3\times$Time/Mass	$0.05 - 12.5$
Mobility related coefficient	Γ	Length^3/Mass	$0.1 - 25$
Diffusion coefficient	D	Length^2/Time	$10^{-6} - 10^{-1}$
Free energy parameters	A, B	Energy/Volume	$10^{-5} - 10^{-2}$
Interfacial width	ξ	Length	0.81
Interfacial parameter	κ_ϕ	Energy/Length	$10^{-5} - 10^{-2}$
Surface tension	σ	Energy/Area	$10^{-5} - 10^{-2}$
Equilibrium contact angle	θ_{eq}	Degrees	90°
Wetting potential	h	Energy/Area	0
Channel length	L	Length	$1000 - 3000$
Channel width	w	Length	$100 - 320$
Channel thickness	b	Length	$5 - 50$
Body force	$\mathbf{F}$	Force/Volume	$10^{-6} - 10^{-3}$
Capillary number	Ca	–	$10^{-2} - 10^{2}$
Péclet number	Pe	–	$10^{1} - 10^{4}$
Modified capillary number	$1/B$	–	$10^{1} - 10^{5}$
Reynolds number	Re	–	$10^{-2} - 10^{0}$
Weber number	We	–	$10^{-2} - 10^{3}$

The density of the two fluids is fixed and set to $\rho = 1$. By tuning the relaxation time $\tau_{f,i}$ for each of the two fluids $(i = 1, 2)$ we vary the dynamic viscosities of the fluids (η_1, η_2) according to Eq. (3.16). A restriction imposed by the lattice Boltzmann method is that $\tau_{f,i} > 0.5$, but it cannot take arbitrarily large values, since this can lead to strong spurious velocities, which scale as τ_f^3 [27]. We have used values $\tau_f \leq 9.0$. The viscosity contrast ratio is defined as $r = (\eta_1 - \eta_2)/(\eta_1 + \eta_2)$. Regarding the second relaxation time parameter τ_g, it is set to unity for reasons explained in section 3.5.1. The mobility coefficient M, and consequently the diffusion coefficient D, which depend on τ_g, can be tuned by varying Γ according to Eq. (3.20). For stability reasons $0.1 \leq \Gamma \leq 25$. With the choice of parameters used throughout the thesis, $D = M(A + 3B\phi_{eq}^2) = B\Gamma$.

Regarding the parameters A, B in the free energy functional, Eq. (3.2), we make the choice $A = -B$ $(B > 0)$ that leads to $\phi_{eq} = \pm 1$ for the two phases. The interfacial parameter κ_ϕ ensures smooth local deviations from ϕ_{eq} near the fluid-fluid interface. For stability reasons

related with the lattice Boltzmann method $\kappa_\phi \leq 2\times10^{-2}$. The width of the interface is fixed to $\xi = 0.81$ throughout the thesis. This choice was previously shown to give accurate results for the variation of ϕ across the fluid-fluid interface [37] and allows a smooth transition between the two phases over a lengthscale of $\sim 5\xi$. The choice of κ_ϕ fixes the value for the free energy parameters A, B, since $\xi = \sqrt{-\kappa_\phi/A}$, and provides a nonzero value for the surface tension $\sigma = \sqrt{-8\kappa_\phi A^3/9B^2}$.

The equilibrium contact angle θ_{eq} is set according to the wetting boundary conditions, which sets the value of the wetting potential h, according to Eq. (3.4), and consequently the value for the normal derivative of the order parameter at solid surfaces $\partial_\perp\phi$ (Eq. (3.3)). In this chapter we study the Saffman-Taylor instability in the neutral wetting regime, i.e. $\theta_{eq} = 90°$, $h = 0$ and $\partial_\perp\phi = 0$.

When choosing the size of the simulation box $LX \times LY \times LZ$, care has to be taken mainly for the thickness of the channel $b = LZ - 2$. When the displacing fluid completely displaces the resident fluid in the x-z plane, we choose $b \geq 5$. In the case, however, when the penetrating fluid forms a finger in the x-z plane, we have to consider thicker channels ($b \geq 25$) in order to correctly resolve the dynamics of the thin wetting films. The width of channel w is chosen according to the desired aspect ratio $\epsilon = b/w$, while the length L is chosen such that a nice, well developed Saffman-Taylor finger forms in the x-y plane.

Finally, according to the desired velocity of the flow, we evaluate the required body force $\mathbf{F} = (F_x, 0, 0)$ using Darcy's law, $U_x = \frac{b^2}{12\eta}F_x$. The body force $\mathbf{F}$ is kept constant throughout each simulation, while the velocity is kept in the range $1 \times 10^{-3} \leq U_x \leq 1 \times 10^{-2}$ to ensure that we work in the low Mach regime.

The results from the simulations on the Saffman-Taylor instability, in Chapters 4 and 5, will be analysed in terms of dimensionless numbers relevant to the problem. There dimensionless numbers are $Ca = \eta U/\sigma$, $Pe = Ub/D$, $1/B = (12/\epsilon^2)(\Delta\eta U/\sigma)$, $Re = \rho Ub/\eta$ and $We = \rho Ub^2/\sigma$. Further discussion on this will follow up in the relevant sections.

4.2 Interface configuration in the x-z plane

Examining the viscous fingering problem in the neutral wetting regime involves not only the study of: a) the leading interface in the x-y plane, but also b) the evolution of the interface

in the x-z plane, as shown by Ledesma *et al.* [14, 15]. The latter is affected by the movement of the contact line at the intersection of the fluid-fluid interface and the solid walls located at z = 0 and z = b.

As pointed out by Ledesma *et al.* [14] the profile of the advancing interface in the channel thickness direction is, in simple terms, determined by the ability of the contact line to move as fast as the leading interface. If the velocities of the contact line and leading interface are comparable in size, then the interface can move so that a meniscus profile remains constant in time. If, however, the contact line moves too slowly to keep up with the leading interface, the displacing fluid penetrates the displaced fluid and forms a finger in the x-z plane. In terms of dimensionless numbers, Ledesma *et al.* proposed that the relevant control parameter distinguishing between these regimes is the product of the capillary $Ca = \eta U/\sigma$ and Péclet $Pe = Ub/D$ numbers [14], where D is the diffusion coefficient. The capillary number represents the relative effect of viscous forces versus surface tension, whereas the Péclet number gives the ratio between advective and diffusive timescales in the region of the moving contact line.

4.2.1 Effect of diffusivity and surface tension

We now present results for the effect of diffusivity and surface tension on the interface profile across the channel thickness direction. We consider a channel of length L and thickness b with periodic boundary conditions in the y direction, which corresponds to an infinite channel width. Initially the channel is filled with the two fluids that are separated by a flat interface perpendicular to the solid wall as shown in Fig. 4.2.

We first ran a set of simulations with fixed forcing, surface tension and viscosities of the two fluids. Thus, the capillary number is kept constant, while we vary the Péclet number by means of the diffusion coefficient D. The viscosity contrast ratio used is $r = (\eta_1 - \eta_2)/(\eta_1 + \eta_2) = 0.90$. Fig. 4.2 shows a time sequence of the interface position for each run. Diffusivity decreases from run (a) to run (d). The interface in runs (a) and (b), which have the highest diffusion coefficient, advances as a meniscus. Nevertheless, it is clear that the meniscus in run (a) is less curved compared with the meniscus in run (b). Sequences in runs (c) and (d) show a change in the interface profile, as a penetrating structure emerges and the less viscous fluid eventually forms a finger in the x-z plane.

Moreover, it is evident from the position of the contact line at equal times that the velocity

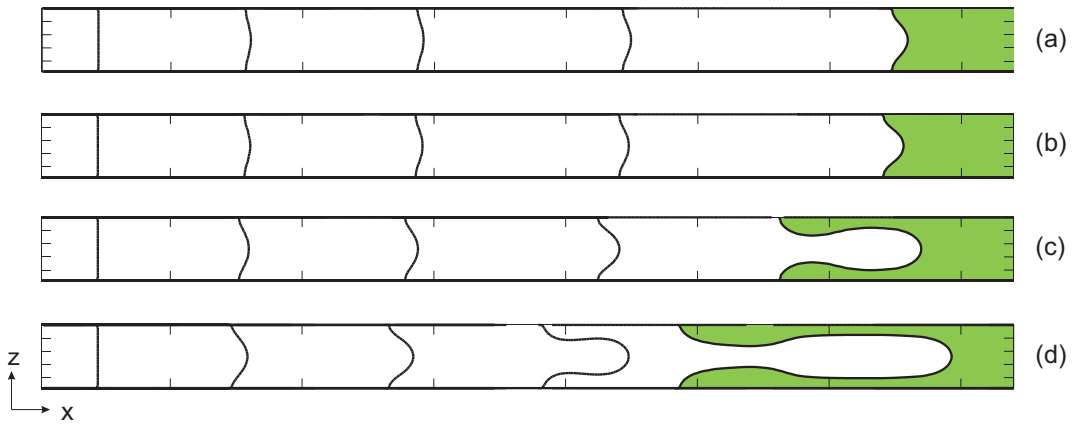

Figure 4.2: Interface evolution in the channel thickness direction for varying diffusion coefficients. The time interval between the plotted interface positions is $\delta t = 2 \times 10^4$ time-steps in lattice units. For all runs $\sigma = 8.19 \times 10^{-3}$, $\eta_1 = 0.33$, viscosity contrast ratio $r = 0.90$ and $b = 23$. Meniscus regime: (a) $D = 1.08 \times 10^{-1}$ and (b) $D = 7.54 \times 10^{-2}$. Thin Film regime: (c) $D = 1.08 \times 10^{-2}$ and (d) $D = 2.15 \times 10^{-3}$.

of the contact line reduces from runs (a) to (d). This is a direct confirmation that the velocity of the contact line decreases with decreasing diffusivity.

We also ran simulations with zero viscosity contrast ($r = 0$). These showed the same qualitative behaviour as the asymmetric case with $r = 0.90$. The details of these simulations are listed in Table 4.2.

Table 4.2: Parameter values for runs with viscosity contrast $r = 0$ and varying diffusion coefficients. For all runs $b = 23$, $\eta_1 = \eta_2 = 0.1$ and $\sigma = 4.6 \times 10^{-3}$.

D	U	Ca	Pe	$CaPe$	Shape
0.073	4.34×10^{-3}	0.094	2.500	0.236	Meniscus
0.049	5.00×10^{-3}	0.109	3.725	0.405	Meniscus
0.024	4.86×10^{-3}	0.106	7.605	0.803	Finger
0.012	5.00×10^{-3}	0.109	15.214	1.654	Finger
0.009	5.00×10^{-3}	0.109	20.278	2.204	Finger

Next we examine the effect of capillarity on the interface profile in the channel thickness direction. This time, we run a set of simulations with fixed forcing and diffusivity, therefore keeping Pe fixed while Ca is varied by means of the surface tension. We plot the time sequence of the interface position for these runs in Fig. 4.3. Surface tension decreases from run (a) to (d). As expected, penetration occurs as Ca increases.

Parameter values are listed in Table 4.3 and Table 4.4 and Fig. 4.4 shows a plot of our

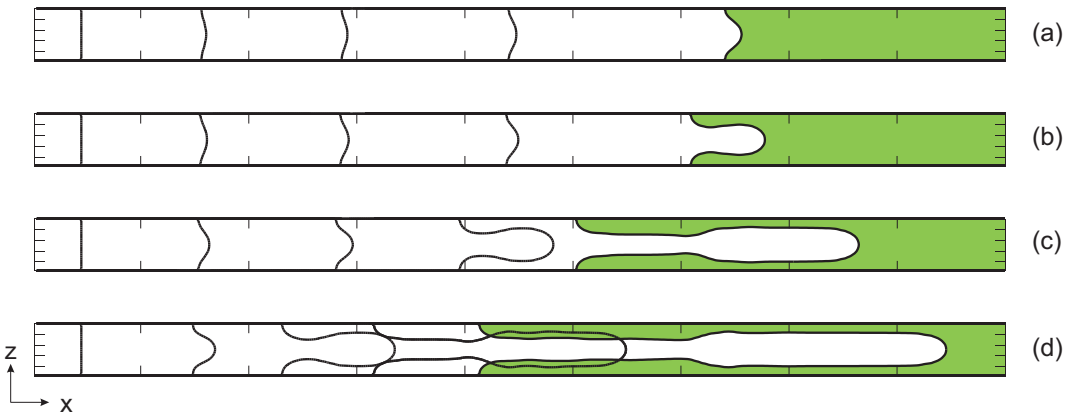

Figure 4.3: Interface evolution in the channel thickness direction for varying surface tension. The time interval between the interfaces is $\delta t = 2 \times 10^4$ time-steps in lattice units. For all runs $D = 7.54 \times 10^{-2}$, $\eta_1 = 0.33$, viscosity contrast ratio $r = 0.9$ and $b = 23$. Meniscus regime: (a) $\sigma = 8.19 \times 10^{-3}$. Thin Film regime: (b) $\sigma = 5.85 \times 10^{-3}$, (c) $\sigma = 3.51 \times 10^{-3}$ and (d) $\sigma = 2.34 \times 10^{-3}$.

results in the (Pe, Ca^{-1}) plane. The threshold from the Meniscus to the Thin Film regime is approximated well by the solid line that corresponds to $Pe = 0.5\, Ca^{-1}$, in agreement with the threshold found by Ledesma *et al.* [14].

Thus, in this section we have verified the existence and extend of the Meniscus and Thin Film regimes described in [14]. Menisci were stable for low capillary and Péclet numbers with an upper bound of

$$CaPe \simeq 0.5\ , \tag{4.1}$$

when surface tension and diffusion dominate over viscous stresses and advection respectively. For larger values of $CaPe$ fingering in the x-z plane is observed. The dependence of the interface profile on the product of $CaPe$ is due to the fact that viscous stresses deform the interface, and therefore favor the formation of fingering in the x-z plane, whereas surface tension tends to restore the interface shape to its equilibrium value. On the other hand, advection causes order parameter gradients in the x-direction that may lead to fingering, and diffusivity generates a slip velocity of the contact line that can compensate the effect of advection. Therefore, starting from a meniscus configuration, characterised by low $CaPe$, we can end up in the Thin Film regime by crossing the bound value of $CaPe \simeq 0.5$, either by decreasing the surface tension, or by increasing the forcing steadily and, therefore, increasing Ca and Pe numbers, or by reducing the diffusivity, and consequently increasing Pe.

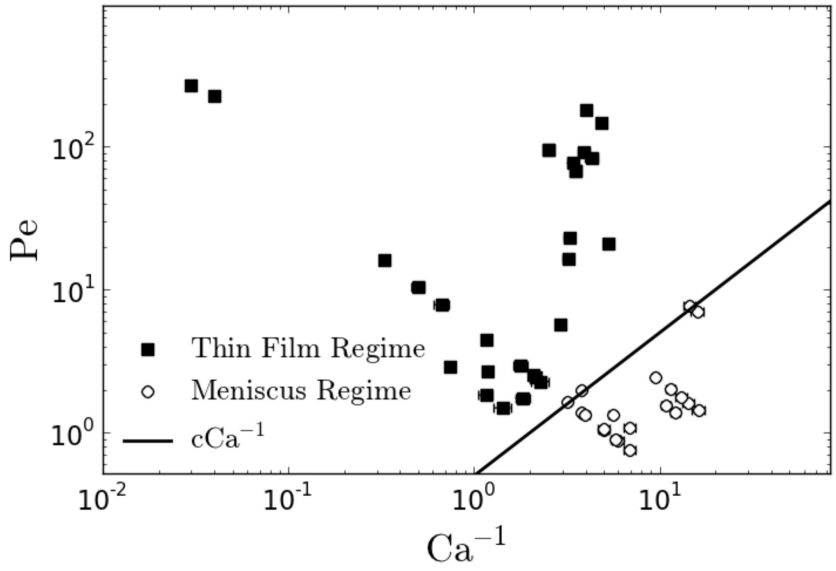

Figure 4.4: Simulations data from Tables 4.3 and 4.4 plotted in the (Pe, Ca^{-1}) plane for fluids with viscosity contrast $r = 0.90$. Results which correspond to the Thin Film regime are denoted by squares(■), while results corresponding to the Meniscus regime are denoted by circles (∘). The solid line is $Pe = cCa^{-1}$, with $c \simeq 0.5$.

4.2.2 Width of the finger in the x-z plane

Next, we turn our attention to the steady state finger in the x-z plane and the relative finger width $\lambda_b = w_b/b$, where w_b is the absolute finger width. Penetrating fingers in the channel thickness direction occur for high values of $CaPe$ as we have seen is section 4.2.1. Our aim is to investigate λ_b and compare our results to previous work on the subject.

The initial interest in the movement of a fluid of negligible viscosity within a channel filled with a viscous fluid lies with Fairbrother & Stubbs [38] as early as 1935. Their aim was to determine whether a bubble of air moving in a capillary tube filled with a viscous liquid would provide information on the actual velocity of the flow. Later, the evaluation of the film thickness left behind at the solid walls due to the movement of an inviscid finger was important to understand Hele-Shaw flows and the Saffman-Taylor instability. Bretherton [39] studied the motion of a long inviscid bubble in a tube filled with a viscous fluid in the limit $Ca \to 0$. He found that the finger width is given by $\lambda_b = 1 - 1.337Ca^{2/3}$ for both the axisymmetric and two-dimensional problem. Taylor [40] examined experimentally systems up to $Ca < 2$ and asserted that his experimental results were in agreement with a decaying exponent of $1/2$ only for $Ca < 0.09$. For $0.09 < Ca < 2$, λ_b decreases more slowly than $1 - Ca^{1/2}$. The thickness

of the residual film left behind a Saffman-Taylor finger in a Hele-Shaw cell was measured by Tabeling *et al.* [41] in the regime up to $Ca < 0.2$. From that they obtained the following regression formula for the finger width, that also involved the aspect ratio of the channel w/b

$$\lambda_b = 1 - 0.238\big[1 - \exp(-0.019w/b)\big]\big[1 - \exp(-8.58Ca^{2/3})\big]. \tag{4.2}$$

Numerical work was performed by Reinelt and Saffman [42], who solved the Stokes equation using a finite difference method up to $Ca \sim 2$ and matched the experimental results by Taylor. Halpern and Gaver [43] examined a much larger range of Ca up to $Ca \approx 10^2$. They performed a boundary element analysis of the Stokes equations to study the penetrating finger and found good agreement with the experimental results of Tabeling *et al.* ($Ca < 0.2$) and the results of Reinelt and Saffman ($Ca < 2$). Their results can be described by the following relation

$$\lambda_b = 1 - 0.417\left[1 - \exp\left(-1.69Ca^{0.5025}\right)\right]. \tag{4.3}$$

Beyond $Ca \approx 20$ they showed that the finger is insensitive to Ca with a saturation value of $\lambda_b = 0.583$. Recent numerical work by Ledesma *et al.* [14] revealed very good agreement with the results of Halpern and Gaver.

So, according to the literature, the finger width λ_b depends on Ca. Numerical work by Ledesma *et al.* [14] has revealed that it also depends on the viscosity contrast $r = (\eta_1 - \eta_2)/(\eta_1 + \eta_2)$. Decreasing the viscosity contrast has a thinning effect on λ_b. Here we proceed to examine the dependence of λ_b on the capillary number. We explore up to five decades in the capillary number $10^{-2} \leq Ca \leq 10^2$, and perform a series of quasi two-dimensional simulations to verify that our simulations are in agreement with previous work. We disregard any variations in the y direction by using periodic boundary conditions along y direction. This corresponds to a channel of infinite width along the y direction, with a flat leading interface along y at each z level.

The details of our simulations are summarised in Table 4.5 and a plot of the results for λ_b as a function of Ca is shown in Fig. 4.5. We used 5 different channels with thickness $b = 23, 28, 51, 60$ and $b = 148$ and fluids with viscosity contrast $r = 0.90$ and $r = 0.97$. A very good match is found with the numerical results of Halpern & Gaver [43], although these correspond to the case $r \to 1$. Already for the case of $r = 0.90$ we reproduce the saturation

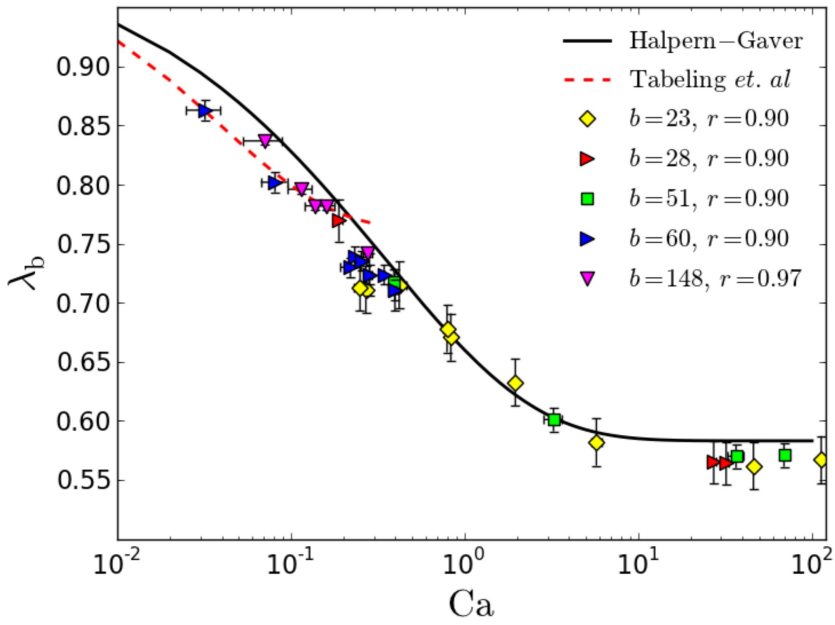

Figure 4.5: Finger width λ_b in the x-z plane as a function of Ca for two-dimensional simulations. The prediction of Halpern and Gaver [43] and the regression formula of Tabeling *et al.* [41], for aspect ratio $w/b \to \infty$, are plotted as solid and dashed lines respectively.

value of λ_b for high Ca, for which we find $\lambda_b \approx 0.566$, 2.9% below the value $\lambda_b \approx 0.583$ of Halpern & Gaver. The smaller saturation value of λ_b is expected due to the tendency of the fingers to thin down with decreasing viscosity contrast [14]. Our saturation value also agrees with Ledesma *et al.* [14] who obtained a saturation value of $\lambda_b \approx 0.573$ for the same viscosity contrast ($r = 0.90$). This clearly provides a good check on our simulations.

As can be seen from Fig. 4.5, the difference between our results with $r = 0.90$ and Halpern & Gaver predictions increases for $Ca < 0.3$. At $Ca \simeq 0.08$ the difference is $\sim 4.7\%$. This is improved with increasing the viscosity contrast to $r = 0.97$, for which the difference is reduced to $\sim 1.7\%$. We also compare our results to the regression formula of Tabeling *et al.* [41], Eq.(4.2), for the case of aspect ratio $w/b \to \infty$ and for $Ca < 0.2$. A very good agreement is achieved as shown in Fig. 4.5.

Finally, we extend simulations to cover equilibrium contact angles[2] ranging from $\theta_{eq} = 0°$ to $\theta_{eq} = 170°$ and use fluids with $r = 0.90$. Our results for λ_b as a function of Ca are shown in Fig. 4.6. For the whole range of θ_{eq} examined, finger widths λ_b are in a good agreement with the numerical prediction of Halpern & Gaver, except for the regime $Ca \leq 10^{-1}$, again

[2] from the less viscous fluid perspective

due to the smaller viscosity contrast. Moreover, the regression formula of Tabeling *et al.* [41], for $b/w \to \infty$, shown as a red dashed line, describes well our results for λ_b in the regime $0.07 \leq Ca \leq 0.2$.

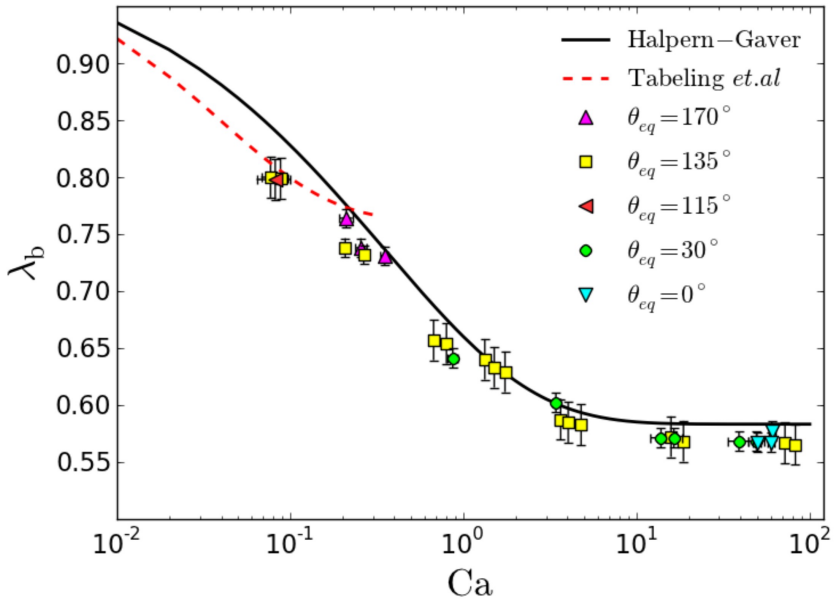

Figure 4.6: Finger width λ_b in the x-z plane as a function of Ca for varying equilibrium contact angle θ_{eq}. The solid line describes the numerical prediction of Halpern and Gaver [43], while the dashed line corresponds to the regression formula of Tabeling *et al.* [41] for $w/b \to 0$.

Fig. 4.6 demonstrates that the finger width λ_b is insensitive to the wetting boundary conditions, since results, irrespective of the contact angle θ_{eq}, collapse on a single curve. This verifies that leading interface dynamics and finger dynamics are decoupled from contact line dynamics. The onset of the penetration process in the x-z plane depends, of course, on the wetting boundary conditions, but once the finger manages to break through in the third dimension, then its size is governed by just Ca and the viscosity contrast r.

4.3 Viscous fingering

We now turn our attention now to the x-y plane and the Saffman-Taylor instability. The aim is to predict the motion of the fluid-fluid interface and establish a control parameter that will be able to describe the finger width λ_f, irrespective of the channel's geometry and the finger's velocity. We recall that Tabeling and Libchaber [12] reached a better agreement of the experimental data for the finger width with the two-dimensional prediction of McLean and

Saffman [11], by using an effective surface tension in a rescaled modified capillary number

$$1/B^* = (12/\epsilon^2)(\Delta\eta U/\sigma^*) \,, \tag{4.4}$$

where $\sigma^* = \sigma\left(1 + \frac{R_\parallel}{R_\perp}\right)$. The surface tension correction took into account the effect of the thin film left behind the fingers at the surfaces at z=0 and z=b. In a recent numerical study of Saffman-Taylor instability Ledesma *et al.* [15] also showed that these corrections to the surface tension can lead to better agreement between numerics and the two-dimensional prediction of McLean and Saffman. In the following subsections, we will investigate the viscous fingering problem in the Meniscus and Thin Film regimes and examine the validity of the above rescaled modified capillary number $1/B^*$ in describing the Saffman-Taylor instability.

4.3.1 Dispersion relation in the two-dimensional limit

Before presenting our results for the viscosity-driven Saffman-Taylor instability, we examine the dispersion relation for the linear stability analysis of the interface, i.e the behavior of an initially flat interface that is subjected to a small perturbation. We showed in section 2.4 that the universal dispersion relation reads

$$\tilde{\omega}(\tilde{k}) = \tilde{k}(1 - \tilde{k}^2) \tag{4.5}$$

where $\tilde{\omega}(\tilde{k}) = \omega(k)wB^{1/2}/rU$ are the dimensionless frequencies and $\tilde{k} = wB^{1/2}k$ the dimensionless wavenumber. To check this we prepared an initially flat interface in x-y plane and perturbed it according to to a single-mode perturbation of wavelength $\Lambda = w$ and a small amplitude defined as $\zeta^{amp}(t) = x_{tip}(t) - \bar{x}(t)$, where x_{tip} and $\bar{x}$ are the tip and the mean position of the interface respectively. The amplitude of the interface as a function of time was recorded for the initial stages of the flow. The amplification factor ω, or growth rate, was extracted from a linear fit of $\log \zeta^{amp}(t)$ versus t.

Since the linear stability analysis that yields the growth rate assumes a two dimensional interface, we approach this here, by considering low values of $CaPe$ that result in a meniscus profile in the x-z plane. Fig. 4.7 shows the dispersion relation obtained from two geometries with $\epsilon = 0.04$ and $\epsilon = 0.10$. As expected, results with smaller ϵ approach better the universal two-dimensional dispersion relation. Furthermore, the observed regime of unstable modes is

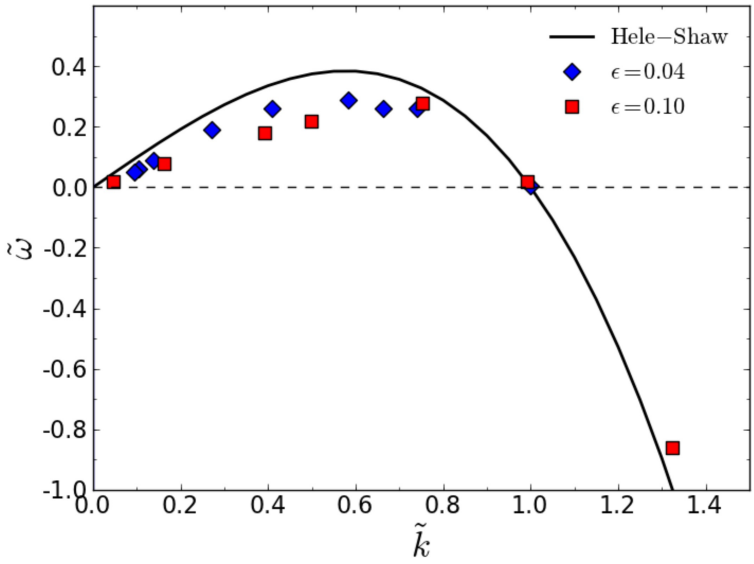

Figure 4.7: Dispersion relation for the linear stability analysis of the interface in the Meniscus regime for two geometries with $\epsilon = 0.04$ and $\epsilon = 0.10$. Fluid viscosities are $\eta_1 = 0.500$, $\eta_2 = 0.017$ giving a viscosity contrast $r = 0.94$.

in a very good agreement with the one predicted from the two-dimensional dispersion relation. We quantify the obtained dispersion relation by fitting our results to a polynomial of general form $p_1\tilde{k}(p_2 - p_3\tilde{k}^2)$, from which we obtain the first unstable mode at $\tilde{k}_{cr} \approx 0.98$ and the most unstable wavevector at $\tilde{k}_{max} \approx 0.566$ compared to $\tilde{k}_{cr} = 1$ and $\tilde{k}_{max} = 0.577$ for the two-dimensional dispersion relation.

4.3.2 Meniscus regime

The Meniscus regime is characterized by $CaPe \leq 0.5$. We restrict ourselves to this regime and perform simulations in a wide range of the classical control parameter [4]

$$1/B = (12/\epsilon^2)(\Delta\eta U/\sigma). \tag{4.6}$$

Our aim is to test whether $1/B$ can describe the viscous fingering problem. That is, if the control parameter of the viscous fingering problem is indeed $1/B$ then all the results for the finger width λ_f should fall on the same universal curve when plotted as a function of $1/B$.

We vary $1/B$ in the range $50 \leq 1/B \leq 5000$ mainly by means of the aspect ratio ϵ and surface tension σ. In particular we examine the cases $\epsilon = 0.05, 0.06, 0.09, 0.17$ and 0.22. Parameter values and our results are listed in Table 4.6.

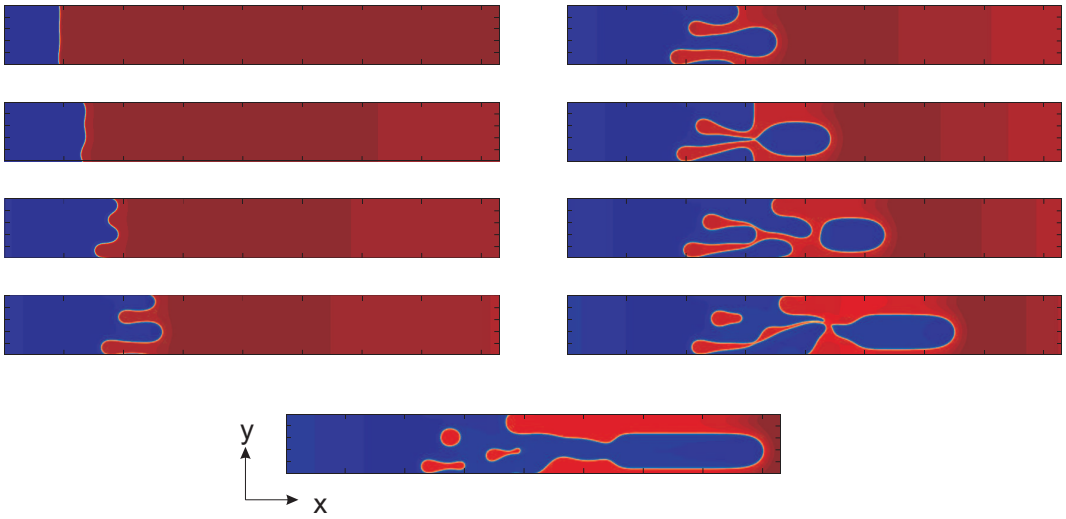

Figure 4.8: Saffman-Taylor fingering process. Interface evolution in the x-y plane at time intervals of $\delta t = 2 \times 10^4$ time-steps in lattice units. Competition between neighboring viscous fingers leads eventually to a single finger in the channel.

Fig. 4.8 shows the time evolution of an initially flat interface in the x-y plane that has been subjected to a small perturbation of wavelength $\Lambda = 4$ and amplitude $\zeta_k = 1$ in lattice units. This demonstrates clearly that the lattice Boltzmann method can capture the dynamics of the viscous fingering problem, since we observe all the stages of the instability, from the selection process of the most unstable wavelength, the competition between neighboring fingers to the final predominance of a single finger in the channel. A three-dimensional image of a single finger in the final stages, from a different simulation, is shown in Fig. 4.9.

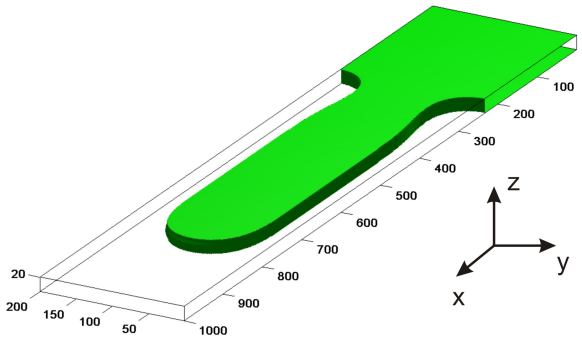

Figure 4.9: A three-dimensional image of a Saffman-Taylor finger in the Meniscus regime in a channel geometry with aspect ratio $\epsilon = 0.09$, $b = 18$, $w = 200$, $1/B = 545.50$ and $\lambda_f = 0.63$.

In Fig. 4.10 we present a plot of our results for the finger width λ_f versus $1/B$. The two-dimensional prediction of McLean & Saffman [11] is also plotted as a solid line for comparison.

First of all, we can clearly see that the results do not fall on the same curve; instead, it seems that results from different geometries fall on different curves. Even though the modified capillary number $1/B$ takes into account the asymmetry of the cell, we get a family of curves λ_f versus $1/B$ for different aspect ratios. Therefore, $1/B$ cannot be the control parameter to the fingering problem. Furthermore, runs with larger aspect ratios, $\epsilon = 0.17$ and $\epsilon = 0.22$, show wider fingers than predicted, while runs with smaller aspect ratio seem to agree better with the two-dimensional prediction. This is expected since decreasing the aspect ratio approaches the two-dimensional case. This tendency is also in agreement with the numerical study of Ledesma *et al.* [15].

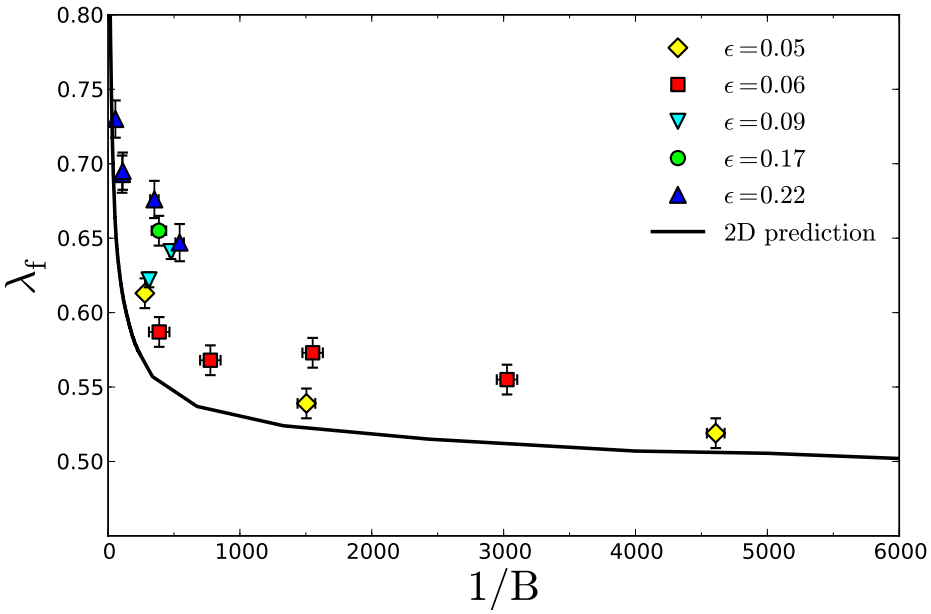

Figure 4.10: Finger width λ_f as a function of control parameter $1/B$ in the Meniscus regime for varying channel aspect ratio ϵ. The two-dimensional prediction by McLean & Saffman [11] is shown by the solid line.

As described in section 2.3, one of the basic assumptions in the early theoretical attempts to study the instability was that variations in the transverse curvature can be neglected, or that $R_\perp = b/2$. However, we have observed that, even in the absence of a thin film left behind at the surfaces, the x-z interface projection has a certain curvature, which is not constant and which can be measured directly. Moreover, $1/R_\perp$ is not negligible and it can be accounted for by defining an effective surface tension $\sigma^* = \sigma(1 + R_\parallel/R_\perp)$ and a rescaled modified capillary

number

$$1/B^* = (12/\epsilon^2)(\Delta\eta U/\sigma^*) = (1/B)/(1 + R_{\|}/R_{\perp}). \tag{4.7}$$

Fig. 4.11 shows a plot of the finger width λ_f as a function of the rescaled control parameter $1/B^*$. It is evident from the figure that, regardless of the aspect ratio, finger widths λ_f fall on the McLean-Saffman curve for the wide range of $1/B^*$ considered. Therefore, we can conclude that in the Meniscus regime rescaling with $1/B^*$ renders the problem effectively two-dimensional, and that the control parameter of the fingering problem is the rescaled parameter $1/B^*$.

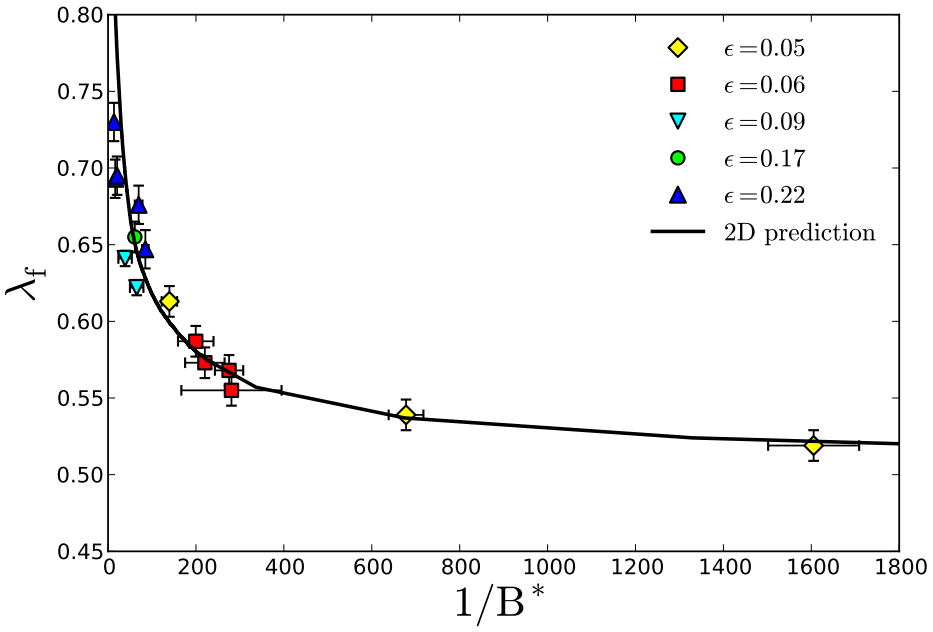

Figure 4.11: Finger width λ_f versus rescaled control parameter $1/B^*$ in the meniscus regime. Results collapse on the two-dimensional prediction by McLean & Saffman [11] which is shown by the solid line.

4.3.2.1 Finger shape

We proceed next to examine the finger shape in the x-y plane and compare them to the semi empirical relation of Pitts [10], which reads

$$\cos\left(\pi y'/2\lambda_f\right) = \exp\left(\pi x'/2\lambda_f\right). \tag{4.8}$$

x' and y' measure the distance from the finger tip in units of half the channel width w. This expression has been shown to describe the interface profile rather well in a wide range of experimental finger widths λ_f [3, 10, 11, 14]. Defining new variables

$$y'' = \pi y'/2\lambda_f \ , \quad x'' = \pi x'/2\lambda_f \ , \tag{4.9}$$

all finger profiles should be able to be reduced to a single curve, with the edges of the fingers located at $y'' = \pm\pi/2$. Fig. 4.12 shows the rescaled finger shapes for our simulations in the Meniscus regime. All finger interface profiles are in very good agreement with the Pitts profile.

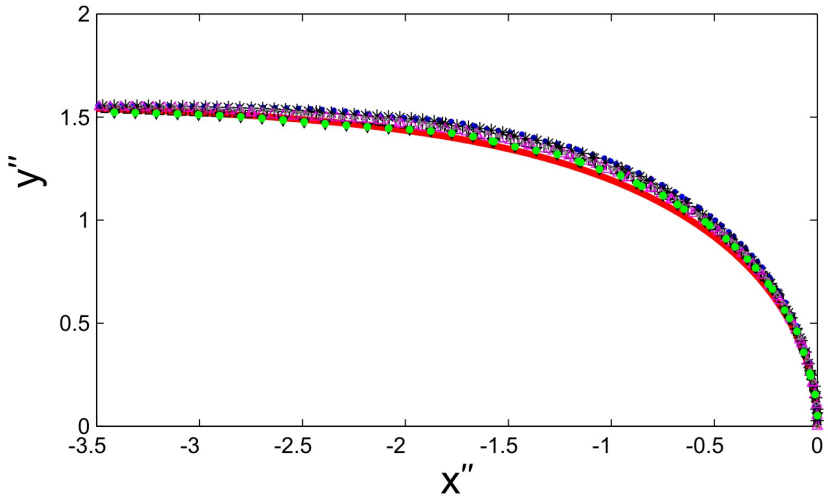

Figure 4.12: Rescaled interface profile for fingers in the Meniscus regime. Pitts' semi empirical relation for the interface profile [10] is shown by the solid red line.

4.3.3 Thin Film regime

We now extend the simulations to the Thin Film regime, where a layer of the displaced fluid is left behind at the walls. We restrict ourselves to parameters $CaPe \gg 1$ and choose relatively thicker channels ($b \geq 25$). This is a restriction imposed by the diffuse nature of the interface. In order to correctly resolve the dynamics of thin wetting films, it is important that the thickness of the wetting film is sufficiently larger than the interface thickness ξ.

In this regime, fingering is observed in the x-z plane as well, as a consequence of the velocity mismatch between contact line (u_{slip}) and leading interface (U) velocities. This has to be distinguished from a Saffman-Taylor finger, since it is produced by the no-slip boundary

conditions at the solid walls, rather than by an interface instability. Fig. 4.13 shows a well developed Saffman-Taylor finger in the Thin Film regime. From the x-y and x-z projections of the interface, depicted in Fig. 4.13(a), we can clearly see that fingering across the channel thickness direction commences from a point well behind the Saffman-Taylor fingering in x-y plane. This provides an indication that contact line dynamics are decoupled from the leading interface dynamics in x-y plane.

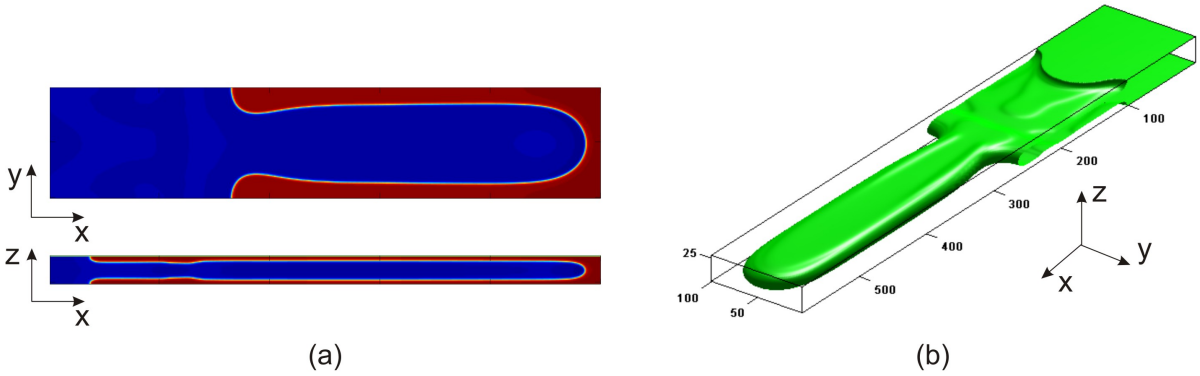

Figure 4.13: Thin Film regime: (a) The x-y and x-z projections of a Saffman-Taylor finger. It is clear from the figure that the fingering procedure is independent in the two planes, which suggests that contact line dynamics are decoupled from the leading interface dynamics. (b) A three-dimensional image of the same Saffman-Taylor finger.

We examine the relative finger width λ_f as a function of the classical control parameter $1/B$. We cover 4 orders of magnitude in $1/B$ ($40 \leq 1/B \leq 43000$) mainly by means of the aspect ratio ϵ and surface tension σ. A first conclusion is that in this regime we observe much wider fingers than in the Meniscus regime, as can be seen from Fig. 4.14, where we plot λ_f as a function of the classical control parameter $1/B$. Our results and parameters used are listed in Table 4.7.

A closer look (see Fig. 4.14(b)) reveals a difference in the behavior of the fingers when examining two regimes of $1/B$. Initially, and for small values of $1/B$, λ_f decreases with increasing $1/B$, as expected, while for larger values of $1/B$, suprisingly, λ_f retains a constant value or even increases in size as $1/B$ increases, contrary to the classical behavior. This regime of increasing finger width starts at a value of $1/B$ that is different for different configurations and continues to persist for increasing $1/B$. It further appears that different limiting values for λ_f exist for varying aspect ratios ϵ with wider fingers observed with increasing aspect ratio. We find that $\lambda_f \to 0.68$ for $\epsilon = 0.125$, $\lambda_f \to 0.73$ for $\epsilon = 0.25$, $\lambda_f \to 0.80$ for $\epsilon = 0.35$ and

$\lambda_f \to 0.87$ for $\epsilon = 0.50$.

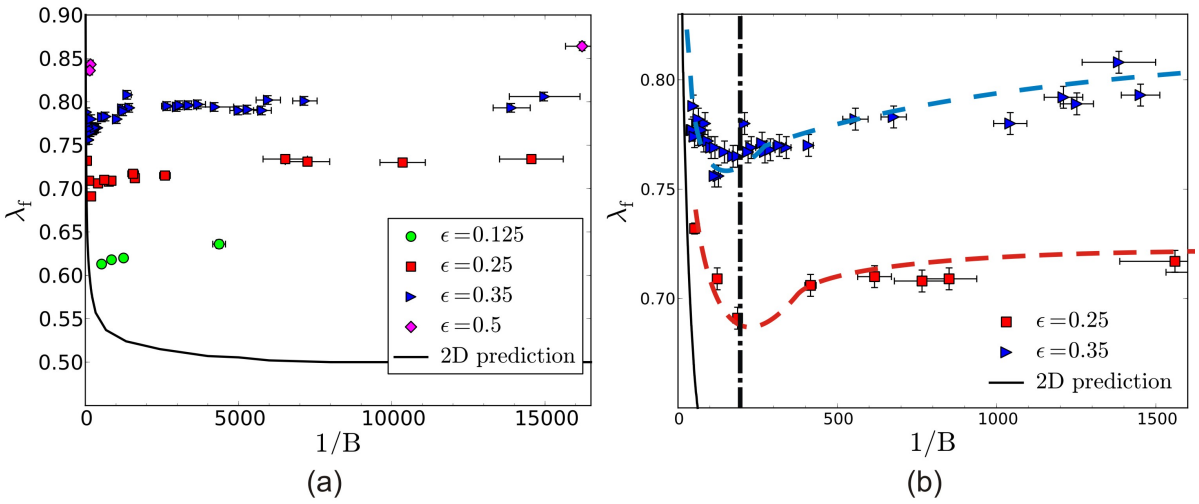

Figure 4.14: (a) Finger width λ_f versus classical control parameter $1/B$ in the Thin Film regime, for varying aspect ratios ϵ. (b) Finger width λ_f versus $1/B$ in the Thin Film regime for $\epsilon = 0.25$ and $\epsilon = 0.35$. We can distinguish two regions in the graph separated by the dash-dotted line (rough approximation). At low $1/B$, λ_f decreases with increasing $1/B$ while for larger values λ_f starts increasing in size.

When examining whether our results for the finger width λ_f rescale with $1/B^*$ as in the Meniscus regime, we find that this no longer holds for the whole range of $1/B^*$ examined. Results rescale with $1/B^*$ only in the low capillary number regime, whereas for high $1/B^*$ results behave qualitatively in the same way as with $1/B$. As can be seen from Fig. 4.15, $1/B^*$ does not describe the fingering problem for high $1/B^*$, since finger widths from different geometries (different aspect ratios) continue to fall on different curves and deviate systematically from the two dimensional prediction.

The fact that increasing the aspect ratio ϵ has a widening effect on the fingers is not consistent with some results, both experimental and numerical, that have appeared in the literature. For example, Tabeling, Zocchi, and Libchaber [41] found that, for high $1/B$, increasing the aspect ratio has a thinning effect on the finger, whereas Ledesma *et al.* [15], who also used lattice Boltzmann simulations to address the problem, observed the same tendency. Their results even extend below the $\lambda_f \to 1/2$ limit of the two-dimensional theory for high values of aspect ratio and $1/B$.

Other work, however, agrees with our conclusions. Reinelt [44] who investigated the viscous fingering problem in numerical calculations, where the effect of the thin wetting film was

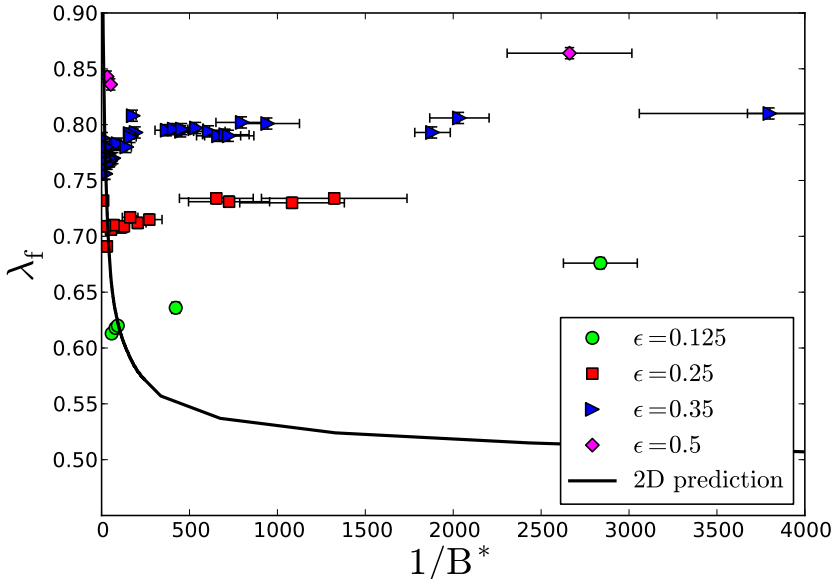

Figure 4.15: Finger width λ_f versus rescaled control parameter $1/B^*$, which takes into account corrections due to curvature effects in the channel thickness direction, in the Thin Film regime. Results scale with $1/B^*$ only in the region of small $1/B^*$ and deviate for larger values.

introduced perturbatively in the two dimensional model, found the same tendency as we do. Moreover, Chevalier *et al.* [45] observed experimentally that the finger width λ_f depends on the aspect ratio for large Ca as we do. They proposed that this should be attributed to inertial effects, since it systematically appeared at high Reynolds numbers $Re = \rho U b/\eta$. They explored a wide range in Re up to 10^2, and they argue that strong inertial effects persist even at velocities below $0.08 ms^{-1}$, which for their experimental systems translates to $Re \approx 5$. Our results vary in the range $10^{-2} \leq Re \leq 10^0$, but already show signs that they are affected by inertial effects. We will examine this further in the following section.

4.3.3.1 Evidence of inertial effects

In our simulations rescaled results for the finger width λ_f with corrections due to curvature effects in the x-z plane, deviate from the two-dimensional prediction for the high $1/B^*$ region as depicted in Fig. 4.15, probably as a consequence of inertial effects.

When inertial effects become important then the Reynolds number $Re = \rho U b/\eta$ that gives the relative importance of inertia to viscous stresses and the Weber number $We = \rho U b^2/\sigma$, which gives the ratio of inertial forces to capillarity, have to be taken into account. In this case

the fluid velocity is given by a modified two-dimensional Darcy's law [46, 47]

$$\rho\left(\frac{6}{5}\frac{\partial U}{\partial t}+\frac{54}{35}U\cdot\nabla U\right)=-\nabla P-\frac{12\eta}{b^2}U. \tag{4.10}$$

Eq. (4.10) can be written in dimensionless form

$$Re^*\left(\frac{6}{5}\frac{\partial U^*}{\partial t}+\frac{54}{35}U^*\cdot\nabla^* U^*\right)=-\nabla^* P^*-U^*\,, \tag{4.11}$$

where Re^* is a rescaled Reynolds number

$$Re^*=\frac{\rho U b^2}{12\eta w}=\frac{b}{12w}Re\,. \tag{4.12}$$

Therefore, actually Re^* should provide a measure of the relative importance of inertia to viscous forces for Hele-Shaw flows.

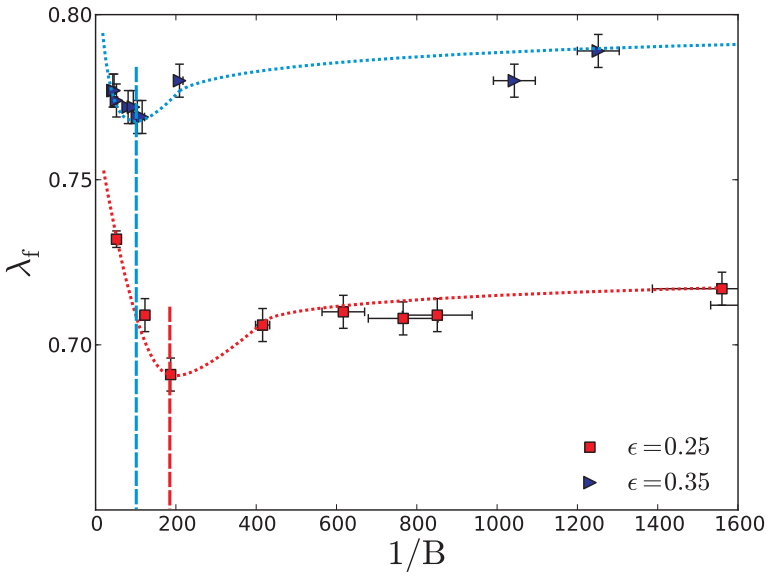

Figure 4.16: Finger width λ_f versus $1/B$. The minimum value for the finger width is obtained at a lower $1/B$ for smaller aspect ratio. Results correspond to simulations with fixed viscosities of the two fluids $\eta_1 = 0.67$ and $\eta_2 = 0.03$, for two geometries with $\epsilon = 0.25$ and $\epsilon = 0.35$.

When examining systems with the same fluids, but different aspect ratios, we observe that the deviation from the classical results commences at smaller $1/B$ for higher aspect ratio ϵ, i.e. larger gap spacing, or smaller width of the channel, as can be seen from Fig. 4.16. This

is consistent with the suggestion that the widening of the fingers with increasing $1/B$ is due to inertial effects. This is because, for two geometries with $\epsilon_1 > \epsilon_2$ at the same $1/B$ value, $Re_1 > Re_2$ (or $Re_1^* > Re_2^*$) and, therefore, inertial effects become important at an earlier stage for the system with larger ϵ.

$$\begin{aligned}(1/B)_1 = (1/B)_2 \quad &\Rightarrow \quad \frac{12}{\epsilon_1^2}\frac{\Delta\eta U_1}{\sigma} = \frac{12}{\epsilon_2^2}\frac{\Delta\eta U_2}{\sigma} \\ &\Rightarrow \quad U_1 > U_2 \Rightarrow Re_1 > Re_2 \, .\end{aligned}$$

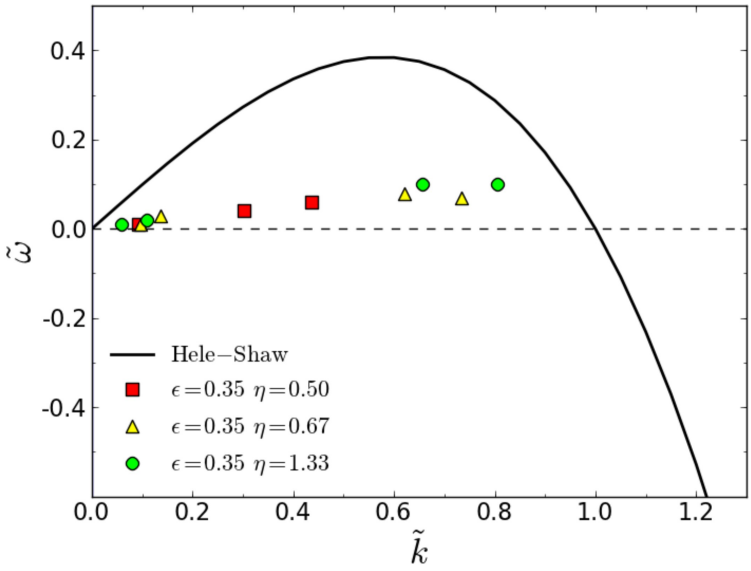

Figure 4.17: Dispersion relation for the linear stability analysis of the interface for the geometry $\epsilon = 0.35$.

Moreover, other evidence that the observed behavior is due to inertial effects comes from examining the dispersion relation. Dias and Miranda [48] employed a perturbative-mode-coupling method to examine how the stability and morphology of the viscosity-driven fingering patterns are affected by inertia. They deduced analytical results for the rectangular Hele-Shaw geometry, and found that inertia has a stabilizing role at the initial stage of the instability; that is, it reduces the growth rate of any given perturbation on the interface. At the later stages they concluded that inertia widens the Saffman-Taylor fingers, as we have observed here. Our results for the dimensionless growth rate $\tilde{\omega}$ as a function of the dimensionless wavevector $\tilde{k}$ for the geometry $\epsilon = 0.35$ are plotted in Fig. 4.17. It is evident that there is considerable decrease in the magnitude of the growth in the whole range of $\tilde{k}$. Another evidence that inertial effects

are observed comes from the fact that the decrease in the growth rate appears to be even more profound in the regime of small $\tilde{k}$, which corresponds to the regime of high $1/B$, where inertial effects are becoming more important.

A reasonable question would be: "Why have we observed a different behavior in the Meniscus and Thin Film regimes and how is this related to the dimensionless Re^* and Weber numbers?"

As explained in section 4.3.3, we were restricted to use relatively thicker channels in the Thin Film regime compared to the Meniscus regime. Furthermore, due to computational limitations we explored systems with higher aspect ratios ($\epsilon \geq 0.25$), as a consequence of which higher capillary numbers were considered in order to achieve high values of $1/B$ that we expected to result in smaller finger widths λ_f. We observed, however, in the Thin Film regime that finger width λ_f increases with increasing $1/B$ or $1/B^*$, something not observed for the Meniscus case. This is because, in the Thin Film regime, Re^* is systematically larger than in the Meniscus regime, as can be seen from Tables 4.6 and 4.7, due to the larger thickness of the cell b and the larger aspect ratios ϵ used, which affects the Re^* since $Re^* = (\epsilon/12)(\rho U b/\eta)$. So, $Re^* \sim 10^{-2}$ in the Thin Film regime, compared with $Re^* \sim 10^{-4} - 10^{-3}$ in the Meniscus regime. Moreover, the Weber number also appears much larger in the Thin Film regime as a consequence of the smaller surface tension[3] used in order to achieve high values of $1/B = (12/\epsilon^2)\Delta\eta U/\sigma$, again as a result of the higher aspect ratios.

4.3.3.2 Inertial effects - Analysis

As we have seen, we can distinguish two regions when examining the behavior of λ_f versus $1/B$ in the Thin Film regime. For low values of $1/B$, λ_f decreases following the classical behavior (region of negligible inertia), while for larger values, λ_f increases in size (inertial region). This leads, inevitably to deviations from two dimensionality. More precisely, in the inertial region we find that:

a) fingers do not thin down with increasing $1/B$, but rather λ_f approaches an asymptotic value λ_f^{lim} from below and

b) results from different geometries and varying aspect ratios ϵ have different limiting values

[3]Due to computational limitations on the maximum fluid viscosity and velocity we explore high values of $1/B$ mainly by means of the surface tension.

λ_f^{lim} as $1/B \to \infty$; in particular λ_f^{lim} increases as ϵ increases.

Chevalier *et al.* [45] suggested that there is a second universal curve in the inertial region of high $1/B$, where results for the finger width λ_f scale with the rescaled Reynolds number Re^*. Their results collapse on a single curve for $Re^* > 0.06$. However, in our simulations we access only up to $Re^* \approx 0.03$ and, therefore, did not verify this scaling. This is because we are restricted regarding the possible values for the velocity, viscosity and channel thickness we can use. Velocities should be kept ≤ 0.01 to ensure that we work in the low Mach regime. So for a system with aspect ratio $\epsilon = 0.25$ ($b = 25$, $w = 100$), $U \sim 0.01$ and using viscosities $\eta_1 = 0.67$, $\eta_2 = 0.03$ (viscosity contrast $r \sim 0.9$) corresponding to $\tau_{f,1} = 2.5$[4] and $\tau_{f,2} = 0.6$, $Re^* \sim 0.007$. For a system with $\epsilon = 0.35$ this becomes $Re^* \sim 0.02$, while for $\epsilon = 0.50$ $Re^* \sim 0.03$.

Chevalier *et al.* also argued that the crossover to the inertial region is controlled by a modified Weber number, combining $1/Re^*$ and $1/B$,

$$We^* = Re^*(1/B) = \frac{\rho u^2 W}{\sigma} = \frac{W}{b} We. \tag{4.13}$$

This implies that above a critical value We^*_{cr} we can expect to enter the inertial regime, where finger widths start to increase.

A simple scaling argument can help understand why the crossover to the inertial regime is controlled by We^*. Considering the relevant forces for the viscous fingering problem and their dependence on the velocity, surface tension scales as u^0, viscous forces as u^1 and inertial forces as u^2. Therefore, at relatively small velocities and consequently small values of the capillary number Ca the dominating forces are surface tension and viscous stresses. At higher velocities, however, the dominating forces are viscous and inertial forces. Therefore, the Reynolds number should be controlling this regime. Therefore, it is reasonable that the threshold between the two limiting cases can be estimated by the Weber number, which gives the ratio of inertia to surface tension.

Next, we proceed to investigate whether the crossover is controlled by We^* in our simulations. Our results, shown in Fig. 4.18, support this hypothesis. When examining systems with the same fluid viscosities and varying aspect ratios, we find that We^*_{cr} is unique and independent of the system geometry. Fig. 4.18(a) shows results for $\epsilon = 0.35, 0.25$ and 0.125 and

[4]Increasing the value of the relaxation time τ_f can lead to strong spurious velocities, which scale as τ_f^3 [27].

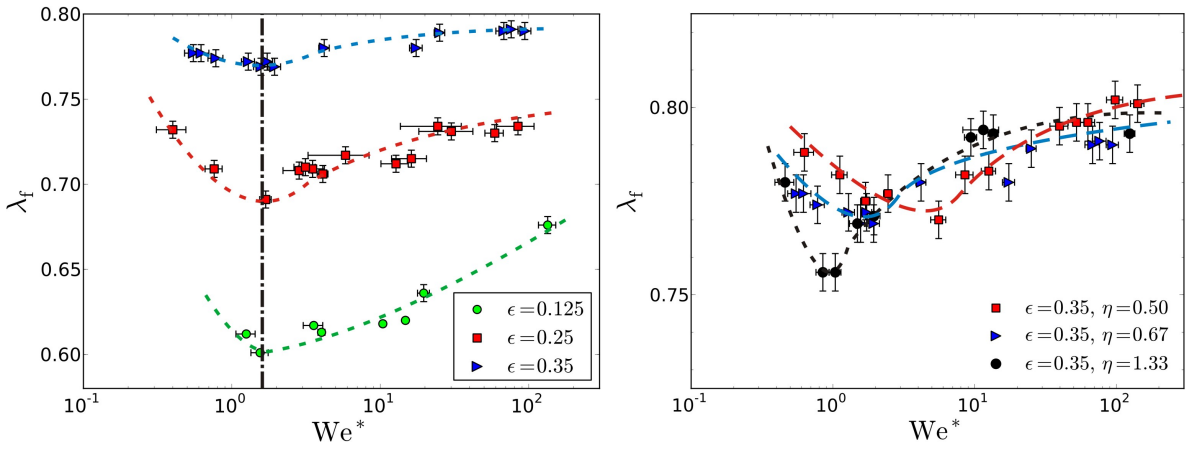

Figure 4.18: Relative finger width λ_f as a function of the modified Weber number We^*: (a) Results from runs with varying aspect ratio ($\epsilon = 0.25$, $\epsilon = 0.35$) and viscosity of the more viscous fluid $\eta = 0.67$. The critical $We_{cr} \approx 1.50$ is plotted with the dashed-dotted line, and is independent of the system geometry. (b) Results for the geometry with $\epsilon = 0.35$ and varying viscosity of the more viscous fluid ($\eta = 0.50$, 0.67 and 1.33). We^*_{cr} shifts to higher values with decreasing the viscosity of the displaced fluid.

viscosities of the fluids $\eta_1 = 0.67$, $\eta_2 = 0.03$, for which $We^*_{cr} \approx 1.50$ for all systems compared with $We^*_{cr} \approx 10$ that Chevalier *et al.* found experimentally. However, from Fig. 4.18(b), where we examine a single geometry with $\epsilon = 0.35$ and varying fluid viscosity ($\eta = 0.50$, 0.67 and 1.33) we find that the critical value We^*_{cr} depends on the viscosity of the more viscous fluid, contrary to their results. More specifically, We^*_{cr} shifts towards higher values with decreasing fluid viscosity. So, for systems with $\eta = 1.33$ we find that $We^*_{cr} \approx 0.85$, while for $\eta = 0.50$ the threshold shifts to $We^*_{cr} \approx 5.50$. We have to note here that numerical simulations by Chevalier *et al.* [45], taking into account a modification of Darcy's law to include inertia, revealed a critical value of $We^*_{cr} \approx 2.0$.

We can include in the modified parameter We^* corrections due to curvature effects across the channel thickness direction (as in $1/B^*$), since results in the non-inertial region scale better with $1/B^*$. Therefore, we can define a rescaled modified Weber number

$$We' = Re^* 1/B^* = \frac{\rho u^2 W}{\sigma}(1 + R_\parallel/R_\perp)^{-1} = \frac{W}{b} We (1 + R_\parallel/R_\perp)^{-1} \,. \tag{4.14}$$

The qualitative behavior of λ_f versus We', however, remains the same as in the plot of λ_f as a function of We^* (Fig. 4.18), with results indicating that the crossover still depends on the fluid viscosity.

4.3.3.3 Comparison with other numerical work

Ledesma *et al.* [15], who also used lattice Boltzmann simulations, did not report inertial effects while studying the Saffman-Taylor instability. They employed a different forcing method in their study and used fluids with the same viscosities. Therefore, they did not study the viscosity-driven Saffman-Taylor instability, as we do, but the instability for the case of fluids with different densities. They set the body force as

$$\rho g = U_{exp} \left(\frac{8\eta}{b^2} \right) \left(\frac{\phi + 1}{2} \right), \tag{4.15}$$

where U_{exp} is the maximum expected velocity for a Poiseuille flow and with the displaced and displacing fluid having equilibrium values for the order parameter as $\phi_{eq} = -1$ and $\phi_{eq} = 1$ respectively. Therefore, the body force ρg acting on the displaced fluid is actually set to zero. In this case the control parameter $1/B$ becomes

$$1/B = w^2 \Delta\rho g/\sigma \ , \tag{4.16}$$

where $\Delta\rho g$ is the difference of the applied forcing on the two fluids.

Furthermore, by modifying the equilibrium distribution functions f_i^{eq} they were solving the Stokes equation and, therefore, precluded any inertial effects. They obtained finger widths $\lambda_f \sim 0.55$ for $\epsilon = 0.35$, already for values of $1/B \sim 1400$. In our case, for the same aspect ratio and $1/B$, and using viscosity of the more viscous fluid $\eta_1 = 0.67$, we found $\lambda_f \sim 0.79$ with $Re^* \sim 0.02$ and $We^* \sim 30$. Increasing the viscosity of the more viscous fluid to $\eta_1 = 2.83$ led to smaller $Re^* \sim 0.002$ and $We^* \sim 3$, but did not improve the situation, since λ_f remained the same. This is because we were still above the critical value of $We^*_{cr} \sim 0.4$ for that viscosity. We did not consider higher viscosity values that could induce smaller Re^* and We^*, because this requires higher relaxation times $\tau_{f,1}$ that can lead to strong spurious velocities at the fluid-fluid interface [27].

4.3.3.4 Width of the finger in the x-z plane

We now return to consider the finger width λ_b of the steady state finger in the x-z plane. Our aim is to investigate whether inertial effects affect the width λ_b of the finger in the x-z

plane, when these affect its width λ_f in the x-y plane. To this end we compare results from the simulations on Saffman-Taylor fingers in the Thin Film regime, presented in section 4.3.3, with the numerical results of Halpern & Gaver [43] and the results from section 4.2.2 that correspond to the limit of $Re^* \to 0$.

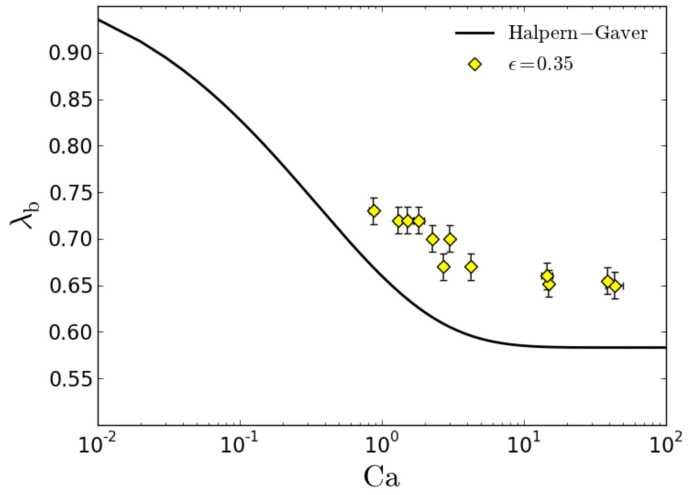

Figure 4.19: Finger width λ_b as a function of Ca for results from three-dimensional simulations on Saffman-Taylor instability in the Thin Film regime ($Re^* \neq 0$). The prediction of Halpern and Gaver [43] is ploted with the solid line.

Here we present results of λ_b from three-dimensional simulations on viscous fingering and channels with aspect ratio $\epsilon = 0.35$. These results cover up to three decades in the capillary number $10^0 \leq Ca \leq 10^2$ and are listed in Table 4.8. It is evident from Fig. 4.19 that the width of the finger λ_b is considerably larger than the numerical results of Halpern & Gaver [43] and our previous results with $Re^* \to 0$ (see Fig. 4.5). This demonstrates that inertial effects are responsible for widening the finger in both the x-y plane x-z planes. Intuitively this makes sense, since inertia will try to slow down the finger at a given flow rate, and the only possible way of achieving this is by making the finger wider in both tranverse and lateral direction. We find that λ_b saturates to a value $\lambda_b \approx 0.65$, 11.5% above the saturation value we obtained for $Re^* \to 0$.

4.4 Summary

In this chapter we have examined the Saffman-Taylor instability in the neutral wetting regime. This corresponds to setting the equilibrium contact angle $\theta_{eq} = 90^\circ$ so that neither of the two

fluids prefer to wet the walls.

We initially studied the interface configuration in the x-z plane. Two regimes were distinguished with different interface profiles. In the first one, coined the Meniscus regime, the less viscous fluid can completely displace the more viscous fluid and the advancing interface maintains a steady meniscus profile. In the second case, however, the less viscous fluid forms a finger and a thin film of the displaced fluid is left behind adhered to the solid walls. In agreement with [14] we found that this process is controlled by the product $CaPe$. Fingering in the x-z plane occurs for high values of $CaPe \geq 0.5$.

Next, we turned our attention to the x-y plane and the viscous fingering problem. In the Meniscus regime the relative finger width scales with a modified capillary number $1/B^*$, that takes into account corrections due to curvature effects in the channel thickness direction. Using this as the control parameter results collapse on the two-dimensional prediction of McLean & Saffman.

In the Thin Film regime, however, we observed much wider viscous fingers. Contrary to the classical prediction of decreasing finger width λ_f with increasing $1/B$, we found that fingers tend to widen at larger values of $1/B$, behavior that persists even when the rescaled modified capillary number $1/B^*$ is used. We argued that inertial effects are responsible for the observed behavior, which is supported by experimental evidence [45] and recent analytical work on inertial effects on Hele-Shaw flows [48, 49].

Table 4.3: Parameter values for runs with viscosity contrast $r = 0.90$ in the Meniscus regime.

b	η_1	σ	D	U	Ca	Pe	CaPe
23	0.333	5.85×10^{-3}	7.54×10^{-2}	3.51×10^{-3}	0.200	1.070	0.214
		5.85×10^{-3}	7.54×10^{-2}	4.41×10^{-3}	0.251	1.344	0.337
		7.02×10^{-3}	9.23×10^{-2}	3.53×10^{-3}	0.168	0.879	0.147
		7.02×10^{-3}	9.23×10^{-2}	4.19×10^{-3}	0.199	1.045	0.208
		7.02×10^{-3}	9.23×10^{-2}	6.59×10^{-3}	0.313	1.642	0.514
		8.19×10^{-3}	1.08×10^{-1}	3.54×10^{-3}	0.144	0.757	0.109
		8.19×10^{-3}	1.08×10^{-1}	4.24×10^{-3}	0.173	0.905	0.156
		8.19×10^{-3}	1.08×10^{-1}	6.50×10^{-3}	0.264	1.387	0.367
		8.19×10^{-3}	7.54×10^{-2}	3.54×10^{-3}	0.144	1.079	0.155
		8.19×10^{-3}	7.54×10^{-2}	4.39×10^{-3}	0.179	1.340	0.240
		8.19×10^{-3}	7.54×10^{-2}	6.49×10^{-3}	0.264	1.981	0.524
28	0.127	6.18×10^{-3}	1.22×10^{-2}	3.05×10^{-3}	0.063	7.002	0.438
		6.18×10^{-3}	1.22×10^{-2}	3.35×10^{-3}	0.069	7.696	0.529
		6.18×10^{-3}	5.85×10^{-2}	3.00×10^{-3}	0.062	1.437	0.088
		6.18×10^{-3}	5.85×10^{-2}	3.72×10^{-3}	0.076	1.781	0.136
		6.18×10^{-3}	5.85×10^{-2}	5.12×10^{-3}	0.105	2.450	0.257
		6.18×10^{-3}	8.13×10^{-2}	4.00×10^{-3}	0.082	1.378	0.113
		6.18×10^{-3}	8.13×10^{-2}	4.52×10^{-3}	0.093	1.557	0.144

Table 4.4: Parameter values for runs with viscosity contrast $r = 0.90$ in the Thin Film regime.

b	η_1	σ	D	U	Ca	Pe	CaPe
23	0.333	1.17×10^{-3}	1.54×10^{-2}	5.27×10^{-3}	1.501	7.871	11.814
		1.17×10^{-3}	1.54×10^{-2}	7.00×10^{-3}	1.996	10.466	20.890
		1.17×10^{-3}	1.54×10^{-2}	1.07×10^{-2}	3.056	16.025	48.969
		2.34×10^{-3}	7.54×10^{-2}	4.90×10^{-3}	0.699	1.495	1.045
		2.34×10^{-3}	7.54×10^{-2}	6.03×10^{-3}	0.859	1.839	1.581
		2.34×10^{-3}	7.54×10^{-2}	9.49×10^{-3}	1.352	2.894	3.912
		3.51×10^{-3}	4.62×10^{-2}	4.59×10^{-3}	0.436	2.286	0.997
		3.51×10^{-3}	4.62×10^{-2}	5.89×10^{-3}	0.560	2.936	1.644
		3.51×10^{-3}	4.62×10^{-2}	9.00×10^{-3}	0.855	4.484	3.835
		3.51×10^{-3}	7.54×10^{-2}	5.76×10^{-3}	0.547	1.756	0.960
		3.51×10^{-3}	7.54×10^{-2}	8.87×10^{-3}	0.842	2.705	2.279
		5.85×10^{-3}	7.69×10^{-2}	8.17×10^{-3}	0.466	2.442	1.138
		5.85×10^{-3}	7.54×10^{-2}	8.38×10^{-3}	0.478	2.557	1.221
		8.19×10^{-3}	1.08×10^{-2}	7.66×10^{-3}	0.312	16.359	5.103
		8.19×10^{-3}	2.15×10^{-3}	7.19×10^{-3}	0.293	76.786	22.487
		8.19×10^{-3}	7.54×10^{-3}	7.54×10^{-3}	0.307	22.986	7.053
28	0.127	3.51×10^{-3}	9.23×10^{-4}	7.53×10^{-3}	27.183	228.339	6207.005
		3.51×10^{-5}	9.23×10^{-4}	8.88×10^{-3}	32.040	269.133	8622.900
		6.18×10^{-3}	5.69×10^{-3}	1.38×10^{-2}	0.283	67.999	19.266
		6.18×10^{-3}	5.69×10^{-3}	1.94×10^{-2}	0.397	95.387	37.911
		6.18×10^{-3}	1.22×10^{-2}	9.20×10^{-3}	0.189	21.123	3.984

Table 4.5: Parameter values for runs that develop a finger in the x-z plane.

b	Ca	Pe	$CaPe$	λ_b
r=0.90				
23	0.250	141.393	35.348	0.713
	0.271	153.176	41.485	0.711
	0.417	11.783	4.909	0.715
	0.792	22.387	17.723	0.678
	0.833	23.566	19.638	0.671
	1.958	55.379	108.451	0.633
	5.736	2615	15001	0.582
	46.00	1840	84640	0.562
	113.08	4523	511514	0.567
28	0.189	21.123	3.984	0.770
	0.283	67.999	19.266	0.724
	0.397	95.387	37.911	0.711
	27.183	228.339	6207.005	0.565
	32.040	269.133	8622.900	0.564
51	0.392	1589	623.323	0.718
	3.249	133	430.685	0.601
	36.551	11868	433777	0.570
	69.040	756	52203	0.571
60	0.032	56.739	1.789	0.863
	0.081	145.499	11.761	0.802
	0.205	147.609	30.262	0.738
	0.220	395.853	87.055	0.730
	0.233	83.806	19.509	0.739
	0.250	179.863	44.932	0.733
	0.255	91.970	23.496	0.736
	0.283	67.999	19.266	0.724
	0.344	5.772	1.983	0.724
	0.397	95.387	37.911	0.711
r=0.97				
148	0.071	80.131	5.709	0.837
	0.114	128.597	14.702	0.796
	0.138	154.726	21.284	0.782
	0.160	179.706	28.711	0.782
	0.276	310.110	85.498	0.742

Table 4.6: Parameter values and finger widths λ_f for runs in the Meniscus regime.

ϵ	η_1	Ca	Re	Re^*	We^*	$1/B$	$1/B^*$	λ_f
0.05	0.333	0.114	6.00×10^{-2}	2.48×10^{-4}	0.138	279.10	139.55	0.613
	0.333	0.314	1.32×10^{-1}	4.36×10^{-4}	1.045	1504.35	677.94	0.539
	0.333	0.627	2.64×10^{-1}	8.71×10^{-4}	4.180	4608.45	1605.31	0.519
0.06	0.333	0.119	3.60×10^{-2}	1.78×10^{-4}	0.058	387.92	199.52	0.587
	0.333	0.238	9.00×10^{-2}	4.46×10^{-4}	0.360	775.83	275.30	0.568
	0.333	0.475	1.80×10^{-1}	8.91×10^{-4}	1.439	1551.67	220.24	0.573
	0.500	0.483	5.42×10^{-2}	2.71×10^{-4}	0.436	1555.27	824.04	0.550
	0.333	0.926	3.51×10^{-1}	1.74×10^{-3}	5.473	3025.75	280.74	0.555
0.09	0.500	0.355	5.98×10^{-1}	4.48×10^{-3}	2.356	503.08	40.83	0.641
	0.500	0.219	3.69×10^{-1}	2.77×10^{-3}	0.899	310.82	65.15	0.622
0.17	0.667	0.978	8.93×10^{-2}	1.25×10^{-3}	0.519	385.76	60.91	0.655
0.22	0.333	0.261	1.49×10^{-1}	2.72×10^{-3}	0.177	55.73	13.51	0.730
	0.333	0.499	2.84×10^{-1}	5.19×10^{-3}	0.644	106.40	16.21	0.693
	0.333	0.523	1.49×10^{-1}	2.72×10^{-3}	0.353	111.47	20.70	0.695
	0.333	1.568	1.49×10^{-1}	2.72×10^{-3}	1.060	351.33	69.59	0.676
	0.333	2.423	2.30×10^{-1}	4.20×10^{-3}	2.533	542.96	84.87	0.647

Table 4.7: Parameter values and finger widths λ_f for runs in the Thin Film regime.

ϵ	η_1	Ca	Re	Re^*	We^*	We^*_{cr}	$1/B$	$1/B^*$	λ_f
0.125	0.67	0.73	6.90×10^{-1}	6.83×10^{-3}	4.02	1.50	531	57.39	0.613
		1.17	1.11×10^{0}	1.10×10^{-2}	10.40		855	79.23	0.618
		1.71	1.08×10^{0}	1.13×10^{-2}	14.77		1248	92.20	0.620
		5.99	4.10×10^{-1}	4.27×10^{-3}	19.61		4367	421.61	0.636
		59.63	2.81×10^{-1}	2.93×10^{-3}	134.16		43502	2836.94	0.676
0.25	0.67	0.29	3.51×10^{-1}	7.03×10^{-3}	0.40	1.50	52	9.01	0.732
		0.67	2.82×10^{-1}	5.87×10^{-3}	0.76		123	18.89	0.709
		1.03	4.13×10^{-1}	8.59×10^{-3}	1.69		187	30.10	0.691
		2.28	4.50×10^{-1}	9.38×10^{-3}	4.10		416	53.35	0.706
		3.38	2.31×10^{-1}	4.82×10^{-3}	3.13		617	68.56	0.710
		4.20	1.69×10^{-1}	3.52×10^{-3}	2.84		766	111.87	0.708
		4.67	1.88×10^{-1}	3.91×10^{-3}	3.50		851	127.13	0.709
		8.55	1.69×10^{-1}	3.48×10^{-3}	5.83		1560	162.26	0.717
		8.87	3.56×10^{-1}	7.35×10^{-3}	12.76		1617	205.50	0.712
		14.25	2.81×10^{-1}	5.80×10^{-3}	16.19		2599	271.56	0.715
		35.78	1.69×10^{-1}	3.48×10^{-3}	24.39		6525	652.54	0.734
		39.75	1.88×10^{-1}	3.87×10^{-3}	30.11		7250	725.04	0.731
		55.65	2.63×10^{-1}	5.47×10^{-3}	59.02		10355	1083.25	0.730
		79.80	2.63×10^{-1}	5.41×10^{-3}	84.63		14556	1323.23	0.734
0.35	0.67	0.48	4.05×10^{-1}	1.19×10^{-2}	0.55	1.50	43	8.55	0.777
		0.51	4.32×10^{-1}	1.27×10^{-2}	0.62		46	8.99	0.777
		0.57	4.86×10^{-1}	1.43×10^{-2}	0.78		52	9.56	0.774
		0.89	5.13×10^{-1}	1.51×10^{-2}	1.29		81	14.13	0.772
		1.03	5.94×10^{-1}	1.75×10^{-2}	1.73		94	15.31	0.772
		1.14	4.86×10^{-1}	1.43×10^{-2}	1.57		104	17.39	0.769
		1.27	5.40×10^{-1}	1.59×10^{-2}	1.94		116	18.84	0.769
		2.28	6.48×10^{-1}	1.91×10^{-2}	4.19		209	30.54	0.780
		11.40	5.40×10^{-1}	1.59×10^{-2}	17.44		1043	143.20	0.780
		13.68	6.48×10^{-1}	1.91×10^{-2}	25.12		1252	166.25	0.789
		52.79	4.46×10^{-1}	1.29×10^{-2}	67.98		5012	665.51	0.790
		55.90	4.73×10^{-1}	1.36×10^{-2}	76.22		5307	706.58	0.791
		62.11	5.25×10^{-1}	1.52×10^{-2}	94.10		5780	726.13	0.790
0.35	1.33	0.87	1.84×10^{-1}	5.31×10^{-3}	0.46	0.85	85	15.44	0.780
		1.18	2.49×10^{-1}	7.20×10^{-3}	0.85		115	22.40	0.756
		1.30	2.76×10^{-1}	7.96×10^{-3}	1.04		127	24.46	0.756
		2.37	2.18×10^{-1}	6.29×10^{-3}	1.49		230	37.13	0.769
		2.71	2.49×10^{-1}	7.20×10^{-3}	1.95		264	41.03	0.771
		12.42	2.63×10^{-1}	7.58×10^{-3}	9.41		1210	162.62	0.792
		14.90	3.15×10^{-1}	9.10×10^{-3}	13.55		1452	196.20	0.793
		43.46	9.19×10^{-2}	2.65×10^{-3}	11.52		4235	612.92	0.794
		142.81	3.02×10^{-1}	8.72×10^{-3}	124.41		13914	1882.27	0.793
0.35	2.83	1.51	6.17×10^{-2}	1.80×10^{-3}	0.27	0.40	146	29.13	0.767
		1.82	7.62×10^{-2}	2.24×10^{-3}	0.39		173	33.34	0.765
		1.97	8.26×10^{-2}	2.43×10^{-3}	0.46		187	36.06	0.765
		2.27	9.26×10^{-2}	2.70×10^{-3}	0.60		220	39.41	0.767
		2.82	1.15×10^{-1}	3.35×10^{-3}	0.92		273	50.07	0.767
		3.00	1.22×10^{-1}	3.57×10^{-3}	1.05		290	52.24	0.768
		3.51	1.43×10^{-1}	4.18×10^{-3}	1.44		340	58.49	0.769
		4.24	1.73×10^{-1}	5.04×10^{-3}	2.09		410	69.52	0.770
		14.54	7.62×10^{-2}	2.24×10^{-3}	3.14		1384	180.18	0.808
		31.49	8.26×10^{-2}	2.43×10^{-3}	7.37		2998	454.99	0.794
		38.76	1.02×10^{-1}	2.99×10^{-3}	11.16		3690	539.52	0.797
		157.46	8.26×10^{-2}	2.43×10^{-3}	36.85		14990	2035.25	0.806
0.50	1.33	3.04	6.00×10^{-1}	2.50×10^{-2}	3.65	0.85	144	51.80	0.836
		3.61	7.13×10^{-1}	2.97×10^{-2}	5.14		171	31.50	0.843
		342.00	5.63×10^{-1}	2.34×10^{-2}	384.75		16211	2661.47	0.864

Table 4.8: Parameter values and finger widths λ_b for runs in the Thin Film regime. The aspect ratio of channel is $\epsilon = 0.35$.

η_1	Ca	Re	Re^*	We^*	We^*_{cr}	$1/B$	λ_b
1.33	1.30	2.76×10^{-1}	7.96×10^{-3}	1.04	0.85	127	0.720
	2.71	2.49×10^{-1}	7.20×10^{-3}	1.95		264	0.670
	14.90	3.15×10^{-1}	9.10×10^{-3}	13.55		1452	0.652
	43.46	9.19×10^{-2}	2.65×10^{-3}	11.52		4235	0.650
	142.81	3.02×10^{-1}	8.72×10^{-3}	124.41		13914	0.645
2.83	1.82	7.62×10^{-2}	2.24×10^{-3}	0.39	0.40	173	0.720
	2.27	9.26×10^{-2}	2.70×10^{-3}	0.60		220	0.700
	3.00	1.22×10^{-1}	3.57×10^{-3}	1.05		290	0.700
	4.24	1.73×10^{-1}	5.04×10^{-3}	2.09		410	0.0.670
	14.54	7.62×10^{-2}	2.24×10^{-3}	3.14		1384	0.660
	38.76	1.02×10^{-1}	2.99×10^{-3}	11.16		3690	0.655
	157.46	8.26×10^{-2}	2.43×10^{-3}	36.85		14990	0.653

Chapter 5

Saffman-Taylor Instability – Complete Wetting Regime

In this chapter we shall examine the viscous fingering problem in the complete wetting regime. That is, we consider the situation where the displacing fluid completely wets the substrate. This is a different case to that previously examined experimentally or numerically throughout the literature. The situation is characterized by vanishing contact angle and thick layers of the wetting phase covering the substrate. Our aim is to investigate the effect of wetting on the instability, along with the importance of the hitherto neglected third dimension in the viscous fingering problem.

Our strategy will be to study the Saffman-Taylor instability by dividing the problem into two subproblems, as we did in Chapter 4, i.e. by studying the evolution of the fluid-fluid interface in the x-z and then the x-y planes. Therefore, we shall start in section 5.1 by examining the forced displacement of the interface in the x-z plane. It is reasonable to expect the same interface configurations as in the neutral wetting case, that is a) a Meniscus configuration where the penetrating fluid completely displaces the resident fluid and b) a Thin Film configuration where the displacing fluid forms a finger in the x-z plane as well as in the x-y plane. We shall examine the penetration process in the x-z plane and establish the relevant control parameters.

Then in section 5.2 we shall describe recent experiments performed in microfluidic devices using colloid polymer mixtures. These experiments, which were conducted by Siti Aminah Setu and Gareth Davies, colleagues in the Physical and Theoretical Chemistry Laboratory in

Oxford University, working under the supervision of Dr. Dirk G.A.L. Aarts, were a primary motivation for this research.

Comparison of lattice Boltzmann simulations to these experiments will be carried out in section 5.3, in light of our findings from section 5.1. In particular, we shall examine the penetration process and the interface configuration in the x-z plane, as well as the width of the finger λ_b and the curvature of the leading interface $\kappa_\perp$ in the x-z plane.

Finally, in section 5.3.4 we shall turn our attention to the x-y plane and the Saffman-Taylor instability itself and examine how the wetting conditions and the interface structure in the x-z plane affect the viscous fingering problem.

5.1 Interface configuration in the x-z plane

We begin our investigation of the viscous fingering problem in the complete wetting regime by studying the forced displacement of the fluid-fluid interface in the x-z plane. In particular, we consider the situation where the less viscous fluid, which is the displacing fluid, completely wets the substrate. Under these wetting conditions we have a wetting layer of the less viscous fluid covering the substrate and, in the absence of any external forcing, the interface configuration is a concave meniscus as shown in Fig. 5.1. The interface will of course move slowly towards the right, due to the action of capillary filling[1]. Here, however, we will concentrate only on the forced displacement of the interface.

Figure 5.1: Schematic representation of the interface configuration in the x-z plane if the less viscous fluid 1 wets the substrate. The system is initially left to relax until a meniscus is formed and then the body force $\rho\mathbf{g}$ is turned on.

As we have seen in section 4.2, for the neutral wetting case, the shape of the advancing interface in the x-z plane depends on the dimensionless Ca and Pe numbers, in agreement with [14]. We proceed here to examine how the different wetting boundary conditions and the

[1]Typical velocities for capillary filling are an order of magnitude smaller than the velocities achieved with the forced displacement of the interface.

presence of a wetting film on the walls affect the penetration process in the x-z plane.

5.1.1 Simulation set-up

We first considered fluids of equal viscosities and densities, which allowed better control over the fluid velocity and made it easier to study the onset of the penetration in the x-z plane. Starting from a flat interface configuration in the x-z plane, we set the wetting layer on the substrate by hand[2] and left the system to relax for 2×10^4 time-steps with no body force acting on the fluids, so that a smooth meniscus was formed, as shown in Fig. 5.1. After this period of time we turned on the body force $\rho \mathbf{g}$. The thickness of the wetting layer ζ was of order the interface width ($\zeta \sim$5 lattice units). This choice is consistent with the thickness of the wetting layer in recent experiments on colloid-polymer mixtures.

Regarding the wetting boundary condition, we set the value of the derivative of the order parameter at the substrate to $\partial_\perp \phi = 0.84$. This is larger than the value that corresponds to a contact angle $\theta_{eq} = 0$, $\partial_\perp \phi = 0.60$, and ensured that we were in the complete wetting regime. This choice proved to be adequate, since it provided a stable wetting layer on the substrate with an approximately constant thickness ζ.

5.1.2 Effect of surface tension and diffusivity

In order to explore the effect of capillarity, simulations were performed at fixed forcing, diffusivity and viscosity, while Ca was varied by changing the surface tension. Note that this choice keeps Pe fixed. Fig. 5.2 shows the interface evolution in the x-z plane for these runs, and details of the simulations are summarised in Table 5.1. As expected, fingering in the x-z plane occurs for high values of Ca, which is achieved by decreasing the surface tension. Moreover, we observe that at the lowest Ca, which corresponds to run(a), the interface advances as a concave meniscus. As we increase Ca, the interface curvature changes sign at $Ca \sim 0.22$ (see run(b)) and in run(c) the interface advances as a convex meniscus. Nevertheless, in runs (a-c), the shape of the interfacial profile remains constant in time and there is no fingering.

Then, at higher $Ca = 0.64$ the interface position becomes decoupled from that of the 'contact line', and a finger is formed as shown in run(d). We stress again that this is due

[2]In simulations where we just imposed the appropriate wetting boundary condition and left the system to develop the thin wetting layer, this process took remarkably long time $\sim 10^6$ time-steps.

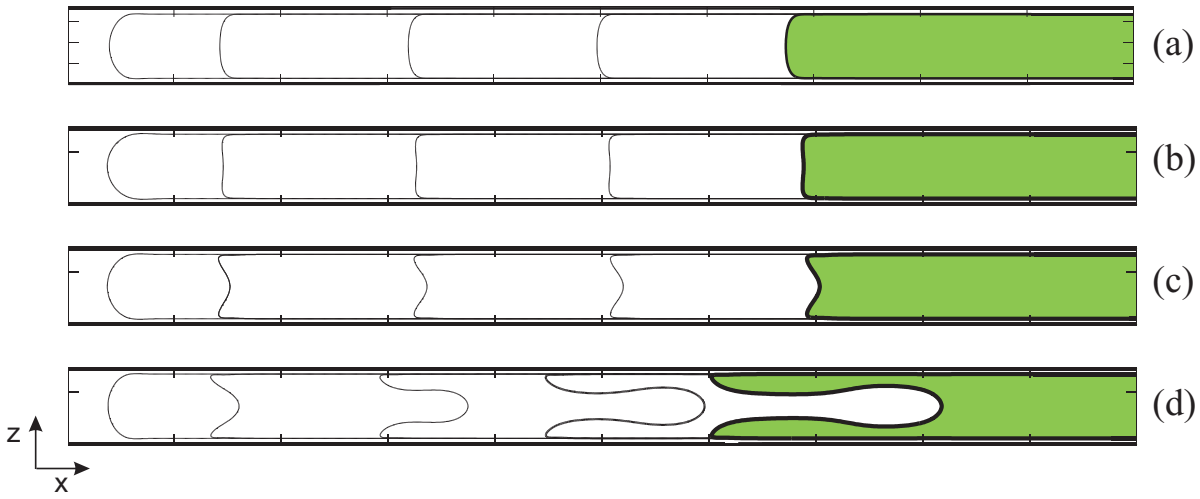

Figure 5.2: Interface evolution in the x-z plane for varying surface tension. The time interval between the plotted interface positions is $\delta t = 5 \times 10^4$ time-steps in lattice units. The thickness of the cell and the wetting layer are $b = 70$ and $\zeta = 5$ respectively in lattice units. Surface tension: (a) $\sigma = 9.36 \times 10^{-3}$, (b) $\sigma = 5.85 \times 10^{-3}$, (c) $\sigma = 3.51 \times 10^{-3}$ and (d) $\sigma = 2.34 \times 10^{-3}$.

to a completely different mechanism to the Saffman-Taylor fingering. It is not driven by an instability of the interface, but rather by the inability of the interfacial region that joins the bulk of the displacing fluid to the thin wetting layer to move as quickly as the leading interface. From now on, we will refer to this interfacial region as an effective 'contact line', although it is not a true contact line as the liquid slides over a wetting layer.

We also studied the effect of the diffusivity on the penetration process. For a set of simulation runs we fixed the viscosity, forcing and surface tension, which corresponds to fixing Ca, while we varied Pe by tuning the diffusion coefficient D. The channel thickness and the

Table 5.1: Parameter values and resulting interface shapes for runs with $\eta = 0.33$ and varying surface tension for two different channels with $b = 70$ and $b = 298$.

Run	b	D	σ	Ca	shape
a	70	1.35×10^{-3}	9.36×10^{-3}	0.132	Meniscus
b			5.85×10^{-3}	0.218	Meniscus
c			3.51×10^{-3}	0.342	Meniscus
d			2.34×10^{-3}	0.641	Finger
e	298	1.24×10^{-2}	6.67×10^{-3}	0.094	Meniscus
f			3.33×10^{-3}	0.241	Meniscus
g			2.38×10^{-3}	0.434	Finger
h			1.67×10^{-3}	0.700	Finger

wetting layer thickness were set to $b = 70$ and $\zeta = 5$ respectively. As can be seen from Fig. 5.3, varying the diffusivity affects the penetration process in the x-z plane as in the neutral wetting case. Even though there is no longer a moving contact line, the results can be interpreted in the same light. Decreasing the diffusion strength decreases the velocity of the fluid-fluid interface in the region where the meniscus meets the surface wetting layer, i.e. the velocity of the effective 'contact line', as can be deduced from Fig. 5.3. This is because the diffusion coefficient controls the time over which the interface can relax to equilibrium.

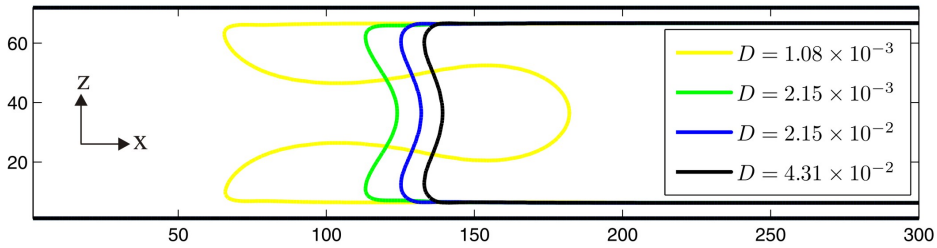

Figure 5.3: Interface snapshot in the x-z plane for varying diffusion coefficients at $t = 5 \times 10^4$ time-steps. The thickness of the cell and the wetting layer are $b = 70$, $\zeta = 5$ respectively in lattice units.

Runs with higher diffusion coefficients $D = 4.31 \times 10^{-2}$, $D = 2.15 \times 10^{-2}$ and $D = 2.15 \times 10^{-3}$ advance as a meniscus, while a run with $D = 1.08 \times 10^{-3}$ develops a finger in the x-z plane, as it can no longer keep up with the leading interface located at z = $b/2$. This is shown in Fig. 5.3 where the interface shape is plotted for different D at $t = 5 \times 10^4$ time-steps. Moreover, another indication of the effect of diffusivity, is the interface curvature in the middle of the channel (z = $b/2$). When comparing results that develop an advancing meniscus, the interface for the smallest diffusion coefficient ($D = 2.15 \times 10^{-3}$) is the most curved.

5.1.3 Onset of penetration

We have seen in section 5.1.2 that, as in the case of neutral wetting, our simulations indicate two possible steady state configurations for the shape of the advancing interface in the x-z plane. The fluid-fluid interface can advance as a meniscus or it can penetrate the displaced fluid and develop a finger in the x-z plane. These configurations appear to be governed by the same mechanisms as in the neutral wetting case and controlled by Ca and Pe. In this section, the objective is to determine whether the relevant control parameters are indeed these dimensionless numbers and to establish the threshold for the transition between the Meniscus

and the Thin Film regimes.

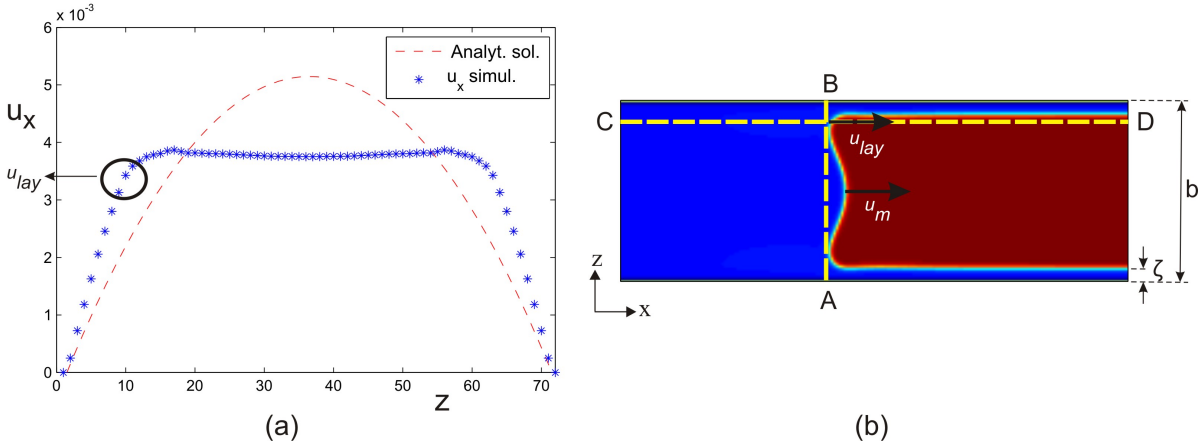

Figure 5.4: (a) The x component of the fluid velocity as a function of the height of the channel z along the line A-B in (b). The fluid velocity of the interfacial region at a height z $\sim \zeta$ is marked with a circle. It is obviously larger than the analytical solution for a one phase flow of a fluid with the same viscosity and comparable with the leading interface velocity. The interface in this case is advancing as a meniscus as can be seen from (b).

We consider fluids with the same viscosities. In Fig. 5.4(a) we plot the fluid velocity along the line A-B in Fig. 5.4(b) for a case when the interface is advancing as a meniscus. Note that there is an increase in the fluid velocity at a height z $\sim \zeta$ when compared to the velocity profile for Poiseuille flow. This is generated by the combined effect of diffusivity and surface tension. The velocity of the interface at a height z $\sim \zeta$, u_{lay}, is comparable with the velocity of the interface in the middle of the channel u_m. Moreover, the velocity in the middle of the channel, u_m, is smaller than the analytical solution, because of the effect of surface tension, which tends to restore the shape of the interface to its equilibrium value and maintain a stable meniscus shape. The increase in the velocity is also obvious in Fig. 5.5, where we plot the x component of the fluid velocity along the line C-D in Fig. 5.4(b), which lies just above the wetting layer at a height z $\sim \zeta$.

In order to study the onset of penetration in the x-z plane we reproduce the scaling argument presented in [24] to obtain the diffusion length-scale L_D and then the velocity u_{lay} of the interface at a height z $\sim \zeta$. We will compare this velocity to the leading interface velocity in the middle of the channel u_m to determine the crossover from the Meniscus to the Thin Film regime, in terms of the dimensionless numbers Ca and Pe.

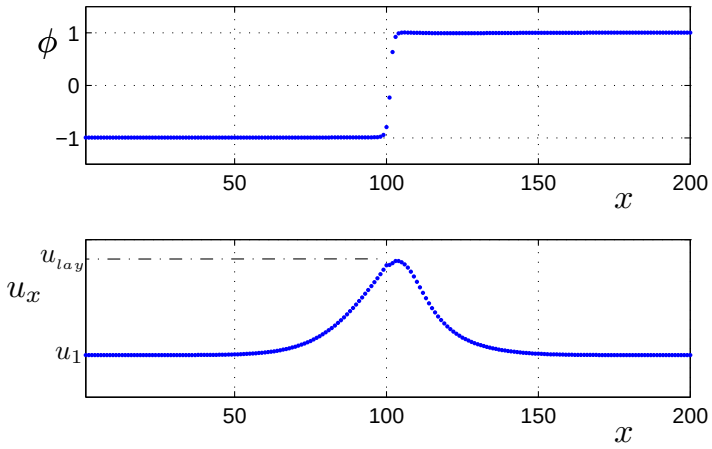

Figure 5.5: (a) The order parameter ϕ (concentration) profile measured along the line C-D in Fig. 5.4(b). This line lies just above the wetting layer at a height z $\sim \zeta$. The two fluids have equilibrium values for concentration $\phi_{eq} = \pm 1$. The interface is located at $\phi = 0$. (b) The x component of the fluid velocity along the same line. There is a very clear peak in the velocity at the position of the interface between the two fluids. Typically $(u_{lay} - u_1)/u_1 \sim 50\%$.

Consider the Stokes equation integrated across the interface in the x direction

$$\int \mathrm{d}x \, [\partial_y P_{yx} + \partial_x P_{xx}] = \int \mathrm{d}x \, \eta \nabla^2 u_x \, . \tag{5.1}$$

Using the definition of the pressure tensor, Eq. (3.6),

$$P_{\alpha\beta} = (p_b - \kappa\phi\nabla^2\phi - \frac{\kappa}{2}(\nabla\phi)^2)\delta_{\alpha\beta} + \kappa(\partial_\alpha\phi)(\partial_\beta\phi)$$

and some algebra we obtain

$$\int \mathrm{d}x \, \partial_x(\rho T) + \int \mathrm{d}x(\phi \, \partial_x\mu) = \eta \int \mathrm{d}x \, \nabla^2 u_x \, . \tag{5.2}$$

The first term is zero for an incompressible fluid and the second one can be integrated by parts to give $[\phi\mu - \int \mathrm{d}x(\mu\partial_x\phi)]$, which scales as $\mu(\Delta\phi/\xi)\xi$. μ, ξ are the chemical potential and interface width respectively.

Making the assumption that the term $\nabla^2 u_x$ does not vary significantly across the interface, and using L_D as the length-scale for the velocity field in the x direction, the right hand side of Eq. (5.2) scales as $\eta(\Delta u_x/L_D^2 + u_{lay}/\zeta^2)\xi$, where $\Delta u_x = u_{lay} - u_1$ and u_1 is the velocity far

away from the interface at a height z $\sim \zeta$ as shown in Fig. 5.5. This leads to

$$\mu\frac{\Delta\phi}{\xi} \approx \eta\Big(\frac{\Delta u_x}{L_D^2} + \frac{u_x}{\zeta^2}\Big) \,. \tag{5.3}$$

In the interfacial region at z $\sim \zeta$ the time variation of the order parameter ϕ is

$$\frac{\partial\phi}{\partial t} \approx u_{lay}\frac{\Delta\phi}{\xi} \tag{5.4}$$

and, using the diffusion-advection equation for the order parameter, we find that it obeys

$$u_{lay}\frac{\Delta\phi}{\xi} \approx \frac{D\Delta\phi}{L_D^2} \Rightarrow L_D^2 \approx \frac{D\xi}{u_{lay}} \,. \tag{5.5}$$

We can eliminate the chemical potential in Eq. (5.3) by using the Gibbs-Thompson relation that gives the value of the chemical potential at a gently curved interface [50]

$$\mu\Delta\phi = \sigma\kappa \,, \tag{5.6}$$

where κ the interface curvature. Furthermore, the curvature κ is set by the characteristics of the channel and the thickness of the wetting layer ζ, since it is affected by the underlying velocity profile. Therefore, we can assume that it scales as $m/(b/2-\zeta)$ with m a constant that should depend in principle on Ca and Pe. Now Eq. (5.3) becomes

$$\frac{\sigma m}{(b/2-\zeta)\xi} \approx \eta\Big(\frac{(u_{lay}-u_1)u_{lay}}{D\xi} + \frac{u_{lay}}{\zeta^2}\Big). \tag{5.7}$$

After a little algebra we extract the following scaling law for the velocity u_{lay},

$$u_{lay} \approx \Big(A^2 + \frac{D\sigma m}{\eta(b/2-\zeta)}\Big)^{1/2} - A \,, \tag{5.8}$$

where $A = \frac{D\xi}{2\zeta^2} - \frac{u_1}{2}$.

We need to compare u_{lay} to the leading interface velocity u_m to resolve whether the interface is advancing as a meniscus or developing a finger in the x-z plane. For a meniscus $u_{lay} = u_m$, leading to the condition

$$mCa^{-1}(Pe^*)^{-1} \approx 1 + \frac{D\xi}{u_m\zeta^2} - \frac{u_1}{u_m} \tag{5.9}$$

where $Ca = \eta u_m/\sigma$ and

$$Pe^* = u_m(b/2 - \zeta)/D. \tag{5.10}$$

Using the expression for the analytical solution for the velocity field for a Poiseuille flow, the term u_1/u_m in Eq. (5.9) can be approximated by $4(\zeta/b)(1-\zeta/b)$ and Eq. (5.9) becomes

$$\Big[mCa^{-1} - \frac{\xi(b/2-\zeta)}{\zeta^2}\Big] Pe^{*-1} \approx 1 - 4\frac{\zeta}{b}\Big(1 - \frac{\zeta}{b}\Big) = C. \tag{5.11}$$

Finally, we arrive at the following condition for a meniscus

$$Pe^* \approx c(Ca^*)^{-1} + \delta\ , \tag{5.12}$$

where $\delta \approx -\frac{\xi(b/2-\zeta)}{\zeta^2} C^{-1}$ and

$$Ca^* = \{1 - 4(\zeta/b)(1-\zeta/b)\}Ca\ . \tag{5.13}$$

Simulations of forced interfaces were performed for a wide range of Ca^* and Pe^* numbers, for varying channel thickness, to check the validity of this prediction and to extract fitting values for the parameters c and δ.

5.1.3.1 Symmetric fluids

We first examined the case of zero viscosity contrast $r = (\eta_1 - \eta_2)/(\eta_1 + \eta_2) = 0$, before extending our simulations to the asymmetric case. The details of our simulations are listed in Table 5.2 and Fig. 5.6 shows a plot of the results in the $(Pe^*, (Ca^*)^{-1})$ plane. We can distinguish two regions in the $(Pe^*, (Ca^*)^{-1})$ plane. At high values of Pe^* and Ca^* the interface develops a finger in the x-z plane and the Thin Film regime is observed, whereas for low values the interface advances as a meniscus. The formula $Pe^* = c(Ca^*)^{-1} + \delta$ is plotted as a solid line, with $c \approx 28$ and $\delta \approx -38$.

Comparing our prediction for the crossover between the Thin Film and Meniscus regimes with the result we obtained in section 4.2.1 for the neutral wetting case and $r = 0.90$, we find qualitatively the same behaviour, although now the offset δ accounts for the presence of the wetting layer[3]. In both situations the penetration process is governed by the interplay of

[3] $\delta = 0$ in the neutral wetting regime.

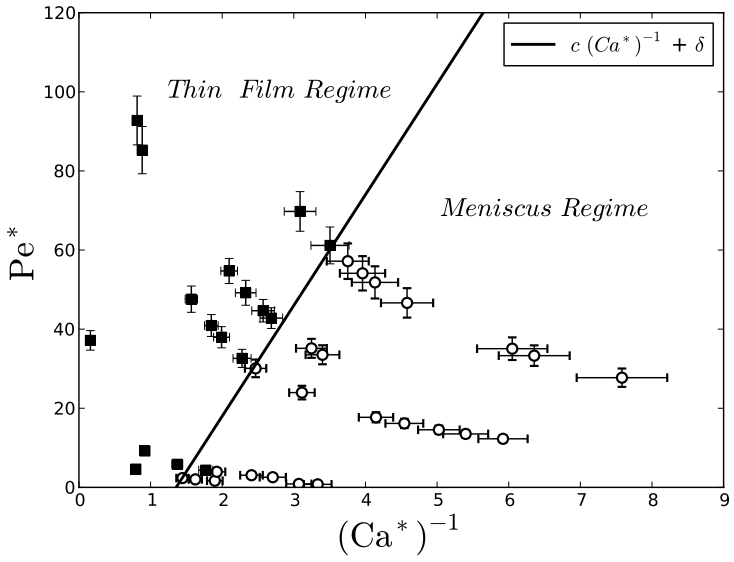

Figure 5.6: Simulation data from Table 5.2 plotted in the $(Pe^*, (Ca^*)^{-1})$ plane for fluids with same viscosities ($r = 0$). Results in the Thin Film regime are denoted by squares (■), whereas results in the Meniscus regime are denoted by circles (○). The solid line is $Pe^* = c(Ca^*)^{-1} + \delta$ with $c \approx 28$ and $\delta \approx -38$.

capillary and Péclet numbers. However, now, in the case of complete wetting it is more difficult to enter the Thin Film regime. Ledesma *et al.* [14] found $c \approx 0.15$ for the neutral wetting case and $r = 0$ compared to $c \approx 28$ that we find here for the case of complete wetting. This substantial difference is entirely due to the wetting properties of the fluids and the presence of the wetting layer. The increased ease with which the 'contact line' can move across the pre-formed wetting layer means that fingering in the x-z plane is strongly suppressed.

Nevertheless, Fig. 5.6 reveals that it is possible to enter the Thin Film regime even in the limit $Pe^* \to 0$ if Ca^* is sufficiently high. This suggests that there is an upper limit to the contribution to the velocity of the 'contact line' resulting from diffusivity.

5.1.3.2 Asymmetric fluids

We have shown that fingering in the x-z plane is controlled by the interplay between Ca^* and Pe^*. We expect that the same will happen for fluids with different viscosities. In our case, since we are focusing on the Saffman-Taylor instability, the displacing fluid, which wets the walls, is the less viscous fluid. We now proceed to examine two different viscosity contrast ratios $r = (\eta_1 - \eta_2)/(\eta_1 + \eta_2) = 0.90$ and 0.36.

Table 5.2: Parameter values for the runs used to generate Fig. 5.6. For all runs $\partial_\perp \phi = 0.84$ and $\eta = 0.333$ ($r = 0$).

b	ζ	σ	D	u_m	Ca	Pe^*	*Shape*
140	6.2	6.55×10^{-3}	6.89×10^{-3}	3.00×10^{-3}	0.153	27.73	Meniscus
	6.2	5.85×10^{-3}	6.16×10^{-3}	3.21×10^{-3}	0.183	33.30	Meniscus
	6.2	5.32×10^{-3}	5.60×10^{-3}	3.08×10^{-3}	0.193	35.06	Meniscus
	6.2	4.09×10^{-3}	4.31×10^{-3}	3.15×10^{-3}	0.257	46.64	Meniscus
	6.2	3.74×10^{-3}	3.94×10^{-3}	3.20×10^{-3}	0.285	51.82	Meniscus
	6.2	3.51×10^{-3}	3.69×10^{-3}	3.13×10^{-3}	0.298	54.12	Meniscus
	6.2	3.39×10^{-3}	3.57×10^{-3}	3.20×10^{-3}	0.314	57.18	Meniscus
	6.1	3.27×10^{-3}	3.45×10^{-3}	3.30×10^{-3}	0.336	61.17	Finger
	6.2	3.04×10^{-3}	3.20×10^{-3}	3.50×10^{-3}	0.384	69.76	Finger
70	5.1	3.27×10^{-3}	4.31×10^{-2}	3.70×10^{-3}	0.377	2.57	Meniscus
	5.3	2.81×10^{-3}	3.69×10^{-2}	3.81×10^{-3}	0.453	3.07	Meniscus
	5.1	2.34×10^{-3}	3.08×10^{-2}	4.48×10^{-3}	0.638	4.36	Finger
	5.0	1.75×10^{-3}	2.31×10^{-2}	4.50×10^{-3}	0.855	5.85	Finger
	5.0	1.17×10^{-3}	1.54×10^{-2}	4.73×10^{-3}	1.347	9.20	Finger
70	5.2	3.04×10^{-3}	3.20×10^{-3}	3.60×10^{-3}	0.394	33.52	Meniscus
	5.2	3.04×10^{-3}	3.20×10^{-3}	3.77×10^{-3}	0.413	35.15	Meniscus
	5.2	2.81×10^{-3}	2.95×10^{-3}	4.25×10^{-3}	0.504	42.79	Finger
	5.2	2.57×10^{-3}	2.71×10^{-3}	4.06×10^{-3}	0.525	44.66	Finger
	5.1	2.34×10^{-3}	2.46×10^{-3}	4.05×10^{-3}	0.577	49.19	Finger
	5.1	2.34×10^{-3}	2.46×10^{-3}	4.50×10^{-3}	0.641	54.71	Finger
35	5.9	3.86×10^{-3}	4.06×10^{-3}	4.30×10^{-3}	0.371	12.28	Meniscus
	5.9	3.51×10^{-3}	3.69×10^{-3}	4.30×10^{-3}	0.409	13.51	Meniscus
	5.9	3.27×10^{-3}	3.45×10^{-3}	4.33×10^{-3}	0.441	14.56	Meniscus
	5.9	2.92×10^{-3}	3.08×10^{-3}	4.30×10^{-3}	0.490	16.17	Meniscus
	5.9	2.69×10^{-3}	2.83×10^{-3}	4.32×10^{-3}	0.536	17.71	Meniscus
	6.0	1.99×10^{-3}	2.09×10^{-3}	4.36×10^{-3}	0.731	23.96	Meniscus
	5.9	1.52×10^{-3}	1.60×10^{-3}	4.15×10^{-3}	0.910	30.08	Meniscus
	5.9	1.52×10^{-3}	1.60×10^{-3}	4.30×10^{-3}	0.943	31.17	Meniscus
	5.9	1.52×10^{-3}	1.60×10^{-3}	4.50×10^{-3}	0.987	32.61	Finger
	6.1	1.29×10^{-3}	1.35×10^{-3}	4.50×10^{-3}	1.166	37.96	Finger
	6.1	1.29×10^{-3}	1.35×10^{-3}	4.85×10^{-3}	1.257	40.92	Finger
	5.9	1.05×10^{-3}	1.11×10^{-3}	4.55×10^{-3}	1.441	47.58	Finger
	6.0	5.85×10^{-4}	6.16×10^{-4}	4.55×10^{-3}	2.594	85.26	Finger
	6.0	5.85×10^{-4}	6.16×10^{-5}	4.95×10^{-3}	2.822	92.76	Finger
	5.9	1.17×10^{-4}	1.54×10^{-3}	4.93×10^{-3}	14.051	37.16	Finger

We note here that for asymmetric fluids we should use the average of the two viscosities in the definition of Ca. This is a consequence of integrating the right hand side of Eq. (5.1) across the interface

$$\int \mathrm{d}x \, \eta \nabla^2 u_x = \frac{(\eta_1 + \eta_2)}{2} \, \xi \nabla^2 u_x \, . \tag{5.14}$$

So, in Eq. (5.12), $Ca = \eta u_m / \sigma$ should be replaced by

$$Ca' = (\eta_1 + \eta_2) \, u_m / 2\sigma \tag{5.15}$$

and $Ca^* = \{1 - 4(\zeta/b)(1 - \zeta/b)\}Ca'$.

Table 5.3: Parameter values and results for viscosity contrast ratio $r = 0.90$. For all runs $b = 70$, $\partial_\perp \phi = 0.84$ and $\eta_1 = 0.333$.

ζ	σ	D	u_m	Ca	Ca'	Pe^*	*Shape*
5.0	1.67×10^{-3}	2.33×10^{-3}	9.54×10^{-2}	1.908	1.002	122.57	Meniscus
5.0	1.67×10^{-3}		1.06×10^{-2}	2.112	1.109	135.69	Meniscus
5.0	1.67×10^{-3}		1.45×10^{-2}	2.898	1.521	186.19	Meniscus
5.1	8.33×10^{-4}		8.91×10^{-3}	3.564	1.871	114.18	Meniscus
5.1	8.33×10^{-4}		1.15×10^{-2}	4.596	2.413	147.24	Finger
5.1	8.33×10^{-4}		1.85×10^{-2}	7.392	3.881	236.81	Finger
4.9	5.56×10^{-4}		1.06×10^{-2}	6.336	3.326	136.17	Finger
4.9	5.56×10^{-4}		1.21×10^{-2}	7.248	3.805	155.77	Finger
4.9	5.56×10^{-4}		1.65×10^{-2}	9.870	5.182	212.11	Finger
4.6	3.33×10^{-4}		1.11×10^{-2}	11.070	5.812	144.05	Finger
4.6	3.33×10^{-4}		1.25×10^{-2}	12.460	6.542	162.13	Finger
4.6	3.33×10^{-4}		1.60×10^{-2}	16.030	8.416	208.59	Finger
5.0	1.67×10^{-3}	4.67×10^{-3}	8.43×10^{-3}	1.686	0.885	54.17	Meniscus
5.0	1.67×10^{-3}		1.09×10^{-2}	2.178	1.143	69.97	Meniscus
5.0	1.67×10^{-3}		1.48×10^{-2}	2.960	1.554	95.10	Meniscus
5.0	8.33×10^{-4}		9.49×10^{-3}	3.794	1.992	60.97	Meniscus
5.0	8.33×10^{-4}		1.22×10^{-2}	4.880	2.562	78.41	Meniscus
5.1	5.56×10^{-4}		9.02×10^{-3}	5.412	2.841	57.79	Meniscus
5.1	5.56×10^{-4}		1.21×10^{-2}	7.248	3.805	77.40	Finger
5.1	5.56×10^{-4}		1.68×10^{-2}	10.080	5.292	107.64	Finger
4.9	3.33×10^{-4}		9.40×10^{-3}	9.400	4.935	60.59	Finger
4.9	3.33×10^{-4}		1.11×10^{-2}	11.11	5.833	71.62	Finger
4.9	3.33×10^{-4}		1.25×10^{-2}	12.480	6.552	80.45	Finger
4.9	3.33×10^{-4}		1.64×10^{-2}	16.370	8.594	105.53	Finger
4.9	1.67×10^{-4}		1.01×10^{-2}	20.280	10.647	65.38	Finger
4.9	1.67×10^{-4}		1.12×10^{-2}	22.38	11.750	72.15	Finger
4.9	1.67×10^{-4}		1.25×10^{-2}	24.960	13.104	80.47	Finger
4.9	1.67×10^{-4}		1.61×10^{-2}	32.140	16.874	103.61	Finger
5.0	8.33×10^{-4}	9.33×10^{-3}	1.03×10^{-2}	4.120	2.163	33.10	Meniscus
5.0	8.33×10^{-4}		1.13×10^{-2}	4.516	2.371	36.28	Meniscus
5.0	8.33×10^{-4}		1.32×10^{-2}	5.260	2.762	42.26	Meniscus
5.0	8.33×10^{-4}		1.60×10^{-2}	6.42	3.368	51.54	Meniscus
5.0	5.56×10^{-4}		1.05×10^{-2}	6.312	3.314	33.80	Meniscus
5.0	5.56×10^{-4}		1.43×10^{-2}	8.586	4.508	45.98	Finger
5.0	5.56×10^{-4}		1.67×10^{-2}	10.026	5.264	53.69	Finger
5.0	3.33×10^{-4}		1.11×10^{-2}	11.070	5.812	35.57	Finger
5.0	3.33×10^{-4}		1.25×10^{-2}	12.490	6.557	40.13	Finger
5.0	3.33×10^{-4}		1.63×10^{-2}	16.270	8.542	52.28	Finger
5.0	2.22×10^{-4}		1.13×10^{-2}	16.980	8.915	36.37	Finger
5.0	2.22×10^{-4}		1.25×10^{-2}	18.750	9.844	40.17	Finger
5.0	2.22×10^{-4}		1.63×10^{-2}	24.495	12.860	52.47	Finger

Results from simulations with $r = 0.90$ are summarized in Table 5.3 and Fig. 5.7(a) shows a plot of the results in the $(Pe^*, (Ca^*)^{-1})$ plane. We get the same qualitative behaviour as in the symmetric case, which was described in section 5.1.3.1. The solid line corresponds to $Pe^* = c(Ca^*)^{-1} + \delta$, with $c \approx 350$ and $\delta \approx -75$. It is obvious that, for the strongly asymmetric case with $r = 0.90$, fingering in the x-z plane is even more strongly suppressed, since much

higher capillary numbers are needed to enter the Thin Film regime.

Table 5.4: Parameter values and results for viscosity contrast ratio $r = 0.36$. For all runs $b = 48$, $\partial_\perp \phi = 0.84$ and $\eta_1 = 0.333$.

b	ζ	σ	D	u_m	Ca	Ca'	Pe^*	*Shape*
48	3.9	7.15×10^{-4}	4.35×10^{-4}	6.00×10^{-3}	0.300	0.220	277.16	Meniscus
	3.9	7.15×10^{-4}	4.35×10^{-4}	6.50×10^{-3}	0.325	0.238	300.46	Meniscus
	3.9	5.41×10^{-4}	3.29×10^{-4}	6.00×10^{-3}	0.396	0.290	366.69	Meniscus
	3.9	5.41×10^{-4}	3.29×10^{-4}	6.50×10^{-3}	0.429	0.315	397.15	Meniscus
	3.9	5.10×10^{-4}	6.29×10^{-4}	6.50×10^{-3}	0.455	0.333	207.65	Meniscus
	3.9	4.70×10^{-4}	2.86×10^{-4}	6.00×10^{-3}	0.456	0.335	422.34	Meniscus
	3.9	4.70×10^{-4}	2.86×10^{-4}	6.50×10^{-3}	0.494	0.362	457.30	Meniscus
	3.9	3.97×10^{-4}	4.88×10^{-4}	6.01×10^{-3}	0.541	0.396	247.50	Meniscus
	3.9	3.97×10^{-4}	4.88×10^{-4}	6.50×10^{-3}	0.585	0.429	267.92	Meniscus
	3.9	3.25×10^{-4}	4.00×10^{-4}	6.01×10^{-3}	0.661	0.485	302.18	Meniscus
	3.9	4.70×10^{-4}	2.86×10^{-4}	7.00×10^{-3}	0.532	0.390	492.35	Finger
	3.9	3.97×10^{-4}	2.41×10^{-4}	7.00×10^{-3}	0.630	0.462	583.87	Finger
	3.9	3.97×10^{-4}	4.88×10^{-4}	7.02×10^{-3}	0.632	0.464	289.46	Finger
	3.9	3.97×10^{-4}	4.88×10^{-4}	7.49×10^{-3}	0.674	0.494	308.77	Finger
	3.9	3.25×10^{-4}	1.97×10^{-4}	7.02×10^{-3}	0.772	0.566	715.65	Finger
	3.9	3.25×10^{-4}	1.97×10^{-4}	7.49×10^{-3}	0.824	0.604	763.36	Finger
	3.9	3.25×10^{-4}	4.00×10^{-4}	7.04×10^{-3}	0.774	0.567	353.55	Finger
	3.9	3.25×10^{-4}	4.00×10^{-4}	7.48×10^{-3}	0.823	0.604	376.12	Finger
	3.9	2.75×10^{-4}	3.38×10^{-4}	7.03×10^{-3}	0.914	0.670	418.23	Finger
	3.9	2.75×10^{-4}	3.38×10^{-4}	7.49×10^{-3}	0.974	0.714	445.87	Finger
	3.9	2.38×10^{-4}	2.93×10^{-4}	7.03×10^{-3}	1.054	0.773	481.63	Finger
	3.9	2.38×10^{-4}	2.93×10^{-4}	7.49×10^{-3}	1.124	0.824	513.69	Finger
48	3.9	9.16×10^{-4}	5.08×10^{-3}	5.90×10^{-3}	0.230	0.169	23.25	Meniscus
	3.9	9.16×10^{-4}	5.08×10^{-3}	6.50×10^{-3}	0.254	0.186	25.61	Meniscus
	3.9	9.16×10^{-4}	5.08×10^{-3}	9.00×10^{-3}	0.351	0.257	35.46	Meniscus
	3.9	9.16×10^{-4}	5.08×10^{-3}	1.00×10^{-2}	0.390	0.286	39.40	Meniscus
	3.9	9.16×10^{-4}	5.08×10^{-3}	1.20×10^{-2}	0.468	0.343	47.28	Meniscus
	3.9	4.16×10^{-4}	2.28×10^{-3}	6.00×10^{-3}	0.516	0.378	52.64	Meniscus
	3.9	9.16×10^{-4}	5.08×10^{-3}	1.36×10^{-2}	0.530	0.389	53.58	Meniscus
	3.9	4.16×10^{-4}	2.28×10^{-3}	6.50×10^{-3}	0.559	0.410	57.03	Meniscus
	3.9	2.26×10^{-4}	1.25×10^{-3}	6.50×10^{-3}	1.027	0.753	104.00	Meniscus
	3.9	2.26×10^{-4}	1.25×10^{-3}	7.48×10^{-3}	1.182	0.867	119.68	Finger
	3.9	2.26×10^{-4}	1.25×10^{-3}	7.52×10^{-3}	1.188	0.871	121.52	Finger
	3.8	4.75×10^{-5}	1.25×10^{-3}	8.00×10^{-3}	6.016	4.411	128.91	Finger
	3.9	8.01×10^{-5}	1.05×10^{-3}	7.03×10^{-3}	3.136	2.299	133.37	Finger
	3.8	8.01×10^{-5}	1.05×10^{-3}	7.55×10^{-3}	3.365	2.467	143.15	Finger
	3.8	8.01×10^{-5}	1.05×10^{-3}	7.93×10^{-3}	3.537	2.593	151.95	Finger
	3.9	1.43×10^{-4}	7.94×10^{-4}	7.00×10^{-3}	1.750	1.283	176.40	Finger
	3.9	1.43×10^{-4}	7.94×10^{-4}	7.50×10^{-3}	1.875	1.375	189.00	Finger
	3.8	1.43×10^{-4}	7.94×10^{-4}	7.94×10^{-3}	1.985	1.455	200.09	Finger
	3.9	8.01×10^{-5}	6.33×10^{-4}	7.00×10^{-3}	3.122	2.289	221.34	Finger
	3.9	8.01×10^{-5}	6.33×10^{-4}	7.52×10^{-3}	3.352	2.458	237.65	Finger
	3.9	8.01×10^{-5}	6.33×10^{-4}	7.94×10^{-3}	3.541	2.596	251.06	Finger
	3.9	8.01×10^{-5}	4.44×10^{-4}	7.00×10^{-3}	3.122	2.289	315.00	Finger
	3.9	8.01×10^{-5}	4.44×10^{-4}	7.52×10^{-3}	3.352	2.458	338.22	Finger

Our results for the case of intermediate viscosity contrast ratio $r = 0.36$ are shown in

Fig. 5.7(b) and details of these simulations are listed in Table 5.4. Qualitatively, we again encounter the same behaviour. For this value of r we extract the fitting values $c \approx 150$ and $\delta \approx -140$.

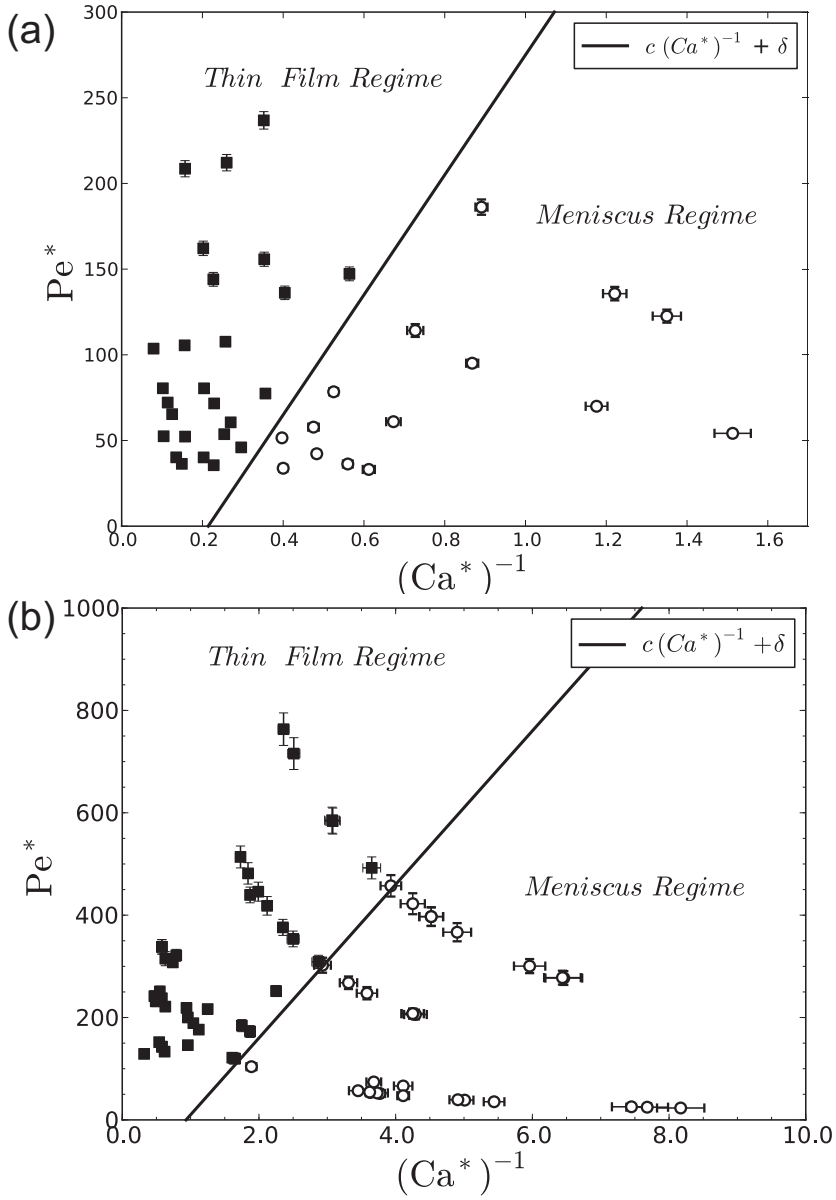

Figure 5.7: (a) Simulation data from Table 5.3 plotted in the $(Pe^*, (Ca^*)^{-1})$ plane for fluids with viscosity contrast $r = 0.90$. Results in the Thin Film regime are denoted by squares (■), whereas results in the Meniscus regime are denoted by circles (○). The solid line corresponds to the prediction $Pe^* = c(Ca^*)^{-1} + \delta$, with $c \approx 350$ and $\delta \approx -75$. (b) Simulation data from Table 5.4 plotted in the $(Pe^*, (Ca^*)^{-1})$ plane for fluids with viscosity contrast $r = 0.36$. The solid line is $Pe^* = c(Ca^*)^{-1} + \delta$, with $c \approx 150$ and $\delta \approx -140$.

Finally, for comparison, we show in Fig. 5.8 the regions of $(Pe^*, (Ca^*)^{-1})$ space that cor-

respond to the Meniscus and Thin Film regimes for varying viscosity contrast r. The degree of viscosity asymmetry greatly influences the penetration process and the onset of fingering in the x-z plane. Increasing the viscosity contrast suppresses the fingering process in the x-z plane.

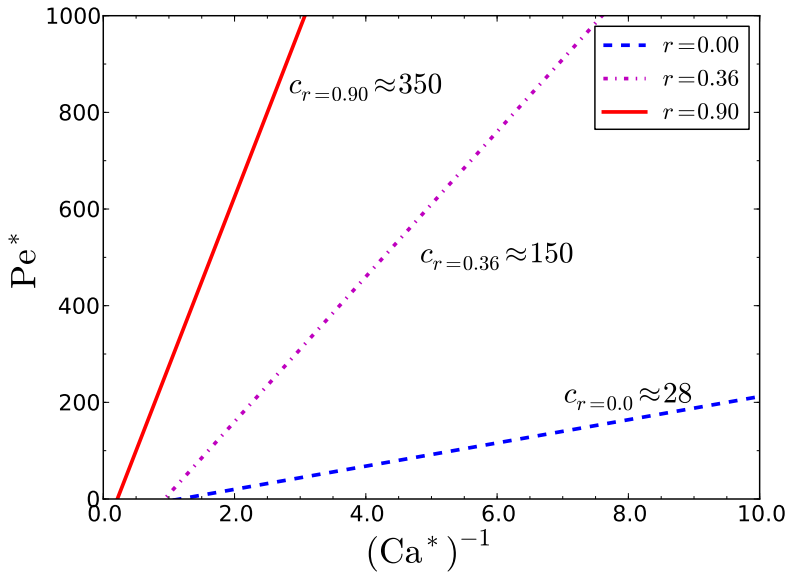

Figure 5.8: Meniscus-Thin Film phase diagram for varying viscosity contrast r. The Thin Film regime where a finger forms in the x-z plane lies above the lines. The onset of fingering in the x-z plane depends on the viscosity contrast r. Increasing the viscosity contrast suppresses finger formation.

5.2 Experimental system and techniques

(The experiments in this chapter were performed, independently, by Siti Aminah Setu and Gareth J. Davies in the lab of Dr. D. Aarts in the Physical and Theoretical Chemistry Laboratory, University of Oxford.)

In this section we shall present the experiments that have provided a primary motivation for this thesis. The aim was to develop a colloid-polymer system suitable for studying hydrodynamic instabilities in micro-channels, and specifically the Saffman-Taylor instability at ultra-low surface tension.

5.2.1 Colloid - polymer mixtures

"The term colloidal refers to a state of subdivision, implying that the molecules or polymolecular particles dispersed in a medium have at least in one direction a dimension roughly between 1 nm and 1 μm, or that in a system discontinuities are found at distances of that order."

This definition of the term "colloidal" by the International Union of Pure and Applied Chemistry (IUPAC) sets the size of colloidal particles in the submicrometer lengthscale. Their size, between μm and nm, means that the effect of gravity acting on the colloidal particles is less important than their thermal energy and that colloids diffuse by Brownian motion. Moreover, due to their lengthscale, these systems are ideal for studying statistical mechanics. They are experimentally easier to observe than molecular systems, due to their slower diffusion and their relative size compared to the wavelength of visible light, while they also show a greater response to external forces and thermal fluctuations.

Interactions between colloids can be tuned in a suspension by adding non-absorbing polymers. These colloid-polymer systems can undergo a phase separation driven by the depletion interaction [51–53], leading to a colloid rich-polymer poor phase and a colloid poor-polymer rich phase[4] with an ultra-low surface tension between them. We can understand why the surface tension σ is ultra-low for these systems if we consider that σ can be expressed as an energy per unit area giving the scaling relation [54, 55]

$$\sigma \sim \frac{\epsilon_{int}}{d^2} \, , \tag{5.16}$$

where ϵ_{int} and d are the strength of the molecular interaction and characteristic lengthscale at the interface respectively. Away from the gas-liquid critical point $\epsilon_{int} \sim k_B T$ (with k_B the Boltzmann's constant and T the absolute temperature) and d is of the order of the molecular diameter. Thus, due to the size of colloidal particles, surface tension for colloidal systems is of order nN/m [56–59], which is roughly six orders of magnitude lower than σ in molecular systems ($\sim mN/m$).

Moreover, for colloidal systems the interface width is $\sim \mu m$ rather than a few nm as for molecular systems. Therefore, colloidal suspensions provide an excellent model system to study properties of fluid-fluid interfaces that are not accessible at the molecular scale [60].

[4] These phases resemble a liquid phase and a gas phase respectively, if we consider only the colloids.

Many hydrodynamic instabilities can be studied in greater detail in both time and space. Here, in particular, our study of Saffman-Taylor instability can also benefit from the use of microfluidic devices, which reduces the volume of colloidal mixtures necessary to perform the experiments. Direct observation of the flow and interface position can be achieved by confocal scanning laser microscopy, which records the fluorescence of excited dye within the colloids..

5.2.2 Experiments

Experiments were carried out independently by Siti Aminah Setu and Gareth J. Davies. We will refer to these sets of experiments as exp.**I** and exp.**II** respectively.

They used dispersions of fluorescently labelled PMMA particles with a diameter of 210 nm in water. A xanthan polymer solution (M_w = 4x10^6 g mol^{-1}, R_g = 264 nm) was added to the dispersion to create a phase separating mixture [61]. The two phases were isolated after the colloid-polymer mixture had phase separated into a colloid rich phase and a polymer rich phase. Thus two colloidal phases were at coexistence when brought into contact again.

The surface tension σ was obtained from the capillary wave spectrum [60] giving σ=30 nN/m (exp.**I**) and σ=9 nN/m (exp.**II**). For exp.**I** a rheological characterization was performed on a TA AR-G2 rheometer, which revealed dynamical viscosities of the two phases η_1 = 15mPa.s and η_2 = 7mPa.s, leading to a viscosity contrast ratio $r = (\eta_1 - \eta_2)/(\eta_1 + \eta_2) \sim 0.36$. For the second set of experiments, the viscosities of the two phases were evaluated by measuring the sedimentation velocities of drops of one colloidal phase in the other and vice versa, which gave η_1 = 17mPa.s and η_2 = 1.5mPa.s and viscosity contrast $r \sim 0.84$. Noticeable shear-thinning, which is known to have a thinning effect on the Saffman-Taylor fingers [62], was observed for the colloidal gas phase from a shear-rate of 10 s^{-1}. However, this was above the maximum shear rate in the experiment, $U/b \sim 0.3$ s^{-1}.

The two liquids were injected into the microfluidic device, which was fabricated using standard soft-lithography techniques. Fig. 5.9 shows a schematic diagram of the microfluidic device used, while the expanded region shows the entrance of the main channel. This choice allows a symmetric flat interface to be formed at the crossroads of the channels.

The colloid-rich phase (liquid phase), which had a lower viscosity η_2 than the polymer-rich phase (gas phase) with viscosity η_1, was pushed into the long channel, of width w and thickness b and viscous fingers formed spontaneously. Typical channel dimensions were $w = 160\mu m$ and

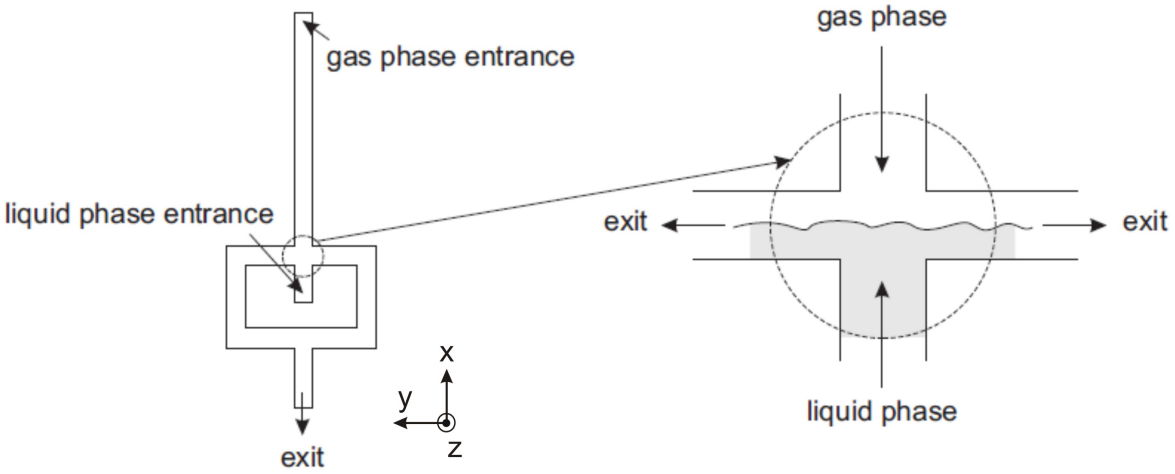

Figure 5.9: Schematic diagram of the microfluidic device used to study the Saffman-Taylor instability. The expanded region shows the position of the interface during equilibrated flow. Figure from [63].

$b = 10\mu m$. Gravity was used to control the flows. In order to monitor the flow of the colloidal phases in three dimensions laser scanning confocal microscopy (Zeiss Exiter) was used.

Fig. 5.10 shows laser scanning confocal microscopy images of the Saffman-Taylor instability. In a wide channel with $w = 1mm$ many fingers are formed as shown in Fig. 5.10(a), while at smaller channel widths only a single finger is present, as shown in Fig. 5.10(b). The wetting boundary condition is illustrated in Fig. 5.11 that shows the three-dimensional profile of a Saffman-Taylor finger brought to rest. A layer of colloid-rich fluid can be seen on the side walls of the microchannel, which occurs because the displacing fluid completely wets the walls.

5.3 Results

5.3.1 Interface configuration in the x-z plane

Experimentally, a first focus in the study of the Saffman-Taylor instability was the interface configuration in the x-z plane. Fig. 5.12(a) shows how the x-z interfacial profile responds to the flow for exp.**I** . At low velocities the interface advances as a concave meniscus. At a modified capillary number $Ca' = (\eta_1 + \eta_2)U/2\sigma \sim 0.4$, the curvature changes sign, but the shape of the interfacial profile remains constant in time. Then, at higher $Ca' \sim 1$ the interface position

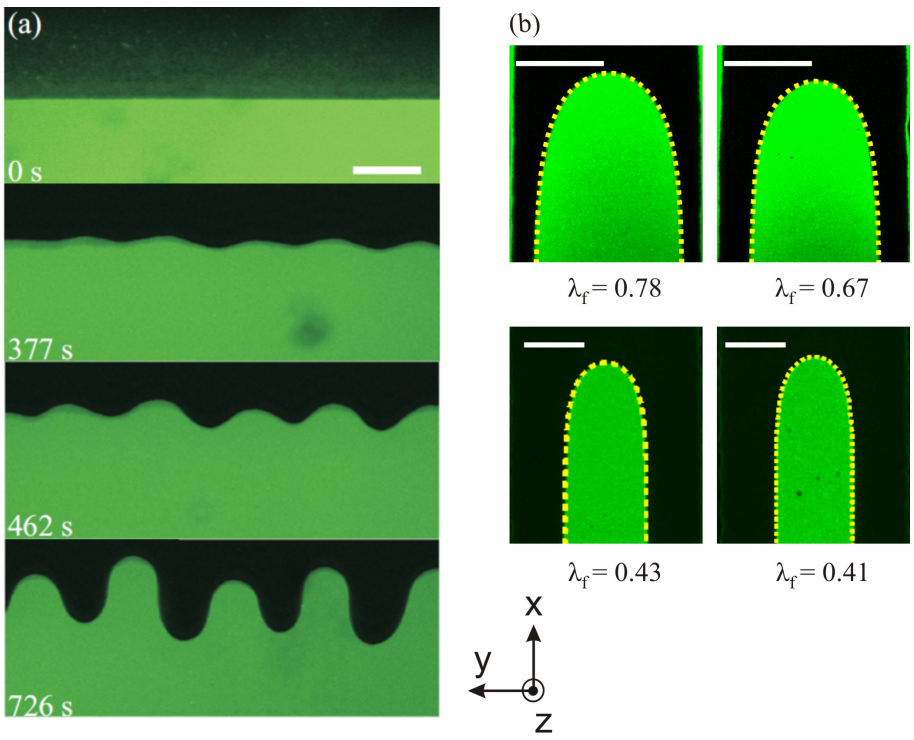

Figure 5.10: Laser scanning confocal microscopy images of the Saffman-Taylor instability in the x-y plane using colloid-polymer mixtures. (a) In a wide channel many fingers develop (exp.**II**). The scale bar indicates 100 μm. (b) Images of single fingers for smaller channels and for different values of finger width λ_f. The top panels correspond to experiments performed by Gareth J. Davies (exp.**II**) with $w = 100\mu m$, while the bottom panels correspond to experiments performed by Siti Aminah Setu (exp.**I**) with $w = 160\mu m$. The dashed curve follows from the Pitts equation [10]. Scale bars indicate 50 μm.

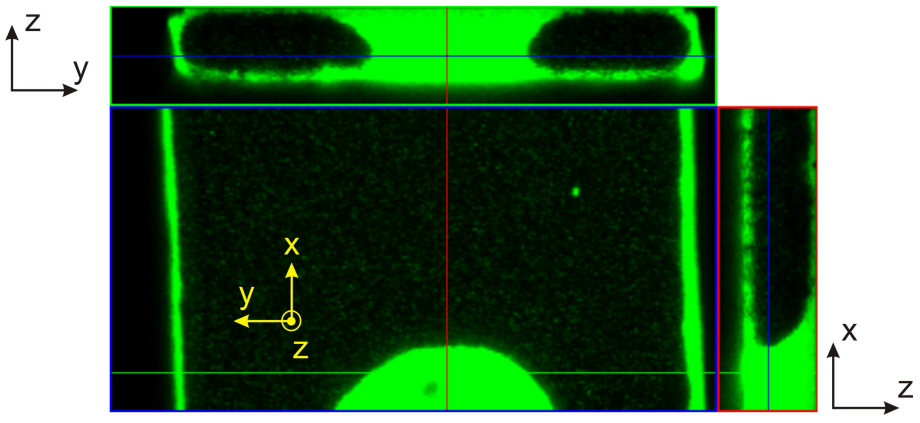

Figure 5.11: Three-dimensional profile of a stable finger brought to rest (exp.**II**). A layer of the colloid-rich fluid, which is the less viscous fluid, covers the walls of the microchannel. This occurs because it completely wets the walls.

becomes decoupled from that of the 'contact line'[5], and a finger is formed in the x-z plane. The finger is of a characteristic shape, with a narrowing near the 'contact line'.

At higher capillary numbers a meandering motion of the finger is observed, where it makes contact with either the top or bottom wall, before continuing to move freely again in the centre of the channel. This is a consequence of the large thermal interface fluctuations in colloid-polymer mixtures. The unstable motion of the finger entraps bubbles of the high viscosity phase in the advancing finger as shown in Fig. 5.12(b).

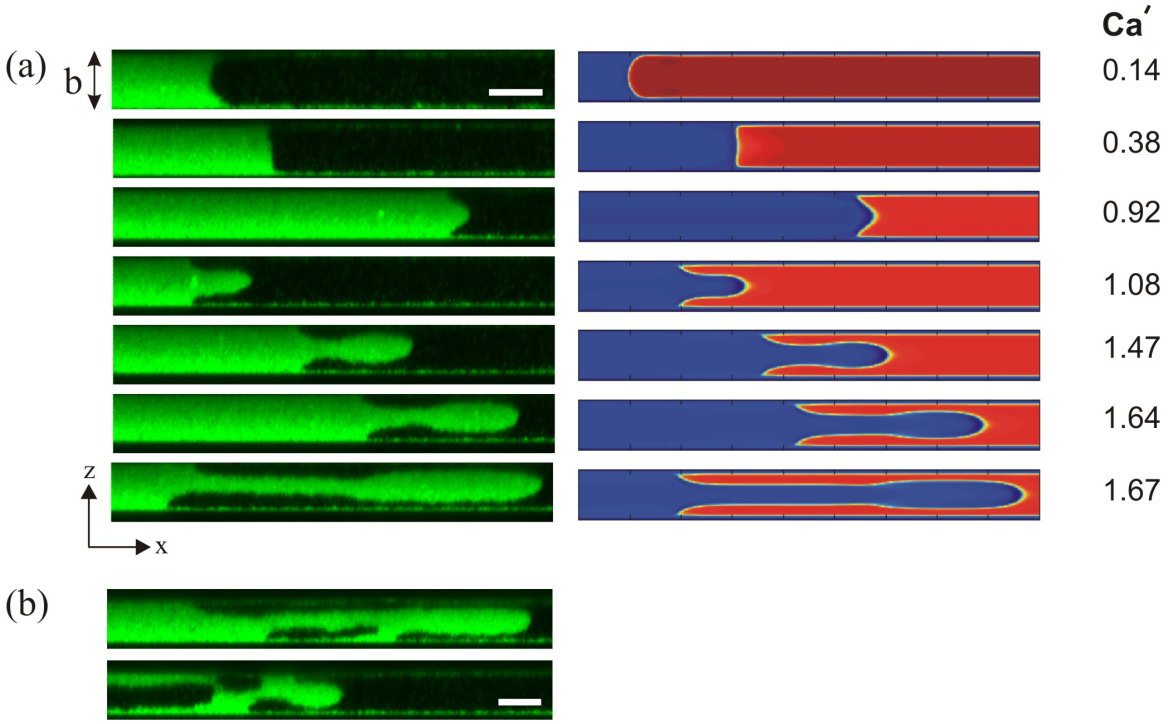

Figure 5.12: (a) Profile of the finger in the x-z plane as a function of the modified capillary number Ca' for fluids with viscosity contrast $r = 0.36$. Laser scanning confocal microscopy images of the leading interface (left panel, exp.**I**) are compared to the simulations (right panel). As the capillary number increases, the interface curvature first changes sign. At a critical capillary number a finger in the x-z plane is formed, indicating that the 'contact line' cannot keep up with the leading interface. (b) At higher capillary numbers the finger merges with the top or bottom wetting layers, before being pulled back to the centre of the channel. This is facilitated by the thermal interface fluctuations. Scale bars indicate 10 μm.

The second column of Fig. 5.12(a) presents free energy lattice Boltzmann simulation results showing how the x-z interfacial profile responds to the flow. When using this approach to model interfaces in molecular fluids, discretisation constraints mean that the diffuse interface is

[5]The liquid slides over a colloid-rich wetting layer such that there is no true contact line. However, there is an obvious line where the curved meniscus meets the surface layer, for which contact line is a natural terminology.

unphysically wide and care must be taken that this does not affect the results. Here, however, the width of the interface in the colloid-polymer mixtures is $\sim \mu m$ allowing a quantitative match between experiment and simulation.

Fig. 5.12(a) shows that there is a close correspondence to the experiments at the same capillary number. Furthermore, the morphology of the fingers in simulations and experiments is qualitatively similar. The advancing finger with a relatively constant width has the same characteristic shape in the x-z plane, with the bridge between the front of the finger and the bulk of the displacing fluid being narrow in the z-direction.

These results give us the confidence to use the lattice Boltzmann simulations to study the Saffman-Taylor instability numerically for a wide range of parameters relevant to the problem that are not easily accessible to the experiments. For example, experimentally, the crossover between the Meniscus and Thin Film regimes would appear to depend solely on the capillary number for a given system. We have already seen in section 5.1.3.2, however, that the shape of the interface in the x-z plane depends on scaled Ca^* and Pe^* numbers. Fingering in the x-z plane occurs for $Pe^* > c(Ca^*)^{-1} + \delta$, where the factors c, δ depend on the viscosity contrast r. The only way to check experimentally the dependence of the crossover on Pe^* is by changing the channel thickness b. We have to be cautious, though, not the exceed the capillary length $l_c = (\sigma/\Delta\rho g)^{1/2}$ which would allow gravity effects to become important. For the experiments reported here $l_c \approx 10\mu m$, which is the same as the channel thickness b used. Therefore, increasing b further was not an option in these experiments.

An important remark regarding the particular choice of experiments used here is that typical values for the Péclet number for experiments with molecular fluids [12, 64] are relatively high, $O(10^2) - O(10^3)$, thus, these experiments lie in the Thin Film regime. However, for systems with a diffuse interface, such as colloid-polymer mixtures [60], or experiments in microchannels, menisci can be observed up to higher capillary numbers, making the crossover from the Meniscus to Thin Film regime easier to observe.

In the experiments (exp.**I**) the finger breaks through in the x-z plane for $u \sim 2.7\times10^{-6}\mu m/s$, which corresponds to $Ca \sim 1.4$ or $Ca' \sim 1$. With the thickness of the wetting layer $\zeta \sim 1\mu m$ the inverse of the scaled capillary number at the breakthrough is $(Ca^*)^{-1} \sim 1.6$. Using the diffusion coefficient of the colloids, $D_{col} \approx 9.91 \times 10^{-14} m^2/s$, to estimate the experimental Pe^*, we obtain $Pe^* \sim 110$, which compares favourably to $Pe^* \sim 100$ in the simulations as shown in

Fig. 5.13. We have to note however that the proper value for the diffusion coefficient D should have been obtained from the evolution of an induced perturbation in the concentration field of the colloid-rich phase, as D is defined by the equation

$$\frac{\partial \phi}{\partial t} = D\nabla^2\phi \,. \tag{5.17}$$

We expect, however, the diffusion coefficient D to be close in value to the diffusion coefficient of the colloids D_{col}.

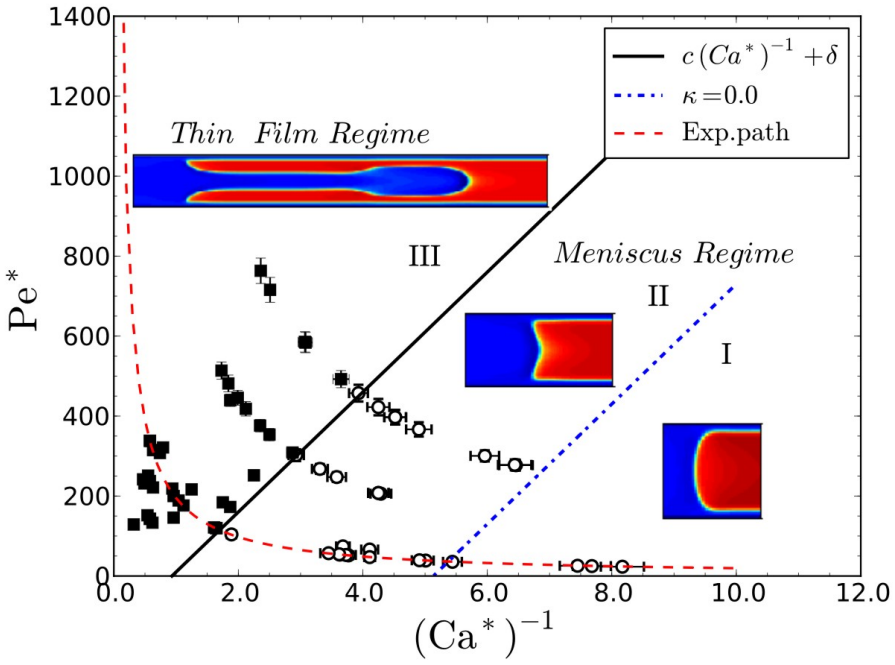

Figure 5.13: Results from lattice Boltzmann simulations. The shape of the interface in the x-z plane for a viscosity contrast $r = 0.36$ depends on the scaled capillary and Peclet numbers, Ca^* and Pe^* (∘ Meniscus regime, ■ Thin Film regime). The snapshots represent the different configurations. The solid line corresponds to the onset of fingering in the z direction; the dash-dotted line indicates an advancing interface with zero curvature κ. The dashed line describes an experimental path, where Pe^* and Ca^* are tuned by varying the leading interface velocity.

Fig. 5.13 shows the Meniscus-Thin Film threshold, for $r = 0.36$, in the $(Pe^*, (Ca^*)^{-1})$ plane given by $Pe^* = c(Ca^*)^{-1} + \delta$, where $c \approx 150$ and $\delta \approx -140$. The snapshots are representative of the different x-z interface configurations. An experimental path (exp.**I**) is also plotted as a dashed red line. This is characterised by $Pe^*(Ca^*)^{-1} = const$, since for a given channel both Pe^* and Ca^* are tuned by varying the applied forcing, which alters the velocity of the interface. More precisely $Pe^*(Ca^*)^{-1} = [2(b/2 - \zeta)\sigma]/[D(\eta_1 + \eta_2)C]$, where $C = 1 - 4(\zeta/b)(1 - \zeta/b)$.

In terms of the lattice Boltzmann method, using the definition for the surface tension σ and diffusivity D, then $Pe^*(Ca^*)^{-1} = [8\xi(b/2-\zeta)]/[3\Gamma(\eta_1+\eta_2)C]$, where Γ is related to the mobility coefficient and ξ is the interface width.

Lattice Boltzmann simulations described in section 5.1.3.2 further revealed that fingering in the x-z plane is strongly suppressed as the difference in viscosity of the two fluids increases. So, much higher capillary numbers are needed both to change the curvature of the meniscus from positive to negative and to induce the formation of a finger. This is evident from Fig. 5.8 and confirmed by the experiments with $r = 0.84$ (exp.**II**), where fingering in the x-z plane commences at $u \sim 5.5 \times 10^{-6} \mu m/s$, which corresponds to $Ca \sim 10.6$ or $Ca' \sim 5.8$.

5.3.2 Width of the steady state finger in the x-z plane

We now study the relative width of the steady state penetrating finger $\lambda_b = w_b/b$ in the x-z plane, where w_b is the absolute finger width.

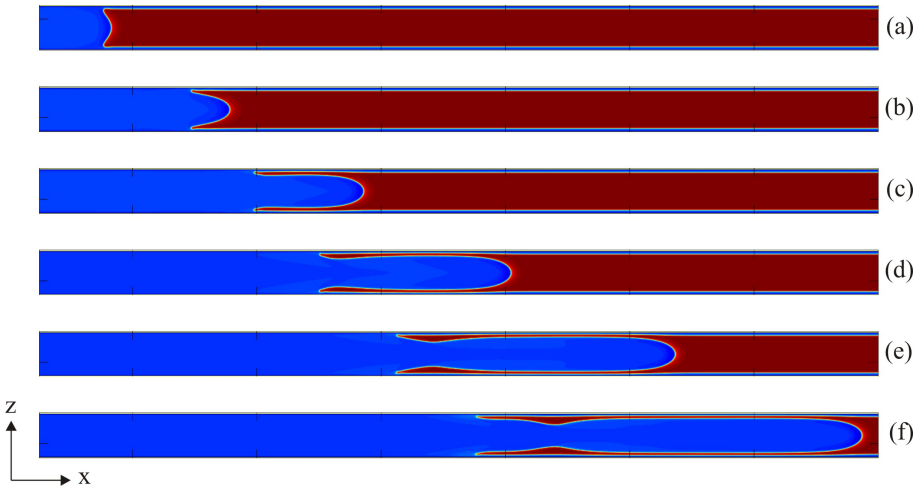

Figure 5.14: Simulation results showing interface snapshots in the x-z plane for viscosity contrast $r = 0.90$. The time interval between the figures is $\delta t = 2 \times 10^4$ time-steps in lattice units. The channel thickness and thickness of wetting layer are $b = 70$ and $\zeta \sim 5$ respectively. $Ca = 32.14$, $Ca^{*-1} = 0.08$, $Pe^* = 103.61$. The x-z finger has a constant width $\lambda_b = 0.799 \pm 0.007$ for $t = 6 \times 10^4$ onwards (d-f), which is very wide compared to the neutral wetting situation, where we found $\lambda_b = 0.566$.

As we have seen in Chapter 4 section 4.2.2, for the neutral wetting case, λ_b depends on Ca and the viscosity contrast r. We therefore calculated λ_b for varying Ca for the cases of viscosity contrast $r = 0.90$, $r = 0.36$ and $r = 0$.

For strongly asymmetric viscosities with $r = 0.90$, we saw in section 5.1.3.2 that the

penetration in the x-z plane is strongly suppressed. We, therefore, have to resort to high Ca in order to achieve a finger-like structure. Remarkably very wide fingers were found in simulations as can be seen from Fig. 5.14, where we present a time sequence of interface snapshots in the x-z plane.

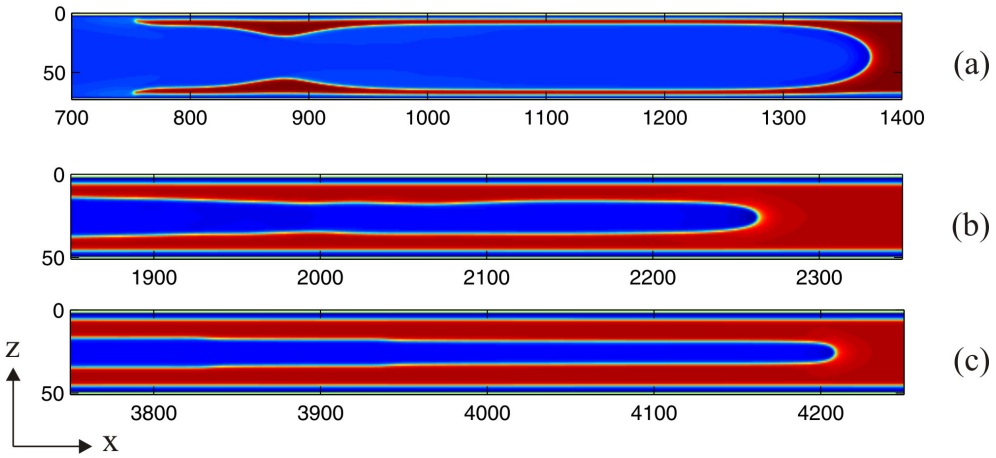

Figure 5.15: Interface snapshots in the x-z plane for viscosity contrasts $r = 0.90$ (a), $r = 0.36$ (b) and $r = 0$ (c) for high values of Ca. The fingers have reached their saturation width λ_b. (a) $Ca = 32.14$, $\lambda_b = 0.799$, (b) $Ca = 62.14$, $\lambda_b = 0.415$ and (c) $Ca = 36.00$, $\lambda_b = 0.290$. Finger width λ_b decreases as the viscosity contrast decreases.

Decreasing the viscosity contrast to $r = 0.36$ and $r = 0$ has a thinning effect on the width of the fingers λ_b, verifying the tendency reported in the numerical study by Ledesma *et al.* [14] for neutral wetting. This is evident from Fig. 5.15, where we show snapshots of the x-z interface, for all the viscosity contrasts examined, in the limit of high Ca, where fingers have reached their saturation width λ_b.

Finger widths λ_b are plotted in Fig. 5.16 as a function of Ca for the different viscosity contrasts. Examining λ_b for each viscosity contrast individually, starting with the case $r = 0.90$, it is obvious that the observed fingers are much wider than the prediction of Halpern and Gaver [43] for $r \to 1$. In fact, if we had examined fluids with $r = 1$ we would have expected λ_b to be even larger, given the tendency of the finger width λ_b to increase with increasing viscosity contrast [14]. For complete wetting, our results for $15 \leq Ca \leq 35$ revealed a finger width of $\lambda_b = 0.799 \pm 0.014$, which seemed to be insensitive to increasing Ca further. On the contrary, for the reversed wetting boundary condition, where the displaced fluid completely wets the walls, Halpern and Gaver predicted a saturation value of $\lambda_b \approx 0.58$ ($r = 1$), and our results in section 4.2.2, and for neutral wetting, revealed $\lambda_b \approx 0.57$ ($r = 0.90$).

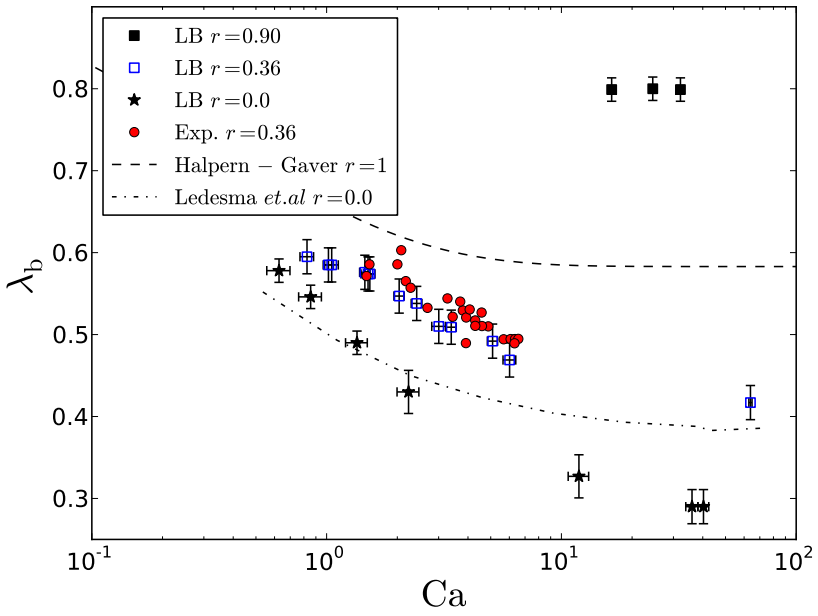

Figure 5.16: Width of the finger λ_b in the x-z plane as a function of Ca for different viscosity contrasts r. For comparison, we plot the numerical predictions by Halpern and Gaver for $r = 1$ [43] given by the dashed curve, as well as the Ledesma *et al.* predictions for $r = 0.0$ and neutral wetting [14] given by the dash-dotted curve.

Smaller values of Ca could not be reached in the Thin Film regime due to computational limitations. In principle we could achieve fingering in the x-z plane for smaller Ca if we resort to very high Pe^*, i.e. by using very small diffusivity. However, for reasons related to the stability of the Lattice Boltzmann method this was not possible.

The increased finger widths λ_b for $r = 0.90$ seem to be solely due to the presence of the wetting layer, since we have seen in section 4.2.2 that, irrespective of the partial wetting boundary condition and the equilibrium contact angle, the λ_b saturation value for large Ca is unique, $\lambda_b \approx 0.57$, and much smaller than the value we obtain here. Experiments with $r = 0.84$ (exp.**II**), although not at the same viscosity contrast as our simulations, support our findings. It is evident from Fig. 5.17 that the penetrating finger in the x-z plane occupies a high fraction of the channel. However, the large thermal interface fluctuations in colloid-polymer mixtures, together with the small separation of the finger and the wetting layer result in a meandering motion of the finger. The finger joins with the wetting layer at either the top or bottom wall, while bubbles of the high viscosity phase are captured behind the finger as shown in

Fig. 5.17(d). This unstable motion of the finger does not allow the formation of stable fingers in the x-z plane and hence measurements of λ_b are not possible.

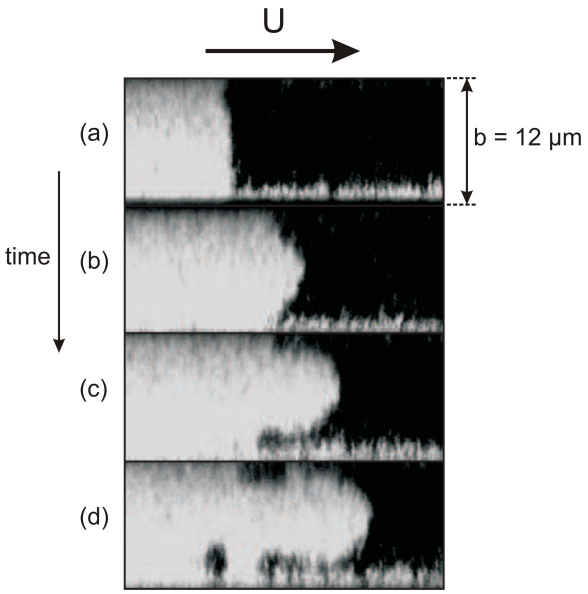

Figure 5.17: Interface snapshots in the x-z plane for experiments (exp.**II**) with $r = 0.84$. The less viscous fluid starts penetrating in the x-z plane (c) at $Ca \approx 10.6$ or $Ca' \approx 5.8$, and the finger formed occupies a high fraction of the channel. Then due to the large thermal interface fluctuations the finger joins with the wetting layer (d), capturing a bubble of the more viscous fluid behind it. Note that the wetting layer at the top wall is not clearly visible, due to scattering effects. Figure from [63].

Next we examine the case of intermediate viscosity contrast $r = 0.36$, for which there are experimental results (exp.**I**). In order to enable a detailed comparison with the experiments, simulations were run with approximately the same ratio of wetting layer to channel thickness ζ/b as in the experiments. We chose channels with $b = 48$ and $\zeta \approx 4 - 5$ compared to $b = 10\mu m$ and $\zeta \approx 1\mu m$ in experiments. A first remark is that experimental finger widths λ_b are in good agreement with results from simulations as shown in Fig. 5.16. Moreover, we verify the tendency reported in the literature of decreasing λ_b with decreasing r [14], both experimentally and numerically, since now fingers are narrower than the case of $r = 0.90$ (simulations) and $r = 0.84$ (exp.**II**). Simulation results revealed a limiting value of $\lambda_b = 0.417$ for high Ca. Testing this experimentally was not possible though, since the regime of $Ca > 10$ could not be reached, again due to the meandering motion of the finger.

Finally, for the symmetric case $r = 0.0$, we find unusually thin fingers, especially for $Ca \geq 10$. For large Ca we find a limiting value of $\lambda_b = 0.29 \pm 0.02$, which is, surprisingly,

much smaller than the neutral wetting case of $\lambda_b = 0.386$ [14]. One would expect that in this situation, the finger width would be the same since fluids have the same viscosities, and therefore the wetting layer would not have any contribution. This remains an open question for experimental exploration.

Here, we present a simple argument to explain the wide fingers observed numerically and experimentally for high viscosity contrasts r. In the case where a wetting layer of a less viscous fluid covers the substrate, the velocity field in the centre of the channel is altered so that it effectively corresponds to Poiseuille flow in a channel with a thickness $b' > b$ as can be seen in Fig. 5.18. Hence the finger effectively sees a larger channel width b' and a wider finger forms.

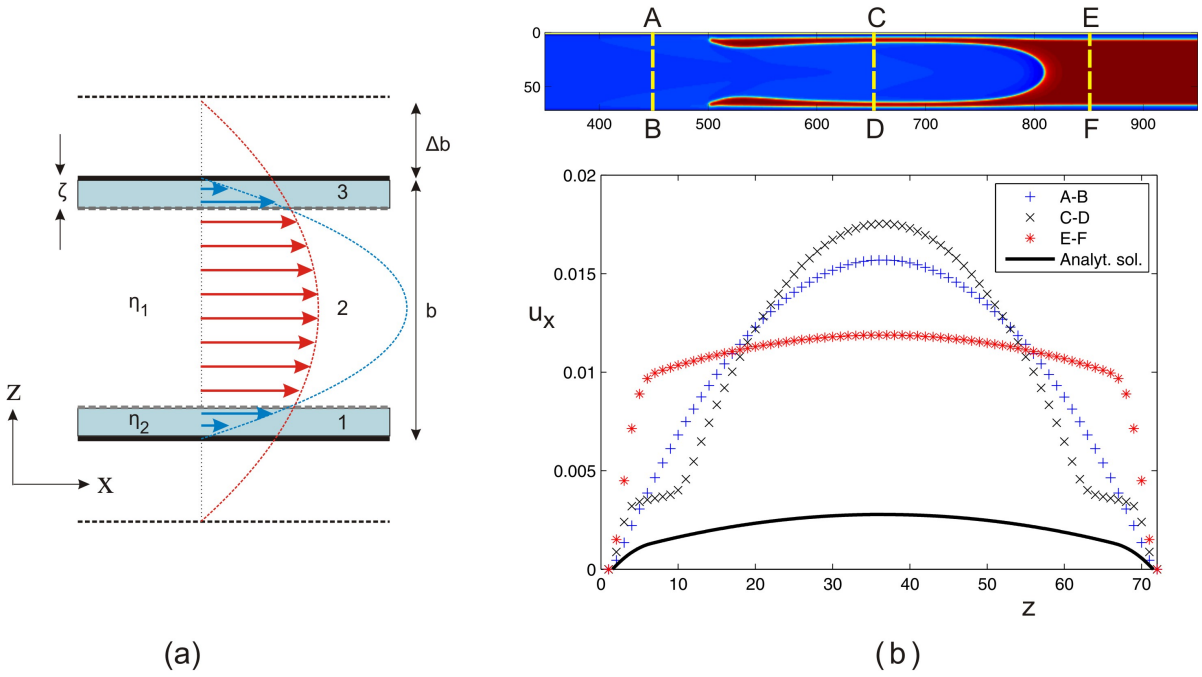

Figure 5.18: (a) Schematic representation of the velocity field in the x-z plane of a channel with thickness b, when a wetting layer ζ of a fluid with viscosity η_2 covers the substrate. The non wetting fluid has a higher viscosity η_1. (b) The x component of the fluid velocity as a function of z along the lines A-B, C-D, E-F in the top panel. The penetrating finger widens as it effectively sees a larger channel with width $b' = b + 2\Delta b$. The analytical solution that corresponds to Eq. (5.19) is much smaller than this velocity field.

Solving the Stokes equation

$$-\frac{dP}{dx} = \eta \frac{d^2u}{dz^2} \tag{5.18}$$

with a wetting layer of thickness ζ covering the substrate, and imposing the appropriate boundary conditions

a) no-slip at z = 0 and z = b,

b) continuity of the velocity and du/dz at the boundary between the two fluids at z = ζ and z = b − ζ, gives

$$u_x^{(1)}(z) = -\frac{1}{2\eta_2}\left(\frac{dP}{dx}\right)z^2 + \left(\frac{dP}{dx}\right)\left[\frac{b}{2\eta_1} + \zeta\left(\frac{1}{\eta_2} - \frac{1}{\eta_1}\right)\right]z \tag{5.19a}$$

$$u_x^{(2)}(z) = -\frac{1}{2\eta_1}\left(\frac{dP}{dx}\right)z^2 + \left(\frac{dP}{dx}\right)\frac{b}{2\eta_1}z + \zeta^2\left(\frac{dP}{dx}\right)\left(\frac{1}{2\eta_2} - \frac{1}{2\eta_1}\right) \tag{5.19b}$$

$$u_x^{(3)}(z) = -\frac{1}{2\eta_2}\left(\frac{dP}{dx}\right)z^2 + \left(\frac{dP}{dx}\right)\left(\frac{b-\zeta}{\eta_2} - \frac{b-2\zeta}{2\eta_1}\right)z + \left(\frac{dP}{dx}\right)\left(\frac{1}{2\eta_1} - \frac{1}{2\eta_2}\right)\left(b^2 - 2b\zeta\right) \tag{5.19c}$$

where the superscripts 1, 2, 3 denote the different regions in Fig. 5.18(a). The velocity field in the middle of the channel, $u_x^{(2)}(z)$, is effectively the one that corresponds to a channel of thickness $b' = b + 2\Delta b$; the penetrating finger senses the underlying velocity field and widens as it would had done in a wider channel. The effective increase in the channel thickness can be evaluated from Eq. (5.19b) as

$$\frac{\Delta b}{b} = \frac{-1 + \sqrt{1 + 4(\zeta/b)^2(\eta_1/\eta_2 - 1)}}{2}\,. \tag{5.20}$$

As expected for $\zeta \to 0$ or $\eta_1 = \eta_2$, $\Delta b \to 0$. For the simulation reported in Fig. 5.14, Eq. (5.20) predicts $\Delta b/b = 0.09$. Using this value we estimate the effective width $\lambda_b' = w_b/(b + 2\Delta b) = 0.67$, compared with the saturation value of $\lambda_b = 0.566$ from our results for neutral wetting and $r = 0.90$. The reason for the discrepancy is that the velocity field in front of the finger, along the line E-F, is in fact much larger than the value predicted by Eq. (5.19), because the analysis here assumes just a channel with three stripes of liquids. Hence, it does not take into account the advancing less viscous fluid that propagates occupying the whole channel thickness further back. As shown in Fig. 5.18(b), due to mass conservation, the velocity along the line E-F has to be larger, thus, leading to a much larger Δb than the value predicted by Eq. (5.20).

5.3.3 Curvature of the leading interface in the x-z plane

We shall now study the interface curvature $\kappa_\perp = 1/R_\perp$ in the x-z plane at z = $b/2$. We examine this numerically for $r = 0.36$ to compare to the results of exp.**I**.

Again, in order to directly compare to the experiments we chose $b = 48$ and $\zeta \sim 4$ as

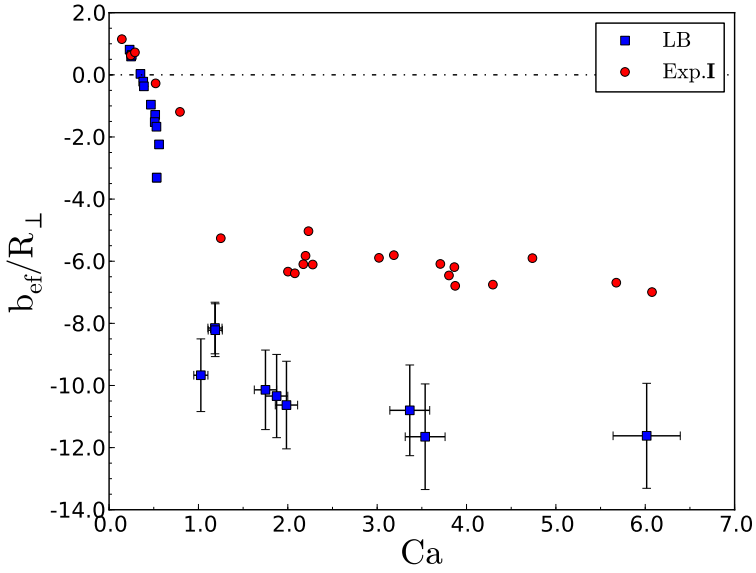

Figure 5.19: Normalised curvature $b_{\rm ef}/R_\perp$ as a function of Ca. The simulation points correspond to the experimental path shown in Fig. 5.13. The channel width is $b = 48$ and the thickness of the wetting layer $\zeta \sim 4$.

this gives approximately the same ratio ζ/b as in the experiments. In the limit $Ca \to 0$ we expect that the curvature $\kappa_\perp$ will be set by the channel's width b and the thickness of the wetting layer ζ, so that $\kappa_\perp \sim 2/(b-2\zeta)$. Defining a normalised curvature $\kappa' = b_{\rm ef}/R_\perp$, where $b_{\rm ef} = (b-2\zeta)$ is the effective width of the cell, $\kappa' \sim 2$ in the limit $Ca \to 0$. Fig. 5.19 shows the normalised curvature $\kappa'_\perp = b_{\rm ef}/R_\perp$ as a function of Ca. The simulation points correspond to the trajectory in the $(Pe^*, (Ca^*)^{-1})$ plane, shown in Fig. 5.13, which best fits the experiments. The breakthrough in the x-z plane and an advancing interface with zero curvature $\kappa' = 0$ occur at approximately the same capillary number Ca or Ca' (Ca^*) in simulations and experiments. We observe, however, that we can not match the experimental interface curvature as Ca increases. This should be attributed to the large thermal fluctuations in the experiments, which effectively increase the radius of curvature at the tip of the penetrating finger. If we had plotted the normalised curvature as a function of the modified capillary numbers Ca' or Ca^* we would have obtained qualitatively the same behaviour. This is because $Ca' = (\eta_1+\eta_2)u/(2\sigma) = Ca/(1+r)$ and $Ca^* = Ca'\{1-4(\zeta/b)(1-\zeta/b)\}$.

We now examine different experimental paths, i.e. paths characterised by different values of $Pe^*(Ca^*)^{-1}$, shown in Fig. 5.20(a), and using channels with $b = 48$, $b = 100$ and $\zeta \sim 4$. Results

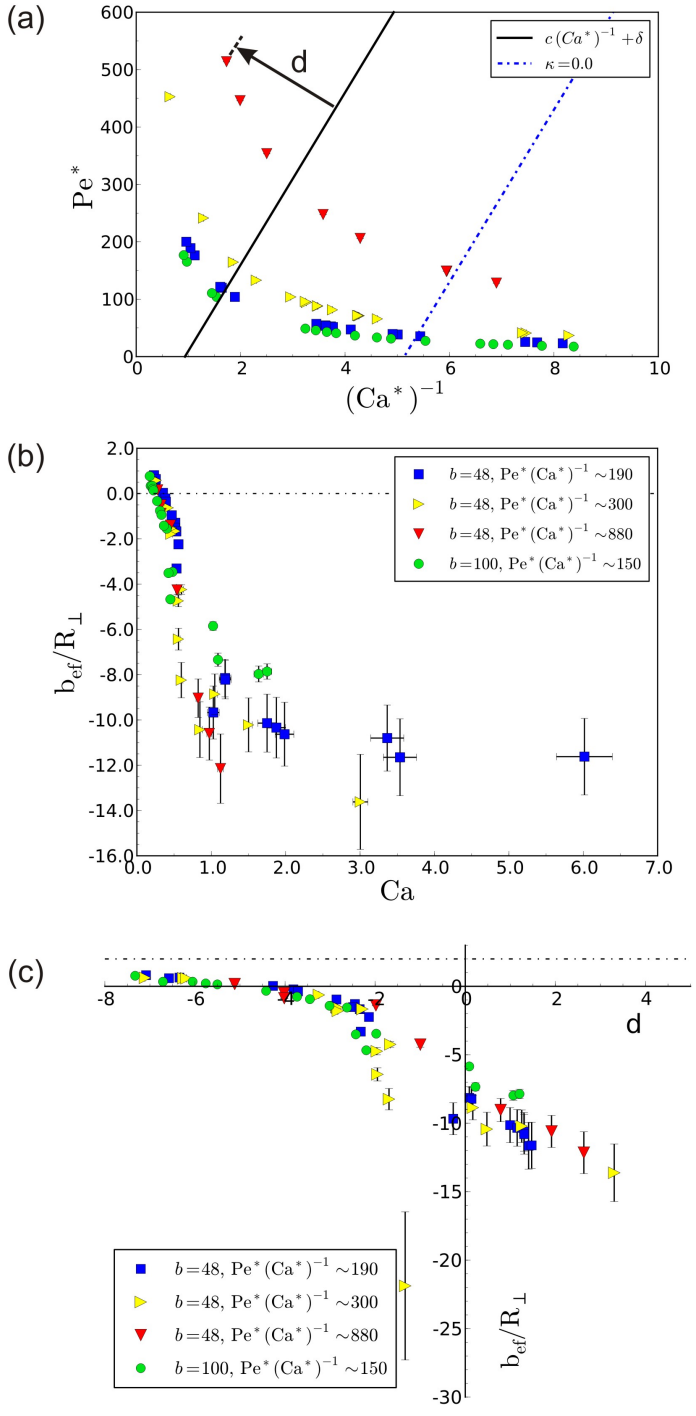

Figure 5.20: (a) Simulation data points in the $(Pe^*, (Ca^*)^{-1})$ plane indicating different experimental paths. d is defined as the distance of the points from the Meniscus-Thin Film threshold. (b) Normalised curvature of the leading interface in the x-z plane, $b_{\text{ef}}/R_\perp$, as a function of Ca for the experimental paths shown in (a). (c) Normalised curvature $b_{\text{ef}}/R_\perp$ as a function of the distance d from the Meniscus-Thin Film threshold in the $(Pe^*, (Ca^*)^{-1})$ plane.

for the normalised curvature along different paths do not collapse on a single curve when plotted as a function of Ca, as shown in Fig. 5.20(b). This is expected since the penetration process in the x-z plane is governed by the interplay of both scaled capillary and Péclet numbers and we expect this to apply to the curvature of the leading interface as well.

However, it would be reasonable to make the assumption that the curvature of the interface at z=$b/2$ should be a function of the distance d from the Meniscus-Thin Film threshold given by $Pe^* = c(Ca^*)^{-1} + \delta$ (see Fig. 5.20(a)). Negative distance d denotes points in the Meniscus regime. To investigate this assumption we examined the systems with different values of $Pe^*(Ca^*)^{-1}$ shown in Fig. 5.20(b). Fig. 5.20(c) shows a plot of our results for the normalised curvature $b_{\text{ef}}/R_\perp$ in the x-z plane versus d. The results indicate an advancing interface with zero curvature at a distance $d \sim -4.5$. Then at approximately $d \sim -1.5$ there is a sudden increase in the magnitude of $b_{\text{ef}}/R_\perp$.This is because the advancing interface is close to penetrating in the x-z plane, which results in a sharp decrease of the interface radius of curvature. After breaking through in the x-z plane ($d > 0$) the curvature reaches a value $b_{\text{ef}}/R_\perp \sim 14$ for large d, i.e. large Ca^* and Pe^*. We note, however, that the estimate for d can not be precise due to the fact that the Meniscus-Thin Film threshold is itself not calculated exactly.

5.3.4 Impact of wetting on the Saffman-Taylor instability

The behaviour of the interface in the x-z plane has turned out to be surprisingly rich for the case of complete wetting. The interface slides over a pre-formed wetting layer maintaining a convex meniscus shape and much higher velocities are needed to breakthrough in the x-z plane than for neutral wetting, meaning that fingering in the x-z plane is strongly suppressed. An interesting question then arises: "What are the implications, if any, of the penetration process in the x-z plane on the fingering process in the x-y plane, the Saffman-Taylor fingering?"

5.3.4.1 Impact of wetting on the onset of the Saffman-Taylor instability

We shall examine here how the onset of fingering in the transverse direction, or x-z plane, affects the onset of fingering in the lateral direction, or x-y plane. In order to do this, we need to consider the linear stability of the interface in the x-y plane, i.e. the plane of the Saffman-Taylor instability. We have already seen, in section 2.4, that the linear stability analysis for

the two-dimensional case yields the universal dispersion relation

$$\tilde{\omega}(\tilde{k}) = \tilde{k}(1 - \tilde{k}^2) \,, \tag{5.21}$$

where $\tilde{k} = wB^{1/2}k$ is the dimensionless wavenumber and $\tilde{\omega}(\tilde{k}) = \omega(k)wB^{1/2}/rU$ are the dimensionless frequencies.

We investigated the stability of the interface for a system of aspect ratio $\epsilon = 0.24$ and viscosity contrast $r = 0.36$. We initialised the system in the same way as when studying the penetration process in section 5.1.1, by letting the system relax until a meniscus was formed in the x-z plane and then switching on the forcing term. In the x-y plane, an initially flat interface was perturbed according to to a single-mode perturbation of wavelength $\Lambda = w$ and a small amplitude ζ^{amp}, defined as $\zeta^{amp}(t) = x_{tip}(t) - \bar{x}(t)$, where x_{tip} and $\bar{x}$ are the tip and the mean position of the interface respectively. The amplitude of the interface as a function of time was recorded for the initial stages of the flow and the amplification factor was extracted from a linear fit of $\log \zeta^{amp}(t)$ versus t.

One should, however, consider the role of the Péclet number that was omitted from the two-dimensional analysis for the dispersion relation. In the dispersion relation, given by Eq. (5.21), the critical dimensionless wavenumber separating the stable from the unstable modes is $\tilde{k}_{cr} = 1$, or in terms of the absolute wavenumber $k_{cr} = 1/(wB^{1/2})$. This just depends on the channel width w and Ca, which enters through $1/B$. We have seen, though, that the structure of the advancing interface in the x-z plane depends on the interplay between the scaled Ca^* and Pe^*. The role of the Péclet number was not so apparent for partial wetting, but its role for complete wetting is more evident and profound. To further investigate this, we explored the dispersion relation for systems with fixed diffusivity, or in more general for systems for which $Pe^*(Ca^*)^{-1} = const.$ In particular, we ran simulations for two different values of $Pe^*(Ca^*)^{-1} = 19.9$ (Exp.path(**I**)) and $Pe^*(Ca^*)^{-1} = 398.0$ (Exp.path(**II**)). These two experimental paths are depicted in Fig. 5.21.

Fig. 5.22 reveals that the dispersion relation indeed depends on Pe^*. Results for the two different values of $Pe^*(Ca^*)^{-1}$ are described by different dispersion relations. For low values of $Pe^*(Ca^*)^{-1}$ (Exp.path(**I**)), i.e. for systems with a diffuse interface, such as colloid-polymer mixtures, the critical wavenumber $\tilde{k}_{cr} \sim 0.7$ indicating that the critical modified capillary

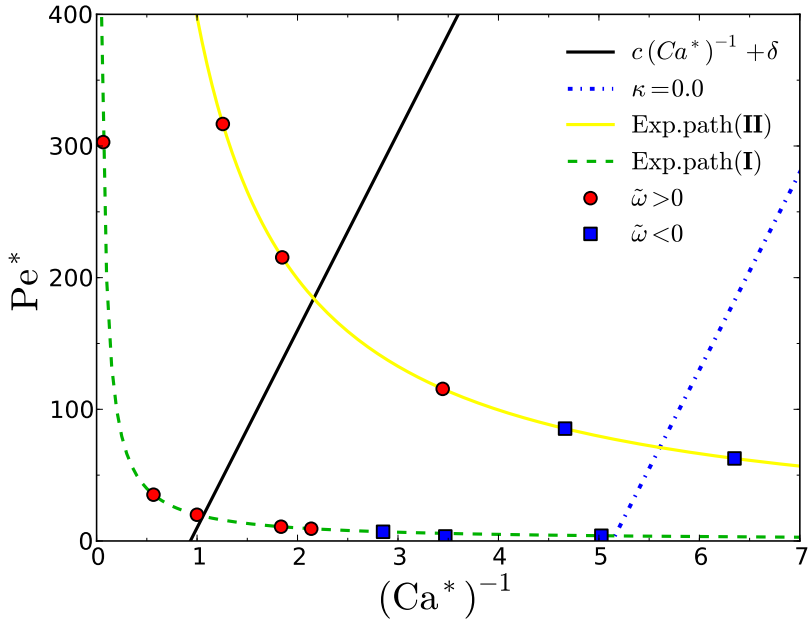

Figure 5.21: Investigating the dispersion relation for complete wetting regime and $r = 0.36$. Simulations were run for two different values of $Pe^*(Ca^*)^{-1} = 19.9$ (Exp.path(**I**) - dash green line) and $Pe^*(Ca^*)^{-1} = 398.0$ (Exp.path(**II**) - solid yellow line). Red circles denote results with a positive growth rate $\tilde{\omega}$, and blue squares results with a negative growth rate. The solid black line corresponds to the onset of fingering in the x-z direction (the threshold between the Meniscus to Thin Film regime), while the dash-dotted line indicates an advancing interface with zero curvature κ. Saffman-Taylor fingering commences in the region between these lines, where the interface in the x-z plane is positively curved ($\kappa > 0$).

number $1/B_{cr}$ (or Ca_{cr}) for the onset of Saffman-Taylor fingering is shifted to higher values. For Exp.path(**II**) the critical wavenumber increases to $\tilde{k}_{cr} \sim 0.85$, but it is still smaller than the classical solution for the Hele-Shaw cell, $\tilde{k}_{cr} = 1.0$. Another interesting feature seen in Fig. 5.22 is that the growth rate for the complete wetting case is much smaller than the one predicted from the classical two-dimensional analysis.

This effect should be attributed to the interface structure in the third, hitherto neglected, dimension, since at a given $\tilde{k}$ and, therefore, at fixed Ca for a given system, one can obtain positive or negative growth rate $\tilde{\omega}$, for a perturbed interface, depending on the value of Pe^*. This is evident from Fig. 5.21, where we plot our results in the $(Pe^*, (Ca^*)^{-1})$ plane. Results with positive growth rate $\tilde{\omega} > 0$, which would lead to Saffman-Taylor fingering, are denoted with red circles, while results with negative growth rate $\tilde{\omega} < 0$ with blue squares. We also plot the line of points with zero curvature. The onset of Saffman-Taylor fingering is in the regime

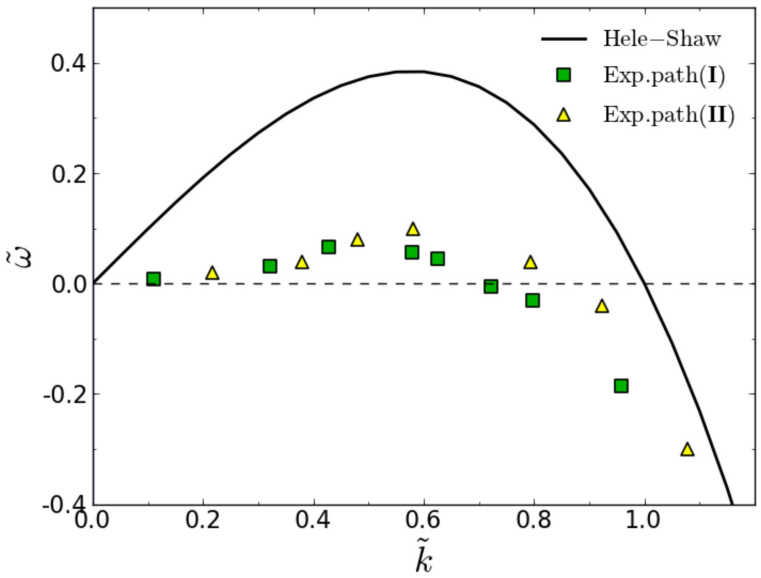

Figure 5.22: Dispersion relation for the complete wetting regime for a system of aspect ratio $\epsilon = 0.24$ and viscosity contrast $r = 0.36$. Results are for two different values of $Pe^*(Ca^*)^{-1} = 19.9$ (Exp.path(**I**)) and $Pe^*(Ca^*)^{-1} = 398.0$ (Exp.path(**II**)), which correspond to the experimental paths shown in Fig. 5.21.

where the interface in the x-z plane is positively curved. So, in conclusion, we have shown, for the first time, that by controlling the interface shape in the x-z plane, we can achieve suppression of the Saffman-Taylor fingering in the x-y plane.

The interface shape in the x-z plane can also be varied by means of the wetting boundary conditions. Fig. 5.23 shows the evolution of a perturbation for two simulations with complete (■) and neutral wetting (□) under otherwise identical conditions. For the case of complete wetting Ca is, in fact, a little higher – $Ca^{wet} = 0.57$ compared to $Ca^{neutr} = 0.48$ – due to the wetting layer of the less viscous fluid - and, therefore, $\tilde{k}$ is smaller for the complete wetting case – $\tilde{k}^{wet} = 0.79$ compared to $\tilde{k}^{neutr} = 0.86$. However, despite this, fingering is suppressed for the case of complete wetting.

Our findings from the numerical study of the Saffman-Taylor instability are qualitatively supported by the experiments with colloid-polymer mixtures in microchannels. Experiments varying viscosity contrast r (exp.**I** and exp.**II**) demonstrated that the onset of Saffman-Taylor fingering in the x-y plane is indeed dependent on the x-z interface structure. The experimental results in Fig. 5.24 show that Saffman-Taylor fingers are seen at a lower $1/B$ for $r \sim 0.36$ than $r \sim 0.84$. More precisely, for $r \sim 0.36$ and $\epsilon = 0.15$, fingering in the x-y plane commences at $1/B \sim 150$ ($Ca \sim 0.3$), which corresponds to $\tilde{k} \sim 0.5$. For a viscosity contrast of $r \sim 0.84$ the

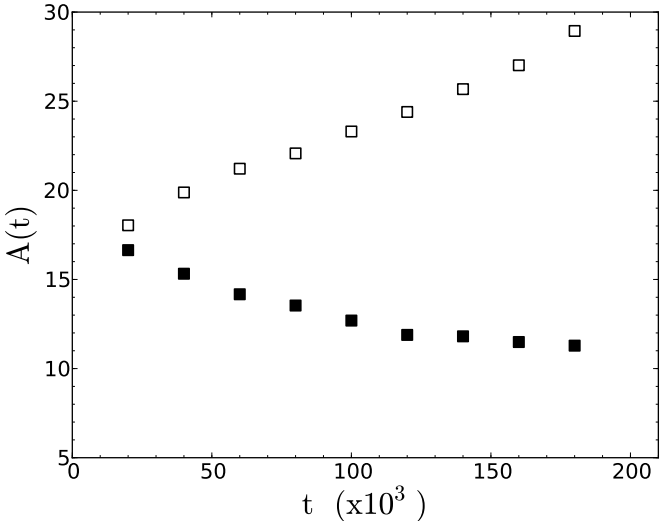

Figure 5.23: Amplitude of an imposed perturbation $A(t)$ as a function of time for complete wetting (■) and neutral wetting (□ - 90° contact angle) under otherwise identical conditions. Aspect ratio of the cell is $\epsilon = 0.24$ ($b = 48$, $w = 200$) and viscosity contrast $r = 0.36$. Saffman-Taylor fingering is clearly suppressed for the case of complete wetting.

onset of fingering is shifted to $1/B \sim 3500$ ($\epsilon = 0.11$, $Ca \sim 3.5$, $\tilde{k} \sim 0.1$), in agreement with the observation from simulations that changing the curvature in the x-z plane and hence the onset of fingering becomes harder. Fingering in the x-z plane is suppressed with increasing viscosity contrast r, which in turn suppresses fingering in the x-y plane, i.e. the Saffman Taylor fingering. This underlines the importance of the hitherto neglected third dimension in the viscous fingering problem.

Limitations in simulation time, however, mean that it is not possible to reach physical system sizes for a direct comparison of finger widths λ_f and critical wavenumbers $\tilde{k}_{cr}$ to experiments. Note that we investigated the dispersion relation for systems with aspect ratio $\epsilon = 0.24$ and $r = 0.36$, compared to $\epsilon = 0.06 - 0.15$ in experiments with the same viscosity contrast. In order to study numerically systems with the same aspect ratios as the experiments, we will have to resort to channels with larger widths w, which however would be computationally too expensive. Nevertheless, lattice Boltzmann simulations proved a valuable tool in examining the viscous fingering problem in the complete wetting regime and demonstrating the importance of the interface structure in the x-z plane on the onset of Saffman-Taylor fingering.

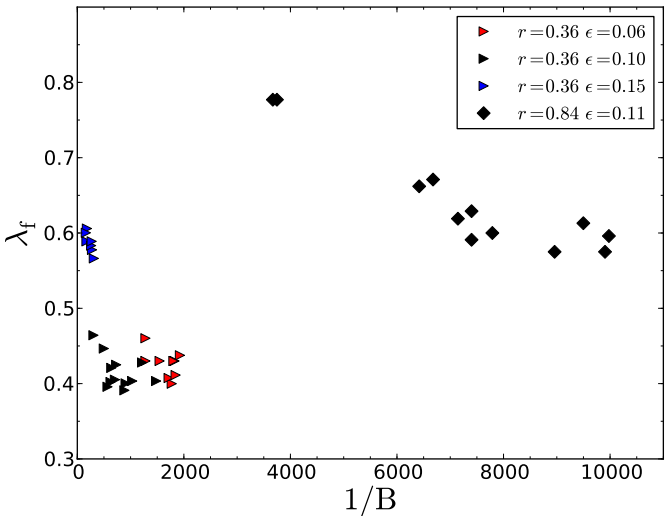

Figure 5.24: Relative finger width λ_f as a function of the classical parameter $1/B$ for experiments with colloid-polymer mixtures. The onset of Saffman-Taylor fingering is shifted to higher values of $1/B$, and consequently Ca, with increasing the viscosity contrast, in line with lattice Boltzmann observations. Fingering in the x-z plane is suppressed with increasing r. This in turn suppresses fingering in the x-y plane, underlining the importance of the hitherto neglected third dimension in the viscous fingering instability.

5.4 Summary

In this chapter, we examined the Saffman-Taylor instability in the complete wetting regime, characterised by vanishing contact angles ($\theta_{eq} = 0°$) and thick wetting layers.

We initially studied the forced displacement of the fluid-fluid interface in the x-z plane. As in the neutral wetting case, two possible interface configurations were distinguished: one in which the interface is advancing as a meniscus and one in which a finger is formed. The mechanism for the penetration process in the x-z plane is again given by the interplay of viscous stresses, surface tension, diffusion and advection. Therefore, the relevant control parameters for fingering in the x-z plane are scaled capillary and Péclet numbers. For high values of Ca^* and Pe^* the advancing interface breaks through in the third dimension. Fingering in the x-z plane is, however, strongly suppressed compared to the neutral wetting case, due to the wetting properties that induce a concave meniscus profile and a wetting layer covering the substrate. Moreover, the onset of the penetration is strongly dependent on the viscosity contrast ratio r.

Our findings from lattice Boltzmann simulations are qualitatively supported by experiments with colloid-polymer mixtures in microchannels. Experiments varying the viscosity contrast

demonstrated that, as the difference in the viscosity of the two fluids increases, the fingering process in the x-z plane is even more strongly suppressed. Much higher capillary numbers are needed for the advancing interface to change the curvature of the meniscus and to induce the formation of a finger in the x-z plane.

Examining the penetrating finger in the x-z plane, revealed that the relevant control parameters describing the relative finger width λ_b remain the same as in the situation where the displaced fluid completely wets the substrate. These are the capillary number [39,40,42,43] and the viscosity contrast ratio r of the fluids [14]. However, much wider fingers were observed for high viscosity contrasts r, both numerically and experimentally, in the complete wetting case, which should be attributed to the presence of the wetting layer. Furthermore, the tendency of decreasing finger widths λ_b with decreasing viscosity contrast was also verified.

Finally, simulations and experiments revealed that the interface shape in the x-z plane has important consequences for the Saffman-Taylor instability itself. The resulting concavity of the interface not only suppresses finger formation in the x-z plane, but this in turn suppresses the onset of viscous fingering in the x-y plane. For the first time we report suppression of the Saffman-Taylor instability by controlling the shape of the interface in the transverse direction or x-z plane, demonstrating the importance of the hitherto neglected third dimension on the viscous fingering problem. These results may be further exploited in enhanced oil recovery [65], where the wettability of the displacing fluid (water and surfactants) can be tuned to displace the oil most effectively.

Chapter 6

The Physics of Liquid Crystals

This chapter gives a brief introduction to liquid crystals and is organised as follows: In section 6.1 we present the basic liquid crystalline phases, which include the nematic, smectic and cholesteric phases. Important aspects of liquid crystals, such as the elastic deformation modes, topological defects and the order parameter for liquid crystal systems are discussed in sections 6.1.1 - 6.1.3. The phenomenological Landau - de Gennes description of liquid crystals is then reviewed in section 6.2. This will be the theoretical framework that we shall use in Chapter 7 to study nematic liquid crystals confined in wedge-structured channels. The dynamics of liquid crystals are presented in section 6.3 and, finally, in section 6.4 we elaborate on the modeling aspects we shall use in the subsequent chapter.

6.1 Liquid crystals - Introduction

Liquid crystals are a state of matter that do not fit into the traditional classification of materials as solids, liquids and gases. As their name implies, liquid crystals are substances that exhibit properties between those of a conventional fluid and those of a solid crystal. As stated by de Gennes [2], a more appropriate name might be "mesomorphic phases", from the Greek word "$\mu\acute{\epsilon}\sigma\eta\ \mu o\rho\phi\acute{\eta}$", meaning intermediate form. While liquid crystals can flow like liquids, their molecules can be oriented in a crystal-like way and possess features that are characteristics of solid crystals, like elasticity or certain optical properties, e.g. birefringence [2, 66, 67].

Liquid crystals consist of strongly anisotropic molecules, either elongated rod-like molecules (calamitic) or disc-like molecules (discotic liquid crystals) [2, 68, 69]. At high temperatures or

low densities the molecules are distributed in a random way and form an isotropic liquid. At low temperatures or high densities the molecules adopt an ordered structure as in solid crystals. In the intermediate regime, however, molecules show long-range correlations with respect to the orientation of their molecular axes, and possess no long-range correlations with respect to their positions. These are the liquid crystal phases.

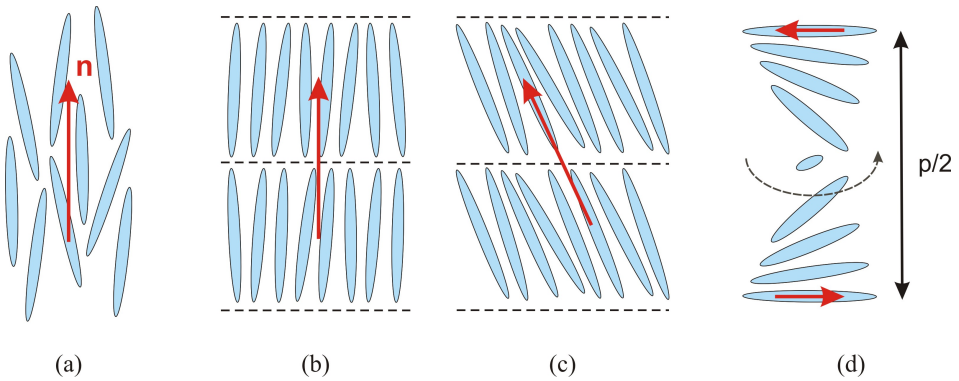

Figure 6.1: Schematic illustrations of liquid crystal phases consisting of elongated molecules: (a) nematic, (b) smectic A, (c) smectic C and (d) cholesteric.

There are a variety of liquid crystal phases. The simplest one, shown in Fig. 6.1(a), is a nematic liquid crystal, in which the molecules are oriented roughly parallel to each other. The average orientation of the nematic molecules, at a given position $\mathbf{r}$ and time t, is described by a unit vector, the director $\mathbf{n}(\mathbf{r},t)$, with orientations $\mathbf{n}$ and $-\mathbf{n}$ being equivalent. More precisely, the director is given as the ensemble average of molecular orientations within a given volume segment or, due to ergodicity, as the time average of a single molecule orientation at a given position. The word nematic comes from the Greek word "$\nu\acute{\eta}\mu\alpha$", meaning thread, from the thread-like textures seen in nematic liquid crystals. These correspond to lines of singularity in the director field, called topological defects or disclinations.

Smectic phases are more ordered than the nematic liquid crystals and, therefore, are found at lower temperatures than that at which the same material would exhibit a nematic phase. In these phases, molecules are arranged in layers. The most common types are smectic A and smectic C. In the smectic A phase the molecules are aligned, on average, along the layer normal, while in the smectic C phase the molecules are tilted within each layer, as shown in Figs. 6.1(b) and 6.1(c). The interlayer spacing can be measured by X-ray scattering.

Finally, cholesteric liquid crystals are a type of chiral liquid crystal, that has a helical

structure as shown in Fig. 6.1(d). The molecules organise in layers with a preferred, in plane, director orientation $\mathbf{n}$ within each layer. The director rotates while moving along the helical axis. The distance over which the nematic director repeats itself is called the cholesteric pitch p. Due to $\mathbf{n}$ and $-\mathbf{n}$ being equivalent the period of this variation is in fact $p/2$. An interesting property of cholesterics is that, due to their periodic structure, they show Bragg reflections at optical wavelengths. Their pitch and hence the wavelength of the Bragg-reflected light depends on temperature, resulting in a change in the colour of the material with variations of temperature. This leads to a number of applications, like fever thermometers, battery testers, detection of hot points in microcircuits, localization of fractures and tumours in humans and conversion of infrared images [70, 71].

6.1.1 Elastic distortions

In a nematic liquid crystal the director field $\mathbf{n}$, which gives the mean orientation of the molecules, prefers to be uniform in the absence of any external influences, such as forces, fields or boundary conditions that impose a certain configuration. Therefore, there is an elastic free energy density cost associated with elastic distortions, which involve gradients of the director field $\nabla\mathbf{n}$. There are three different, independent elastic deformation modes to second order in $\mathbf{n}$, known as *splay, twist* and *bend* [2, 66, 67] and shown in Fig. 6.2. These elastic distortions correspond to the following terms being non-zero:

$$(\nabla \cdot \mathbf{n}) \qquad \text{splay} , \tag{6.1}$$

$$\mathbf{n} \cdot (\nabla \times \mathbf{n}) \qquad \text{twist} , \tag{6.2}$$

$$\mathbf{n} \times (\nabla \times \mathbf{n}) \qquad \text{bend} . \tag{6.3}$$

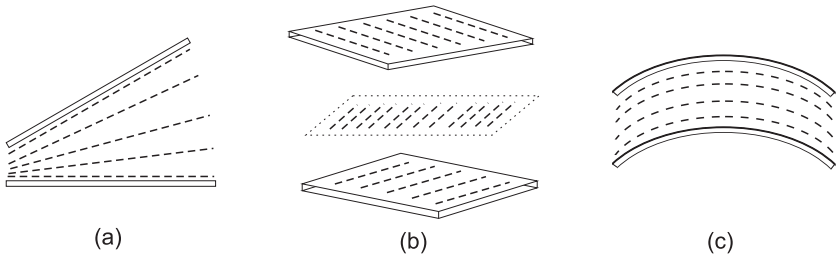

Figure 6.2: Schematic illustration of the three elastic distortions in a nematic liquid crystal: (a) splay, (b) twist and (c) bend.

Then the elastic free energy density associated with the three elastic distortions is given, in the standard Frank-Oseen form [72], by

$$f_{el}^{FO} = \frac{K_1}{2}(\nabla \cdot \mathbf{n})^2 + \frac{K_2}{2}[\mathbf{n} \cdot (\nabla \times \mathbf{n})]^2 + \frac{K_3}{2}[\mathbf{n} \times (\nabla \times \mathbf{n})]^2 \ , \tag{6.4}$$

where K_1, K_2 and K_3 are elastic constants penalising splay, twist and bend distortions respectively. For the case of a cholesteric liquid crystal, the twist is supplemented by a term that provides information about the chirality q_{ch} and the pitch size p, giving $\frac{K_2}{2}[\mathbf{n} \cdot (\nabla \times \mathbf{n}) + q_{ch}]^2$. Then the state of minimum energy is the one for which $\mathbf{n} \cdot (\nabla \times \mathbf{n}) = -q_{ch}$, where $q_{ch} = \pi/p$. It is easily verified that the director field $\mathbf{n} = (\cos(q_{ch}z), \sin(q_{ch}z), 0)$ satisfies this relation.

6.1.2 Disclinations

There are many situations where the nematic liquid crystal cannot adopt a configuration of uniform director field. Example are when boundary conditions or external fields impose a certain configuration. It is then possible to obtain singularities in the director field, where the director varies discontinuously with position and cannot be defined. Fig. 6.3(a) shows a schematic illustration of the director fields around singular points, called disclinations or defects [2, 72], encountered in nematic liquid crystals. Four essential types of disclinations can be classified, based on the director field in the vicinity of the disclination, which are characterised by their topological strength s. The strength of the disclination shows how many times the director rotates by 2π on the closed loop around the defect core. For the disclinations with $s = \pm 1$, the director rotates by 2π, while for $s = \pm 1/2$ it rotates by π. Disclinations can be either lines or points. It is found that disclinations with $s = \pm 1/2$ are always associated with a line, while disclinations with $s = \pm 1$ can be either lines or point disclinations [2]. When the material is viewed under crossed polarizers, disclinations give rise to the Schlieren textures of Fig. 6.3(b). The points where four brushes meet correspond to disclinations with $s = \pm 1$, while the ones where two brushes meet correspond to disclinations with $s = \pm 1/2$.

6.1.3 Order parameter

In an isotropic liquid, averaging over all molecular orientations results in zero alignment. On the contrary, in a nematic liquid crystal averaging over all molecular orientations gives a non-

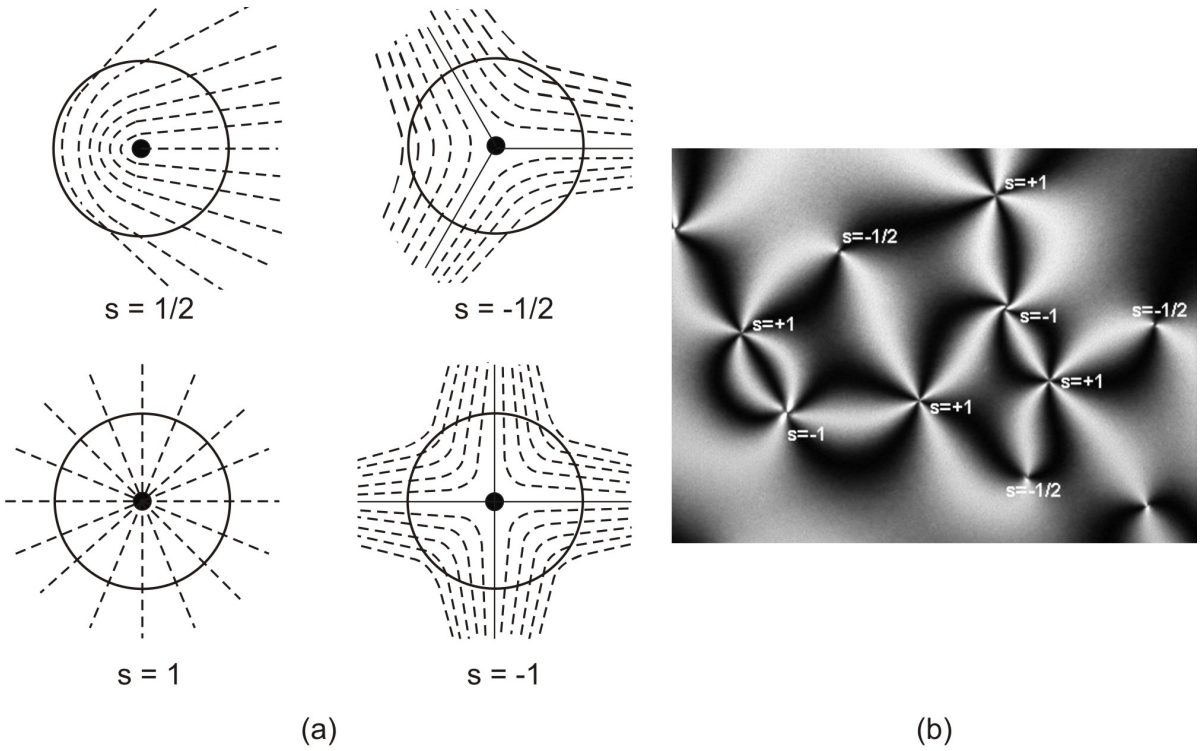

Figure 6.3: (a) Schematic illustration of two-dimensional topological defects and the director fields around them for different topological strengths s. (b) Schlieren texture in a nematic liquid crystal. Image from [73].

zero preferred orientation, which defines the director **n**. We need to specify the degree of ordering in a liquid crystal, i.e. quantify to what extent the individual molecular orientations are aligned with the averaged director field **n**.

Define a unit vector **m** describing the orientation of a single molecule as shown in Fig. 6.4(a). Then θ is the angle between **m** and **n** and $f(\theta)$[1] is the probability distribution describing the state of alignment. $f(\theta)d\Omega$ gives the probability of finding a molecule in a small angle around the direction (θ,ϕ). Since the director orientations **n** and -**n** are indistinguishable, $f(\theta)$ has to be periodic and symmetric around $\theta = \pi/2$, i.e. $f(\theta) = f(\theta + \pi)$. A typical distribution function $f(\theta)$ is shown in Fig. 6.4(b).

Then one way of quantifying the degree of ordering would be through the average of the

[1]The molecules are assumed to have complete cylindrical symmetry about **m**, hence there is no dependence on ϕ.

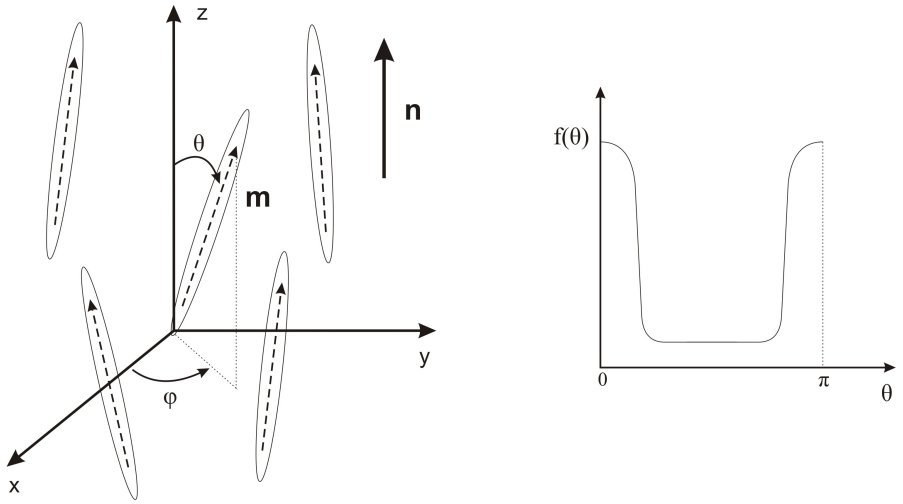

(a) (b)

Figure 6.4: (a) Schematic illustration of rodlike molecules in a nematic liquid crystal. The average alignment is described by the director **n**, which is here taken to be along the z axis. (b) A typical distribution function $f(\theta)$ of the molecular orientations in a nematic liquid crystal.

component of **m** along **n**

$$< \mathbf{m} \cdot \mathbf{n} > = < \cos\theta > = \int f(\theta) \cos\theta \; d\Omega = 2\pi \int_0^\pi f(\theta) \cos\theta \sin\theta \; d\theta \; . \tag{6.5}$$

However, this gives zero, since the integrand is an antisymmetric function in the interval $0 \leq \theta \leq \pi$. So we have to resort to higher multipoles. The first one to give a non-trivial answer is the average of the second Legendre polynomial, $P_2(\cos\theta)$,

$$\begin{aligned} q = < P_2(\cos\theta) > &= \frac{1}{2} < 3\cos^2\theta - 1 > \\ &= \frac{1}{2} \int f(\theta) \left(3\cos^2\theta - 1\right) \; d\Omega \\ &= \frac{1}{2}(2\pi) \int_0^\pi f(\theta) \left(3\cos^2\theta - 1\right) \sin\theta \; d\theta \; . \end{aligned} \tag{6.6}$$

When there is perfect alignment of all molecular orientations **m** with **n**, $f(\theta)$ is strongly peaked around $\theta = 0$ and $\theta = \pi$ and $q = 1$. On the other hand, if all molecules lie perpendicular to **n**, $\theta = \pi/2$ and $q = -1/2$. Finally in the case when molecules are randomly oriented as in an isotropic fluid, then $f(\theta) = 1/(4\pi)$ and Eq. (6.6) gives $q = 0$. Thus q, which is called the nematic degree of order, describes the degree of alignment in a liquid crystal.

A liquid crystal requires a tensorial 3×3 order parameter $\mathbf{Q}$ in order to fully describe all of its orientational degrees of freedom: two angles for the director field $\mathbf{n}$, one angle describing the possible biaxial ordering with respect to the director $\mathbf{n}$, the nematic degree of order q and the degree of biaxiality B. This order parameter is defined as [2]

$$Q_{\alpha\beta} \equiv \frac{q}{2}\left(3n_\alpha n_\beta - \delta_{\alpha\beta}\right) + \frac{B}{2}\left(e_\alpha^{(1)} e_\beta^{(1)} - e_\alpha^{(2)} e_\beta^{(2)}\right). \tag{6.7}$$

By definition $\mathbf{Q}$ is symmetric and traceless

$$Q_{\alpha\beta} = Q_{\beta\alpha}\,, \qquad Q_{\alpha\alpha} = 0. \tag{6.8}$$

It is always possible to find a coordinate system in which the tensor order parameter is diagonal

$$\mathbf{Q} = \mathrm{diag}\left(q, -(q+B)/2, -(q-B)/2\right), \tag{6.9}$$

where its largest eigenvalue is the nematic degree of order q and the corresponding eigenvector the director $\mathbf{n}$. $B = 0$ in the case of a *uniaxial* nematic, while for $B \neq 0$ the tensor is *biaxial*. $\mathbf{e^{(1)}}$, $\mathbf{e^{(2)}}$ in Eq. (6.7) are the eigenvectors that correspond to the other two eigenvalues with $\mathbf{e^{(2)}} = \mathbf{n} \times \mathbf{e^{(1)}}$. Finally, we note that for an isotropic fluid $\mathbf{Q} = 0$.

6.2 Landau-de Gennes modelling

6.2.1 Nematic-Isotropic transition

The nematic-isotropic transition was first described, within the spirit of Landau theories, by de Gennes [2]. The bulk free energy density is expanded in terms of the invariants of the nematic order parameter tensor, Eq. (6.7). The simplest expression, with minimum number of terms to describe the isotropic-nematic transition for a uniaxial nematic, is [2]

$$f_b = \tfrac{1}{2}A_1(T)\; Q_{\alpha\beta}Q_{\beta\alpha} - \tfrac{1}{3}A_2(T)\; Q_{\alpha\beta}Q_{\beta\gamma}Q_{\gamma\alpha} + \tfrac{1}{4}A_3(T)\left(Q_{\alpha\beta}Q_{\beta\alpha}\right)^2\,, \tag{6.10}$$

where the A's are material parameters that in general depend on the temperature T. For lyotropic liquid crystals these coefficients also depend on the concentration of the liquid crystal

molecules.

There is no linear invariant in Eq. (6.10) since $Q_{\alpha\alpha} = 0$. Eq. (6.10) ensures that $\mathbf{Q} = 0$, i.e. an isotropic fluid, can be a state of minimum energy, while the presence of a non-vanishing cubic term ensures that the nematic-isotropic transition is of first order. Experimentally, discontinuities, although small, have been observed in the density and specific heat at the transition [2].

A possible choice for the coefficients in Eq. (6.10) is $A_1 = A_0(1 - \gamma/3)$, $A_2 = A_3 = A_0\gamma$, where A_0 is a constant and γ is related to the temperature or concentration. Then Eq. (6.10) becomes

$$f_b = A_0\left[\frac{1}{2}(1 - \frac{\gamma}{3})Q_{\alpha\beta}^2 - \frac{\gamma}{3}Q_{\alpha\beta}Q_{\beta\gamma}Q_{\gamma\alpha} + \frac{\gamma}{4}(Q_{\alpha\beta}^2)^2\right] . \tag{6.11}$$

By assuming uniaxial ordering, Eq. (6.7) simplifies to $Q_{\alpha\beta} = q\left(3n_\alpha n_\beta - \delta_{\alpha\beta}\right)/2$, and the invariants of the order parameter in Eqs. (6.10) and (6.11) read as

$$Q_{\alpha\beta}Q_{\beta\alpha} = 3q^2/2 , \qquad Q_{\alpha\beta}Q_{\beta\gamma}Q_{\gamma\alpha} = 3q^3/4 . \tag{6.12}$$

The bulk free energy density is then rewritten in terms of the nematic degree of order q

$$f_b = A_0\left[\frac{3}{4}\left(1 - \frac{\gamma}{3}\right)q^2 - \frac{\gamma}{4}q^3 + \frac{9\gamma}{16}q^4\right] . \tag{6.13}$$

Fig. 6.5(a) shows the Landau-de Gennes free energy density as a function of the nematic degree of order q for different values of γ. The inset shows that the free energy exhibits two minima of equal depths at the value $\gamma = 2.7$, which sets the location of the first order nematic-isotropic transition.

Minimising Eq. (6.13) with respect to q gives

$$\frac{\partial f_b}{\partial q} = 0 = A_0 q\left[\frac{3}{2}\left(1 - \frac{\gamma}{3}\right) - \frac{3\gamma}{4}q + \frac{9\gamma}{4}q^2\right] , \tag{6.14}$$

with solutions

$$q = 0 , \qquad q = \frac{1}{6} \pm \frac{1}{2}\sqrt{1 - \frac{8}{3\gamma}} , \tag{6.15}$$

shown in Fig. 6.5(b). It is easily seen that the order parameter q is discontinuous at the transition value of $\gamma = 2.7$, since the system jumps from the isotropic branch ($q = 0$) to the

nematic branch with $q > 0$.

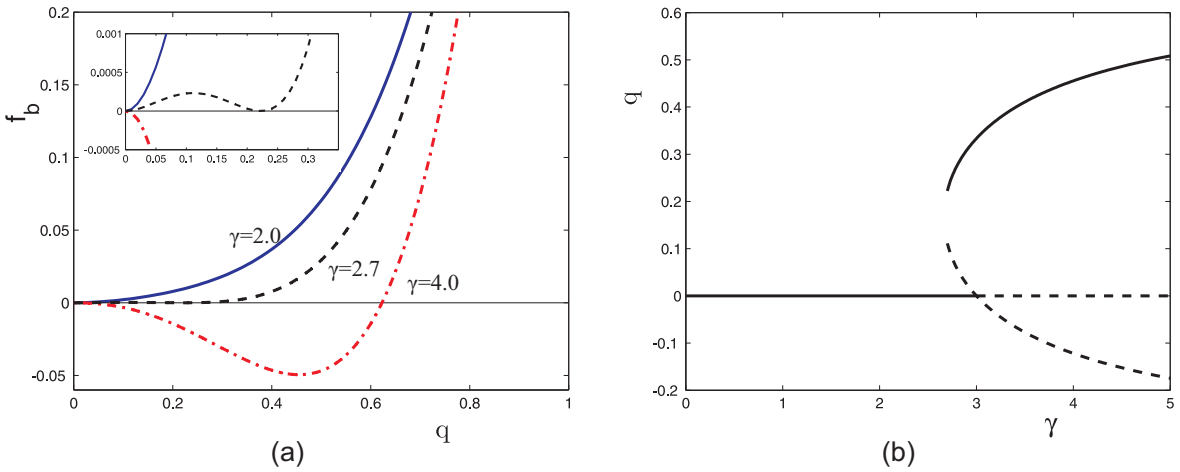

Figure 6.5: (a) The bulk free energy density Eq. (6.13) as a function of the nematic degree of order q for different values of γ and $A_0 = 1$. (b) Nematic degree of order q as a function of γ. The solid (dashed) line corresponds to the stable (unstable) solutions Eq. (6.15).

Now it is easy to interpret the role of the three terms in the Landau-de Gennes free energy density, Eq. (6.11). The first term drives the nematic-isotropic transition, the second one ensures that the transition is of first order, while the last term ensures that the free energy is bounded from below.

6.2.2 Elastic distortions

We have seen that the bulk free energy density describing a liquid crystal system has to be supplemented by a part, which penalises elastic distortions. Again, the elastic free energy density is constructed phenomenologically, now from the invariants of the tensor order parameter **Q** [74]

$$f_{el} = \frac{L_1}{2}(\partial_\alpha Q_{\beta\gamma})^2 + \frac{L_2}{2}(\partial_\alpha Q_{\alpha\gamma})(\partial_\beta Q_{\beta\gamma}) + \frac{L_3}{2} Q_{\alpha\beta}(\partial_\alpha Q_{\gamma\epsilon})(\partial_\beta Q_{\gamma\epsilon}) \,, \tag{6.16}$$

where the $L's$ are elastic constants that depend on the material temperature and concentration. Eq. (6.16) contains two terms with gradients of the order parameter **Q** up to second order and one term with both the order parameter and quadratic gradient terms. This choice was shown to yield the correct behaviour for the temperature dependence of the elastic coefficients and is sufficient to match the Frank elastic constants for the three elastic modes, splay, bend and twist [74].

Eq. (6.16) can be mapped to the standard Frank-Oseen expression, Eq. (6.4), where the elastic free energy is written in terms of the director field $\mathbf{n}$. In order to do this Eq. (6.4) is rewritten as [75]

$$\begin{aligned} f_{el}^{FO} &= \frac{1}{2}K_1\left(\partial_i n_i\right)\left(\partial_j n_j\right) \\ &+\frac{1}{2}K_2\left[\left(\partial_j n_i\right)\left(\partial_j n_i\right)-\left(\partial_i n_i\right)\left(\partial_j n_j\right)-n_i n_j\left(\partial_i n_k\right)\left(\partial_j n_k\right)\right] \\ &+\frac{1}{2}K_3 n_i n_j\left(\partial_i n_k\right)\left(\partial_j n_k\right)\ . \end{aligned} \tag{6.17}$$

Using the definition of a uniaxial tensor order parameter, $Q_{ij} = q\left(3n_i n_j - \delta_{ij}\right)/2$, the three terms in Eq. (6.16) can be expressed in terms of the director field $\mathbf{n}$

$$\left(\partial_k Q_{ij}\right)\left(\partial_k Q_{ij}\right) = \frac{9q^2}{2}\left(\partial_k n_i\right)\left(\partial_k n_i\right), \tag{6.18}$$

$$\left(\partial_j Q_{ij}\right)\left(\partial_k Q_{ik}\right) = \frac{9q^2}{4}\left[\left(\partial_j n_j\right)\left(\partial_k n_k\right)+n_j n_k\left(\partial_j n_i\right)\left(\partial_k n_i\right)\right], \tag{6.19}$$

$$Q_{ij}\left(\partial_i Q_{kl}\right)\left(\partial_j Q_{kl}\right) = \frac{q^3}{4}\left[27 n_i n_j\left(\partial_i n_k\right)\left(\partial_j n_k\right)-9\left(\partial_i n_k\right)\left(\partial_i n_k\right)\right]. \tag{6.20}$$

Inserting Eqs. (6.18)-(6.20) into Eq. (6.16) and comparing with Eq. (6.17) yields the following relations between the elastic constants [74]

$$\begin{aligned} K_1 &= \frac{9q^2}{4}(2L_1 + L_2 - qL_3)\ , \\ K_2 &= \frac{9q^2}{4}(2L_1 - qL_3)\ , \\ K_3 &= \frac{9q^2}{4}(2L_1 + L_2 + 2qL_3)\ . \end{aligned} \tag{6.21}$$

In order to simplify calculations and study the qualitative behaviour of a nematic liquid crystal, it is sometimes useful to make the approximation that all elastic constants are equal, $K_1 = K_2 = K_3 = K$, known as the one elastic constant approximation. In this case the elastic free energy Eq. (6.16) reduces to

$$f_{el} = \frac{L}{2}\left(\partial_\alpha Q_{\beta\gamma}\right)^2\ , \tag{6.22}$$

and it is easily seen that

$$K = \frac{9q^2}{2}L\ . \tag{6.23}$$

6.3 Hydrodynamics - Equations of motion

Having reviewed the equilibrium properties of a nematic liquid crystal within a Landau-de Gennes framework, we now turn our attention to the dynamics of liquid crystals. One of the most interesting features of liquid crystals is that they can flow. Moreover, the delicate coupling of the liquid crystal orientation to the fluid flow leads to a plethora of interesting new phenomena [2, 76]. Flow in general can rotate the liquid crystal molecules, due to their rodlike shape, and affects their alignment. Conversely, disturbances in the orientation of the molecules can induce flow, since the system will attempt to realign. This effect is known as *backflow*.

The hydrodynamics of nematic liquid crystals was first formulated by Ericksen and Leslie [76]. The equations of motion, known as the Ericksen-Leslie formulation of nematodynamics, are based on the director field $\mathbf{n}$. They are, however, valid only for the case of constant nematic degree of order q. Therefore we can not use this formulation to study systems with defects or close to a phase transition, where q varies.

In these situations, therefore, it is favorable to use the formulation based on the $\mathbf{Q}$ tensor, developed by Edwards, Beris and Grmela [75, 77]. The dynamics of the order parameter $\mathbf{Q}$ is described by the equation [75, 77]

$$(\partial_t + u_\alpha \partial_\alpha)\mathbf{Q} - \mathbf{S}(\mathbf{W}, \mathbf{Q}) = \Gamma_H \mathbf{H} \,, \tag{6.24}$$

where Γ_H is a collective rotational diffusion constant and

$$\mathbf{S}(\mathbf{W}, \mathbf{Q}) = (\xi_{lc}\mathbf{D} + \mathbf{\Omega})(\mathbf{Q} + \frac{1}{3}\mathbf{I}) + (\mathbf{Q} + \frac{1}{3}\mathbf{I})(\xi_{lc}\mathbf{D} - \mathbf{\Omega}) - 2\xi_{lc}(\mathbf{Q} + \frac{1}{3}\mathbf{I})Tr(\mathbf{Q}\mathbf{W}). \tag{6.25}$$

$\mathbf{D} = \frac{1}{2}(\mathbf{W} + \mathbf{W}^\mathbf{T})$ and $\mathbf{\Omega} = \frac{1}{2}(\mathbf{W} - \mathbf{W}^\mathbf{T})$ are the symmetric and antisymmetric part of the velocity gradient tensor $W_{\alpha\beta} = \partial_\beta u_\alpha$ respectively, while ξ_{lc} is a constant related with the molecular details of a given liquid crystal.

Eq. (6.24) describes how the order parameter is advected by the flow, but also, due to the elongated shape of the molecules, rotated and stretched by velocity gradients. The right hand side describes how $\mathbf{Q}$ relaxes towards the minimum of the free energy according to the molecular field

$$\mathbf{H} = -\frac{\delta \mathcal{F}}{\delta \mathbf{Q}} + \frac{1}{3}\mathbf{I}\mathrm{Tr}(\frac{\delta \mathcal{F}}{\delta \mathbf{Q}}) \,. \tag{6.26}$$

The fluid obeys both the continuity and the Navier-Stokes equation

$$\rho(\partial_t + u_\beta \partial_\beta) u_\alpha = \partial_\beta \sigma_{\alpha\beta} + \partial_\beta \tau_{\alpha\beta} + \eta \partial_\beta (\partial_\alpha u_\beta + \partial_\beta u_\alpha) \ , \tag{6.27}$$

where ρ, η are the fluid density and an isotropic viscosity respectively. Eq. (6.27) is of similar form to a simple fluid, but with the stress tensor, $\Pi_{\alpha\beta} = \sigma_{\alpha\beta} + \tau_{\alpha\beta}$, now reflecting the additional complications of liquid crystal hydrodynamics. $\Pi_{\alpha\beta}$ is comprised of a symmetric, $\sigma_{\alpha\beta}$, and an antisymmetric, $\tau_{\alpha\beta}$, part

$$\begin{aligned} \sigma_{\alpha\beta} &= -P_0 \delta_{\alpha\beta} + 2\xi_{lc} \left(Q_{\alpha\beta} + \frac{1}{3}\delta_{\alpha\beta} \right) Q_{\gamma\epsilon} H_{\gamma\epsilon} \\ &\quad -\xi_{lc} H_{\alpha\gamma} \left(Q_{\gamma\beta} + \frac{1}{3}\delta_{\gamma\beta} \right) - \xi_{lc} \left(Q_{\alpha\gamma} + \frac{1}{3}\delta_{\alpha\gamma} \right) H_{\gamma\beta} \\ &\quad -\partial_\alpha Q_{\gamma\nu} \frac{\delta \mathcal{F}}{\delta \partial_\beta Q_{\gamma\nu}} \ , \end{aligned} \tag{6.28}$$

$$\tau_{\alpha\beta} = Q_{\alpha\gamma} H_{\gamma\beta} - H_{\alpha\gamma} Q_{\gamma\beta} \ , \tag{6.29}$$

where $P_0 = \rho T - \frac{L}{2}(\partial_\alpha Q_{\beta\gamma})^2$ is the isotropic pressure.

6.4 Modeling liquid crystal systems

6.4.1 Hybrid lattice Boltzmann method

We shall use a hybrid lattice Boltzmann method to numerically study liquid crystal systems confined in sawtoothed geometries in Chapter 7. In particular, we solve the Navier-Stokes equation, Eq. (6.27), using a D3Q19 lattice Boltzmann algorithm and the evolution equation for the $\mathbf{Q}$ tensor, Eq. (6.24), using a finite difference predictor-corrector scheme to reduce the computational memory requirements.

Starting from the evolution of the $\mathbf{Q}$ tensor, Eq. (6.24), we need to construct first the Landau-de Gennes free energy of the system, as explained in section 6.2, by combining the

bulk term, Eq. (6.11), and the elastic contribution, Eq. (6.16),

$$\begin{aligned}\mathcal{F}^{LdG} &= \int_V (f_b + f_{el})\, dV + \int_S f_w\, dS \\ &= \int_V \Bigg(A_0 \Big[\frac{1}{2}(1-\frac{\gamma}{3})Q_{\alpha\beta}^2 - \frac{\gamma}{3} Q_{\alpha\beta}Q_{\beta\gamma}Q_{\gamma\alpha} + \frac{\gamma}{4}(Q_{\alpha\beta}^2)^2 \Big] \\ &\qquad + \frac{L_1}{2}(\partial_\alpha Q_{\beta\gamma})^2 + \frac{L_2}{2}(\partial_\alpha Q_{\alpha\gamma})(\partial_\beta Q_{\beta\gamma}) + \frac{L_3}{2} Q_{\alpha\beta}(\partial_\alpha Q_{\gamma\epsilon})(\partial_\beta Q_{\gamma\epsilon}) \Bigg) dV \\ &\quad + \int_S f_w\, dS\ . \end{aligned} \tag{6.30}$$

The last term (surface integral) accounts for the interactions of liquid crystal molecules with solid surfaces. Walls can impose different ordering of the liquid crystal at the boundaries to the ordering in the bulk. This is often referred to as anchoring of the director on the walls. Here, we model this by using a Rapini-Papoular-like surface free energy density [78]

$$f_w = W(Q_{\alpha\beta} - Q^0_{\alpha\beta})^2, \tag{6.31}$$

where W denotes the uniform anchoring strength and $Q^0_{\alpha\beta} = q(3n^0_\alpha n^0_\beta - \delta_{\alpha\beta})/2$ corresponds to the preferred director orientation $\mathbf{n^0}$ imposed by the walls.

The molecular field, Eq. (6.26), necessary to integrate Eq. (6.24), is then given by

$$\begin{aligned}(H_b)_{\alpha\beta} &= -A_0 \Big[(1-\frac{\gamma}{3})Q_{\alpha\beta} - \gamma Q_{\alpha\mu}Q_{\mu\beta} + \gamma Q_{\alpha\beta}Q_{\mu\nu}Q_{\nu\mu} \Big] \\ &\quad -\tfrac{1}{3}A_0\gamma Q_{\mu\nu}Q_{\nu\mu}\delta_{\alpha\beta}\ , \end{aligned} \tag{6.32a}$$

$$\begin{aligned}(H_{el})_{\alpha\beta} &= L_1 \partial_\gamma\partial_\gamma Q_{\alpha\beta} \\ &\quad + \tfrac{1}{2}L_2 \Big[\partial_\beta\partial_\gamma Q_{\alpha\gamma} + \partial_\alpha\partial_\gamma Q_{\beta\gamma} - \tfrac{2}{3}\delta_{\alpha\beta}\,\partial_\epsilon\partial_\gamma Q_{\epsilon\gamma} \Big] \\ &\quad + L_3 \Big[-\tfrac{1}{2}\partial_\alpha Q_{\gamma\epsilon}\,\partial_\beta Q_{\gamma\epsilon} + \partial_\gamma Q_{\gamma\epsilon}\,\partial_\epsilon Q_{\alpha\beta} + Q_{\gamma\epsilon}\,\partial_\gamma\partial_\epsilon Q_{\alpha\beta} \\ &\qquad -\tfrac{1}{6}\delta_{\alpha\beta}\,(\partial_\kappa Q_{\gamma\epsilon})^2 \Big], \end{aligned} \tag{6.32b}$$

$$(H_w)_{\alpha\beta} = -W(Q_{\alpha\beta} - Q^0_{\alpha\beta})\ . \tag{6.32c}$$

In the case of planar degenerate anchoring, which refers to the *common alignment of the molecules along any direction parallel to the solid surface* [2] we use the free energy density

proposed by Fournier and Galatola [79]

$$f_w = W_1^{deg}(\tilde{Q}_{\alpha\beta} - \tilde{Q}^{\perp}_{\alpha\beta})^2 + W_2^{deg}(\tilde{Q}_{\alpha\beta}\tilde{Q}_{\alpha\beta} - \tfrac{9}{4}q_0^2)^2, \tag{6.33}$$

where W_1^{deg}, W_2^{deg} denote degenerate anchoring strengths and

$$\tilde{Q}_{\alpha\beta} = Q_{\alpha\beta} + \tfrac{1}{2}q_0\delta_{\alpha\beta}\ , \qquad \tilde{Q}^{\perp}_{\alpha\beta} = P_{\alpha\mu}\tilde{Q}_{\mu\xi}P_{\xi\beta}\ , \qquad P_{\alpha\beta} = \delta_{\alpha\beta} - \nu_\alpha\nu_\beta\ . \tag{6.34}$$

$P_{\alpha\beta}$ is a surface projection operator and $\boldsymbol{\nu}$ is a unit vector normal to the surface. The first term in Eq. (6.33) penalises deviations of $\tilde{Q}_{\alpha\beta}$ from its projection on the substrate $\tilde{Q}^{\perp}_{\alpha\beta}$.The second term in Eq. (6.33) penalises deviations from the preferred nematic order, which we take here to be equal to the equilibrium nematic degree of order in the bulk q_0. The molecular field, analogous to Eq. (6.32c), is then evaluated using Eq. (6.26).

Once the molecular field is known, the evolution equation of the $\mathbf{Q}$ tensor, Eq. (6.24), is solved by a predictor-corrector scheme. We rewrite Eq. (6.24) as

$$\partial_t\mathbf{Q} = -u_\alpha\partial_\alpha\mathbf{Q} + \mathbf{S}(\mathbf{W},\mathbf{Q}) + \Gamma_H\mathbf{H} = f(t_n,\mathbf{Q})\ . \tag{6.35}$$

The algorithm we use proceeds in two steps:

$$\text{Prediction step:} \qquad Q^{(1)}_{\alpha\beta,t_n+\Delta t} = Q_{\alpha\beta,t_n} + \Delta t\, f(t_n, Q_{\alpha\beta,t_n}), \tag{6.36a}$$

$$\text{Correction step:} \qquad Q^{(2)}_{\alpha\beta,t_n+\Delta t} = Q_{\alpha\beta,t_n} + \Delta t\, f(t_n, Q^{(1)}_{\alpha\beta,t_n+\Delta t}), \tag{6.36b}$$

with the solution for the order parameter at time $t = t_n + \Delta t$, $Q_{\alpha\beta,t_n+\Delta t}$ given by

$$Q_{\alpha\beta,t_n+\Delta t} = \frac{1}{2}\left[Q^{(1)}_{\alpha\beta,t_n+\Delta t} + Q^{(2)}_{\alpha\beta,t_n+\Delta t}\right]. \tag{6.37}$$

We then solve the continuity and Navier-Stokes equation, Eq. (6.27) using a lattice Boltzmann algorithm. The evolution equation of the lattice distribution functions, Eq. (3.15), is modified to account for the additional contributions to the pressure tensor due to the liquid crystal system as

$$f_i(\mathbf{r} + \mathbf{e_i}\Delta t, t + \Delta t) = f_i(\mathbf{r},t) - \frac{1}{\tau_f}[f_i(\mathbf{r},t) - f_i^{eq}(\mathbf{r},t)] + \Delta t\, F_i + \Delta t\, p_i^{(1)} + \Delta t\, p_i^{(2)}\ , \tag{6.38}$$

where the terms $p_i^{(1)}$, $p_i^{(2)}$ are related to $\sigma_{\alpha\beta}$, Eq. (6.28), and $\tau_{\alpha\beta}$, Eq. (6.29). By performing a Chapman-Enskog expansion [33] on Eq. (6.38) we evaluate the moments of $p_i^{(1)}$, $p_i^{(2)}$ so that the Navier-Stokes equation, Eq. (6.27), is recovered

$$\sum_{i=0}^{18} p_i^{(1)} = 0, \qquad \sum_{i=0}^{18} p_i^{(1)} e_{i\alpha} = \partial_\beta \sigma_{\alpha\beta}, \qquad \sum_{i=0}^{18} p_i^{(1)} e_{i\alpha} e_{i\beta} = u_\alpha \partial_\gamma \sigma_{\beta\gamma} + u_\beta \partial_\gamma \sigma_{\alpha\gamma}, \tag{6.39a}$$

$$\sum_{i=0}^{18} p_i^{(2)} = 0, \qquad \sum_{i=0}^{18} p_i^{(2)} e_{i\alpha} = \partial_\beta \tau_{\alpha\beta}, \qquad \sum_{i=0}^{18} p_i^{(2)} e_{i\alpha} e_{i\beta} = u_\alpha \partial_\gamma \tau_{\beta\gamma} + u_\beta \partial_\gamma \tau_{\alpha\gamma}. \tag{6.39b}$$

The fluid velocity $\mathbf{u}$ is given by

$$\rho u_\alpha = \sum_{i=0}^{18} f_i e_{i\alpha} + \tfrac{1}{2} \left[F_\alpha + \partial_\beta \sigma_{\alpha\beta} + \partial_\beta \tau_{\alpha\beta} \right] \Delta t. \tag{6.40}$$

Taking into account the constraints Eq. (6.39) for $p_i^{(1)}$ and $p_i^{(2)}$ we can define the pressure terms as a power series in the velocity

$$p_i^{(1)} = \tfrac{w_i}{c^2} \left(e_{i\alpha} \partial_\beta \sigma_{\alpha\beta} + \tfrac{3}{2c^2} \left[e_{i\alpha} e_{i\beta} - \tfrac{c^2}{3} \delta_{\alpha\beta} \right] \left(u_\alpha \partial_\gamma \sigma_{\beta\gamma} + u_\beta \partial_\gamma \sigma_{\alpha\gamma} \right) \right), \tag{6.41a}$$

$$p_i^{(2)} = \tfrac{w_i}{c^2} \left(e_{i\alpha} \partial_\beta \tau_{\alpha\beta} + \tfrac{3}{2c^2} \left[e_{i\alpha} e_{i\beta} - \tfrac{c^2}{3} \delta_{\alpha\beta} \right] \left(u_\alpha \partial_\gamma \tau_{\beta\gamma} + u_\beta \partial_\gamma \tau_{\alpha\gamma} \right) \right), \tag{6.41b}$$

with the coefficients w_i as listed in Chapter 3, section 3.3.1.

The difference between the hybrid algorithm and the usual lattice Boltzmann method for modeling liquid crystal hydrodynamics [80,81] is that the input for the equilibrium distribution functions f_i^{eq} does not depend on $\mathbf{Q}$ and that both terms in the pressure tensor, $\sigma_{\alpha\beta}$, Eq. (6.28), and $\tau_{\alpha\beta}$, Eq. (6.29) enter as forcing terms in Eq. (6.38).

6.4.2 Boundary conditions

Minimising the free energy functional of the nematic liquid crystal, Eq. (6.30), and assuming the one elastic constant approximation, leads to an equilibrium boundary condition for the $\mathbf{Q}$ tensor at a surface

$$L \frac{\partial Q_{ij}}{\partial x_k} \nu_k + \frac{\partial f_w}{\partial Q_{ij}} = 0 \,. \tag{6.42}$$

Numerically, we use the value of the derivative of the $\mathbf{Q}$ tensor on the substrate to fill the solid nodes neighbouring the boundary, in a similar way to that described in Chapter 3, section 3.4,

for the concentration field.

An alternative way of treating the solid nodes located next to the fluid nodes, that we shall use in Chapter 7, is to treat the order parameter according to [82]

$$\frac{dQ_{ij}}{dt} = \Gamma_H \, H_{ij}^{surf} \ , \tag{6.43}$$

where H_{ij}^{surf} is the appropriate molecular field for the surface nodes given by

$$H_{ij}^{surf} \equiv L \, \frac{\partial Q_{ij}}{\partial x_k} \, \nu_k + \frac{\partial f_w}{\partial Q_{ij}}. \tag{6.44}$$

Eq. (6.43) is solved using a finite difference method to update the value of the Q tensor on the solid nodes

$$Q_{ij,t+\Delta t} = Q_{ij,t} + \Delta t \, \Gamma_H \, H_{ij}^{surf}. \tag{6.45}$$

At equilibrium the molecular field H_{ij}^{surf} is zero leading to the boundary condition Eq. (6.42).

6.4.3 Nematic correlation length ξ_N and extrapolation length ξ_s

Significant quantities when liquid crystal systems are studied numerically are the nematic correlation length ξ_N and the extrapolation length ξ_s. The former is important for systems with defects, since ξ_N sets the length-scale over which the nematic degree of order q varies and, therefore, determines roughly the size of a defect. Assuming a uniaxial nematic and spatial variations of q only, i.e. $\nabla \mathbf{n} = 0$ and $\nabla q \neq 0$, ξ_N can be evaluated by minimising Eq. (6.30) within the Euler-Lagrange formalism. Linearising the resulting Euler-Lagrange equation for small spatial perturbations from equilibrium $q(x_i) = q_{eq} + \Delta q(x_i)$, gives the nematic correlation length ξ_N [82]

$$\xi_N = \sqrt{\frac{L_1 + 2L_2/3 + L_3}{A_0 \left[(1 - \frac{\gamma}{3}) - \gamma q_{eq} + \frac{9}{2} \gamma q_{eq}^2 \right]}} \ . \tag{6.46}$$

The extrapolation length ξ_s measures the relative importance of elasticity to surface anchoring and is defined as [2, 82]

$$\xi_s = \frac{K}{W} \ . \tag{6.47}$$

Hence, strong anchoring corresponds to the limit $\xi_s \to 0$, while large extrapolation lengths indicate weak surface anchoring.

6.5 Summary

This chapter has given a brief introduction to liquid crystalline order. The main types of liquid crystal phases were presented and basic aspects, like the elastic deformation modes and topological defects were explained.

The equilibrium properties of a nematic liquid crystal and the nematic-isotropic transition were described using a Landau-de Gennes free energy based on a tensor order parameter. This free energy approach will be used in Chapter 7 to study nematic liquid crystals confined in wedge-structured channels.

We also reviewed the hydrodynamic equations of motion of liquid crystal systems. These are the time evolution of the tensor order parameter Eq. (6.24) and the Navier-Stokes equation Eq. (6.27). They are complex and need to be solved numerically. To this end we define a hybrid lattice Boltzmann algorithm.

Chapter 7

Liquid Crystals in Confinement

Packing of anisotropic particles can lead to interesting phenomena in fields ranging from biology to engineering. In biological systems the organization of the cell is determined, among other things, by the packing of fibril-like particles, the actin filaments, into functional structures [83, 84]. The plethora of liquid crystalline mesomorphic phases is another excellent example, where packing leads to different phases with increasing concentration. Confinement effects add to the complexity and enhance the richness of these phenomena, because the interactions of the liquid crystal molecules with the solid boundaries may impose different ordering of the molecules than in the bulk. This competition between surface anchoring and nematic ordering can lead to novel, intricate structures. Many of the next generation liquid crystal display devices exploit this interplay by using structured or patterned surfaces as an essential element of their design. So, while most liquid crystal display devices used today are monostable, i.e. have one stable state of minimum energy and require an applied field to maintain a second optically contrasting state, patterned surfaces and confinement can be used to construct bistable display devices, which exhibit two or more stable states [85–93]. The advantage gained from introducing bistability is that power consumption is reduced, since power is only needed to switch between the states but not to maintain them.

In this chapter we report work on colloidal, nematic liquid crystals in sawtoothed structured geometries. We investigate the dependence of the stable director configurations on the confinement geometry. We start in section 7.1 by presenting experimental work using *fd* virus particles in microchannels. The experiments were conducted by Oliver J. Dammone, a colleague in the Physical and Theoretical Chemistry Laboratory in Oxford University, working

under the supervision of Dr. Dirk G.A.L. Aarts, and were a primary motivation for this research.

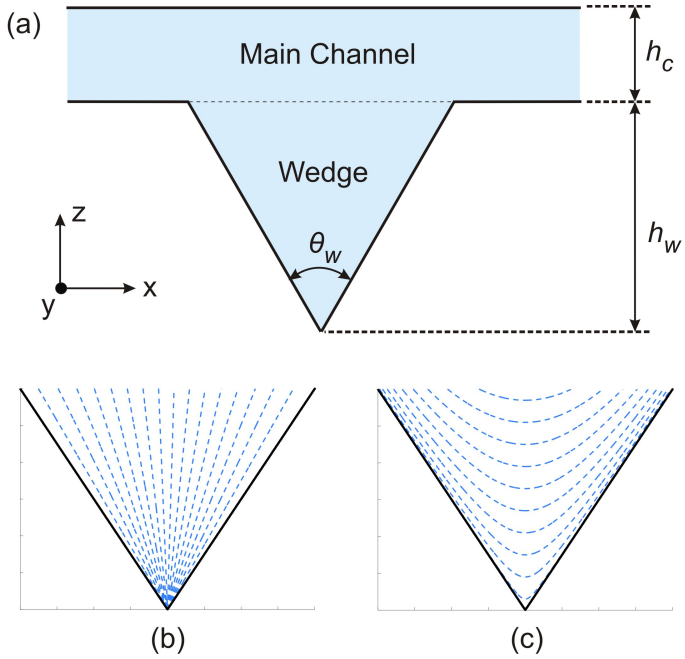

Figure 7.1: (a) Schematic illustration of the channel geometry used for the study of nematic liquid crystals in sawtoothed structured geometries. The channel is comprised of the main channel with height h_c, and the wedge with height h_w and opening angle θ_w. (b) and (c) Schematic illustrations of the possible configurations in a wedge. (b) Pure splay originating from the tip of the wedge. (c) Bend configuration. This configuration includes both splay and bend deformations.

Then in section 7.2 we present the numerical part of the study of liquid crystal systems confined in channels with wedge-structured walls. Schematic illustration of the channel geometry is shown in Fig. 7.1(a). In particular, we first examine, in section 7.2.2, only the wedge part of the channel and investigate the dependence of the possible equilibrium configurations, bend or splay, on the elastic constants. Our aim is to evaluate the threshold for transition from a splay to bend configuration for various ratios of the elastic constants K_1/K_3. Analytical predictions provide a way of testing the numerical predictions [93, 94]. Subsequently, in section 7.2.3 we investigate the dependence of the final equilibrium configurations on the complete channel geometry and, in particular, the main channel. We also consider other relevant parameters, such as the nematic correlation length, anchoring strength and ratio of elastic constants.

For a splay configuration originating from the tip of the wedge, the presence of the main channel, with a horizontal nematic configuration, inevitably leads to frustration of the director

field and the formation of defects. These defects are not located only at the boundaries as, for example, in previous work on bistable devices [85–87, 91–93] or sawtoothed geometries [95], but rather in the bulk of the wedge. We shall examine the relative position of the defect within the wedge, as a function of the wedge opening angle θ_w, and its dependence on the channel geometry, nematic correlation length, anchoring strength and ratio of elastic constants, in sections 7.2.3.1-7.2.3.4.

7.1 Experiments in structured microchannels using *fd* virus particles

(The experiments in this chapter were performed by Oliver J. Dammone in the lab of Dr. D. Aarts in the Physical and Theoretical Chemistry Laboratory, University of Oxford.)

fd virus particles were used as a colloidal nematic liquid crystal. These have been shown to provide an excellent model system for both static and dynamic behaviour [96–98] of liquid crystal systems. The particles are monodisperse and have a contour length of 0.88 μm and diameter of 6.6 nm, which means that direct observation of the particles is feasible by optical microscopy techniques. In order to do this 1% of the particles were fluorescently labeled. The position and orientation of individual particles were then visualized in three dimensions by means of laser scanning confocal microscopy (LSCM), as shown in Figs. 7.2(a) and 7.2(b).

This further enables the construction of the director field directly from single particle information. Image analysis software was used [99] to firstly identify each rod's position and orientation. Then, by subsequently averaging over typically ten images and binning the orientation in small squares, such that each local orientation was constructed from at least 150 particles, an accurate average orientation could be obtained. Processed images with the constructed director fields are shown in Fig. 7.3(a).

The microfluidic channel geometry used is shown in Figs. 7.1(a) and 7.2(c). One of the walls was structured with wedges with a range of opening angles. The depth of the channels was $b = 10\mu m$, which is smaller than the cholesteric pitch [100], and the confinement was 'pseudo 2D'. This was confirmed by three dimensional LSCM scans. The other channel dimensions were $h_c = 500\mu m$ and $h_w = 750\mu m$ or $1125\mu m$ (see Fig. 7.2(c)).

The structured microfluidic channels were filled by capillary action. Directly before filling

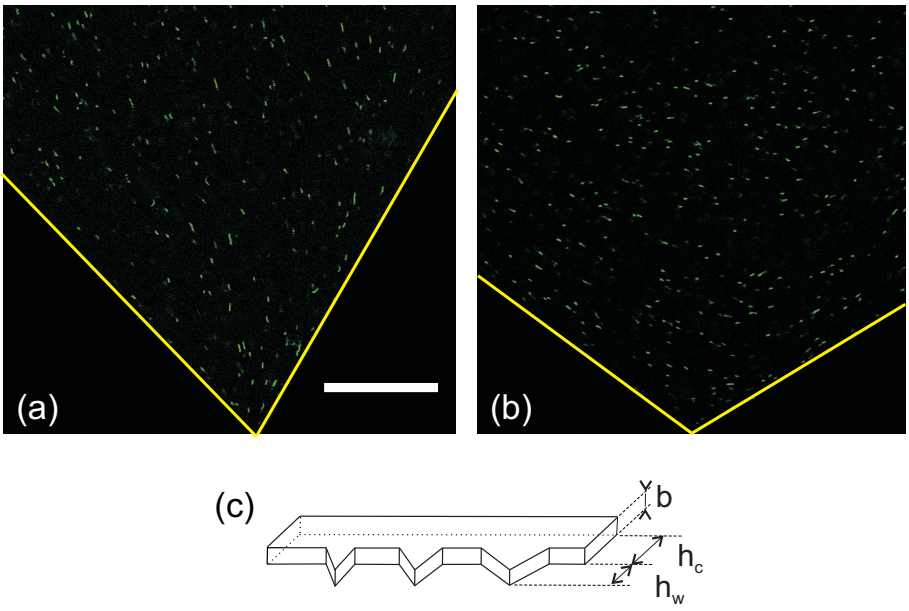

Figure 7.2: (a) and (b) Laser Scanning Confocal Microscopy images of the *fd* virus, showing a splay (a) and a bend deformation (b). Scale bar is $25\mu m$. (c) Geometry of microfluidic channel.

the channels were plasma cleaned, which changes the hydrophilicity of the channels and offers a way to control the speed of filling. This enabled the initial conditions of the experiments to be set by the coupling between the nematic director and flow [101]: low filling speeds created an initial disordered configuration, while high filling speeds resulted in the rods immediately adopting metastable bend deformations, which only slowly reached the equilibrium configuration. The channels were slowly filled and, from a disordered configuration, the equilibrium was reached within a couple of hours.

The diffusion of the particles close to the walls was followed using fluorescence microscopy and it was observed that the particles pointed along the walls. This is indicative of degenerate, planar, strong anchoring. No particles were seen sticking to the walls.

By varying the wedge opening angle θ_w splay and bend configurations were observed. Fig. 7.2(a) and 7.2(b) display confocal microscopy images of the fluorescently labeled rods in the wedge, showing a splay and a bend deformation respectively. When the images were analysed the director field was constructed, as shown in Fig. 7.3(a) for a range of wedge angles θ_w. Focusing on the tip of the wedge, up to a height $\sim h_w/3$, virtually defect free splay deformations were observed below 70° and bend deformations above 80°.

Fig. 7.3(b) shows results from lattice Boltzmann simulations, obtained using $K_1 = K_3$,

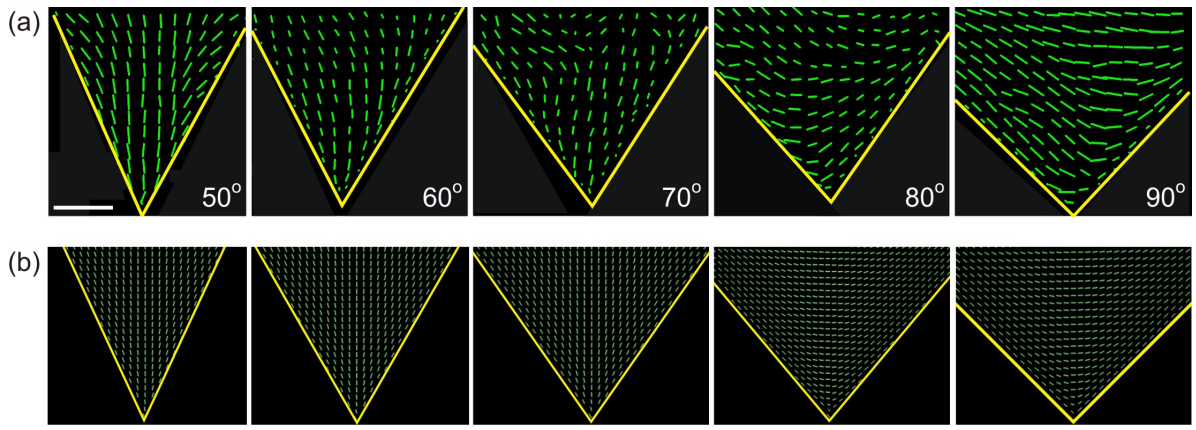

Figure 7.3: Director field in the wedge for varying wedge angle $\theta_w = 50°$ - $90°$. (a) Director fields from experiments calculated by averaging over 10 images. The length of the rods indicate the degree of ordering. Scale bar is $50\mu m$. (b) Director field from lattice Boltzmann simulations. In both cases the transition from a splay to a bend configuration occurs between $\theta_w = 70°$ - $80°$.

in close correspondence with the experiments. In the subsequent sections we will study the director configurations in greater detail using lattice Boltzmann simulations.

7.2 Lattice Boltzmann simulations - Nematic in a Wedge

7.2.1 Simulation set-up

We consider a nematic liquid crystal, consisting of rod-like molecules, that is confined in a wedge of opening angle θ_w and height h_w, as shown in Fig. 7.1(a). The wedge is connected by a main channel of height h_c. Periodic boundary conditions are imposed in the x and y directions. The possible configurations for the director field $\mathbf{n}$ in this geometry are: a) pure splay originating from the tip of the wedge and b) a configuration that comprises both bend and splay elastic deformations. Through the course of this chapter we will refer to the former as the splay configuration and the latter as the bend configuration. Schematic illustrations of these configurations are shown in Figs. 7.1(b) and 7.1(c).

Next, we briefly explain the parameter selection process. Table 7.1 summarises all the parameters relevant to the simulations, as well as any quantities derived from these that will be regularly used throughout the following sections. First of all, the simulation lattice spacing Δx is set to unity, while for stability reasons related with the finite difference method that we use to solve the evolution of the $\mathbf{Q}$ tensor, the timestep $\Delta t = 0.2$. The density of the nematic

Table 7.1: List of the parameters relevant to the simulations on nematic liquid crystals confined in wedge structured geometries.

Description	Symbol	Dimension	Typical Value
Wedge opening angle	θ_w	Degrees	$20^\circ - 100^\circ$
Main channel height	h_c	Length	$3 - 65$
Wedge height	h_w	Length	100
Simulation lattice spacing	Δx	Length	1.0
Simulation timestep	Δt	Time	0.2
Density of fluid	ρ	Mass/Volume	1.0
Frank elastic constants	$K_i (i = 1, 2, 3)$	Force	$10^{-2} - 10^{0}$
Elastic constants	$L_i (i = 1, 2, 3)$	Force	$10^{-2} - 10^{-1}$
Nematic degree of order	q	–	0.8
Reduced temperature/ concentration	$\gamma_i (i = 1, 2, 3)$	–	$\gamma_1 = 4.5$, $\gamma_2 = 5.0$, $\gamma_3 = 2.6$
Free energy parameter	A_0	Energy/Volume	$10^{-2} - 10^{-1}$
Nematic correlation length	ξ_N	Length	$0.5 - 1.0$
Extrapolation length	ξ_s	Length	$\ll 1$
Uniform Anchoring strength	W	Energy/Area	$10^{-1} - 10^{0}$
Degenerate Anchoring strength	W_1^{deg}, W_2^{deg}	Energy/Area	$10^{-1} - 10^{0}$
Rotational diffusion coefficient	Γ_H	Time×Length / Mass	1.0
Isotropic pressure	P_0	Mass / (Length×Time^2)	10^{-1}

liquid crystal is fixed to $\rho = 1$. Then we choose the value for K_1, with typical values of order $K_1 \sim 10^{-2} - 10^{0}$. The value for K_3 is set according to the desired ratio K_1/K_3. Usually we also set $K_1 = K_2$, but this does not affect our results, since the bend splay transition depends solely on the ratio K_1/K_3. Then using Eq. (6.21), that maps the Frank-Oseen elastic constants ($K's$) to the ones within a Landau-de Gennes approximation ($L's$), we evaluate the appropriate values for the $L's$ to be used in the simulations. To this end we also need the nematic degree of order q, which we choose to be $q = 0.8$ as in the experiments. In order to achieve this, we choose the appropriate value for γ in Eq. (6.11), or alternatively we can choose values γ_1, γ_2 and γ_3 for the square, cubic and quartic terms in Eq. (6.11) respectively. We mainly use the values $\gamma_1 = 4.5$, $\gamma_2 = 5.0$ and $\gamma_3 = 2.6$. Then we fix the value for the nematic correlation length ξ_N, which sets the lengthscale for variations in the nematic degree of order q, and also sets the size of the defect core. We choose this to be $\xi_N = 0.5$ and 1.0, which leads to a lengthscale of $\sim$ 4-7Δx between the defect core and the bulk, where the bulk nematic degree of order $q = 0.8$ is recovered. With the value of ξ_N fixed, the value for the free energy parameter A_0 in Eq. (6.11) is determined using Eq. (6.46). Typical values for $A_0 \sim 10^{-2} - 10^{-1}$. The rotational diffusion coefficient is fixed to $\Gamma_H = 1.0$. This choice is arbitrary and does not affect the results

presented in this chapter, since we are only interested in the final equilibrium configuration at each wedge angle θ_w, and not how the system approaches equilibrium.

Finally, to represent the interactions of the liquid crystal molecules with the solid walls we use strong planar anchoring for the majority of the simulations reported in this chapter, mirroring the experimental situation. This is achieved by fixing the value of the $\mathbf{Q}$ tensor on the solid nodes neighbouring the boundary, in the preferred orientation $\mathbf{n^0}$ imposed by the solid walls, according to $Q_{\alpha\beta} = q_0 \left(3n^0_\alpha n^0_\beta - \delta_{\alpha\beta}\right)/2$, where the nematic degree of order q_0 is equal to the nematic degree of order in the bulk. This effectively corresponds to setting the anchoring strength $W \to \infty$. Nevertheless, we still need to assign a value for the anchoring strength W. We use values such that the extrapolation length $\xi_s = K/W \ll 1$, with typical values in the range $W \sim 10^0 - 10^1$. The same applies for the case of planar degenerate anchoring (anchoring strengths $W_1^{deg} = W_2^{deg}$) that we shall use in section 7.2.3.4. Note that, the limit of weak anchoring does not present any significant interest, since in this limit the liquid crystal would just adopt a uniform alignment configuration. Nevertheless we shall briefly examine the effect of anchoring in section 7.2.3.3.

The preceding parameters are in simulation units, but can be straightforwardly related to a set of physical units. First, we match the simulation system size to the liquid crystal experimental system size. Second, we fix the isotropic pressure $P_0 = \rho T - \frac{L}{2}(\partial_\alpha Q_{\beta\gamma})^2$ to a physical value, which can be taken to be 1 atm. Third, the rotational viscosity γ^{rot} [2] is related to the parameter Γ_H via $\gamma^{rot} = 2q^2/\Gamma_H$. Once the mass, length and time-scales are specified, all simulation parameters can be related to experimental quantities.

7.2.2 Elastic energy of the wedge

A nematic liquid crystal confined in the wedge-structured geometry, shown in Fig. 7.1(a), will evolve towards the global minimum of the free energy. This, however, may not be the one that corresponds to the minimum of the free energy of just the wedge region. Here, we first examine the wedge part of the channel and evaluate the threshold of the transition from a splay to bend configuration for various ratios of the elastic constants. This will enable us in the subsequent sections to compare the effect of the whole geometry, main channel and wedge, on the minimum free energy configuration and the splay-bend transition.

The director field $\mathbf{n}$ is restricted in the x-z plane, in which case the elastic free energy

density associated with the system is

$$f_{el} = \frac{K_1}{2} (\nabla \cdot \mathbf{n})^2 + \frac{K_3}{2} (\nabla \times \mathbf{n})^2 \ . \tag{7.1}$$

By assuming a certain profile for the director field $\mathbf{n}$ for the two possible configurations in the wedge, we can analytically evaluate the elastic free energy associated with each one. For the splay configuration (see Fig. 7.1(b)) the director is

$$\mathbf{n} = \hat{\mathbf{r}} \ . \tag{7.2}$$

Therefore, using polar coordinates, the elastic free energy for the splay configuration is

$$\begin{aligned} \mathcal{F}_{el}^{s} &= \int \frac{K_1}{2} (\nabla \cdot \mathbf{n})^2 d\mathbf{r} \\ &= \int_{\frac{\pi}{2}-\frac{\theta_w}{2}}^{\frac{\pi}{2}+\frac{\theta_w}{2}} \int_{r_c}^{r_a} \frac{K_1}{2} \left(\frac{1}{r}\right)^2 r dr d\theta \\ &= \frac{1}{2} \theta_w K_1 \ln\left(\frac{r_a}{r_c}\right) \ , \end{aligned} \tag{7.3}$$

where small and large lengthscale cutoffs r_c, r_a, respectively, have been introduced to avoid the divergence of the integral. The large lengthscale cutoff r_a is needed to keep the wedge geometry to a finite size, whereas the small cutoff r_c is introduced to exclude the region of the defect core formed at the tip of the wedge.

For the bend configuration (see Fig. 7.1(c)) we can assume a director field that consists of hyperbolae [94]

$$\frac{x^2}{a^2} - \frac{z^2}{b^2} = -c^2 \ , \tag{7.4}$$

where bc is the intersection with the z-axis, and the tangent to the hyperbolae has a limiting value $\pm b/a$. The director field, then, is given by

$$\mathbf{n} = (n_x, n_z) = \left(\frac{z}{\sqrt{z^2 + x^2 \cot^4(\frac{\theta_w}{2})}}, \frac{x \cot^2(\frac{\theta_w}{2})}{\sqrt{z^2 + x^2 \cot^4(\frac{\theta_w}{2})}} \right) . \tag{7.5}$$

The elastic free energy associated with the bend configuration is

$$\begin{aligned}\mathcal{F}_{el}^{b} &= \int \left(\frac{K_1}{2} (\nabla \cdot \mathbf{n})^2 + \frac{K_3}{2} (\nabla \times \mathbf{n})^2 \right) d\mathbf{r} \\ &= \int \left(\frac{K_1}{2} f_{el}^{b,1} + \frac{K_3}{2} f_{el}^{b,3} \right) d\mathbf{r} \,, \end{aligned} \tag{7.6}$$

where

$$f_{el}^{b,1} = \frac{x^2 z^2 \cot^4(\frac{\theta_w}{2})}{\sin^4(\frac{\theta_w}{2}) \left[z^2 + x^2 \cot^4\left(\frac{\theta_w}{2}\right) \right]^3} \,, \tag{7.7}$$

$$f_{el}^{b,3} = \frac{\cot^4(\frac{\theta_w}{2}) \left[z^2 - x^2 \cot^4\left(\frac{\theta_w}{2}\right) \right]^2}{\left[z^2 + x^2 \cot^4\left(\frac{\theta_w}{2}\right) \right]^3} \,. \tag{7.8}$$

Using polar coordinates we evaluate the two contributions to the free energy

$$\begin{aligned}\mathcal{F}_{el}^{b,1} &= \int_{\frac{\pi}{2}-\frac{\theta_w}{2}}^{\frac{\pi}{2}+\frac{\theta_w}{2}} \int_{r_c}^{r_a} \frac{K_1}{2} f_{el}^{b,1} r dr d\theta \\ &= K_1 \frac{2\pi - 2\theta_w + \sin(2\theta_w)}{8\sin^2(\theta_w)} \ln\left(\frac{r_a}{r_c}\right), \end{aligned} \tag{7.9}$$

$$\begin{aligned}\mathcal{F}_{el}^{b,3} &= \int_{\frac{\pi}{2}-\frac{\theta_w}{2}}^{\frac{\pi}{2}+\frac{\theta_w}{2}} \int_{r_c}^{r_a} \frac{K_3}{2} f_{el}^{b,3} r dr d\theta \\ &= K_3 \frac{(2\pi - 2\theta_w)(2 + \cos(2\theta_w)) + 3\sin(2\theta_w)}{8\sin^2(\theta_w)} \ln\left(\frac{r_a}{r_c}\right). \end{aligned} \tag{7.10}$$

Therefore, the total free energy for the bend configuration is

$$\mathcal{F}_{el}^{b} = \left(K_1 \frac{2\pi - 2\theta_w + \sin(2\theta_w)}{8\sin^2(\theta_w)} + K_3 \frac{(2\pi - 2\theta_w)(2 + \cos(2\theta_w)) + 3\sin(2\theta_w)}{8\sin^2(\theta_w)} \right) \ln\left(\frac{r_a}{r_c}\right). \tag{7.11}$$

We can extract the threshold between the two configurations, for varying ratios of the elastic constants K_1 and K_3, by equating the expressions Eq. (7.3) and Eq. (7.11). This leads to [94]

$$\frac{K_1}{K_3} = \frac{(2\theta_w - 2\pi)(2 + \cos(2\theta_w)) - 3\sin(2\theta_w)}{-4\theta_w + 2\pi + 2\theta_w \cos(2\theta_w) + \sin(2\theta_w)} \,. \tag{7.12}$$

7.2.2.1 Results from lattice Boltzmann simulations

In order to verify the threshold prediction, Eq. (7.12), we ran a set of simulations with different ratios K_1/K_3 in channels with $r_w = h_c/h_w = 0.65$. This acts as a test for our simulations. In particular we examined the ratios $K_1/K_3 = 8.0$, 4.5, 2.1 and 1.0. We fixed the value for $K_1 = 1 \times 10^{-1}$ and the value for K_3 was set according to the ratio K_1/K_3. Numerical values for the other parameters used were $A_0 = 3 \times 10^{-2}$, $\gamma_1 = 4.5$, $\gamma_2 = 5.0$, $\gamma_3 = 2.6$, $\Gamma_H = 1$, while the nematic correlation length was set to $\xi_N \sim 0.5$. The choice of $\gamma's$ lead to a nematic degree of order in the bulk $q_0 \sim 0.8$, as in the experiments.

By making a suitable choice of the initial conditions in the channel, we obtained the two different configurations at each opening angle θ_w. The first initial condition (**I.c.1**) we considered, corresponded to a situation where the main channel, with height h_c, was filled with a liquid crystal with a mean orientation along the x-axis. We introduced a, uniformly distributed, random noise such that the orientation of the liquid crystal molecules lay in the interval $[-5°, 5°]$ from the x-axis. The nematic degree of order was uniform and set to $q = q_0$. The wedge was then set to have nematic degree of order $q = 0$, which corresponds to a disordered liquid crystal. This situation is similar to the one used in experiments with *fd* virus. Our simulations revealed that this initial condition favors a bend configuration in the wedge, due to the horizontal initial configuration in the main channel.

The second initial condition (**I.c.2**) we considered was one with the nematic degree of order set to $q = 0$ in the whole channel. Our results indicated that this favors, at least in the initial stages, splay that extends even beyond the wedge region into the main channel. This is probably due to the transition process from a disordered state to an ordered state, that is guided and dictated by the strong anchoring imposed by the side walls.

Fig. 7.4 shows the configurations obtained from two simulations starting from these initial conditions for $K_1/K_3 = 4.5$ and opening angle $\theta_w = 80°$. Starting from **I.c.1** resulted in a bend deformation, while starting from **I.c.2** led to splay.

The threshold θ_{cr} for the splay-bend transition, at each ratio of K_1/K_3, is extracted by considering only a circular sector of the wedge of radius r_a, as shown in Fig. 7.4, and comparing the corresponding elastic free energies, $\mathcal{F}^s_{el}$ and $\mathcal{F}^b_{el}$, of the two possible configurations at each opening angle θ_w. Care is taken to consider the radius r_a for the circular sector such that

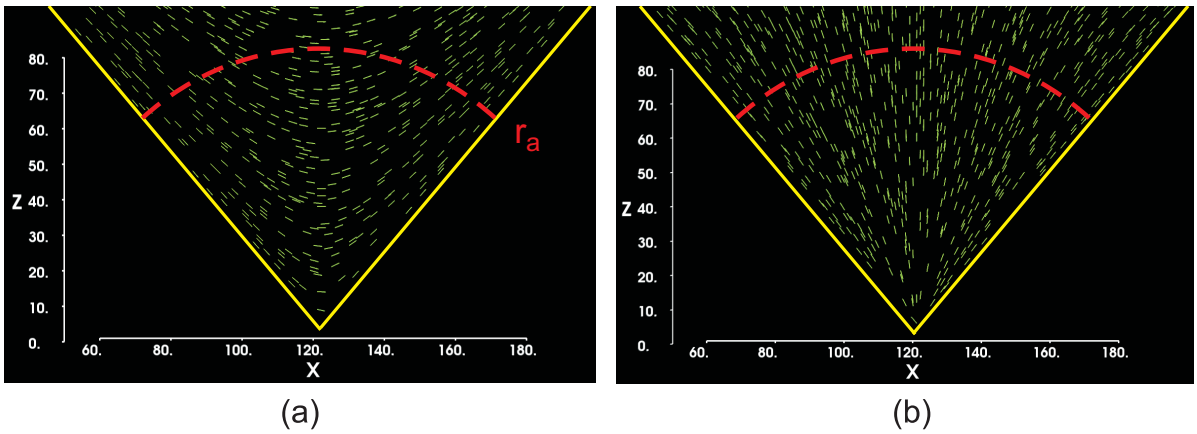

Figure 7.4: Configurations in a wedge of opening angle $\theta_w = 80°$ for ratio of elastic constants $K_1/K_3 = 4.5$. (a) Starting from initial conditions **I.c.1**, as explained in the text, leads to a bend configuration. (b) Starting from initial conditions **I.c.2**, leads to a splay configuration. By comparing the elastic free energies of the circular sector of radius r_a, $\mathcal{F}^b_{el}$ (a) and $\mathcal{F}^s_{el}$ (b), and varying the wedge angle θ_w we extract the threshold of the splay-bend transition.

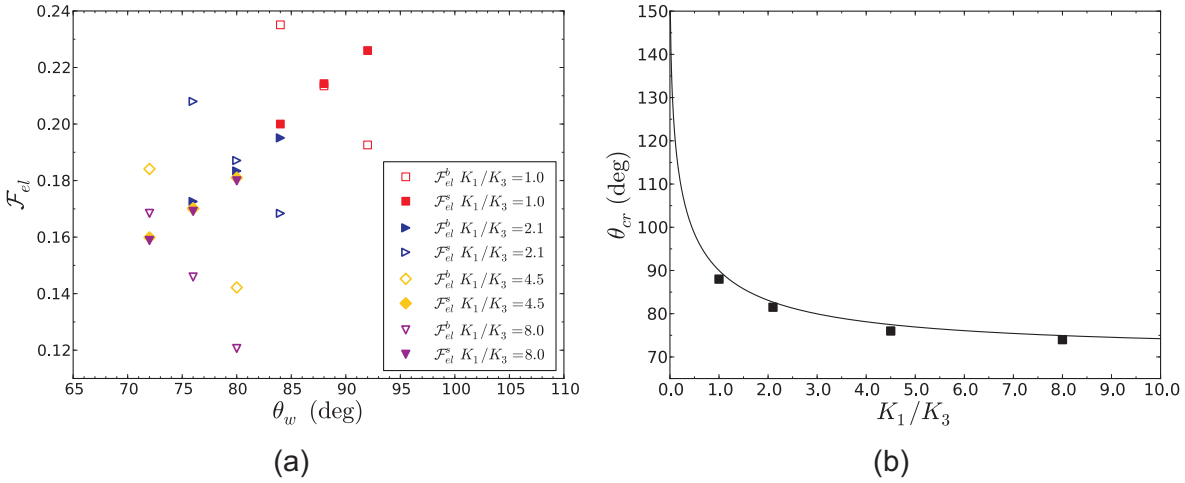

Figure 7.5: (a) Elastic free energies $\mathcal{F}_{el}$ of splay ($\mathcal{F}^s_{el}$) and bend ($\mathcal{F}^b_{el}$) configurations in the circular sector with r_a, as a function of the wedge angle θ_w. (b) Threshold θ_{cr} for the transition from a splay to bend configuration as a function of the ratio of elastic constants K_1/K_3. Only the free energy of the circular sector region of the wedge is considered. The solid line corresponds to the predicted threshold, Eq. (7.12), whereas squares (■) show results from lattice Boltzmann simulations.

defects and boundary conditions imposed by the main channel do not affect the configuration in the circular sector. As expected $\mathcal{F}^s_{el}$ decreases with decreasing θ_w, while $\mathcal{F}^b_{el}$ increases. The threshold θ_{cr} is then located at the intersection of these energies. The elastic free energies of the two possible configurations as a function of wedge angle θ_w are shown in Fig. 7.5(a), while

our results for the threshold θ_{cr} for the splay-bend transition are plotted in Fig. 7.5(b). The predicted threshold θ_{cr}, from Eq. (7.12), is plotted with the solid line. Very good agreement is found, which indicates that the initial assumption, Eq. (7.5), for the bend director field is a good approximation.

7.2.3 Global minimum of the Free Energy

Next we turn our attention in the complete channel geometry and investigate how the main channel affects the transition between the splay and bend configurations. We shall first examine systems with ratio of elastic constants $K_1/K_3 = 1$.

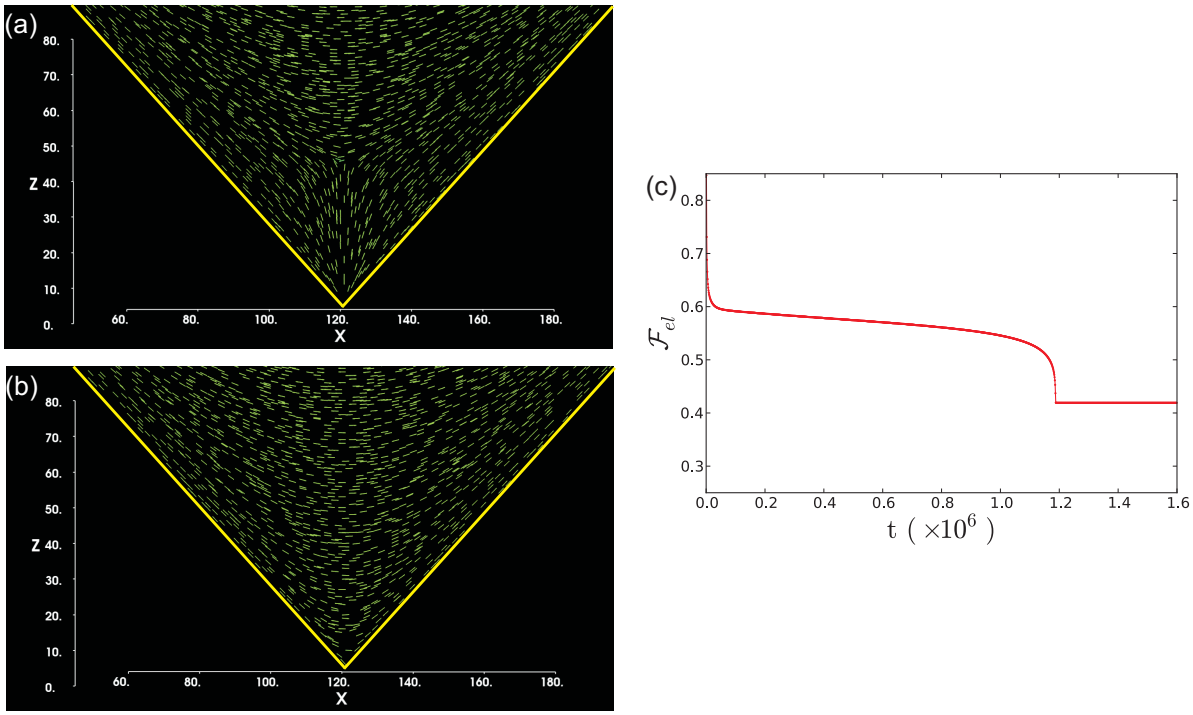

Figure 7.6: Snapshots at different times of a system with $K_1/K_3 = 1$ and $\theta_w = 84^\circ < \theta_{cr}$. (a) At $t = 1.0 \times 10^6$ a splay configuration originates from the tip of the wedge, while a bend configuration is located at larger z. (b) The bend region expands towards the tip of the wedge until eventually only a bend configuration is observed in the whole wedge at $t = 1.6 \times 10^6$. (c) The elastic free energy $\mathcal{F}_{el}$ of the system as a function of time. $\mathcal{F}_{el}$ drops significantly at $t \sim 1.2 \times 10^6$ as the wedge reaches a bend configuration. Even though the free energy of the wedge is lower for a splay configuration, the system evolves to expel the defect that is energetically costly.

Fig. 7.6 shows snapshots at different times of a system with wedge angle $\theta_w = 84^\circ$, and starting from **I.c.1**. At this opening angle we expect the final equilibrium configuration to

correspond to a splay configuration. As can be seen from Fig. 7.6(a), which corresponds to time $t = 1.0 \times 10^6$ in lattice units, splay originates from the tip of the wedge, while a bend region is located at higher z. A defect of strength $s = -1/2$ is formed, where splay and bend meet. Gradually, the defect moves downwards until eventually it reaches the tip of the wedge at $t \sim 1.2 \times 10^6$. This is accompanied by a considerable drop in the elastic free energy $\mathcal{F}_{el}$ of the system, which is evident from Fig. 7.6(c) that shows the time variation of $\mathcal{F}_{el}$. The system evolves towards the global minimum of the free energy of the whole channel and it is affected by the presence of the main channel with the horizontal nematic configuration. Therefore, it reduces its elastic energy significantly by expelling the defect and adopting a bend configuration in the wedge (see Fig. 7.6(b)). As a result bend configurations are stable at angles below the threshold θ_{cr} found in section 7.2.2.1, which was evaluated based on the free energy of just the wedge.

By decreasing the wedge angle θ_w further, we encounter situations where a splay region is stable, while a bend region is located at larger z. Inevitably, this involves the formation of a defect, as can be seen from Fig. 7.7, that shows the equilibrium configuration for a wedge of $\theta_w = 70°$. The defect of strength $s = -1/2$ is located at a height z = z_d measured from the tip of the wedge.

A number of simulations were carried out, varying the opening angle and measuring the relative height of the defect within the wedge, defined as

$$\tilde{h} = z_d/h_w. \tag{7.13}$$

Our aim is to examine the impact of the geometry on the defect position, and therefore, we also vary the height of the main channel. These results will be presented in the following section.

7.2.3.1 Effect of the main channel

Here we investigate the effect of the channel geometry on the defect position. In particular, we examine three different geometries, with ratios of channel height to wedge height $r_w \equiv h_c/h_w$=0.03, 0.21 and 0.65. For the simulations reported in this section we keep the correlation length $\xi_N \sim 0.5$, while the ratio of elastic constants is fixed to $K_1/K_3 = 1$.

In order to establish the absolute minimum of the elastic free energy of the whole geometry,

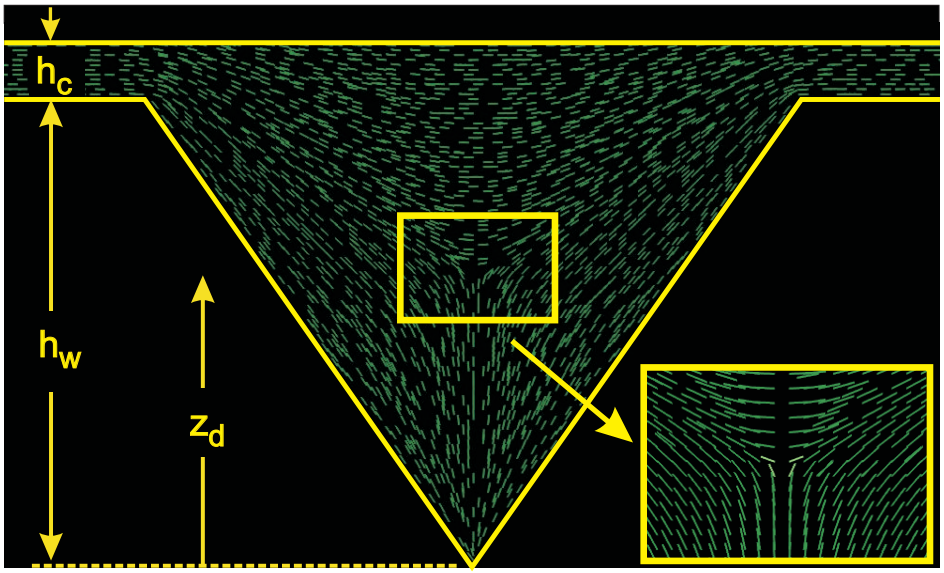

Figure 7.7: Equilibrium configuration for a wedge of opening angle $\theta_w = 70°$ and height h_w. The splay configuration originates from the tip of the wedge. A defect of strength $s = -1/2$ is formed in the bulk of the wedge at a height $z = z_d$ from the tip of the wedge, where the splay configuration meets the bend configuration imposed by the main channel of height h_c.

and the relative position of the defect that corresponds to this minimum, we compared results from simulations with and without dynamics, as well as with varying the initial configuration of the director field **n** in the channel. This was done to check that the system did not become stuck in a metastable state. Moreover, two initial conditions were chosen such that, in the case of a defect forming, the defect approaches its final position following a different path. The first one corresponded to **I.c.1**, introduced in section 7.2.2.1, which leads to a defect initially formed at high $\tilde{h}$ that descends towards its final position, as in the situation of Fig. 7.6. The second initial condition considered (**I.c.3**) was one with a mean horizontal director configuration in the whole channel geometry. This favored a bend initial configuration and, in the case of a defect forming, it approached its final position from below by rising in the wedge.

Simulations without dynamics were carried out by setting the velocity field to zero. An important remark is that, although, in principle we could just run simulations without dynamics to obtain the equilibrium configuration with the minimum free energy, simulations with dynamics proved helpful with overcoming lattice pinning effects. In the simulations with dynamics the defect position was slightly higher than in the ones without dynamics, but nevertheless, the difference in the elastic energies was less than 1%.

Our results for the defect position $\tilde{h}$ versus opening angle θ_w are plotted in Fig. 7.8. Firstly,

we observe that the splay configuration is suppressed, for all geometries examined, down to opening angles $\theta_w \sim 72°$. This is much lower than the wedge threshold of $\theta_{cr} \sim 88°$ found in section 7.2.2.1 for $K_1 = K_3$. So, a pure bend configuration is the minimum energy configuration obtained for a range of opening angles $\theta_w \geq 72°$. At $\theta_w \sim 70°$ we observe a sudden jump in the defect position $\tilde{h}$. This corresponds to the angle at which the energy cost due to the presence of the defect is compensated by the energy gain of the splay configuration. As the opening angle θ_w decreases further, the relative height $\tilde{h}$ of the defect increases, with a limiting asymptotic value of $\tilde{h} \to 1$ for small θ_w, i.e. the defect lies at the border between the wedge and the main channel.

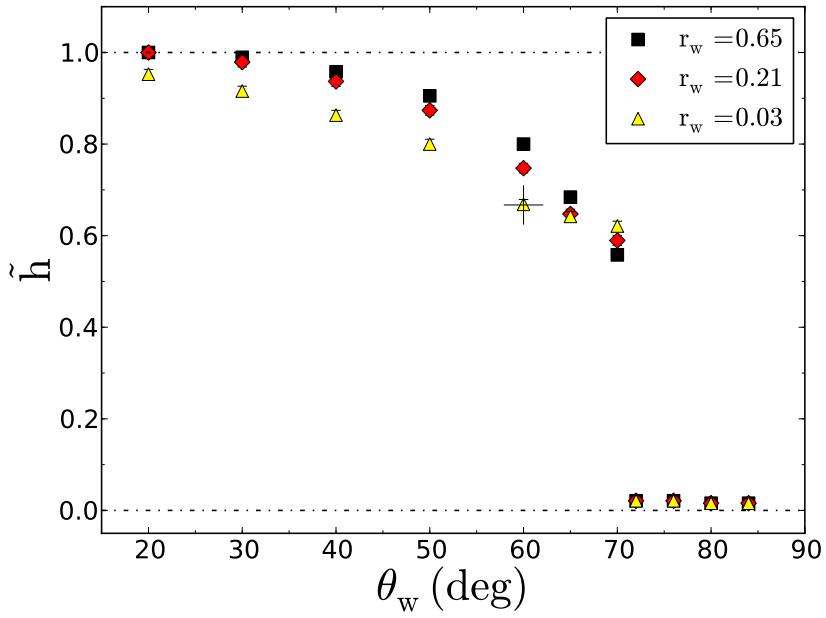

Figure 7.8: The relative position of defect in the wedge $\tilde{h}$ as a function of the wedge opening angle θ_w for varying channel geometry. r_w gives the ratio of the height of the main channel h_c to the height of the wedge h_w. The cross denotes the position $\tilde{h} = 0.667$ at $\theta_w = 60°$, which is the position of the orthocentre of an equilateral triangle and the expected position of the defect in the case of $r_w \to 0$.

Furthermore, when examining simulations at fixed θ_w but varying ratio r_w, we can distinguish two regimes in Fig. 7.8. For angles $65° < \theta_w < 72°$, as the main channel height h_c decreases, and consequently r_w decreases, the defect moves upwards within the wedge. Keeping in mind that we are in a regime of opening angles $\theta_w < \theta_{cr}$, and therefore in the splay regime, the higher defect position for smaller r_w is a consequence of the fact that the wedge plays a

more dominant role in determining the minimum of the free energy of the whole geometry. However, this trend does not continue for angles $\theta_w \leq 65°$. This is due to the fact that, as the defect rises within the wedge, at a certain point it starts to feel the presence of the upper wall, which due to the strong anchoring imposing a horizontal orientation of the liquid crystal molecules. This in turn has the reversed effect on the defect position, by forcing the defect to be located at a lower $\tilde{h}$ for smaller r_w.

It is noteworthy that one way of testing the validity of our results for the defect position is to check $\tilde{h}$ in the case of $r_w \to 0$ and opening angle $\theta_w = 60°$. In this limiting case, we expect the defect to be located at the orthocentre of the wedge, which is at $\tilde{h} = 0.667$. For the simulation results plotted in Fig. 7.8 we found $\tilde{h} = 0.668$ for $r_w = 0.03$.

7.2.3.2 Effect of the nematic correlation length

We next examine the effect of the nematic correlation length ξ_N on the director $\mathbf{n}$ configuration in the wedge. We ran simulations increasing the nematic correlation length to $\xi_N \sim 1.0$, using the geometry with $r_w = 0.21$ and keeping the ratio of elastic constants fixed to $K_1/K_3 = 1$.

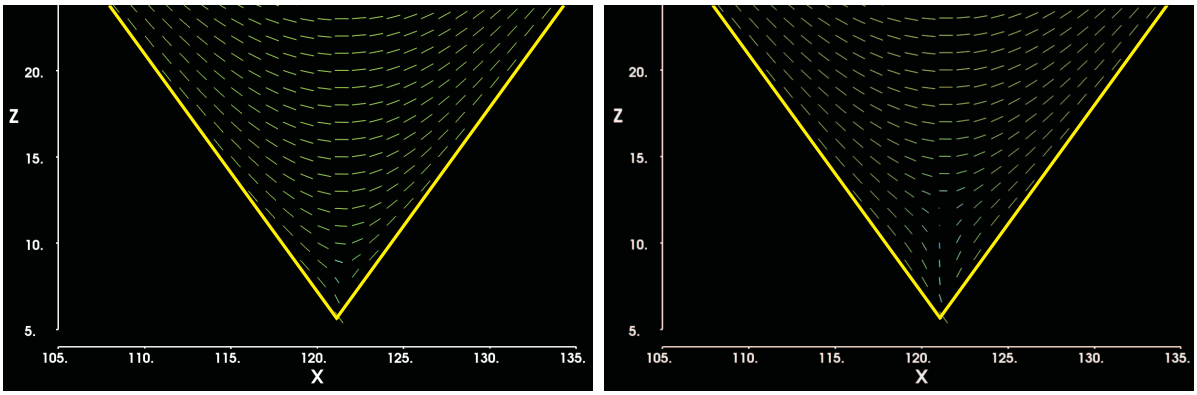

Figure 7.9: Equilibrium configurations for a wedge of opening angle $\theta_w = 72°$ and nematic correlation length: (a) $\xi_N \sim 0.5$ and (b) $\xi_N \sim 1$.

A first remark is that, for the case of $\xi_N \sim 1.0$, simulations revealed that the final configuration is independent of the initial conditions in the wedge, in contrast to the behaviour observed for $\xi_N \sim 0.5$. This indicates that metastability effects are now becoming very weak.

For $\xi_N \sim 0.5$, we saw in section 7.2.3.1 that splay configurations are stable for $\theta_w \leq 70°$. Fig. 7.9 reveals that the onset of stable splay configurations commences at a slightly larger

angle θ_w for $\xi_N \sim 1.0$ than for $\xi_N \sim 0.5$. This can be explained in light of the higher energy cost of the defect in the case of $\xi_N \sim 1.0$. Increasing the nematic correlation length[1] means that the defect becomes larger, and, therefore, the defect is energetically more costly. As a consequence, a larger splay region is needed to balance the extra energy cost of the defect, since we are at angles θ_w for which splay is energetically more favorable than bend.

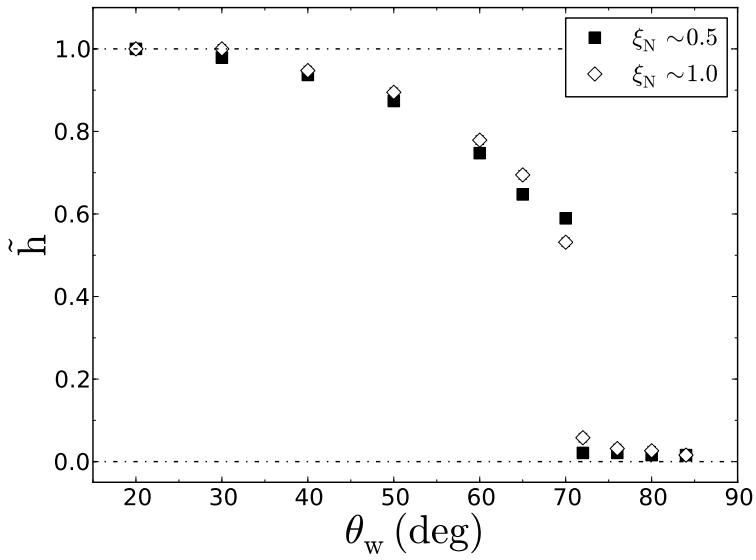

Figure 7.10: Relative position of the defect in the wedge $\tilde{h}$ as a function of the wedge opening angle θ_w for varying nematic correlation length ξ_N. Results from simulations with $r_w = 0.21$ and $K_1 = K_3$.

For this reason the defect is located at a higher position within the wedge for $\xi_N \sim 1.0$. This is evident from Fig. 7.10 that shows a plot of our results for the relative position of the defect $\tilde{h}$ as a function of the wedge angle θ_w for nematic correlation lengths $\xi_N \sim 0.5$ and $\xi_N \sim 1.0$. Nevertheless, in both cases the jump in the defect position commences around $\theta_w \sim 70^\circ$, although it is not so steep for $\xi_N \sim 1.0$.

7.2.3.3 Effect of the anchoring strength

In sections 7.2.2 and 7.2.3 we assumed strong planar anchoring imposed by the side and top walls. The choice of strong anchoring was made to be consistent with recent experiments with rodlike *fd* virus in microchannels.

[1] To be more precise, the relevant parameter here is the ratio of the nematic correlation length to the height of the wedge ξ_N/h_w.

In this section we check the effect of the anchoring strength on the wedge configuration. We consider systems with $r_w = 0.21$, $\xi_N \sim 1.0$, elastic constants $K_1 = K_3 = K = 0.1$, and examine anchoring strengths $W = 10^{-2}$ and $W = 10^{-4}$, which correspond to intermediate and weak anchoring respectively. The strength of the surface anchoring can be interpreted in terms of the extrapolation length $\xi_s = K/W$ [2], which measures the relative strength of elasticity with respect to surface anchoring. Hence, strong anchoring corresponds to the limit $\xi_s \to 0$.

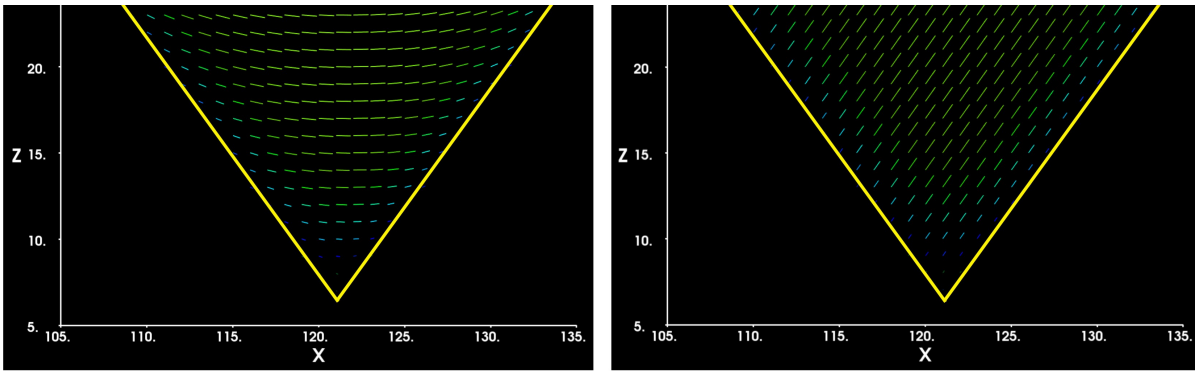

Figure 7.11: Equilibrium configurations for a wedge of opening angle $\theta_w = 72°$ and anchoring strengths: (a) $W = 10^{-2}$ and (b) $W = 10^{-4}$. The smaller vectors near the walls indicate a lower nematic degree of order at the solid surfaces. Results are from simulations with elastic constants $K_3 = K_1$, $\xi_N \sim 1.0$ and geometry $r_w = 0.21$.

Fig. 7.11 shows the director field in the region of the wedge tip for an opening angle of $\theta_w = 72°$ for the anchoring strengths examined. As the anchoring strength is reduced, the less important the walls become in determining the director configuration in the wedge. For an anchoring strength $W = 10^{-2}$ ($\xi_s = 10$) there is still a bend state and we encounter a bend-splay transition. We can clearly see, however, that the liquid crystal molecules do not align fully with the side walls. It looks more like a horizontal nematic, that just bends slightly at the side walls. For the strong anchoring case (see Fig. 7.9(b)), by contrast, perfect alignment with the side walls was observed. By decreasing the anchoring strength further to $W = 10^{-4}$ ($\xi_s = 1 \times 10^3$), the walls have no effect on the liquid crystal system, which just adopts a nematic configuration with almost no elastic deformations as can be seen in Fig. 7.11(b). This is persistent in the whole geometry and for all opening angles θ_w. We note that the main channel can not impose a horizontal configuration in the wedge due to the weak anchoring and because there is more diagonal surface than horizontal. In the limit $W \to 0$ all nematic

directions should be equally favorable.

Moreover, for the anchoring strengths examined here, we observed a decrease in the nematic degree of order at the solid boundaries, which is indicative of weak anchoring [102–107]. This *surface melting* was not observed for strong anchoring and is illustrated in Fig. 7.11 by the smaller vectors near the solid surfaces.

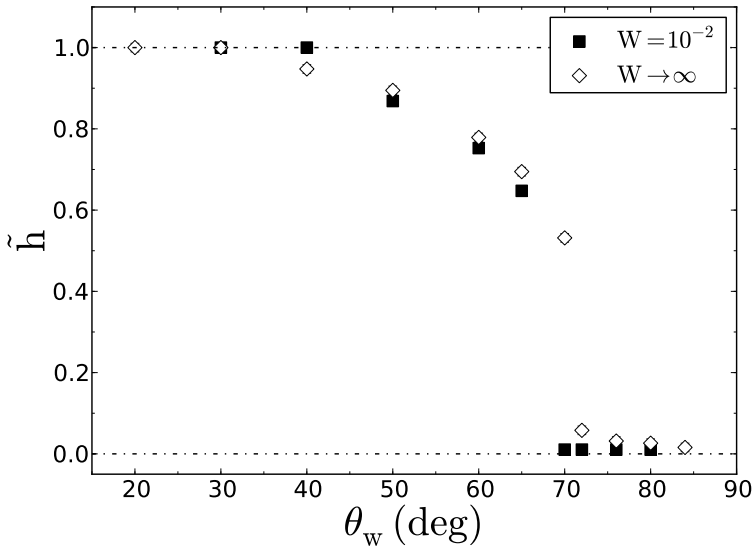

Figure 7.12: Relative position of defect in the wedge $\tilde{h}$ as a function of the wedge opening angle θ_w for varying anchoring strength W. Results are from simulations with elastic constants $K_3 = K_1$, $\xi_N \sim 1.0$ and geometry $r_w = 0.21$. Surface anchoring $W = 10^{-2}$ corresponds to extrapolation length $\xi_s = 10$, while the strong anchoring to $\xi_s \to 0$.

Examining now the relative defect position $\tilde{h}$, shown in Fig. 7.12, we found that the bend-splay transition is shifted to smaller angles $\theta_w \sim 65° - 70°$ for the case of intermediate anchoring $W = 10^{-2}$. The results for strong anchoring are also plotted for comparison. This is expected since there is no longer complete alignment with the side walls and the anchoring does not favor splay to such an extent.

Another important remark is that when the defect reaches the main channel ($\tilde{h} = 1$) for angles $\theta_w \leq 40°$, it is not located symmetrically at the top of the wedge but rather, as shown in Fig. 7.13, moves towards one of the apexes of the wedge. This occurs now, in contrast to the strong anchoring case, due to the lower penalty cost associated with deviations from the preferred orientation at the boundary and because the system significantly reduces its elastic energy by expelling the defect. Clearly the location of this new transition depends on the

relative importance of elasticity over surface anchoring, i.e. on the extrapolation length ξ_s.

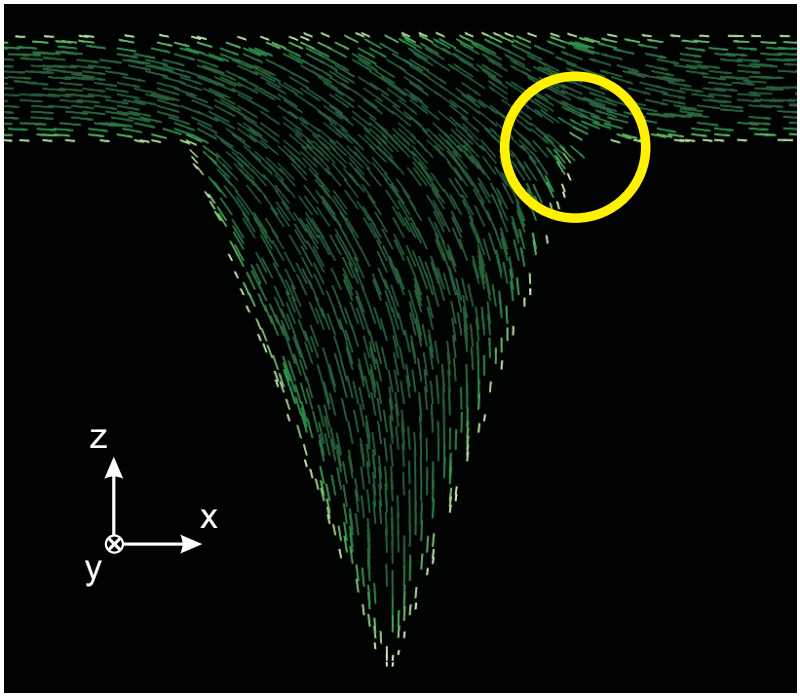

Figure 7.13: Equilibrium configuration in a wedge of $\theta_w = 40°$, with elastic constants $K_3 = K_1$, $\xi_N \sim 1.0$, anchoring strength $W = 10^{-2}$ and geometry $r_w = 0.21$. The defect rises in the wedge until eventually it reaches the right apex of the wedge, marked with a yellow circle. This is accompanied by a significant decrease in the free energy.

7.2.3.4 Changing the ratio of elastic constants K_1/K_3

We now extend our simulations to a ratio $K_1/K_3 = 1/10$. Initial two-dimensional simulations, with periodic boundary conditions imposed along the y direction, revealed that fixing the preferred orientation on the side walls of the wedge is not sufficient to keep the director field $\mathbf{n}$ restricted to the x-z plane. This is due to the higher energy cost of bending deformations, as K_3 is larger. Therefore, the system tries to minimize its energy by rotating the molecules in such a way, that they have a considerable component along the y direction, i.e. perpendicular to the plane of the wedge. By doing this the system also avoids the presence of a defect.

In order to restrict the liquid crystal molecules to the x-z plane, we ran a set of three-dimensional simulations where additional walls, located at y = 0 and y = b, were implemented in the x-z plane. We chose the thickness of the channel to be $b = 3$. The geometry used is shown in Fig. 7.14. We enforced planar degenerate anchoring on the walls at y = 0 and y = b,

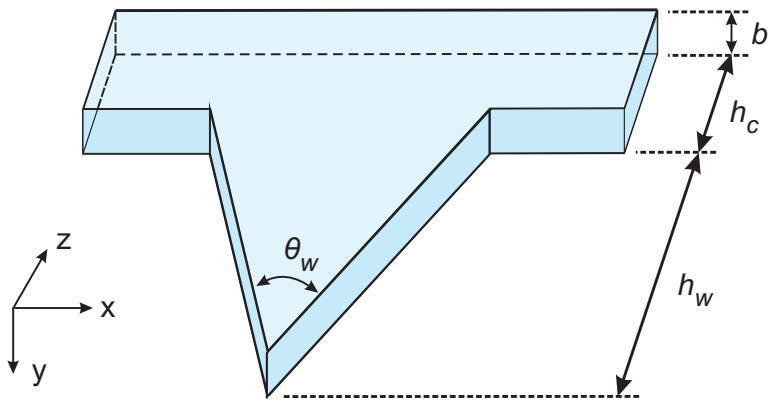

Figure 7.14: Three-dimensional channel geometry used to study the liquid crystal system with $K_1/K_3 = 1/10$. Degenerate planar anchoring is imposed on the walls located at y = 0 and y = b. The thickness b of the channel is small enough (compared to h_c and h_w) that the boundary conditions restrict the liquid crystal molecules to lie in the x-z plane.

while on the side walls of the wedge we set the preferred director orientation as before. In this case, due to the confinement imposed by the top and bottom walls, the molecules remain in the x-z plane.

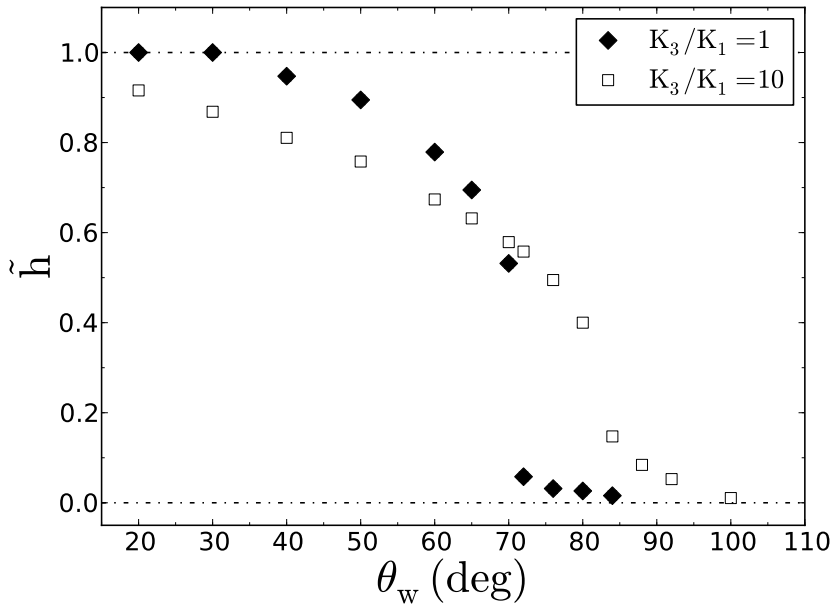

Figure 7.15: The relative position of defect in the wedge $\tilde{h}$ as a function of the wedge opening angle θ_w for different ratios of elastic constants K_1/K_3. ξ_N~1.0 and geometry with $r_w = 0.21$.

For $K_1/K_3 = 1/10$, it is reasonable to expect that the splay-bend threshold will be shifted to higher angles θ_w than for $K_1/K_3 = 1$, due to the lower (higher) free energy cost of a

splay (bend) configuration. Our results for the defect position $\tilde{h}$ as a function of θ_w, shown in Fig. 7.15, support this. A pure bend configuration is observed only for angles $\theta_w \geq 100°$, compared to $\theta_w \geq 76°$ for the case of $K_1/K_3 = 1$. Moreover, $\tilde{h}$ reaches smaller values than for $K_1/K_3 = 1$ in the regime of small angles. This is due to the fact that higher $\tilde{h}$ would cause stronger bending deformations in the main channel. This, however, is energetically more costly and, therefore, not favorable. Fig. 7.16 shows the director field for the two different ratios of K_1/K_3 near the top of the wedge for $\theta_w = 40°$. For $K_1/K_3 = 1$ elastic distortions are evident in the main channel, while for $K_1/K_3 = 1/10$ the director field in the main channel remains uniformly aligned.

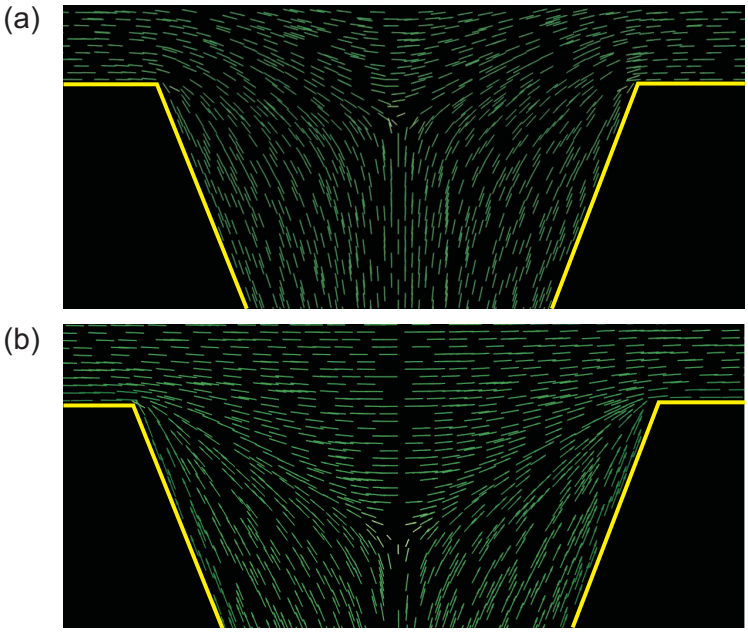

Figure 7.16: Director field in the regime of the wedge entrance for opening angle $\theta_w = 40°$ and different ratios of elastic constants: a) $K_1/K_3 = 1$ and b) $K_1/K_3 = 1/10$. $\xi_N \sim 1.0$ and $r_w = 0.21$.

7.3 Discussion - Comparison to experiments using *fd* virus particles

In this chapter we examined a nematic liquid crystal confined in a wedge-structured geometry, where the equilibrium director configuration is determined by the interplay between the surface anchoring imposed by the confining walls and elasticity. Experiments presented in section 7.1

using *fd* virus as a colloidal nematic liquid crystal revealed a splay-bend transition occurring between wedge angles $\theta_w = 70^\circ - 80^\circ$. Stable bend configurations were observed for $\theta_w \geq 80^\circ$, while splay deformations were favorable for $\theta_w \leq 70^\circ$. The complete alignment of the *fd* virus particles at the side walls indicates strong planar anchoring and, therefore, the location of the splay-bend transition depends on the ratio of splay K_1 to bend K_3 elastic constants. From reported values of elasticities of liquid crystals with a similar flexibility to the *fd* virus we expect $K_1/K_3 \approx 1$ [108].

Extensive lattice Boltzmann simulations enabled a fuller exploration of the parameter space and revealed the underlying origin of the transition and its dependence on rod flexibility and channel geometry. Using the ratio $K_1/K_3 = 1$ in simulations showed that, if only the wedge part of the channel was considered, the splay-bend transition would occur at $\theta_w \sim 90^\circ$. However, taking into account the complete channel geometry, with the main channel having a horizontal nematic configuration, shifts the transition to smaller angles. Numerical results showed a splay-bend transition occurring at the same regime of wedge angles θ_w as in the experiments, when the ratio of elastic constants splay to bend is $K_1/K_3 = 1$. This verifies that the expected ratio K_1/K_3 for semi-flexible rods, like the *fd* virus, is approximately $K_1/K_3 \sim 1$, although, more detailed experiments are required to specify the exact value.

Furthermore, our simulations suggest that this is a sharp transition occurring at the same wedge angle $\theta_w \sim 70^\circ$, irrespective of the main channel's height h_c. In fact the relevant parameter is the ratio of the nematic correlation length to the height of the wedge ξ_N/h_w. For angles $\theta_w \leq 70^\circ$ a splay configuration originates from the tip of the wedge and the inevitable frustration of the director field leads to the formation of an $s = -1/2$ defect in the bulk of the wedge. In the limit of strong anchoring, our simulations enable us to predict the position of the defect within the wedge as a function of opening angle, and elucidate its role in the change of director structure. For intermediate anchoring strengths we demonstrated that, for small angles θ_w, the defect can be expelled towards one of the apexes of the wedge.

Finally, decreasing the ratio of elastic constants to $K_1/K_3 = 1/10$ showed that the splay-bend transition is shifted to higher wedge opening values as expected. More precisely, we found numerically that pure bend deformations are in this case restricted to above $\theta_w \sim 100^\circ$.

One concluding remark is that, even though our study was restricted to finding the equilibrium configuration in the case where the director field $\mathbf{n}$ in the main channel has a horizontal

orientation, the system could be further studied to find the geometry that supports two stable equilibrium configurations. This again should depend on the ratios of elastic constants. Such a geometry might be useful for the design of bistable display devices [85–93].

Chapter 8

Conclusions and Future Work

In this thesis we studied two soft condensed matter topics. The first one dealt with a "textbook" instability, the Saffman-Taylor instability. This refers to the forced displacement of a viscous fluid in a Hele-Shaw cell by a less viscous fluid, leading to the formation of viscous fingers. Recent experiments using colloid-polymer mixtures in microchannels enabled, for the first time, a full three-dimensional, direct observation of fluid interfaces and the Saffman-Taylor instability. The research presented in this thesis was spurred on by these experiments and the unique opportunities offered by their combination with numerical simulations.

As a means of numerically studying the viscous fingering instability we used a free energy lattice Boltzmann algorithm, which proved a powerful tool in disentangling the physics of the instability. The method constitutes a diffuse interface model, meaning that the fluid-fluid interface is not sharp, but rather has a finite width. Therefore, discretisation constraints originating from the need to have a smooth transition from one fluid phase to the other, mean that the fluid-fluid interface is unphysically wide when modeling nm-wide interfaces in molecular fluids, and care must be taken that this does not affect the results. However, in colloid-polymer mixtures the width of the interface is $\sim \mu m$, which allows a quantitative comparison of simulations to experiments.

In Chapter 4 we examined the Saffman-Taylor instability in the neutral wetting case, when neither of the two fluids prefer to wet the walls of the channel. Turning our attention first to the x-z plane we distinguished two regimes, based on the shape of the advancing interface. The interface can either completely displace the more viscous fluid in the x-z plane, in which case it advances as a meniscus, or it can penetrate forming a finger in the gap of the cell and leaving

a thin film of the displaced fluid behind. These regimes, coined the Meniscus and the Thin Film regime respectively, are determined by the interplay of capillary and Péclet numbers. We verified that the penetration process in the x-z plane is controlled by the product $CaPe$, in agreement with the numerical work of Ledesma *et al.* [14].

We then considered the x-y plane and the Saffman-Taylor instability. We found that in the Meniscus regime the relative finger width λ_f scales with a modified capillary number $1/B^*$, which takes into account corrections due to curvature effects in the x-z plane, in agreement with [15]. These effects had been completely ignored in the early theoretical attempts to study the instability, since one of the basic assumptions of researchers was that the curvature of the interface in the x-z plane was constant. In the Thin Film regime, however, we observed much wider fingers that did not scale with $1/B^*$. In contrast to the classical behavior of fingers becoming narrower with increasing capillary number, we observed that finger widths λ_f were increasing or maintaining a constant value with increasing $1/B^*$. We demonstrated that this was a consequence of the higher modified Reynolds numbers Re^* and Weber numbers We^* achieved in the Thin Film regime when compared to the Meniscus regime. Therefore, this effect should be attributed to inertial effects, in agreement with experimental evidence [45] and recent analytical work on inertial effects in Hele-Shaw flows [48, 49].

In Chapter 5, we examined for the first time the Saffman-Taylor instability in the complete wetting regime, when the displacing fluid completely wets the walls. The same interface configurations, Meniscus and Thin Film, were distinguished in the x-z plane as for neutral wetting. The relevant control parameters for the penetration process are now capillary and Péclet numbers, scaled to take account of the thickness of the wetting layer. However, fingering in the x-z plane is now strongly suppressed and it is more difficult to enter the Thin Film regime than it was in the neutral wetting case. Much higher capillary and Péclet numbers are needed to change the concavity of the meniscus and induce a penetrating interface structure. Furthermore, increasing the viscosity contrast makes fingering in the x-z plane even harder. This in turn suppresses fingering in the x-y plane and the onset of the Saffman-Taylor instability. Our results emphasize the importance of the third dimension on the Saffman-Taylor instability and demonstrate that dynamics in the x-z plane are coupled to the dynamics in the x-y plane. A similar suppression of the instability is observed in the experiments on colloid-polymer mixtures.

An area still to explore is the relative finger width λ_f in the complete wetting regime. In particular, it is interesting to examine the dependence of λ_f on the viscosity contrast, since we have seen that this controls the interface structure in the x-z plane, which in turn affects the onset of fingering in the x-y plane. However, full three-dimensional simulations in the complete wetting regime require large simulation domains and were not investigated in this thesis due to the limitations in simulation time. Experimental results of λ_f plotted in Fig. 5.24, show that finger widths for viscosity contrast $r = 0.36$ are not only obtained at smaller capillary numbers, but are also much narrower than λ_f obtained for $r = 0.84$.

The second part of the thesis examined nematic liquid crystals confined in wedge-structured channels. This was motivated by recent experiments in microchannels using *fd* virus particles as a colloidal, nematic liquid crystal. The director configuration in confined geometries is determined by the complex interplay of confinement, surface anchoring and elasticity. Considering strong anchoring we showed that decreasing the wedge opening angle leads to a bend to splay transition, the location of which depends on the ratio of splay to bend elastic constants K_1/K_3. Decreasing the ratio K_1/K_3 shifts the transition to higher values of the wedge opening angle as expected. Moreover, when a splay configuration originates from the tip of the wedge, the inevitable frustration of the director field leads to formation of a defect in the centre of the wedge. We demonstrated that the position of the defect within the wedge can be controlled by varying the wedge opening angle.

For intermediate anchoring strengths, i.e. larger extrapolation lengths ξ_s, the defect may no longer be located in the bulk of the wedge, but can be expelled towards one of the apexes of the wedge. This is because the energy associated with the surface anchoring is not too large, and an overall reduction in the free energy is achieved by expelling the defect. Clearly this transition depends on the relative importance of surface anchoring strength and elasticities, and therefore can be interpreted in terms of the extrapolation length ξ_s. Increasing ξ_s will shift this transition to higher wedge angles. So an open area for investigation is to determine the location of the transition as a function of ξ_s and the wedge geometry.

Another fruitful direction for future research, that combines both of the problems considered in this thesis, is to investigate the Saffman-Taylor instability using an isotropic-nematic mixture. Experimental work using a molecular nematic liquid crystal as the more viscous fluid was carried out in radial Hele-Shaw channels [109, 110] leading to dendritic and side-wrinkling

fingers and in linear channels leading to asymmetric fingers, while for large values of $1/B$ side-wrinkling, tip-splitting and side-branching occurred [111]. However, there are still open questions. For example, it would be interesting to investigate the instability, both numerically and using the *fd* virus to allow direct observation of the interface, to examine how the flow alignment of the director field and the resulting anisotropic viscosity in the nematic phase of the liquid crystal, or the anchoring at the isotropic-nematic interface and wetting effects affect the instability.

Preliminary work has been done on simulating an isotropic-nematic mixture. In this case the Landau-de Gennes free energy functional, Eq. (6.30), is modified to allow for a binary phase separation into two phases, an isotropic phase with concentration ϕ_1 and a nematic phase with concentration ϕ_2 ($\phi_1 < \phi_2$). Moreover, the hydrodynamic equations of motion are supplemented by a convection-diffusion equation that describes the dynamics of the concentration field. Numerically, the parameter γ (see Eq. (6.11)), which controls the location of the isotropic-nematic transition, is coupled to the concentration ϕ so that in the isotropic (nematic) phase $\gamma < 2.7$ ($\gamma > 2.7$). In this case the mixture phase separates into two phases with different concentrations, which in turn drives the orientational ordering.

Our aim is to, then, include activity in our simulations and examine active systems. These systems, such as suspensions of bacteria, swimming algae, cytoskeletal gels cross-linked by molecular motors etc, are receiving increasing theoretical and experimental attention [112–121]. They are called "active", because they continually burn energy and, hence, are driven out of thermodynamic equilibrium even in the absence of any external forcing. One of their most striking properties is that they can exhibit spontaneous flow. As a first step, we would like to investigate the behavior of mixtures that phase separate into an isotropic and an active nematic phase. It would be interesting to study how activity affects the phase separation dynamics, and especially if it can drive phase separation in cases where the passive counterpart mixture would not have phase separated. Once the system is phase separated, and independent active nematic droplets are formed in an isotropic fluid environment, it would be interesting to examine how these droplets interact and set up an independent spontaneous flow and collective swarming. Finally, we would also like to study systems with spatially inhomogeneous activity, which have shown a much richer phenomenology than uniform systems [122].

Bibliography

[1] P. G. Saffman and G. Taylor. The penetration of a fluid into a porous medium or Hele-Shaw cell containing a more viscous liquid. *Proceedings of the Royal Society of London. Series A, Mathematical and Physical Sciences*, 245(1242):312–329, 1958.

[2] P. G. de Gennes and J. Prost. *The Physics of Liquid Crystals (International Series of Monographs on Physics)*. Oxford University Press, USA, 2 edition, 1995.

[3] D. Bensimon, L. P. Kadanoff, S. Liang, B. I. Shraiman, and C. Tang. Viscous flows in two dimensions. *Rev. Mod. Phys.*, 58:977–999, 1986.

[4] G. Tryggvason and H. Aref. Numerical experiments on Hele Shaw flow with a sharp interface. *Journal of Fluid Mechanics*, 136:1–30, 1983.

[5] G. M. Homsy. Viscous fingering in porous media. *Annual Review of Fluid Mechanics*, 19(1):271–311, 1987.

[6] S. A. Khan, G. A. Pope, and J. A. Trangenstein. Micellar/polymer physical-property models for contaminant cleanup problems and enhanced oil recovery. *Transp. Porous Media*, 24(1):35–79, 1996.

[7] R. Juanes, H. S. Al-shuraiqi, A. H. Muggeridge, C. A. Grattoni, and M. J. Blunt. Experimental and numerical validation of an analytical model of viscous fingering in two-phase, three-component flow. *Earth Science*, v(1):1–29, 2005.

[8] T. T. Norton and E. J. Fernandez. Viscous fingering in size exclusion chromatography: Insights from numerical simulation. *Industrial & Engineering Chemistry Research*, 35(7):24602468, 1996.

[9] M. P. Ryan. *Magmatic Systems*. Orlando, FL: Academic Press, 1994.

[10] E. Pitts. Penetration of fluid into a Hele-Shaw cell: the Saffman-Taylor experiment. *Journal of Fluid Mechanics*, 97(01):53–64, 1980.

[11] J. W. McLean and P. G. Saffman. The effect of surface tension on the shape of fingers in a Hele-Shaw cell. *Journal of Fluid Mechanics*, 102:455–469, 1981.

[12] P. Tabeling and A. Libchaber. Film draining and the Saffman-Taylor problem. *Phys. Rev. A*, 33(1):794–796, 1986.

[13] C. W. Park and G. M. Homsy. Two-phase displacement in Hele Shaw cells: theory. *Journal of Fluid Mechanics*, 139:291–308, 1984.

[14] R. Ledesma-Aguilar, A. Hernández-Machado, and I. Pagonabarraga. Three-dimensional aspects of fluid flows in channels. I. Meniscus and thin film regimes. *Physics of Fluids*, 19(10):102112, 2007.

[15] R. Ledesma-Aguilar, I. Pagonabarraga, and A. Hernández-Machado. Three-dimensional aspects of fluid flows in channels. II. Effects of meniscus and thin film regimes on viscous fingers. *Physics of Fluids*, 19(10):102113, 2007.

[16] R. Benzi, S. Succi, and M. Vergassola. The lattice Boltzmann equation: theory and applications. *Physics Reports*, 222(3):145–197, 1992.

[17] S. Succi. *The lattice Boltzmann equation for fluid dynamics and beyond.* Numerical mathematics and scientific computation. Clarendon Press; Oxford University Press, 2001.

[18] C. M. Pooley and K. Furtado. Eliminating spurious velocities in the free-energy lattice Boltzmann method. *Phys. Rev. E*, 77:046702, 2008.

[19] M. R. Swift, W. R. Osborn, and J. M. Yeomans. Lattice Boltzmann simulation of nonideal fluids. *Physical Review Letters*, 75(5):830–833, 1995.

[20] M. R. Swift, E. Orlandini, W. R. Osborn, and J. M. Yeomans. Lattice Boltzmann simulations of liquid-gas and binary fluid systems. *Phys. Rev. E*, 54(5):5041–5052, 1996.

[21] D. Jacqmin. Contact-line dynamics of a diffuse fluid interface. *Journal of Fluid Mechanics*, 402:57–88, 2000.

[22] P. Seppecher. Moving contact lines in the Cahn-Hilliard theory. *International Journal of Engineering Science*, 34(9):977 – 992, 1996.

[23] A. J. Briant, A. J. Wagner, and J. M. Yeomans. Lattice Boltzmann simulations of contact line motion. I. Liquid-gas systems. *Phys. Rev. E*, 69(3):031602, 2004.

[24] A. J. Briant and J. M. Yeomans. Lattice Boltzmann simulations of contact line motion. II. Binary fluids. *Phys. Rev. E*, 69(3):031603, 2004.

[25] P. G. de Gennes. Wetting: statics and dynamics. *Rev. Mod. Phys.*, 57(3):827–863, 1985.

[26] J. M. Yeomans. Mesoscale simulations: Lattice Boltzmann and particle algorithms. *Physica A: Statistical and Theoretical Physics*, 369(1):159 – 184, 2006.

[27] C. M. Pooley, H. Kusumaatmaja, and J. M. Yeomans. Contact line dynamics in binary lattice Boltzmann simulations. *Phys. Rev. E*, 78:056709, 2008.

[28] D. D'Humières, I. Ginzburg, M. Krafczyk, P. Lallemand, and L.-S. Luo. Multiple-relaxation-time lattice Boltzmann models in three dimensions. *Royal Society of London Philosophical Transactions Series A*, 2002.

[29] K. N. Premnath and J. Abraham. Three-dimensional multi-relaxation time (MRT) lattice-Boltzmann models for multiphase flow. *J. Comput. Phys.*, 224:539–559, 2007.

[30] J. Cahn. Critical-Point Wetting. *J. Chem. Phys.*, 66:3367, 1977.

[31] D. M. Anderson, G. B. McFadden, and A. A. Wheeler. Diffuse-interface methods in fluid mechanics. *Annual Review of Fluid Mechanics*, 30(1):139–165, 1998.

[32] P. L. Bhatnagar, E. P. Gross, and M. Krook. A model for collision processes in gases. I. Small amplitude processes in charged and neutral one-component systems. *Phys. Rev.*, 94:511–525, 1954.

[33] L.-S. Luo. Theory of the lattice Boltzmann method: Lattice Boltzmann models for nonideal gases. *Phys. Rev. E*, 62:4982–4996, 2000.

[34] A. J. C. Ladd and R. Verberg. Lattice-Boltzmann Simulations of Particle-Fluid Suspensions. *J. Stat. Phys.*, 104:1191, 2001.

[35] P. Lallemand and L.-S. Luo. Theory of the lattice Boltzmann Method: Dispersion, Dissipation, Isotropy, Galilean Invariance, and Stability. *Physical Review E Statistical Physics Plasmas Fluids And Related Interdisciplinary Topics*, 61(6 Pt A):6546–62, 2000.

[36] R. Du, B. Shi, and X. Chen. Multi-relaxation-time lattice Boltzmann model for incompressible flow. *Physics Letters A*, 359(6):564–572, 2006.

[37] V. M. Kendon, M. E. Cates, J.-C. Desplat, I. Pagonabarraga, and P. Bladon. Inertial effects in three-dimensional spinodal decomposition of a symmetric binary fluid mixture: a lattice Boltzmann study. *Journal of Fluid Mechanics*, 440(1):49, 2000.

[38] F. Fairbrother and A. E. Stubbs. Studies in electro-endosmosis. Part VI. The "bubble-tube" method of measurement. *J. Chem. Soc.*, pages 527–529, 1935.

[39] F. P. Bretherton. The motion of long bubbles in tubes. *Journal of Fluid Mechanics Digital Archive*, 10(02):166–188, 1961.

[40] G. I. Taylor. Deposition of a viscous fluid on the wall of a tube. *Journal of Fluid Mechanics*, 10(02):161–165, 1961.

[41] P. Tabeling, G. Zocchi, and A. Libchaber. An experimental study of the Saffman-Taylor instability. *Journal of Fluid Mechanics*, 177:67–82, 1987.

[42] D. A. Reinelt and P. G. Saffman. The penetration of a finger into a viscous fluid in a channel and tube. *SIAM Journal on Scientific and Statistical Computing*, 6(3):542–561, 1985.

[43] D. Halpern and D. P. Gaver. Boundary element analysis of the time-dependent motion of a semi-infinite bubble in a channel. *Journal of Computational Physics*, 115(2):366 – 375, 1994.

[44] D. A. Reinelt. The effect of thin film variations and transverse curvature on the shape of fingers in a hele–shaw cell. *Physics of Fluids*, 30(9):2617–2623, 1987.

[45] C. Chevalier, M. Ben Amar, D. Bonn, and A. Lindner. Inertial effects on SaffmanTaylor viscous fingering. *Journal of Fluid Mechanics*, 552(-1):83–97, 2006.

[46] P. Gondret and M. Rabaud. Shear instability of two-fluid parallel flow in a Hele-Shaw cell. *Physics of Fluids*, 1997.

[47] C. Ruyer-Quil. Inertial corrections to the Darcy law in a Hele-Shaw cell. *Comptes Rendus de l Academie des Sciences Series IIB Mechanics*, 329(5):337–342, 2001.

[48] E. O. Dias and J. A. Miranda. Influence of inertia on viscous fingering patterns: Rectangular and radial flows. *Phys. Rev. E*, 83:066312, 2011.

[49] E. O. Dias and J. A. Miranda. Inertial effects on rotating Hele-Shaw flows. *Phys. Rev. E*, 83:046311, 2011.

[50] A. J. Bray. Theory of phase-ordering kinetics. *Advances in Physics*, 43(3):357 – 459, 1994.

[51] S. Asakura and F. Oosawa. On interaction between two bodies immersed in a solution of macromolecules. *The Journal of Chemical Physics*, 22(7):1255–1256, 1954.

[52] S. Asakura and F. Oosawa. Interaction between particles suspended in solutions of macromolecules. *J. Polym. Sci.*, 33(126):183–192, 1958.

[53] A. Vrij. Polymers at interfaces and the interactions in colloidal dispersions. *Pure and Applied Chemistry*, 48(4):471–483, 1976.

[54] J. S. Rowlinson and B. Widom. *Molecular theory of capillarity*. International series of monographs on chemistry. Clarendon Press, 1982.

[55] P. G. de Gennes. *Scaling concepts in polymer physics*. G - Reference, Information and Interdisciplinary Subjects Series. Cornell University Press, 1979.

[56] G. A. Vliegenthart and H. N. W. Lekkerkerker. Measurement of the interfacial tension of demixed colloid-polymer suspensions. *Progress in Colloid Polymer Science*, 105(1):27–30, 1997.

[57] E. H. A. de Hoog and H. N. W. Lekkerkerker. Measurement of the interfacial tension of a phase-separated colloid-polymer suspension. *The Journal of Physical Chemistry B*, 103(25):5274–5279, 1999.

[58] E. H. A. de Hoog and H. N. W. Lekkerkerker. Breakup of an elongated droplet in a centrifugal field. *The Journal of Physical Chemistry B*, 105(47):11636–11640, 2001.

[59] B. Chen, B. Payandeh, and M. Robert. Order parameter and interfacial tension of a colloid-polymer system. *Physical Review E Statistical Physics Plasmas Fluids And Related Interdisciplinary Topics*, 62(2 Pt B):2369–72, 2000.

[60] D. G. A. L. Aarts, M. Schmidt, and H. N. W. Lekkerkerker. Direct visual observation of thermal capillary waves. *Science*, 304(5672):847–850, 2004.

[61] E. A. G. Jamie, G. J. Davies, M. D. Howe, R. P. A. Dullens, and D. G. A. L. Aarts. Thermal capillary waves in colloid-polymer mixtures in water. *Journal of Physics: Condensed Matter*, 20(49):494231, 2008.

[62] A. Lindner and C. Wagner. Viscoelastic surface instabilities. *Comptes Rendus Physique*, 10(8):712 – 727, 2009.

[63] D. Gareth. Development of colloid-polymer mixtures for the study of hydrodynamic instabilities in microfluidics. *Part II Thesis, Chemistry, University of Oxford (MChem)*, 2008.

[64] P. Petitjeans and T. Maxworthy. Miscible displacements in capillary tubes. Part 1. Experiments. *Journal of Fluid Mechanics*, 326:37–56, 1996.

[65] T. Dang-Vu, R. Jha, S.-Y. Wu, D. D. Tannant, J. Masliyah, and Z. Xu. Wettability determination of solids isolated from oil sands. *Colloids and Surfaces A: Physicochemical and Engineering Aspects*, 337(1-3):80 – 90, 2009.

[66] S. Chandrasekhar. *Liquid crystals*. Cambridge University Press, 1992.

[67] I. W. Stewart. *The Static and Dynamic Continuum Theory of Liquid Crystals: A Mathematical Introduction*. Liquid crystals book series. Taylor & Francis, 2004.

[68] O. D. Lavrentovich. Defects in liquid crystals: Surface and interfacial anchoring effects. *Chemical Physics*, Patterns o:161–195, 2003.

[69] S. Chandrasekhar, B. Sadashiva, and K. Suresh. Liquid crystals of disc-like molecules. *Pramana*, 9:471–480, 1977. 10.1007/BF02846252.

[70] M. S. Vijaya and G. Rangarajan. *Materials Science*. Tata McGraw-Hill, 2004.

[71] M. Shlens, M. R. Stoltz, and A. Benjamin. Orthopedic applications of Liquid Crystal Thermography. *The Western journal of medicine*, 122(5):367–370, 1975.

[72] F. C. Frank. I. Liquid crystals. On the theory of liquid crystals. *Discuss. Faraday Soc.*, 25:19–28, 1958.

[73] http://dept.kent.edu/spie/liquidcrystals/textures1.html.

[74] K. Schiele and S. Trimper. On the elastic constants of a nematic liquid crystal. *Physica Status Solidi (b)*, 118(1):267–274, 1983.

[75] A. N. Beris and B. J. Edwards. *Thermodynamics of Flowing Systems: with Internal Microstructure (Oxford Engineering Science Series)*. Oxford University Press, USA, 1994.

[76] F. M. Leslie. Theory of flow phenomena in nematic liquid crystals. *Advances In Liquid Crystals*, 4:235–253, 1968.

[77] B. J. Edwards, A. N. Beris, and M. Grmela. Generalized constitutive equation for polymeric liquid crystals Part 1. Model formulation using the Hamiltonian (poisson bracket) formulation. *Journal of Non-Newtonian Fluid Mechanics*, 35(1):51 – 72, 1990.

[78] M. Nobili and G. Durand. Disorientation-induced disordering at a nematic-liquid-crystal-solid interface. *Phys. Rev. A*, 46:R6174–R6177, Nov 1992.

[79] J.-B. Fournier and P. Galatola. Modeling planar degenerate wetting and anchoring in nematic liquid crystals. *Europhysics Letters*, 72(3):403, 2005.

[80] C. Denniston, E. Orlandini, and J. M. Yeomans. Lattice Boltzmann simulations of liquid crystal hydrodynamics. *Physical Review E - Statistical, Nonlinear and Soft Matter Physics*, 63(5 Pt 2):056702, 2000.

[81] C. Denniston, D. Marenduzzo, E. Orlandini, and J. M. Yeomans. Lattice Boltzmann algorithm for three-dimensional liquid-crystal hydrodynamics. *Philosophical Transactions of the Royal Society - Series A: Mathematical, Physical and Engineering Sciences*, 362(1821):1745–1754, 2004.

[82] M. Ravnik and S. Žumer. Landau-de Gennes modelling of nematic liquid crystal colloids. *Liquid Crystals*, 36(10-11):1201–1214, 2009.

[83] O. Medalia, I. Weber, A. S. Frangakis, D. Nicastro, G. Gerisch, and W. Baumeister. Macromolecular architecture in eukaryotic cells visualized by cryoelectron tomography. *Science*, 298(5596):1209–1213, 2002.

[84] M. S. E. Silva, J. Alvarado, J. Nguyen, N. Georgoulia, B. M. Mulder, and G. H. Koenderink. Self-organized patterns of actin filaments in cell-sized confinement. *Soft Matter*, 7:10631–10641, 2011.

[85] R. N. Thurston, J. Cheng, and G. D. Boyd. Mechanically bistable liquid-crystal display structures. *IEEE Transactions on Electron Devices*, 27(11):2069 – 2080, 1980.

[86] C. Tsakonas, A. J. Davidson, C. V. Brown, and N. J. Mottram. Multistable alignment states in nematic liquid crystal filled wells. *Applied Physics Letters*, 90(11):111913, 2007.

[87] S. Ladak, A. Davidson, C. V. Brown, and N. J. Mottram. Sidewall control of static azimuthal bistable nematic alignment states. *Journal of Physics D: Applied Physics*, 42(8):085114, 2009.

[88] T. J. Spencer and C. M. Care. Lattice Boltzmann scheme for modeling liquid-crystal dynamics: Zenithal bistable device in the presence of defect motion. *Phys. Rev. E*, 74:061708, 2006.

[89] A. Majumdar, C. J. P. Newton, J. M. Robbins, and M. Zyskin. Topology and bistability in liquid crystal devices. *Phys. Rev. E*, 75:051703, 2007.

[90] G. Carbone, G. Lombardo, R. Barberi, I. Musevic, and U. Tkalec. Mechanically induced biaxial transition in a nanoconfined nematic liquid crystal with a topological defect. *Physical Review Letters*, 103(16):167801, 2009.

[91] L. A. Parry-Jones, R. B. Meyer, and S. J. Elston. Mechanisms of flexoelectric switching in a zenithally bistable nematic device. *Journal of Applied Physics*, 106(1):014510, 2009.

[92] A. J. Davidson, C. V. Brown, N. J. Mottram, S. Ladak, and C. R. Evans. Defect trajectories and domain-wall loop dynamics during two-frequency switching in a bistable azimuthal nematic device. *Phys. Rev. E*, 81:051712, 2010.

[93] A. J. Davidson and N. J. Mottram. Conformal mapping techniques for the modelling of liquid crystal devices. *European Journal of Applied Mathematics*, 23(Special Issue 01):99–119, 2012.

[94] Paul van der Schoot and Ronald Otten, from the Department of Applied Physics, Eindhoven University of Technology, proposed a possible choice for the director field for the two configurations in a wedge and carried out the analytical calculations.

[95] J. M. Romero-Enrique, C.-T. Pham, and P. Patricio. Scaling of the elastic contribution to the surface free energy of a nematic liquid crystal on a sawtoothed substrate. *Phys. Rev. E*, 82:011707, 2010.

[96] M. P. Lettinga and E. Grelet. Self-diffusion of rodlike viruses through smectic layers. *Physical Review Letters*, 99:197802, 2007.

[97] Z. Dogic, K. R. Purdy, E. Grelet, M. Adams, and S. Fraden. Isotropic-nematic phase transition in suspensions of filamentous virus and the neutral polymer Dextran. *Phys. Rev. E*, 69:051702, 2004.

[98] E. Pouget, E. Grelet, and M. P. Lettinga. Dynamics in the smectic phase of stiff viral rods. *Phys. Rev. E*, 84:041704, 2011.

[99] J. Crocker. Methods of Digital Video Microscopy for Colloidal Studies. *Journal of Colloid and Interface Science*, 179(1):298–310, 1996.

[100] Z. Dogic and S. Fraden. Cholesteric phase in virus suspensions. *Phase Transitions*, (15):7820–7824, 2000.

[101] M. P. Lettinga, Z. Dogic, H. Wang, and J. Vermant. Flow behavior of colloidal rodlike viruses in the nematic phase. *Langmuir*, 21(17):8048–8057, 2005.

[102] S. Faetti, M. Gatti, V. Palleschi, and T. J. Sluckin. Almost critical behavior of the anchoring energy at the interface between a nematic liquid crystal and a SiO substrate. *Physical Review Letters*, 55:1681–1684, 1985.

[103] R. Barberi and G. Durand. Order parameter of a nematic liquid crystal on a rough surface. *Phys. Rev. A*, 41:2207–2210, 1990.

[104] G. Barbero and G. Durand. Curvature induced quasi-melting from rough surfaces in nematic liquid crystals. *J. Phys. II France*, 1(6):651–658, 1991.

[105] G. Skačej, A. L. Alexe-Ionescu, G. Barbero, and S. Žumer. Surface-induced nematic order variation: Intrinsic anchoring and subsurface director deformations. *Phys. Rev. E*, 57:1780–1788, 1998.

[106] V. Mocella, C. Ferrero, M. Iovane, and R. Barberi. Numerical investigation of surface distortion and order parameter variation in nematics. *Liquid Crystals*, 26(9):1345–1350, 1999.

[107] D. L. Cheung and F. Schmid. Monte Carlo simulations of liquid crystals near rough walls. *The Journal of Chemical Physics*, 122(7):074902, 2005.

[108] S.-D. Lee and R. B. Meyer. Computations of the phase equilibrium, elastic constants, and viscosities of a hard-rod nematic liquid crystal. *The Journal of Chemical Physics*, 84(6):3443–3448, 1986.

[109] A. Buka, P. Palffy-Muhoray, and Z. Rácz. Viscous fingering in liquid crystals. *Physical Review A*, 36(8):3984, 1987.

[110] A. Buka. Pattern formation in liquid crystals. *Physica Scripta*, 1989(T25):114, 1989.

[111] L. Lam, H. C. Morris, R. F. Shao, S. L. Yang, Z. C. Liang, S. Zheng, and H. Liu. Dynamics of viscous fingers in Hele-Shaw cells of liquid crystals Theory and experiment. *Liquid Crystals*, 5(6):1813–1826, 1989.

[112] D. Humphrey, C. Duggan, D. Saha, D. Smith, and J. Kas. Active fluidization of polymer networks through molecular motors. *Nature*, 416(6879):413–416, 2002.

[113] T. B. Liverpool and M. C. Marchetti. Instabilities of isotropic solutions of active polar filaments. *Physical Review Letters*, 90:138102, 2003.

[114] Y. Hatwalne, S. Ramaswamy, M. Rao, and R. A. Simha. Rheology of active-particle suspensions. *Physical Review Letters*, 92:118101, 2004.

[115] K. Kruse, J. F. Joanny, F. Jülicher, J. Prost, and K. Sekimoto. Asters, vortices, and rotating spirals in active gels of polar filaments. *Physical Review Letters*, 92:078101, 2004.

[116] R. Voituriez, J. F. Joanny, and J. Prost. Spontaneous flow transition in active polar gels. *Europhysics Letters*, 70(3):7, 2005.

[117] M. E. Cates, S. M. Fielding, D. Marenduzzo, E. Orlandini, and J. M. Yeomans. Shearing active gels close to the isotropic-nematic transition. *Physical Review Letters*, 101(6):4, 2008.

[118] M. E. Cates, O. Henrich, D. Marenduzzo, and K. Stratford. Lattice Boltzmann simulations of liquid crystalline fluids: active gels and blue phases. *Soft Matter*, 5:3791–3800, 2009.

[119] D. Marenduzzo, E. Orlandini, M. E. Cates, and J. M. Yeomans. Steady-state hydrodynamic instabilities of active liquid crystals: hybrid lattice Boltzmann simulations. *Physical Review E - Statistical, Nonlinear and Soft Matter Physics*, 76(3 Pt 1):031921, 2007.

[120] A. Baskaran and M. C. Marchetti. Statistical mechanics and hydrodynamics of bacterial suspensions. *Proceedings of the National Academy of Sciences of the United States of America*, 106(37):15567–15572, 2009.

[121] L. Giomi, L. Mahadevan, B. Chakraborty, and M. F. Hagan. Excitable patterns in active nematics. *Physical Review Letters*, 106:218101, 2011.

[122] D. Marenduzzo and E. Orlandini. Hydrodynamics of non-homogeneous active gels. *Soft Matter*, 6(4):774–778, 2010.